APPLIED COMPUTATIONAL ELECTROMAGNETICS SOCIETY JOURNAL

November 2017
Vol. 32 No. 11
ISSN 1054-4887

The ACES Journal is abstracted in INSPEC, in Engineering Index, DTIC, Science Citation Index Expanded, the Research Alert, and to Current Contents/Engineering, Computing & Technology.

The illustrations on the front cover have been obtained from the research groups at the Department of Electrical Engineering, The University of Mississippi.

EMERITUS EDITORIAL ASSISTANTS

NOVEMBER 2017 REVIEWERS

THE APPLIED COMPUTATIONAL ELECTROMAGNETICS SOCIETY

JOURNAL

Vol. 32 No. 11 November 2017

TABLE OF CONTENTS

Realistic Full Wave Modeling of Focal Plane Array Pixels

Salvatore Campione [1], Larry K. Warne [1], Roy E. Jorgenson [1], Paul S. Davids [2], and David W. Peters [2]

[1] Electromagnetic Theory Department
Sandia National Laboratories, Albuquerque, NM 87185, USA
sncampi@sandia.gov, lkwarne@sandia.gov, rejorge@sandia.gov

[2] Applied Photonic Microsystems Department
Sandia National Laboratories, Albuquerque, NM 87185, USA
pdavids@sandia.gov, dwpeter@sandia.gov

Abstract ─ In this paper we investigate full-wave simulations of realistic implementations of multifunctional nanoantenna enabled detectors (NEDs). We focus on a 2x2 pixelated array structure that supports two wavelengths of operation. We design each resonating structure independently using full-wave simulations with periodic boundary conditions mimicking the whole infinite array. We then construct a supercell made of a 2x2 pixelated array with periodic boundary conditions mimicking the full NED; in this case, however, each pixel comprises 10-20 antennas per side. In this way, the cross-talk between contiguous pixels is accounted for in our simulations. We observe that, even though there are finite extent effects, the pixels work as designed, each responding at the respective wavelength of operation. This allows us to stress that realistic simulations of multifunctional NEDs need to be performed to verify the design functionality by taking into account finite extent and cross-talk effects.

Index Terms ─ Cross-talk, finite extent, multifunctional detectors, nanoantenna enabled detectors.

I. INTRODUCTION

Infrared detector arrays based on narrow bandgap, III-V semiconductors have made tremendous progress in the last decade [1]. Within III-V semiconductor alloys, those containing antimony have enabled certain heterostructures to exhibit a broken gap that is advantageous in some newer detector designs [2, 3]. These narrow bandgap semiconductors also show promise in electronic applications such as high-frequency, low-noise high-electron-mobility-transistors [4]. Highly doped semiconductor materials acting as plasmonic materials have also been explored [5-7].

In recent years, infrared detection has been enhanced through the use of plasmonic nanoantenna arrays on top of semiconductor heterostructures that contain the active material of a photodetector [8-12] (see schematic in Fig. 1 (a)). We define these detectors as *nanoantenna enabled detectors* (NEDs). The nanoantenna arrays generate enhanced fields that induce enhanced absorption within the active material of a photodetector, enhancing its overall performance. The standard way to design such a nanoantenna array is by using full-wave simulations employing periodic boundary conditions: this kind of simulation mimics an infinitely extended array.

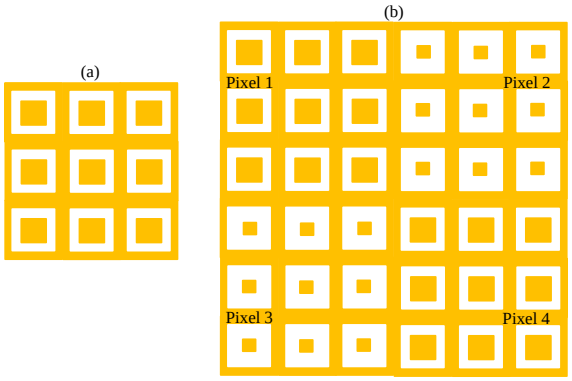

Fig. 1. (a) Illustration of a gold nanoantenna array. (b) Illustration of a multifunctional nanoantenna enabled detector made of a 2x2 pixel array, where each pixel may perform a different functionality.

In general, there is the need to have multifunctional detectors, and this can be potentially realized using NEDs. Two alternative options exist: (1) one NED that can change its performance via external stimuli, such as a bias voltage; and (2) multiple NEDs interleaved in space (see schematic in Fig. 1 (b), also referred to as pixelated arrays), where each pixel is designed to perform different functionalities. While the former is a very attractive platform, the difficulties that are inherent

Submitted On: November 2, 2016
Accepted On: October 4, 2017

to such a tunable design make the use of pixelated arrays the most viable solution for multifunctional NEDs. Functionalities may include different polarization properties, different spectral properties, etc. In this paper, we focus on modeling dual-band NEDs made of pixelated arrays. While each resonating structure can be independently designed using full-wave simulations with periodic boundary conditions, there is no guarantee that a pixelated array would perform as desired. This is because, (1) the extent of each pixel is finite, and thus comprises of a finite number of unit cells and may not fulfill the infinite condition imposed by the periodic boundary conditions; and (2) the cross-talk between contiguous pixels may dramatically affect the NED performance. We then construct a supercell made of a 2x2 pixelated array with periodic boundary conditions that allows us to take into account both the finite extent of each pixel as well as their cross-talk. We observe that the pixels work as designed, each responding at the respective wavelength of operation with some smaller interactions between pixels. However, this allows us to stress that realistic simulations of multifunctional NEDs need to be performed to verify the design functionality and improve their performance.

II. DESIGN OF THE NANOANTENNA STRUCTURES AT THE TWO WAVELENGTHS OF OPERATION

We aim to design a multifunctional NED structure that contains subpixels that work at different wavelengths. For simplicity of discussion, we focus on 4 pixels, displaced in a 2x2 pixelated array in a checker pattern as in Fig. 1 (b), where each diagonal pair works at two different wavelengths: 1) ~10 μm with ~1.5 μm bandwidth; and 2) ~8 μm with ~1 μm bandwidth. Each pixel is based on a gold nanoantenna design as in Fig. 1 (a) on top of a semiconductor heterostructure as illustrated in Fig. 2 (a). The complex index of refraction $n_c = n + ik$ of the absorber layer is reported versus wavelength in Fig. 2 (b). The monochromatic time harmonic convention, $\exp(-i\omega t)$, is used here and throughout the paper, and is suppressed hereafter. We employ finite difference time domain (FDTD) simulations using the commercial software FDTD Lumerical. The commercial software accepts the dispersive properties in Fig. 2 (b) and creates a multi-coefficient material model for use in the FDTD simulation.

We first design the two nanoantenna designs separately using full-wave simulations employing periodic boundary conditions. We have explored various mesh discretizations as to achieve a converged, accurate result. The design working at ~10 μm is shown in Fig. 3. The total absorption spectrum versus wavelength under normal plane wave incidence is reported as a black line in Fig. 3: high absorption is observed at ~9.75 μm and also at ~6.7 μm. The important aspect of this design is that it exhibits a minimum in absorption at ~8 μm to minimally interfere with the second band of interest (ideally this minimum should be zero). We plot in the same figure as red dashed curve the absorption in the absorber layer: one can note that this is a lower amount of energy than the black curve, indicating that the remaining energy is dissipated by the nanoantennas and the back mirror. We report electric field magnitude plots (in a *x*-*y* plane cut within the absorber layer) as insets of Fig. 3 at the wavelengths indicated by the vertical cyan lines, and one can see enhanced fields at the two resonances.

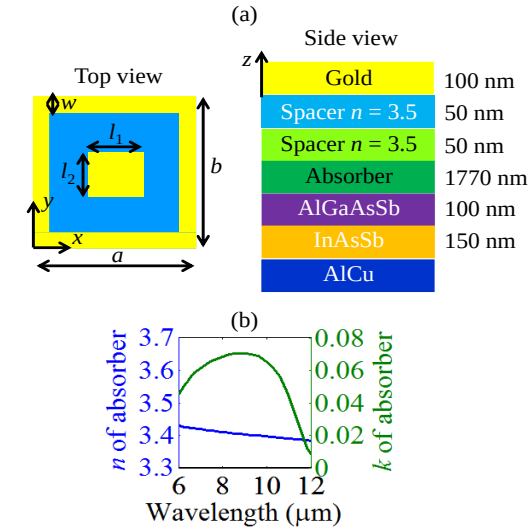

Fig. 2. (a) Top view and side view of a unit cell of the nanoantenna array on top of the semiconductor heterostructure: periods *a* and *b*, patch sides l_1 and l_2, and width *w*. (b) Real part *n* and imaginary part *k* of the complex index of refraction of the absorber versus wavelength.

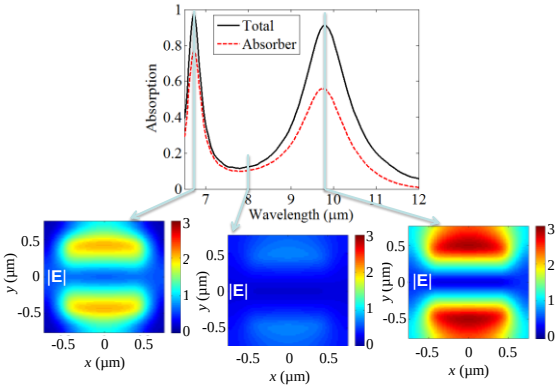

Fig. 3. Absorption spectrum of the nanoantenna design working at ~10 μm with $a = b = 1500$ nm, $l_1 = l_2 = 900$ nm and $w = 50$ nm. The insets show maps of the magnitude of the electric field at ~6.7 μm, ~8 μm, and ~9.75 μm.

The design working at ~8 µm is shown in Fig. 4, where we report the total absorption spectrum versus wavelength under normal plane wave incidence as a black line: high absorption is observed at ~8 µm. The important aspect of this design is that it exhibits a minimum in absorption at ~10 µm to minimally interfere with the second band of interest. We plot in the same figure as red dashed curve the absorption in the absorber layer: one can note that this is a lower amount of energy than indicated by the black curve, indicating that the remaining energy is dissipated by the nanoantennas and the back mirror. We report electric field magnitude plots (in a *x*-*y* plane cut within the absorber layer) at the wavelengths indicated by the vertical cyan lines, and one can see enhanced fields at the resonance supported by this structure.

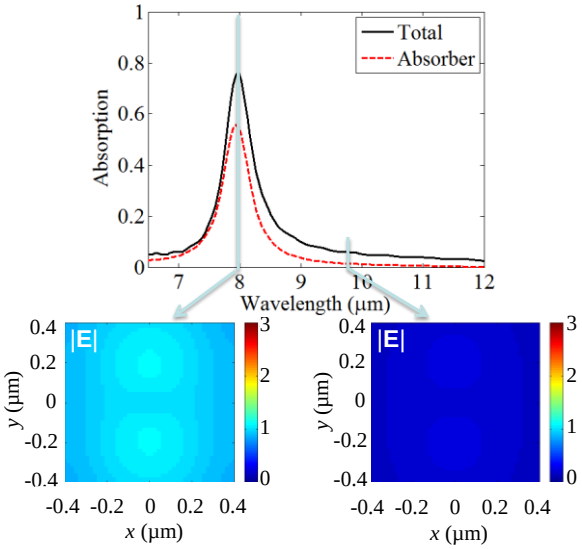

Fig. 4. Absorption spectrum of the nanoantenna design working at ~8 µm with $a = b = 800$ nm, $l_1 = l_2 = 150$ nm and $w = 50$ nm. The insets show maps of the magnitude of the electric field at ~8 µm and ~9.75 µm.

III. REALISTIC DUAL-BAND NANOANTENNA ENABLED DETECTORS

We construct a 30 µm x 30 µm NED supercell made of a 2x2 pixelated array as shown in Fig. 5, where each 15 µm x 15 µm pixel in the main diagonal is a finite extent version of the design reported in Fig. 4 and each 15 µm x 15 µm pixel in the anti-diagonal is a finite extent version of the design reported in Fig. 3: because of the different periods of the two designs, the main diagonal pixels contain 10 unit cells x 10 unit cells, whereas the anti-diagonal pixels contain 18 unit cells x 18 unit cells. Because of the finite extent of each pixel, it is of interest to determine if the detector will behave as designed, or rather the optical properties would be affected by cross-talk between the different pixels.

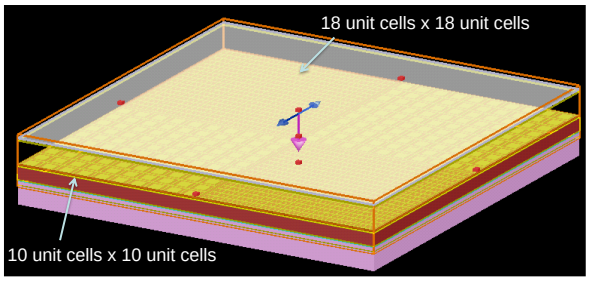

Fig. 5. Illustration of the 2x2 pixelated array NED in checker pattern. Note the finite extent of each pixel.

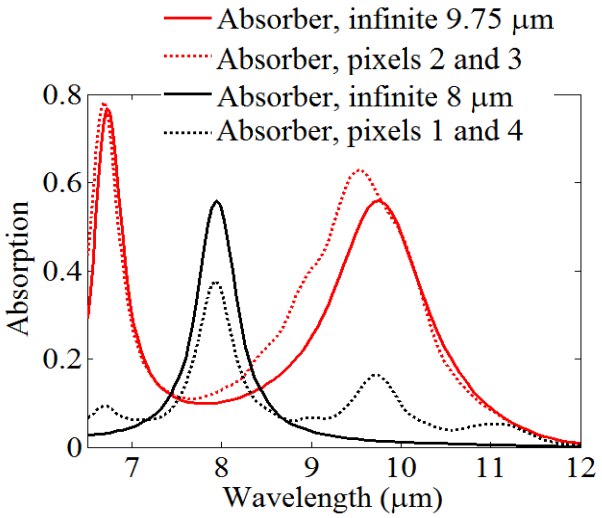

Fig. 6. Absorption spectrum of the dual-band detector in Fig. 5, highlighting the contributions of main-diagonal and anti-diagonal pixels separately (dotted lines). The results are compared to the infinite arrays (solid lines).

The simulated structure is $5\lambda x5\lambda$ at $\lambda = 6$ µm. In order to accurately model the pixelated array, we made use of a supercomputer and used a mesh similar to the one employed in the periodic simulations. We first plot in Fig. 6 the absorption spectrum of the dual-band detector in Fig. 5, restricting the contributions to the main-diagonal (Pixels 1 and 4) and anti-diagonal pixels (Pixels 2 and 3) separately (as indicated in Fig. 1 (b)). One can see that the pixel supporting the resonance at ~10 µm behaves better than designed, given that the absorber receives more power (see solid versus dotted red curves). Some minor finite extent and cross-talk effects are observed as a shoulder at ~9 µm. When looking at the result relative to the pixel supporting the resonance at ~8 µm, we see that it behaves worse than designed. In particular, we see that the absorber receives less power, and absorbs in frequency bands where it shouldn't, due to evident finite extent and cross-talk effects. Nonetheless, the overall behavior of the NED array is satisfactory, and these realistic simulations

can be used to assess (and possibly improve) NED performance.

The complete NED supercell detector design operation is summarized in Fig. 7, where we report the total absorption spectrum versus wavelength under normal plane wave incidence as a black line: high absorption is observed at ~9.75 μm, ~8 μm, and ~6.7 μm --- the three resonances observed in Sec. 2 for the individual designs. We plot in the same figure as red dashed curve the absorption in the absorber layer: one can note that this is a lower amount of energy than the black curve, indicating that the remaining energy is dissipated by the nanoantennas and the back mirror. We report electric field magnitude plots in the insets of Fig. 7 (in a *x*-*y* plane cut within the absorber layer) at the wavelengths indicated by the vertical cyan lines, and one can see enhanced fields at the resonances, with the anti-diagonal pixels mainly illuminated at ~9.75 μm, and the main-diagonal pixels mainly illuminated at ~8 μm. This shows that, although some cross-talk is inevitably present, the dual-band detector can actually work effectively as designed. Because these are uniformly illuminated arrays, it seems reasonable that the cross-talk effects observed in Fig. 7 are likely due to just off-resonance response of the pixels to the uniform illumination.

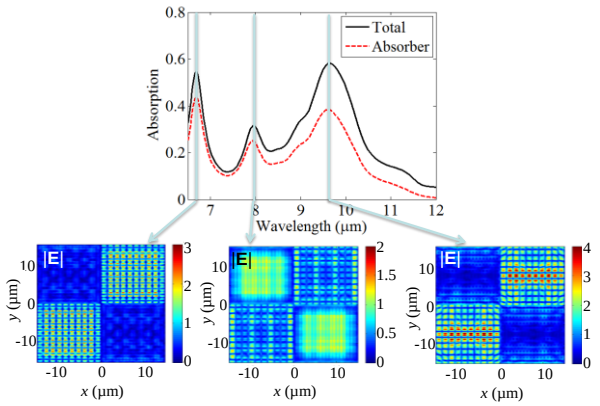

Fig. 7. Absorption spectrum of the dual-band NED in Fig. 5. The insets show maps of the magnitude of the electric field at ~6.7 μm, ~8 μm, and ~9.75 μm.

IV. CONCLUSION

In this paper we have investigated full-wave simulations of realistic implementations of multifunctional nanoantenna enabled detectors. We have shown that it is pivotal to simulate the entire structure comprising finite extent pixels to correctly account for the cross-talk between contiguous pixels. We observed that, even though there are finite extent and cross-talk effects affecting the performance of the dual-band NED, the pixels work as designed, each responding at the respective wavelength of operation. Nonetheless, realistic simulations of multifunctional detectors need to be performed to verify the design functionality by taking into account finite extent and cross-talk effects. Although we have analyzed normal incidence illumination of our NED detector structure, the envisioned applications will be subjected to up to 10 degrees oblique incidence illumination. We have modeled both transverse electric (TE) and magnetic (TM) oblique incidence (10 degrees) and observed very minimal change to the normal incidence case.

ACKNOWLEDGMENT

This work was supported by the Laboratory Directed Research and Development program at Sandia National Laboratories. Sandia National Laboratories is a multimission laboratory managed and operated by National Technology and Engineering Solutions of Sandia, LLC.; a wholly owned subsidiary of Honeywell International, Inc., for the U.S. Department of Energy's National Nuclear Security Administration under contract DE-NA-0003525.

REFERENCES

[1] N. K. Dhar, R. Dat, and A. K. Sood, "Advances in infrared detector array technology," in *Optoelectronics - Advanced Materials and Devices*, S. L. Pyshkin and J. M. Ballato, Eds., InTech, 2013.

[2] P. Martyniuk, M. Kopytko, and A. Rogalski, "Barrier infrared detectors," *Opto-Electronics Review*, vol. 22, pp. 127-146, 2014.

[3] E. A. Plis, "InAs/GaSb type-II superlattice detectors," *Advances in Electronics*, vol. 2014, p. 12, 2014.

[4] C. Liu, Y. Li, and Y. Zeng, "Progress in antimonide based III-V compound semiconductors and devices," *Engineering*, vol. 2, pp. 617-624, 2010.

[5] S. Law, R. Liu, and D. Wasserman, "Doped semiconductors with band-edge plasma frequencies," *Journal of Vacuum Science & Technology B*, vol. 32, p. 052601, 2014.

[6] D. Wei, C. Harris, C. C. Bomberger, J. Zhang, J. Zide, and S. Law, "Single-material semiconductor hyperbolic metamaterials," *Optics Express*, vol. 24, pp. 8735-8745, 2016/04/18 2016.

[7] S. Law, D. C. Adams, A. M. Taylor, and D. Wasserman, "Mid-infrared designer metals," *Optics Express*, vol. 20, pp. 12155-12165, 2012/05/21 2012.

[8] D. W. Peters, C. M. Reinke, P. S. Davids, J. F. Klem, D. Leonhardt, J. R. Wendt, *et al.*, "Nanoantenna-enabled midwave infrared focal plane arrays," pp. 83533B-83533B-6.

[9] S. Choi and K. Sarabandi, "Bowtie nanoantenna integrated with indium gallium arsenide antimonide for uncooled infrared detector with enhanced sensitivity," *Applied Optics*, vol. 52, pp. 8432-8438,

2013/12/10 2013.
[10] D. W. Peters, P. S. Davids, J. K. Kim, D. Leonhardt, T. E. Beechem, S. W. Howell, *et al.*, "Application of plasmonic subwavelength structuring to enhance infrared detection," pp. 899419-899419-6, 2014.
[11] M. D. Goldflam, E. A. Kadlec, B. V. Olson, J. F. Klem, S. D. Hawkins, S. Parameswaran, *et al.*, "Enhanced infrared detectors using resonant structures combined with thin type-II superlattice absorbers," *Applied Physics Letters*, vol. 109, p. 251103, 2016/12/19 2016.
[12] M. D. Goldflam, S. D. Hawkins, S. Parameswaran, A. Tauke-Pedretti, L. K. Warne, D. W. Peters, *et al.*, "Next-generation infrared focal plane arrays for high-responsivity low-noise applications," in *2017 IEEE Aerospace Conference*, pp. 1-7, 2017.

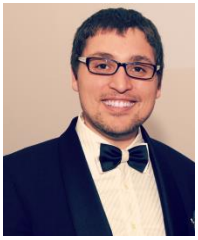

Salvatore Campione received a Laurea triennale degree (cum laude) and a Laurea Magistrale degree (cum laude) in Electronic Engineering from the Polytechnic of Turin, Italy, in 2007 and 2009, respectively. He also received a Master of Science degree in electrical and computer engineering from the University of Illinois at Chicago, IL, USA, in 2009, and a Doctor of Philosophy degree in electrical and computer engineering from the University of California Irvine, CA, USA, in 2013.

Dr. Campione has been a visiting scholar at the U.S. Army Charles M. Bowden Research Center, RDECOM, Redstone Arsenal, Huntsville, AL, USA in 2012 and at the Center for Integrated Nanotechnologies at Sandia National Laboratories, Albuquerque, NM, USA in 2012 and 2013. He joined Sandia National Laboratories, Albuquerque, NM, USA as a Postdoctoral Appointee in 2014, and became a Senior Member of Technical Staff in 2016. He has published more than 65 peer-reviewed journal articles, more than 100 conference papers, 1 issued patent, and 2 book chapters. His research interests include electromagnetic theory, antennas, metamaterials and their applications, plasmonics in nanostructures, and optical devices for energy and optoelectronic applications.

Dr. Campione is a member of ACES, SPIE, IEEE, the IEEE Photonics Society, the IEEE Antennas and Propagation Society, and the IEEE Eta Kappa Nu (IEEE-HKN) Society. Among other awards, he received a 2013 Marconi Society Paul Baran Young Scholar Award, the 2016 IEEE-HKN Outstanding Young Professional Award, and the 2017 ACES Early Career Award.

Larry K. Warne received the B.S.E.E. degree from Fairleigh Dickinson University, Teaneck, NJ, in 1976 and the M.S.E.E. and Ph.D. degrees from the California Institute of Technology, Pasadena, in 1977 and 1984, respectively.

Since 1978, he has been employed at Sandia National Laboratories, Albuquerque, NM, where he is currently a Distinguished Member of the Technical Staff.

Roy E. Jorgenson was born in Portland, OR, on May 11, 1955. He received the B.S.E.E. degree from the University of Colorado, Boulder, in 1977 and the M.S. and Ph.D. degrees in electrical engineering from the University of Illinois at Urbana-Champaign, in 1985 and 1989, respectively.

He served as an Officer in the U.S. Army at Field Station Berlin, Berlin, Germany, until 1983. Since 1989, he has been with Sandia National Laboratories, Albuquerque, NM.

Paul S. Davids received his Ph.D in theoretical condensed matter physics in 1993 from Indiana University while as a graduate research associate in Theoretical Division at Los Alamos National Lab. He was then a postdoc in the Electronics Device and Materials group from 1993-1996. He then joined Intel Oregon and held various research positions from 1996-2008. He joined Sandia National lab in 2008 where he is currently a PMTS. He has over 75 papers and 23 issued patents with 18 pending.

David W. Peters received the B.S., M.S., and Ph.D. degrees in electrical engineering from the Georgia Institute of Technology, Atlanta, in 1992, 1993, and 2001, respectively. His graduate research was in the area of numerical modeling of diffractive optic structures. He is currently with Sandia National Laboratories, Albuquerque, NM, working on modeling of diffractive optics and photonic bandgap structures.

Dr. Peters is a Member of the Optical Society of America.

The Analogy between Offset Configurations of Parabolic Reflectors and Reflectarrays

Payam Nayeri [1], Atef Z. Elsherbeni [1], and Fan Yang [2]

[1] Electrical Engineering Department
Colorado School of Mines, Golden, CO 80401, USA
pnayeri@mines.edu, aelsherb@mines.edu

[2] Electronic Engineering Department
Tsinghua University, Beijing, China
fan_yang@tsinghua.edu.cn

Abstract ─ The analogous relationship between the design parameters of offset parabolic reflectors and offset reflectarrays is delineated. Each antenna is specified with four design parameters that best describe the system setup, and the mathematical relationship between the design parameters of these two antenna systems are determined. The presented study allows one to determine the analogous reflectarray system based on the design parameters of the offset reflector and vice versa. This makes it possible to simplify the configuration setup in offset reflectarrays using a coordinate system and a set of parameters that is very suitable for reflectarray design and analysis.

Index Terms ─ Antenna array, focal depth, offset parabolic reflector, reflectarray antenna.

I. INTRODUCTION

Parabolic reflector antennas have long served as the most suitable antenna for high-gain operation in both terrestrial and spaceborne applications [1, 2]. Since the breakthrough of printed antenna technology however, a new generation of high-gain antennas has been introduced, which not only possesses many of the favorable features of parabolic reflectors, but also integrates them with printed array technology. This hybrid antenna, known as reflectarray, offers many promising features such as low-weight and low-profile, and low-cost, and as such has received a great deal of attention over the years [3, 4].

Reflectarray antennas are essentially built based on the concept of reflector antennas, and given the fact that reflector antenna technology is mature and well developed, it certainly is beneficial to take advantage of the developments that have been made in reflector design over generations. To this end, one should be able to describe a reflectarray system that exactly mimics the parabolic reflector system. However, in many cases, the design parameters for the reflectarray don't correlate directly with the reflector design parameters. This is due to the fact that for each antenna, the design parameters are given in manner that best describes its own system. While this is less of an issue for axisymmetric designs [5], the offset configuration is more complex. In particular, many important reflector design parameters such as focal depth are typically misinterpreted, while other parameters such as feed tilt angle, and offset height are essentially nonexistent in offset reflectarrays.

In this paper, we first review the offset parabolic reflector design characteristics, and then define a unique set of parameters that describes the offset reflectarray system. We then present the mathematical formulation that converts the design parameters of the parabolic reflector system to the reflectarray design parameters and vice versa. Comparison between the radiation patterns of an analogous reflector and reflectarray antenna is also presented which shows very similar performance. The work presented here simplifies the configuration setup in offset reflectarrays, by using a coordinate system and a set of parameters that is well suited for design and analysis of offset reflectarrays. Furthermore, it can be advantageous for complex reflectarray configurations, such as offset dual-reflectarray systems [6].

II. THE OFFSET SYSTEM CONFIGURATIONS

In any offset reflector configuration, many parameters exist that can be utilized to achieve the required design goals [2]. However, the most important reflector design parameters that can fully describe a focused offset system can be given in terms of four key parameters. The geometrical model of the offset parabolic reflector system is given in Fig. 1 (a), where the design parameters are:

Submitted On: July 12, 2017
Accepted On: October 10, 2017

- D = reflector diameter;
- F = focal length;
- H = offset height;
- ψ_B = feed tilt angle.

Note that the first three parameters completely describe the geometrical setup of the parabolic reflector, however since in general the primary feed does not point to the reflector center (C), for a full system specification it is necessary to specify the feed tilt angle. In the general case, the feed points to point B on the reflector surface as shown in Fig. 1 (a).

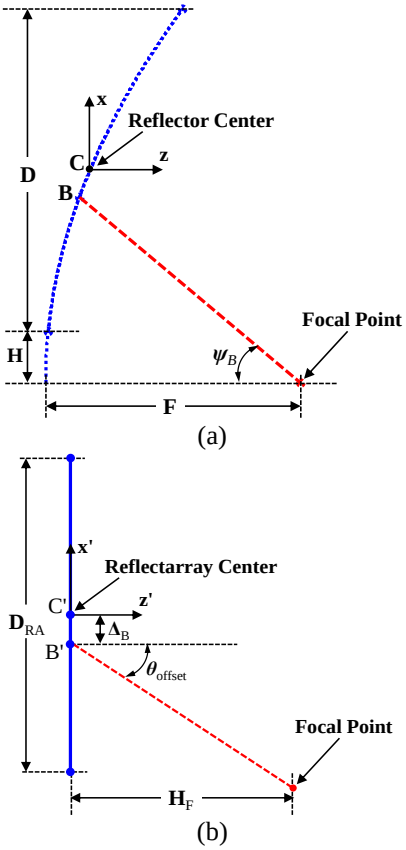

Fig. 1. The geometrical model and key parameters of the offset systems: (a) parabolic reflector, and (b) reflectarray.

Similar to the parabolic reflector, the offset reflectarray system can also be fully specified with four key parameters. The geometrical model of the offset reflectarray system is given in Fig. 1 (b), where the design parameters are:

- D_{RA} = reflectarray diameter;
- H_F = focal point to aperture distance;
- Δ_B = offset distance from reflectarray center;
- θ_{offset} = feed offset angle.

Similar to the reflector system, the primary feed points to a point on the reflectarray aperture (B') which is not necessarily the geometrical center, where the optimal position for B' is determined by efficiency analysis, as described in [7].

The two sets of parameters described here for these offset configurations make it possible to fully describe the systems. In order to establish an analogy between these two systems, one must be able to derive the relationship between the parameters in the two sets. It should be noted here that in the reflector system, the main beam of the antenna points in the z-direction in the coordinate setup of Fig. 1 (a). For the reflectarray system however, one has the option to control the beam direction by adding a progressive phase to the aperture. More discussion on this will be given in the next section.

III. THE ANALOGOUS OFFSET REFLECTOR AND REFLECTARRAY SYSTEMS

In the previous section, the key system design parameters for offset reflectors and reflectarrays were described. In general, in order to analyze the antennas one makes use of a coordinate system that best suits the geometrical setup, which are different for the reflector and reflectarray systems. In this section however, in order to establish the analogy between these two systems, we will use the coordinate setup of the reflector antenna. It is implicit that once the relationship between the design parameters is determined, one can describe the systems in any desired coordinate system.

A. Transformation from reflector to reflectarray system

The geometrical models of the offset configurations in the reflector coordinate setup are shown in Fig. 2. Here we consider the case where the reflector design parameters (F, D, H, ψ_B) are given. First, we derive some additional parameters for the reflector using the four main parameters that would aid in our calculations. The angle subtended to the reflector lower tip, and the distance from focal point to this point are given as:

$$\psi_L = 2\tan^{-1}\left(\frac{H}{2F}\right), \tag{1}$$

$$R_L = \frac{2F}{1+\cos\psi_L}. \tag{2}$$

Similarly, the angle subtended to the reflector upper tip, and the distance from focal point to this point are given by (3) and (4). Note that with this setup, the feed subtended angle, ψ_S, is identical in both systems and is given by (5):

$$\psi_U = 2\tan^{-1}\left(\frac{D+H}{2F}\right), \tag{3}$$

$$R_U = \frac{2F}{1+\cos\psi_U}, \tag{4}$$

$$\psi_S = \psi_U - \psi_L. \tag{5}$$

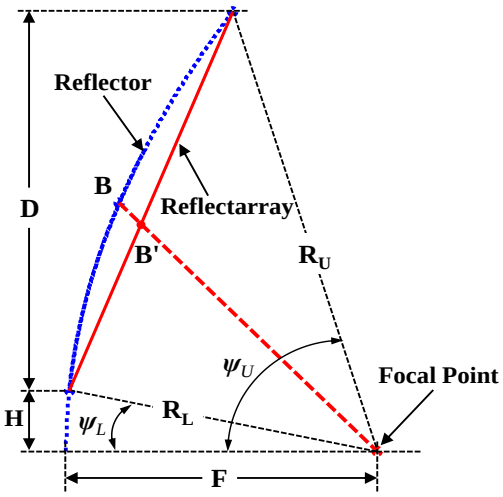

Fig. 2. The analogous geometrical setup of the offset reflector and reflectarray systems.

With these parameters defined, now let us derive the reflectarray system parameters in this coordinate setup. The system setup is given in Fig. 3, where the feed subtended angle is given as:

$$\psi_S = \theta_U + \theta_L \,. \tag{6}$$

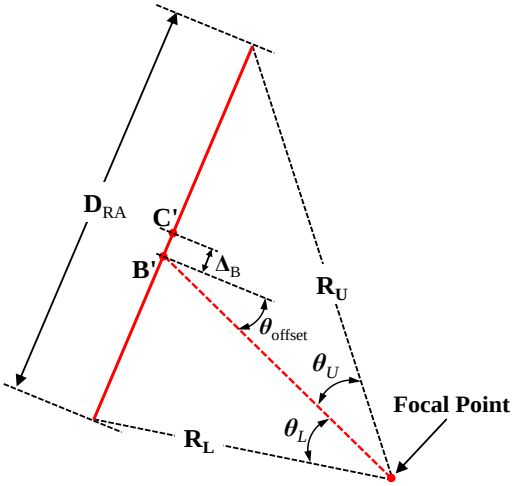

Fig. 3. The geometrical setup of the offset reflectarray in the reflector coordinates.

These angles can be given in terms of reflector parameters as:

$$\theta_L = \psi_B - \psi_L, \quad \theta_U = \psi_U - \psi_B \,. \tag{7}$$

The diameter of the reflectarray antenna can now be calculated in terms of these parameters as:

$$D_{RA} = \sqrt{R_U^2 + R_L^2 - 2R_U R_L \cos\psi_S} \,. \tag{8}$$

As discussed earlier, with the reflectarray antenna one can direct the main beam to any desired direction. However, in the study presented here we aim at describing analogous systems, thus the main beam for the reflectarray points in the same direction as the reflector, as shown in Fig. 4. Note that in the current setup, the reflectarray aperture is tilted by a certain angle with respect to the reflector coordinates which is given by:

$$\theta_{\text{tilt}} = \cos^{-1}\left(\frac{D}{D_{RA}}\right). \tag{9}$$

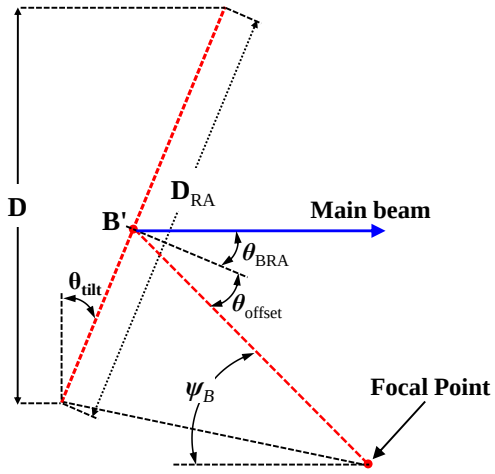

Fig. 4. The main beam direction and geometrical setup of the offset reflectarray system.

To direct the reflectarray main beam in the same direction as the reflector, one must have $\theta_{\text{BRA}} = \theta_{\text{tilt}}$, where θ_{BRA} is the angle with respect to the normal on the reflectarray aperture. The feed offset angle for the reflectarray can then be given as

$$\theta_{\text{offset}} = \psi_B - \theta_{\text{BRA}} \,. \tag{10}$$

The distance from focal point to B' can now be given as:

$$r_f = R_L \frac{\sin(\frac{\pi}{2} - \theta_L + \theta_{\text{offset}})}{\sin(\frac{\pi}{2} - \theta_{\text{offset}})} \,. \tag{11}$$

The focal point to reflectarray aperture distance, and the feed point offset distance from reflectarray center can now be given in terms of these parameters as:

$$H_F = r_f \cos(\theta_{\text{offset}}), \tag{12}$$

$$\Delta_B = \frac{1}{2}\left(\sqrt{r_f^2 + R_U^2 - 2r_f R_U \cos\theta_U} - \sqrt{r_f^2 + R_L^2 - 2r_f R_L \cos\theta_L}\right) \,. \tag{13}$$

The equations given in this section can fully describe the analogous reflectarray system in terms of the reflector design parameters. In particular, the four parameters of the offset reflectarray are computed from Equations (8), (10), (12), and (13), respectively. In the next section, we will derive the equations to describe the

analogous reflector system based on the reflectarray main design parameters.

B. Transformation from reflectarray to reflector system

Now let's consider the case where the reflectarray design parameters (H_F, D_{RA}, Δ_B, θ_{offset}) are given. The geometrical setup of the reflectarray is essentially identical to the previous case shown in Fig. 3. Similarly, we derive the distance from focal point to the reflectarray upper and lower tips using:

$$R_L = \sqrt{r_f^2 + (\frac{D_{RA}}{2} - \Delta_B)^2 - 2r_f(\frac{D_{RA}}{2} - \Delta_B)\cos(\frac{\pi}{2} - \theta_{offset})}\,, \tag{14}$$

$$R_U = \sqrt{r_f^2 + (\frac{D_{RA}}{2} + \Delta_B)^2 - 2r_f(\frac{D_{RA}}{2} + \Delta_B)\cos(\frac{\pi}{2} + \theta_{offset})}\,, \tag{15}$$

where r_f is the distance from focal point to B' and can be derived using (12). The feed angles subtended to the upper and lower tips are then given as:

$$\theta_L = \cos^{-1}\left(\frac{(\frac{D_{RA}}{2} - \Delta_B)^2 - R_L^2 - r_f^2}{-2r_f R_L}\right), \tag{16}$$

$$\theta_U = \cos^{-1}\left(\frac{(\frac{D_{RA}}{2} + \Delta_B)^2 - R_U^2 - r_f^2}{-2r_f R_U}\right). \tag{17}$$

Using the geometrical formula for a paraboloid, the distance from focal point to the upper and lower edges can also be given using:

$$R_L = \frac{2F}{1+\cos\psi_L}, \tag{18}$$

$$R_U = \frac{2F}{1+\cos(\psi_L + \psi_S)}, \tag{19}$$

where ψ_S is the total feed subtended angle as given in (5). The angle subtended to the reflector upper tip can be derived by solving these two equations simultaneously as:

$$\psi_L = \mathrm{Re}\left\{-i\ln\left(-\frac{R_L - R_U + 2i\sin(\frac{\psi_S}{2})}{R_L - R_U e^{i\psi_S}}\right)\right\}. \tag{20}$$

The reflector design parameters can now be computed using:

$$F = \frac{R_L}{2}\left(1+\cos(\psi_L)\right), \tag{21}$$

$$H = R_L\sin(\psi_L), \tag{22}$$

$$D = R_U\sin(\psi_L + \psi_S) - H, \tag{23}$$

$$\psi_B = \cos^{-1}\left(\frac{D}{D_{RA}}\right) + \theta_{offset}. \tag{24}$$

These equations make it possible to describe an analogous offset reflector system in terms of the reflectarray design parameters. One important note here is that in the reflectarray to reflector transform, the direction of the main beam of the reflectarray cannot be defined independently. In the setup outlined here, the direction of the reflectarray main beam is in the same direction as the reflector. However as discussed earlier, the reflectarray can be designed to scan the beam in any desired direction, but in any case, all the important reflector characteristics such as focal depth, offset height, and feed tilt angle, will be identical. In other words, with the same configuration setup for both antennas (Fig. 2), the reflectarray allows for more flexibility in the system design.

IV. COMPARISON OF ANALOGOUS PARABOLIC REFLECTOR AND REFLECTARRAY ANTENNA SYSTEMS

The formulations presented in the previous section allow one to accurately determine the important parameters of offset reflectarray systems in a fashion that has been well established for parabolic reflector antennas. Here, let us study the performance of an analogous parabolic reflector and reflectarray system. A Ka-band reflectarray antenna with an aperture diameter of 190 mm, designed for the center frequency of 32 GHz is considered. We select a balanced feed antenna with a q value ($\cos^q\theta_f$ radiation pattern model) of 6.5. The optimal values of the reflectarray design parameters are determined based on efficiency analysis, and are summarized in Table 1. For the analogous reflector antenna, the design parameters are determined using the formulation presented in Section III, and are also summarized in this table.

The F/D ratio for this system is 0.83. As discussed earlier, the main beam direction of the reflectarray (θ_{BRA}) is determined based on the parabolic reflector parameters, and should be equal to 19°. The 2D-model (cross-sectional view) of this parabolic reflector and reflectarray system is similar to that shown in Fig. 2.

Table 1: Design parameters for the offset reflectarray and reflector

Reflectarray	D_{RA}	H_F	Δ_B	Θ_{OFFSET}
	190 mm	144.71 mm	6 mm	20°
Reflector	D	F	H	ψ_B
	179.64 mm	148.93 mm	12.78 mm	39°

For the parabolic reflector antenna, the design is essentially complete; however, for the reflectarray antenna, the array nature of the system requires one to also specify the element spacing. Here we set the element spacing to 4.7 mm (~λ/2 at 32 GHz). This corresponds to 1184 elements on the aperture of the reflectarray. In this study we are comparing the idealized performance

of both systems, thus for the reflectarray we use ideal elements, i.e., elements with no reflection loss (|Γ| = 1), and the exact (non-quantized value) required phase shift. Also for the parabolic reflector we use perfect electric conductor. The 3D model of the parabolic reflector antenna in FEKO [8], and the required element phase shift on the aperture of the reflectarray antenna are given in Fig. 5.

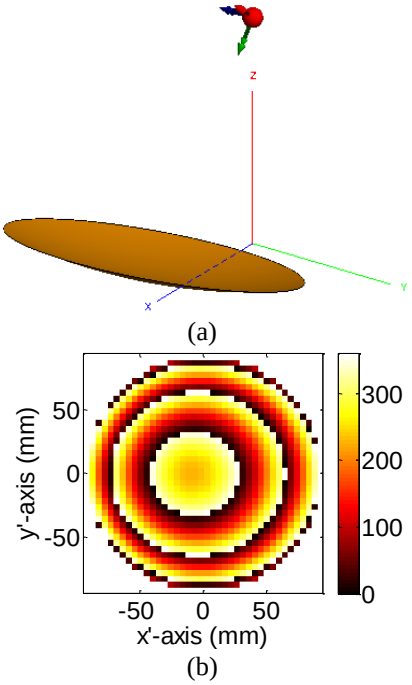

Fig. 5. (a) The parabolic reflector antenna model in FEKO. (b) The element phase distribution on the analogous reflectarray antenna aperture.

The radiation patterns of the antennas are obtained using the equivalence principle and a physical optics (PO) based analysis. For the parabolic reflector, we use the PO solver in FEKO [8]. For the reflectarray antenna we use the aperture field analysis technique as described in [9]. Note that from a computational perspective, both analysis techniques are similar and use the principle of equivalence to compute the surface currents on the antenna apertures and derive the far-field radiation characteristics. The principal plane normalized co-polarized radiation patterns for both antennas is given in Fig. 6, where it can be seen that a very similar radiation pattern is obtained with these two antennas. The simulated gain values are 34.54 dBi and 34.40 dBi for the parabolic reflector and reflectarray, respectively [10]. The slightly lower gain for the reflectarray is attributed to the discontinuous nature of the array (as opposed to the continuous aperture for the parabolic reflector); however this can be improved by using smaller element spacing.

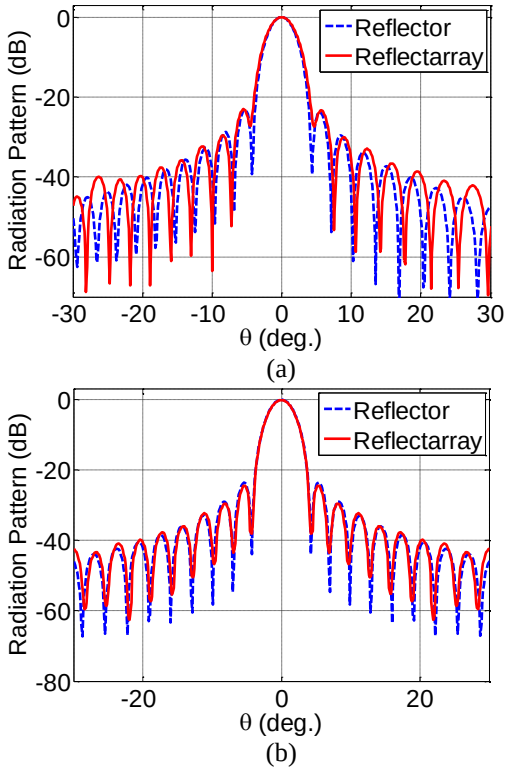

Fig. 6. Principal plane radiation patterns of the reflector and reflectarray: (a) *xz*-plane and (b) *yz*-plane.

VI. CONCLUSION

We derive the analogical relationship between offset parabolic reflectors and reflectarrays. Both the offset reflector and reflectarray systems are defined using four design parameters, and the mathematical relationship between the design parameters of these two antenna systems is determined. A comparison between the radiation patterns of an analogous Ka-band parabolic reflector and reflectarray antenna is also presented which show very similar performance. The presented study simplifies the system setup in offset reflectarrays, by using a coordinate system and a set of parameters that is well suited for reflectarray design and analysis. It can potentially be implemented in offset dual-reflectarray antennas.

REFERENCES

[1] C. J. Sletten, *Reflector and Lens Antennas: Analysis and Design Using Personal Computers*. Artech House Inc., 1988.

[2] Y. Rahmat-Samii, "Reflector Antennas," in *Antenna Handbook: Theory, Applications, and Design*, Y. T. Lo and S. W. Lee, Van Nostrand Reinhold, 1988.

[3] J. Huang and J. A. Encinar, *Reflectarray Antennas*. New York, NY, USA: Wiley-IEEE, 2008.

[4] D. M. Pozar, S. D. Targonski, and H. D. Syrigos,

"Design of millimeter wave microstrip reflectarrays," *IEEE Trans. Antennas Propag.*, vol. 45, no. 2, pp. 287-296, Feb. 1997.

[5] E. Almajali, D. McNamara, J. Shaker, and M. R. Chaharmir, "Derivation and validation of the basic design equations for symmetric sub-reflectarrays," *IEEE Trans. Antennas Propag.*, vol. 60, no. 5, pp. 2336-2346, May 2012.

[6] C. Tienda, M. Arrebola, J. A. Encinar, and G. Toso "Analysis of a dual-reflectarray antenna," *IET Microw. Antennas Propag.*, vol. 5, no. 13, pp. 1636-1645, 2011.

[7] A. Yu, F. Yang, A. Z. Elsherbeni, J. Huang, and Y. Rahmat-Samii, "Aperture efficiency analysis of reflectarray antennas," *Microwave and Optical Technology Letters*, vol. 52, no. 2, pp. 364-372, Feb. 2010.

[8] FEKO v7.0, EM Software & Systems Inc., 2014.

[9] P. Nayeri, A. Z. Elsherbeni, and F. Yang, "Radiation analysis approaches for reflectarray antennas," *IEEE Antennas Propag. Magazine*, vol. 55, no. 1, pp. 127-134, Feb. 2013.

[10] P. Nayeri, A. Z. Elsherbeni, and F. Yang, "The analogy between offset configurations of parabolic reflectors and reflectarrays," *IEEE Antennas and Propagation Society International Symposium*, Vancouver, Canada, July 2015.

Payam Nayeri received his Ph.D. in Electrical Engineering from The University of Mississippi, University, MS, USA, in 2012. Nayeri joined the Electrical Engineering Department at Colorado School of Mines as an Assistant Professor in 2015. His research is in the area of adaptive microwave and antenna systems, wireless energy harvesting, and active and wideband antenna arrays. He is a Member of IEEE, Sigma Xi, and Phi Kappa Phi, and has authored over seventy journal articles and conference papers. He has been the recipient of several prestigious awards, including the IEEE Antennas and Propagation Society Doctoral Research Award in 2010 and the Best Student Paper Award of the 29th International Review of Progress in ACES.

Atef Z. Elsherbeni received his Ph.D. degree in Electrical Engineering from Manitoba University, Winnipeg, Manitoba, Canada, in 1987. Elsherbeni was with the University of Mississippi from 1987 to 2013. He was a Finland Distinguished Professor from 2009 to 2011. He joined the Electrical Engineering and Computer Science Department at Colorado School of Mines in August 2013 as the Dobelman Distinguished Chair Professor. Currently he is the Head of the Electrical Engineering Department. His research interest includes the scattering and diffraction of EM waves, finite-difference time-domain analysis of antennas and microwave devices, field visualization and software development for EM education, interactions of electromagnetic waves with the human body, RFID and sensor integrated FRID systems, reflector and printed antennas and antenna arrays, and measurement of antenna characteristics and material properties. Elsherbeni is a Fellow Member of IEEE and ACES. He is the Editor-in-Chief for ACES Journal. He was the General Chair for the 2014 APS-URSI Symposium and was the President of ACES Society from 2013 to 2015.

Fan Yang received the B.S. and M.S. degrees from Tsinghua University, Beijing, China, in 1997 and 1999, respectively, and the Ph.D. degree from the University of California at Los Angeles (UCLA), in 2002. In 2004, he joined the Electrical Engineering Department, The University of Mississippi as an Assistant Professor, and was promoted to an Associate Professor. In 2011, he joined the Electronic Engineering Department, Tsinghua University as a Professor, and has served as the Director of the Microwave and Antenna Institute since then. Yang's research interests include antennas, surface electromagnetics, computational electromagnetics, and applied electromagnetic systems. He has published over 300 journal articles and conference papers, six book chapters, and four books. Yang served as an Associate Editor of the IEEE Transactions on Antennas and Propagation (2010-2013) and an Associate Editor-in-Chief of Applied Computational Electromagnetics Society (ACES) Journal (2008-2014).

A Tunable Antenna with the Combination of Two Kinds of Liquid Materials

Gaosheng Li [1,2], Gui Gao [1], Li-an Bian [1], Zhonghao Lu [1], and Chaoyun Song [2]

[1] College of Electronic Science
National University of Defense Technology, Changsha, 410073, China
Gaosheng7070@vip.163.com, dellar@126.com, 441934302@qq.com, luzhnudt@163.com

[2] Department of Electrical Engineering and Electronics
University of Liverpool, Liverpool, L69 3GJ, United Kingdom
Chaoyun.song@liv.ac.uk

Abstract ─ A tunable antenna consists of two kinds of liquid materials is designed and investigated for the first time. Compared with single liquid antenna, the antenna with two kinds of liquids offers more flexibility for the designing. Insoluble liquid such as oil can be used together with the distilled water, the sea water or saline water. A thin pole is added to make use of the fluidity of liquid and bring adjustment to the antenna according to the principle of communicating vessels. The comparison of pure liquid and the combination of different materials are carried out first. Furthermore, the influence of the distribution of the liquid materials, the feeding locations and the length of the feeding probe are analyzed. The simulation results indicate the radiation potential and the reconfigurability of the antenna. To drag out or push in the adjustment pole as well as to change the parameters of the structure can bring the variations of the antenna performance effectively, including the matching and the radiation features.

Index Terms ─ Hybrid antenna, liquid antenna, monopole antenna, tunable antenna, water antenna.

I. INTRODUCTION

Liquid antennas have drawn more and more attentions during recent years. The popular types of liquid antennas include Dielectric Resonator Antenna (DRA) and monopole antenna. Since the investigations on the two types of antennas remain a hot topic, it is convenient for drawing on the experiences of the conventional ones [1-4]. A liquid-based DRA was introduced [5]. The miniaturization of the antenna due to the high relative permittivity of water was demonstrated. Furthermore, a DRA-based technique was proposed for measuring liquid permittivity. A low-profile broadband antenna was designed [6]. It was a hybrid structure combined the resonance of a dielectric resonator and a monopole together. A hybrid antenna with solid and liquid materials was discussed [7], with the focus of the influence of the feeding locations and the distribution of the liquid. A water dielectric patch antenna array for Wi-Fi communication application was presented [8]. The new idea was that the conventional metal patches were replaced by water. A shunt-excited seawater monopole antenna was studied in the paper [9]. Dynamic-type seawater monopole antenna of high efficiency was realized by using a shunt-excited feeding structure, which was formed by a conducting tube and a Gamma-shape feeding arm. A pump was applied to provide seawater for the antenna. It offered a potential for designing high-efficiency dynamic-type sea-water monopole antennas. A seawater half-loop antenna of VHF band was developed for maritime wireless communications [10]. The antenna was made of a capacitive coupling feeding structure and a stream of seawater produced by a water pump. This antenna could be turned off in real time, which made it suitable for maritime wireless communications. A mechanically reconfigurable microstrip antenna which applied a liquid actuator as the dielectric layer to reduce the size was designed in the paper [11]. By using direct polymer vacuum deposition on a liquid, the dielectric liquid could be encapsulated inside the polymer to form an actuator, which changed the liquid thickness. When the actuator was mounted within the antenna, its resonant frequency could be changed by changing the liquid thickness. A transparent water dielectric patch antenna fed by an L-shaped probe was designed in the paper [12]. The presented design had an operation style similar with the conventional metallic microstrip antenna [13]. A broad bandwidth could be obtained by applying a thick supporting substrate between the ground and the water patch.

The liquid antennas published till now have achieved fairly good performance and have shown potentials abilities in the applications of various areas. But there was only one kind of liquid in all of them, and there were limited styles for the realization of the liquid antennas. We attempt in this paper to make use of two kinds of

Submitted On: August 5, 2017
Accepted On: October 4, 2017

liquid to provide more design flexibility for the antenna. At the same time, an additional structure will benefit the adjustment of the antenna.

II. DESIGN AND SIMULATIONS

A. Structure and performance of the untunable liquid antennas

As shown in Fig. 1, a tube made of a solid dielectric material is fabricated on the substrate and the ground layer to hold the liquid. At the beginning, a liquid material such as sea water, distilled water, oil or saline water can be injected into the tube to produce liquid antennas with fairly good radiation and matching performance. Furthermore, the combination of oil and water can be carried out to obtain hybrid antennas with more flexibility.

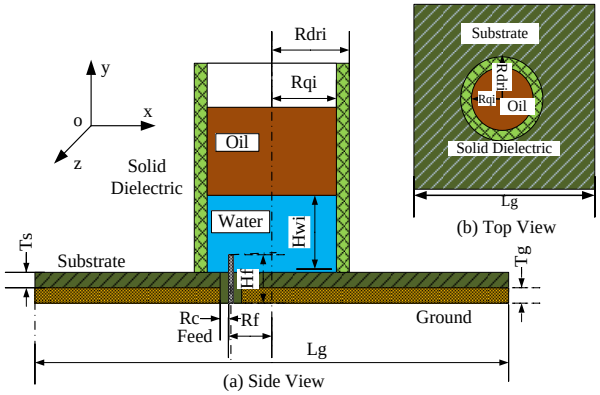

Fig. 1. Structure of the untunable liquid antennas: (a) side view and (b) top view.

The commercial software of CST Microwave Studio is used to carry out the model building and the simulations. In the simulations, the solid material is chosen to be glass with the relative permittivity of 4.82 and the thickness of 1.0 mm. The relative permittivity of the sea water and the distilled water are 74.0 and 78.4, respectively, while the relative permittivity of oil is 2.33. The thickness of the substrate is 3.0 mm and that of the ground is 0.8 mm. Rogers TMM10 with the permittivity of 9.2 is used as the substrate.

There are several types of interfaces referring to the scenarios in this manuscript. The saline water and the sea water tend to act as conductive objects, so do the surfaces of them. While the distilled water and the oil remain dielectric materials and act as non-conductive objects. The discipline of general electromagnetic radiation and reflection characteristics also has an effect on the liquid interfaces.

Four curves of the reflection coefficients are shown in Fig. 2, each of which is corresponding to a specific configuration of the liquid inside of the tube, namely, a single liquid of distilled water, oil, sea water and the combination of oil and seawater. The total height of the liquid is 36 mm for both single pure liquid and the combined materials. The height of the oil is 20 mm and that of the sea water is 16 mm when they operate together, and the water (with a density of 1.0 g/cm^3) lies in the bottom layer as the higher density compared to the oil (with a density of 0.8 g/cm^3).

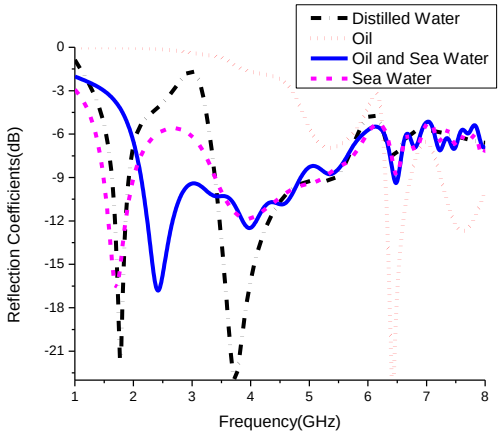

Fig. 2. Reflection coefficient curves of several untunable liquid antennas.

It could be seen from the curves that all the four configurations can operate at one or two certain frequency bands among 1.0-8.0 GHz. The distilled water has the best matching performance with the reflection coefficient S11<-10 dB in the frequency ranges of 1.65-1.90 GHz and 3.41-4.66 GHz, whose relative bandwidth are 14.08% and 30.98%, respectively, with the valley of reflection points of -21.74 dB and -23.13 dB. The pure oil and the sea water achieve the highest and the lowest frequency, respectively, with a rather large gap of 4.73 GHz (1.70 GHz and 6.43 GHz).

For the validation verification of the simulations, a result of the S11 curve obtained from another software ANSYS HFSS (High Frequency Structure Simulator) is presented in Fig. 3, with the liquid materials of distilled water and oil. The result from CST is shown for a comparison. Similar matching performance could be seen from the two calculations, especially for the positions of the resonant frequency points.

Figure 4 presents the curves of the radiation patterns of different liquid materials and their combination at 4.0 GHz, namely pure oil, distilled water and oil, sea water and oil, pure sea water. The gain values of them are 2.63 dBi, 5.88 dBi, 3.51 dBi and 3.63 dBi, respectively. The combination of distilled water and oil get the highest gain, while that of the pure oil is the lowest. To be mentioned, the gain and radiation pattern of the distilled water and the sea water is nearly the same under this configuration, so we only offer one of them here in Fig. 4. The direction of the main lobe varies a lot according

to the changes of material, as it could be observed from the figure.

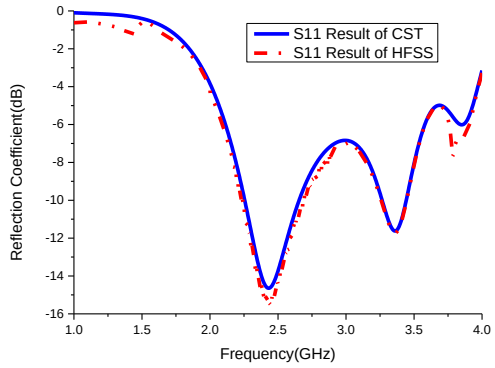

Fig. 3. The comparison of S11 from CST and HFSS.

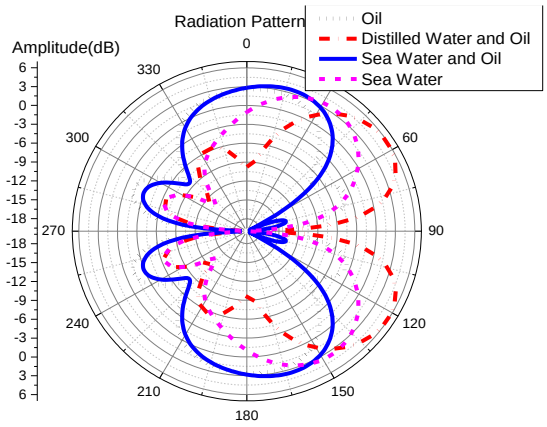

Fig. 4. Radiation patterns of different materials (Pure Oil, Distilled Water and Oil, Sea Water and Oil, Pure Sea Water).

Similarly, we compared the radiation pattern results from HFSS and CST, as shown in Fig. 5. Both curves refer to the combination of distilled water and oil.

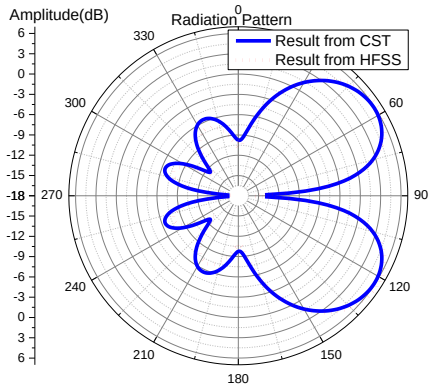

Fig. 5. Comparison of the radiation patterns from HFSS and CST.

It could be seen from Fig. 5 and Fig. 3 that the gaps between the absolute values of the two curves have little impact for the discussion about the antenna performance.

B. Structure of tunable liquid antennas

To make the antenna tunable, we make use of the principle of the communicating vessel, as shown in Fig. 6. The liquid of the same kind of material will have the same height of surface in the tube, no matter what the shape of it or how thick or thin the diameter is. As for a different kind of liquid, the height will increase when the density decreases, and the variation of the height is linear. For example, if the height of the water in the tube is 80 mm, that of the oil will be 100 mm according to their difference of density.

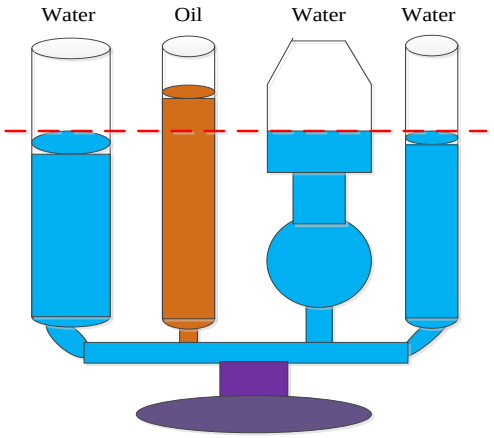

Fig. 6. The diagram of a communicating vessel.

Further flexibilities would be obtained when the structure is changed to the scenario as shown in Fig. 7. Where, Lg= 80 mm, Hd=36 mm, Rqi=3 mm, Rdo=5 mm, Rdri=4 mm, Rdro=6 mm, and Rqo=5 mm. An outside cavity is formed by adding a shell with a bigger diameter. The liquid materials now acquire a new space to stay. The fluidity of them could then achieve a better usage. Oil and seawater are used to form the main part of the radiation, and they are arranged inside of the inner cavity.

There is a thin pole mounted in the right outer part of the structure that can be dragged out or be pushed in, thus the water can flow into the exterior shell or be blocked in a certain cavity as we want. Furthermore, a kind of solid dielectric material (DRT (Dielectric Response Technology) from the company of IMCC (Intelligent Material of Ceramic Company in Nanjing, China)) is used to substitute glass to make the shell, whose dielectric permittivity is 30.0 (1.0-12.0 GHz). The user-defined parameters for the specific materials are supported in CST.

Actually, there is a series of formulas to calculate the dimensions of the antenna corresponding to certain performance requirements, mainly according to the

design theory of dielectric resonant antennas. However, for the demonstration of the feasibility of the tunable cavity antenna with two kinds of liquid materials, the operation frequency together with the dimensions of the antenna could be chosen to be a set of values of common size.

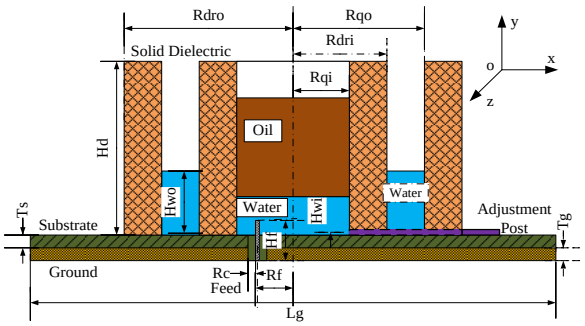

(a) Side view

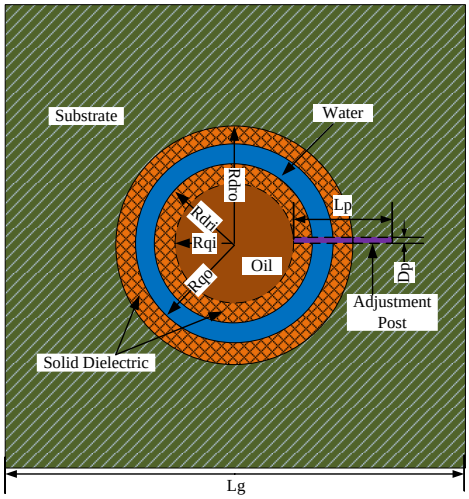

(b) Top view

Fig. 7. Structure of the tunable liquid antenna (the oil is injected into the inner cavity of the structure): (a) side view and (b) top view.

C. Influence of the distribution of the liquid

The different performance will be achieved when the distribution of the liquid is changed. The calculated results of S11 in four typical statements are shown in Fig. 8. The heights of the sea water in the inner cavity are 16 mm, 11 mm, 5 mm and 0 mm, respectively. So the heights of the outer part are in the reverse order of the above numbers. The oil remains 20 mm and will vary its position as the changing of the seawater.

The highest operating frequency occurs when the whole sea water flows out of the inner cavity. The configuration of 11 mm of seawater remains inside of the cavity obtains the best performance with the minimal S11 of -35 dB and the broadest bandwidth of 22.99%. Detailed data are shown in Table 1, where the phrase of "In 5" means the height of the liquid in the inner cavity is 5 mm, while the "Out 11" means the height of the liquid in the outer cavity is 11 mm.

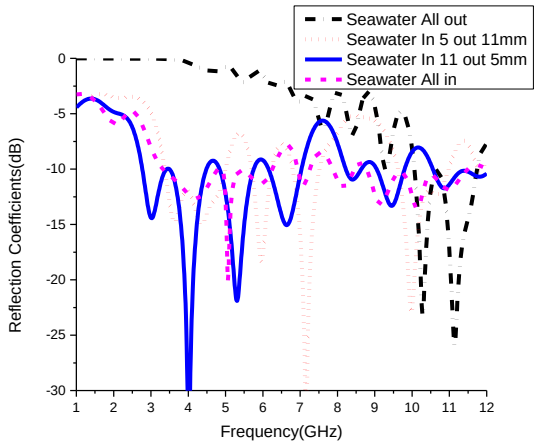

Fig. 8. S11 corresponding to the variation of the liquid distribution.

Table 1: Frequency features of the four distribution statements of the liquid materials

Liquid Distribution (mm)	Resonant Freq. (GHz)	Freq. Range of Center (GHz)	Relative Bandwidth @ Central Freq.
In 16, Out 0	4.21, 5.07, 9.15	4.83-5.43	11.70%
In 11, Out 5	4.02, 5.30, 6.65	3.45-4.48	22.99%
In 5, Out 11	5.97, 7.16, 9.99	6.78-7.53	10.48%
In 0, Out 16	9.28, 10.29, 11.15	10.66-11.76	9.81%

The radiation patterns of the four configurations at their resonant frequencies are shown in Fig. 9. There are not much different in shape, but the values of side lobes, back lobes and gains are not the same. The highest gain is obtained when the height of the seawater outside of the cavity 16 mm, and the widest main lobe is achieved when the height is 5 mm. The minimal back lobe occurs when the water is totally constrained inside of the cavity.

Figure 10 provides a 3 D radiation pattern of the hybrid antenna at the frequency of 10.29 GHz, with the height of the exterior sea water to be 16 mm and the oil is constrained totally inside of the tube. The gain of the antenna is 8.22 dBi, and the side lobe is 7.7 dB lower than the main lobe. The highest gain in the back lobe is only -18.6 dBi.

If the liquid is injected into the exterior ring of the structure at the beginning, as shown in Fig. 11, the radiation performance would be different from the above, as shown in Fig. 12.

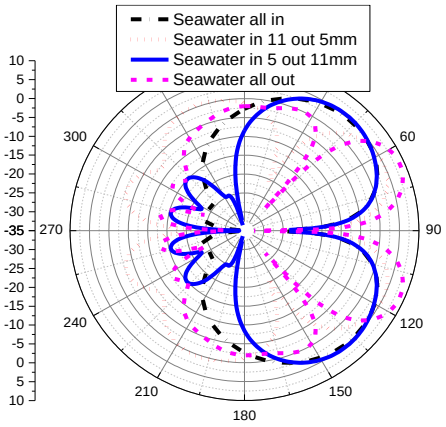

Fig. 9. Radiation patterns of different liquid distributions (the oil located inside of the inner cavity).

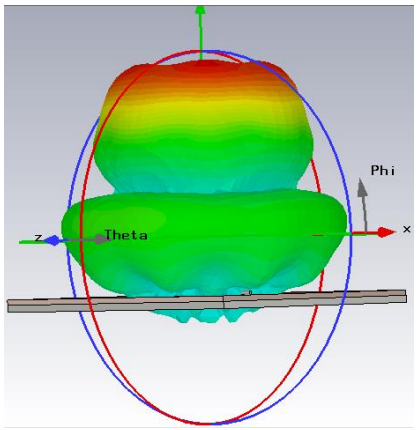

Fig. 10. The 3 D radiation pattern of the tunable antenna with the sea water stay outside at 10.29 GHz.

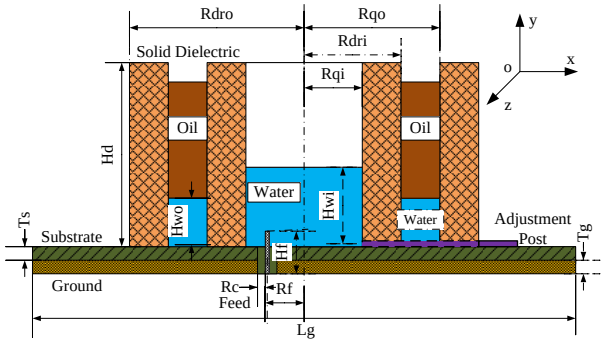

Fig. 11. Structure of the tunable liquid antenna (the oil is injected into the outer cavity of the structure).

Moreover, the heights of the solid dielectric material are expected to be changed to hold the liquid effectively. It can be seen that neither the gain values nor the heights of the side lobes remain the same with those in Fig. 9. The highest gain occurs when the inner height of the water is 5 mm, as shown in Fig. 12.

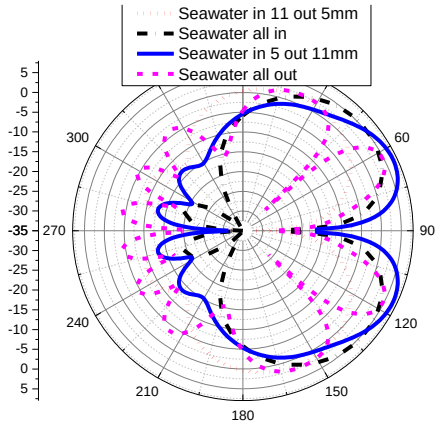

Fig. 12. Radiation patterns of liquid distributions at another original state (the oil located outside of the inner cavity).

D. Influence of the length of the feeding probe

Figure 13 indicates the influence of the length of the feeding probe. Here, the feeding locations are at the center of the bottom of the inner liquid. All the lengths from 1.5 mm, 2.0 mm, 2.8 mm to 4.0 mm can generate valid excitations and the longer one operates better in a lower band with a longer wavelength.

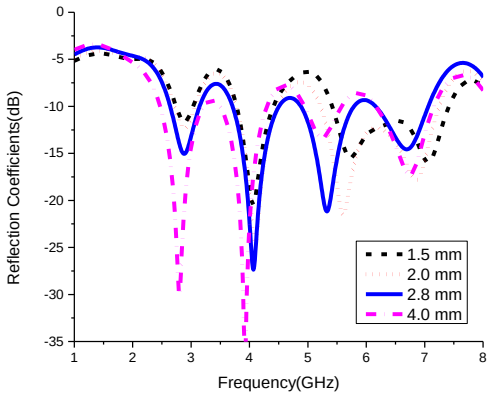

Fig. 13. Influence of the length of the feeding probe on S11.

If we change the excitation by reducing or increasing the length of the probe, the radiation would get variations too, as shown in Fig. 14. The gains of the antenna with a probe length of 1.5 mm, 2.0 mm, 2.8 mm and 4.0 mm are 2.25 dBi, 2.19 dBi, 1.82 dBi and 3.90 dBi, respectively. And as it can be seen from the figure, the shape of that of 1.5 mm and 2.0 mm are very similar, while that of the other two has distinguished features.

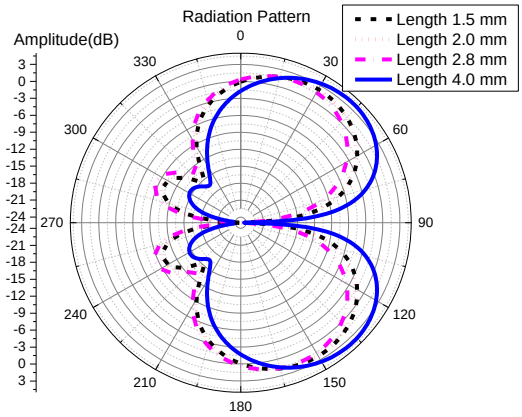

Fig. 14. Radiation pattern vs. the length of the probe.

E. Influence of the feeding locations of the probe

As we choose solid dielectric materials to build the shell and the cavity of the antenna, there is a special freedom for the designing of the antenna. That is, the feeding location of the probe can be moved from the inner liquid to the outer liquid as well as to the dielectric shell.

Figure 15 shows the reflection coefficients of several probe locations, including the center of the inner liquid and a distance of 3 mm, 7 mm and 8 mm to the center. The latter three distances stand for that of the probe put in the inner liquid, in the inner shell and at the interface of the inner shell and the outer liquid. It is very close for the resonance frequency of the location of 7 mm and 8 mm, which is 5.56 GHz and 5.61 GHz, respectively. It is very high for the central feeding of the antenna (7.16 GHz) and much lower for that inside of the liquid but with a bias from the center (4.05 GHz).

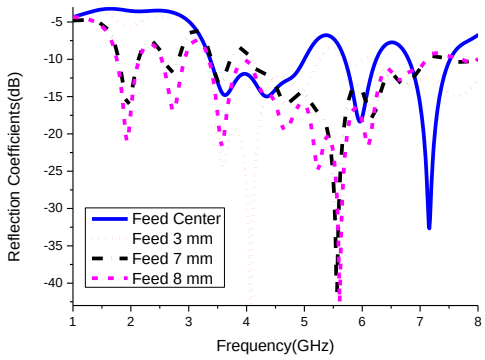

Fig. 15. Reflection coefficients vs. feeding locations of the probe (oil inside).

At the same time, the variation of the feeding positions will influence the radiation pattern, as shown in Fig. 16. It could be found from the figure that the pattern changes a lot when the excitation probe is put in the center of the antenna or be moved to the outer area. The gains of the four locations are 8.2 dBi, 0.7 dBi, 8.3 dBi and 7.1 dBi, respectively, from center to the outside. And there is much difference for the largest radiation directions of them.

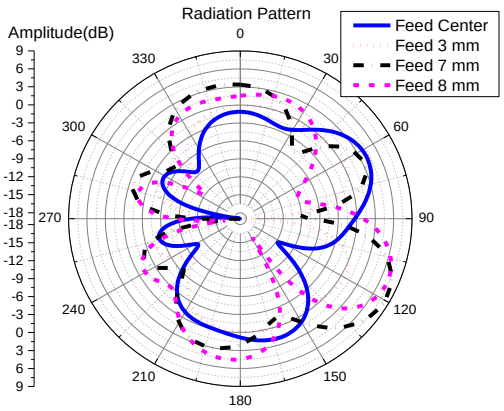

Fig. 16. Radiation pattern vs. the feeding location.

There are some tips for CST simulation for liquid antennas. Although the waveguide ports are the most accurate way to excite a field, discrete edge ports are sometimes more convenient to use. They have two pins to be connected to the structure. This kind of port is often used as feeding point source for antennas. At higher frequencies (e.g., the length of the discrete port is longer than a tenth of a wavelength) the S-parameters may differ from those when using waveguide ports because of the improper match between the port and the structure.

For the liquid antenna model consisting of several parts needs to be meshed. The solution methods require consistent meshes at the interfaces of different parts in order to set up the matrix equations correctly. If the meshes were created independently for all the blocks, the meshes might become inconsistent at the interfaces. The typical solution to this problem is to create a "non-manifold" simulation model first. This intermediate operation converts coincident faces from two solids to a single common double-sided face. Once it is done, the edges and faces can be meshed first, and the volume mesh can then be created.

The transient solver based on the Finite Integration Technique (FIT) is recommended, due to the memory efficient computation together with a robust hexahedral meshing to successfully simulate the complex structures.

III. CONCLUSION

This paper is the first to investigate the liquid antenna with two different liquids. The simulation results have revealed that this new type of antenna can offer a lot of flexibility and reconfigurability of the radiation and the matching performance of the antenna, which offers a new design freedom for the liquid antennas. However, this paper is just an initial study, thus, it

could be further investigated to improve the antenna performance. To enable the adjustment characteristic of the liquid antenna is another important problem and the method mention in this paper is only an elementary one that needs further optimizations.

REFERENCES

[1] D. Batra and S. Sharma, "Dual band dielectric resonator antenna for wireless application," *International Journal of Electronics*, vol. 99, no. 9, pp. 1323-1331, 2012.

[2] S. Coizzone, G. Buchber, and W. Elmarissi, "Miniaturized dielectric resonator antenna array for GNSS applications," *International Journal of Antennas and Propagation*, vol. 2016, no. 6, pp. 1-11, 2016.

[3] A. Nemati and B. A. Ganji, "UWB monopole antenna with switchable band-notch characteristic using a novel MEMS afloat," *ACES Journal*, vol. 30, no. 12, pp. 1306-1312, 2015.

[4] T. Sedghi, V. Rafii, and M. Moosazadeh, "UWB monopole antenna with compact polygon-shaped patch for portable devices," *ACES Journal*, vol. 29, no. 1, pp. 67-70, 2014.

[5] R. Zhou, H. Zhang, and H. Xin, "Liquid-based dielectric resonator antenna and its application for measuring liquid real permittivities," *IET Microwaves, Antennas & Propagation*, vol. 8, no. 4, pp. 255-262, 2014.

[6] L. Xing, Y. Huang, Q. Xu, S. Alja'afreh, and T. Liu, "A broadband hybrid water antenna for hand-portable applications," *IEEE Antennas and Wireless Propagation Letters*, vol. 15, pp. 174-177, 2016.

[7] C. Lin, G. Li, P. Liu, Y. Qin, and Y. Huang, "A hybrid antenna with solid and liquid materials," *International Symposium on Antennas and Propagation*, Okinawa, Japan, Oct. 2016.

[8] J. Sun and K.-M. Luk, "Design of a 2*2 water dielectric patch antenna array for Wi-Fi applications," *The 4th IEEE Asia-Pacific Conference on Antennas and Propagation*, Bali Island, Indonesia, pp. 237-238, June 2015.

[9] C. Hua and Z. Shen, "Shunt-excited sea-water monopole antenna of high ffficiency," *IEEE Transactions on Antennas and Propagation*, vol. 63, no. 11, pp. 5185-5190, 2015.

[10] C. Hua and Z. Shen, "Sea-water half-loop antenna for maritime wireless communications," *The 4th IEEE Asia-Pacific Conference on Antennas and Propagation*, Bali Island, Indonesia, pp. 231-232, June 2015.

[11] K. Noda, M. Ohkado, B. Nguyen, K. Matsumoto, H. Fujikawa, and I. Shimoyama, "Frequency-tunable microstrip antenna with liquid actuator using gradually widened transmission line," *IEEE Antennas and Wireless Propagation Letters*, vol. 14, pp. 551-555, 2015.

[12] Y. Li and K.-M. Luk, "A transparent water dielectric patch antenna," *The 4th IEEE Asia-Pacific Conference on Antennas and Propagation*, Bali Island, Indonesia, pp. 319-320, June 2015.

[13] M. M. Elsewe, V. K. Dandu, and D. Chatterjee, "Ultra-wideband low profile, U-slot microstrip patch antennas: L-probe feed design guidelines," *ACES Journal*, vol. 31, no. 11, pp. 1322-1329, 2016.

Gaosheng Li received his B.S. degree in Electromagnetic Field and Microwave, and his M.S. degree as well as his Ph.D. in Electronic Science and Technology from the National University of Defense Technology (NUDT), Changsha, China, in 2002, 2004 and 2013, respectively.

He has been with NUDT as a Teaching Assistant from 2004 to 2006, and a Lecturer from 2006 to 2011, and then as an Associate Professor since 2011. From 2014 to 2016, he was with Nanjing University of Aeronautics and Astronautics (NUAA) and Wuxi Huace Electronic Systems Co., Ltd., China as a Postdoctoral Research Fellow. From 2016 to 2017, he is a Visiting Scholar at the University of Liverpool (UoL), United Kingdom, sponsored by China Scholarship Council (CSC). His research interests include Antennas and Propagation (AP), Electromagnetic Compatibility (EMC), Wireless Propagation and Microwave Systems.

Li is the author or coauthor of 6 books and 96 papers published in journals and conference proceedings. He owns 18 Chinese patents and 6 software copyrights. He won 2 national scientific prizes in 2007 and 2013, respectively. Li is a Committee Member of IEEE EDAPS 2017 and ICCT 2017. He is a Member (2008) of the IEEE AP Society and EMC Society, a Member (2016) of IET, and a Member (2011) of the Institute of Electronics, Information and Communication Engineers (IEICE), a Member (2017) of Applied Computational Electromagnetics Society (ACES), a Member (2017) of Chinese Physical Society (CPS), as well as a Senior Member (M'2008, SM'2014) of the Chinese Institute of Electronics (CIE).

Gui Gao received the B.S. in Information Engineering, the M.S. and Ph.D. degrees in Remote Sensing Information Processing from National University of Defense Technology (NUDT), Changsha, China, in 2002, 2003 and 2007, respectively. From 2007, he joined the Faculty of

Information Engineering, School of Electronic Science and Engineering, NUDT, where he is currently an Associate Professor. From 2016, he was with School of Information Science and Engineering, Central South University, Changsha, China, as a distinguished professor.

His research interests include SAR ATR (automatic target recognition), statistical modeling of SAR image, SAR Ship Detection, and SAR GMTI (ground moving target indication). He is the author of more than 70 journal papers and has written three books. He obtained an award of the Excellent Master Thesis of Hunan Province in 2006, award of Excellent Doctor Thesis of the Chinese Army in 2008, awards of Outstanding Young People in NUDT and Hunan Province of China in 2014 and 2016, and award of Natural Science in Hunan province. Also, in 2016, he was selected as Young Talents of Hunan.

Gao is a Member of the IEEE Geoscience and Remote Sensing Society (GRSS), a Member of the Applied Computational Electromagnetics Society (ACES), and a Member of the Chinese Institute of Electronics (CIE), and a dominant Member of Young Scientist Forum of CIE. He is the Leader Guest Editor of International Journal of Antenna and Propagation, and in Editorial Board of Chinese Journal of Radars. He was also the Co-chairman of several important conferences in the field of remote sensing. He was the Excellent Reviewer of the journal of Xi'an Jiaotong University in 2013.

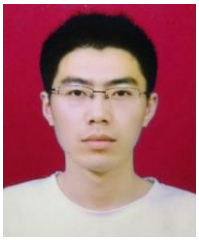

Li-an Bian received the M.Sc. degree in Electromagnetic Field and Microwave Technology from Tianjin University, Tianjin, China, in 2013, and is presently working on his Ph.D. degree in the same major from National University of Defense Technology, Changsha, China. Additionally, he was an Assistant, taught the course of Optical Communication Technology at Huaihua University from 2013 to 2014.

His research interests include graphene devices, photonic crystals and vortex electromagnetic wave and so on. So far, he got 10 papers published as the first author.

Zhonghao Lu received the M.S. degree and Ph.D. degree in Electronic Science and Technology from the National University of Defense Technology (NUDT), Changsha, China, in 2008 and 2013, respectively. He is currently a Lecturer in NUDT.

His current research interests are in the general areas of microwave devices design, antenna design and electromagnetic compatibility testing. His has got a national scientific prize and is the author of 20 papers.

Chaoyun Song received the B.Sc. degree in Information Science and Technology from Xi'an Jiaotong-Liverpool University (XJLU), Suzhou, China, in 2011. He pursued his M.Eng. degree in Microwave Technology from 2011-2012 in the University of Liverpool. He is currently working towards the Ph.D. degree in Electrical Engineering and Electronics at the University of Liverpool, United Kingdom.

His current research interests include wireless energy harvesting, antennas and microwave circuits.

Modeling and Realization of Cavity-Backed Dual Band SIW Antenna

Mehmet A. Belen [1], Peyman Mahouti [2], Alper Çalışkan [2], and Aysu Belen [2]

[1] Department of Electric and Electronic Engineering
University of Artvin Çoruh, Artvin, TURKEY
mehmetalibelen@artvin.edu.tr

[2] Department of Electronics and Communication Engineering
University of Yıldız Technical, Istanbul, TURKEY
pmahouti@gmail.com, acaliskan@gmail.com, aysuyldrm07@gmail.com

Abstract ─ Herein, substrate integrated waveguide technology is applied in order to design high performance dual-band microstrip patch antennas. Two microstrip patch antenna designs were studied and modeled in 3D electromagnetic simulators. The obtained optimal models were then realized and measured. The measurement performance of the proposed antenna designs were then measured for 2.4 and 5.6 GHz. The results suggest that the proposed model consisting of a modified microstrip cavity-backed antenna and a defected ground structure is a high performance and low cost solution for 2.4 and 5.6 GHz applications.

Index Terms ─ Antenna design, defected ground structure, dual band, cavity-backed antenna, Substrate integrated waveguide.

I. INTRODUCTION

Waveguides are metallic transmission lines that are used at microwave frequencies, typically to interconnect transmitters and receivers with antennas. Waveguides are better mediums for delivering low-loss signal transmission as compared to microstrip transmission lines. However, traditional rectangular waveguides are expensive and are considerably large in size. Substrate integrated waveguide (SIW) is a technology that provides the performance advantages of classic waveguide structures, along with the cost and size benefits of planar PCB designs [1]. The brilliant virtue of SIW is its ability to integrate all the components such as active and passive elements, antennas etc., on the same PCB board. SIW also acts as a low-loss feeding network which enhances the performance of antenna design. There has been increasing interest in implementing SIW technology in active circuits and complete systems including active integrated antennas [2–8]. In Fig. 1 (a), a basic SIW structure is presented. SIW technology is essentially a hybrid of microstrip and dielectric-filled waveguide technologies. Surface and ground metal layers of a PCB substrate provide two of the waveguide walls. Two parallel rows of vias form the side walls of the waveguide.

One of the most commonly used circuit stages in PCB board technology is microstrip antennas that have a wide range of applications. These stages are preferred because of their simple designs. By employing SIW technology, it is possible to enhance the many advantages of microstrip antennas such as low cost, smaller size, easy integration of antenna stages to circuit etc. Antennas designed with SIW technology have excellent performance because they suppress the propagation of surface waves, increase the bandwidth, and decrease both end-fire radiation and cross-polarization radiation. The cavity-backed structure of the antenna design can also overcome hitches like heat dissipation and unwanted surface wave modes.

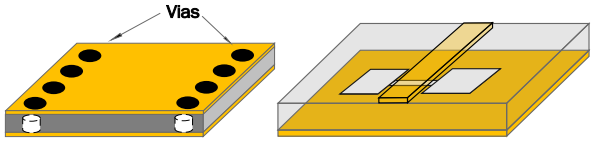

Fig.1. Schematic of: (a) SIW and (b) DGS structure.

Employment of defected ground structures (DGS) has been suggested in order to enhance the performance characteristics of microstrip microwave circuits. DGS are realized by defecting a ground plane on a PCB board with special shapes so as to disturb the shielded current distribution and effect the input impedance, with respect to the shape and its dimension (Fig. 1 (b)) [9]. The positions and lengths of the dumbbell sections control the response and insertion loss attenuation of the design. DGS increases the effective values of dielectric constant of substrates (ε_{eff}).

In the research conducted, by designing and realization of a dual band microstrip patch antenna

Submitted On: June 29, 2016
Accepted On: October 4, 2017

designs had been studied by using DGS and SIW technology. A few modifications were done to the design given in [10] such as splitting the back part of the cavity in order to open the feeding network from the rear and the dumbbell-shaped DGS structures so as to enhance the gain and reflection performances of the models and then applied to antenna designs suitable for 2.4 and 5.6 GHz RF applications. The proposed antennas are prototyped over Rogers 4350 (dielectric constant 3.66, thickness 1.52 mm). In Section II a brief explanation about the design procedure and its parameters is given. Section III presents the simulation and measurement performances of the proposed SIW antenna designs. Finally the last Section presents the conclusions reached.

II. DESIGN OF DUAL BAND SIW ANTENNA

In [10], a SIW cavity-backed patch antenna design for X band applications is presented. In this study, the design suggested in [10] is tuned by using Eqs. 1-3 [11] to operate at 2.4 and 5.6 GHz bands. The design schematic and parameters of the design are presented in Fig. 2 and Table 1;

$$width = w = \frac{C}{2 f_0 \sqrt{\frac{\varepsilon_r + 1}{2}}}, \quad (1)$$

$$\varepsilon_{eff} = \frac{\varepsilon_r + 1}{2} + \frac{\varepsilon_r - 1}{2} \left| \frac{1}{\sqrt{1 + 12\left(\frac{h}{w}\right)}} \right|, \quad (2)$$

$$Length = \frac{c}{2 f_0 \sqrt{\varepsilon_{eff}}} - 0.824h \left(\frac{\left(\varepsilon_{eff} + 0.3\right)\left(\frac{w}{h} + 0.264\right)}{\left(\varepsilon_{eff} - 0.258\right)\left(\frac{w}{h} + 0.8\right)} \right). \quad (3)$$

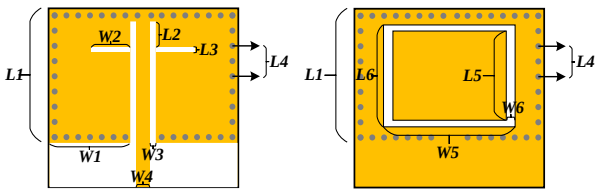

(a) (b)

Fig. 2. (a) Top and (b) bottom schematic of SIW antenna.

By placing vias in the edge of the patch area it is possible to create waveguide walls for the SIW design. By using this method it is possible to enhance the reflection coefficient (S_{11}) characteristics of the antenna design; this can be observed from Fig. 3 where the SIW structure has reduced the reflection of the model to -15 dB. The top layer of design consists of a microstrip patch antenna aimed to operate in ISM band applications.

All the antenna models in this work are designed and simulated in the CST 3D simulation environment. The dimension values given in Table 1 are obtained through trial and error and optimization toolbox of CST for obtaining the best realizable design parameters and performance in 2.4 & 5.6 GHz bandwidths.

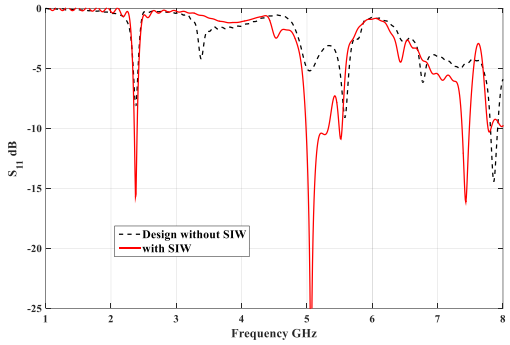

Fig. 3. Simulated reflection coefficient characteristic of antenna design with and without SIW.

Table 1: The dimension values of SIW antenna

Widths (mm)		Lengths (mm)	
W_1	23.5	ℓ_1	41.4
W_2	9.4	ℓ_2	10.5
W_3	1.9	ℓ_3	1.8
W_4	3.1	ℓ_4	6
W_5	37.1	ℓ_5	25
W_6	3.15	ℓ_6	30.3
Via diameter		0.6	

Figure 4 shows the manufactured SIW antenna. A few modifications were done after the manufacturing so as to enhance the performance of the proposed antenna.

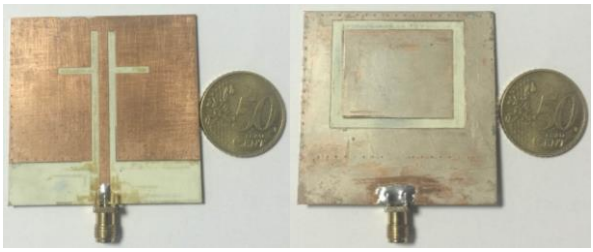

(a) (b)

Fig. 4. Top view of the manufactured SIW antenna: (a) top layer and (b) bottom layer.

The schematic view and the parameters of the modified SIW antenna are given in Fig. 6 and Table 2. The rear part of the cavity is split in two sections in order to open the feeding network from behind and configure the reflection coefficient characteristic of the antenna so that the resonance at 5 GHz shifted to

5.6 GHz. The effect of gap on the cavity back (w_9) to the reflection performance of design can be seen from Fig. 5. The positions and lengths of the dumbbell sections control the response and insertion loss attenuation of the design.

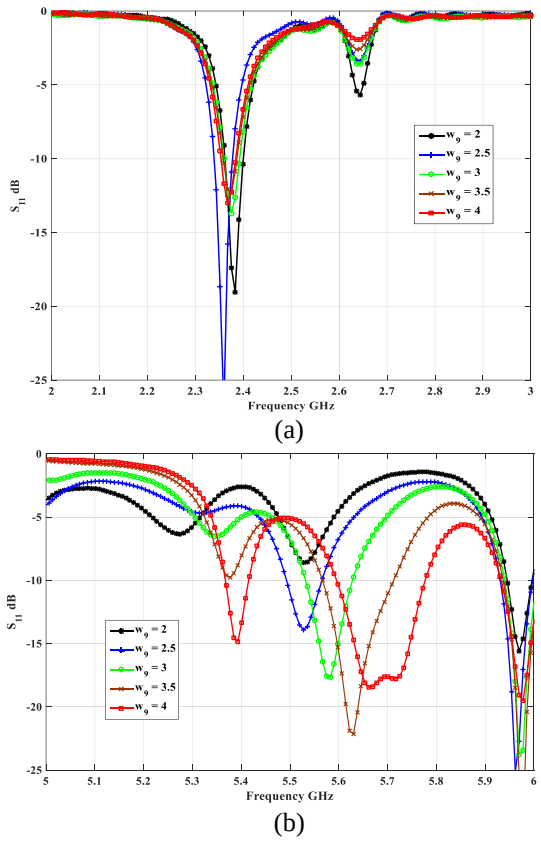

Fig. 5. The effect of gap on the cavity back (w_9) to the reflection characteristic.

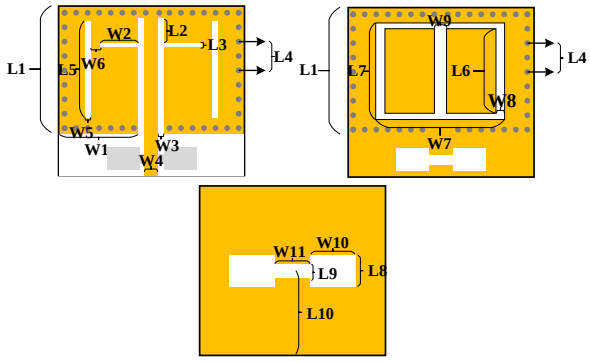

Fig. 6. Schematic of modified SIW antenna.

The two defected areas (w_5, l_5) are added to the top layer, thus achieving a higher radiation efficiency at 5.6 GHz. The DGS will affect the disturbance at the shielded current distribution which, in turn, will influence the input impedance of the design. In the next section, the experimental and simulation results of both SIW antenna designs are presented.

Table 2: The dimension values of modified SIW antenna

Widths (mm)		Lengths (mm)	
W_1	23.5	ℓ_1	41.4
W_2	9.4	ℓ_2	10.5
W_3	1.9	ℓ_3	1.8
W_4	3.1	ℓ_4	6
W_5	1.5	ℓ_5	25
W_6	7	ℓ_6	30.3
W_7	37.1	ℓ_7	25
W_8	3.15	ℓ_8	3
W_9	3	ℓ_9	0.3
W_{10}	1	ℓ_{10}	6.57
W_{11}	3.2	Via diameter	1

III. SIMULATION AND MEASUREMENTS

In this section, the measurement results of the prototyped designs given in Fig. 7 are compared with the simulated results.

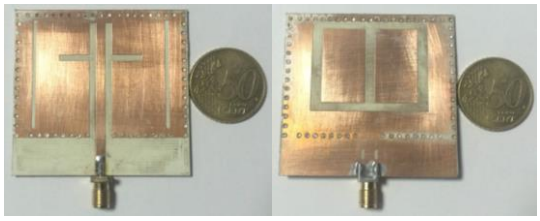

Fig. 7. Top view of the manufactured modified SIW antenna: (a) top layer and (b) bottom layer.

Both, the simulation as well as measurement results of the reflection performance of the manufactured antennas are given in Fig. 8.

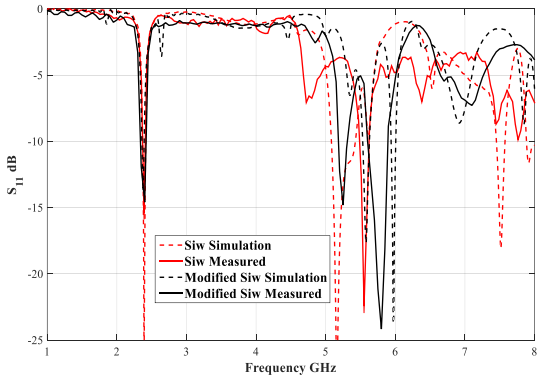

Fig. 8. Simulated and measurement reflection performance.

The maximum far field gain of the proposed SIW antennas is measured using the measurement setup shown in Fig. 9. By using two identical antennas given in [12], the far field gain and radiation pattern results of the proposed antennas are obtained.

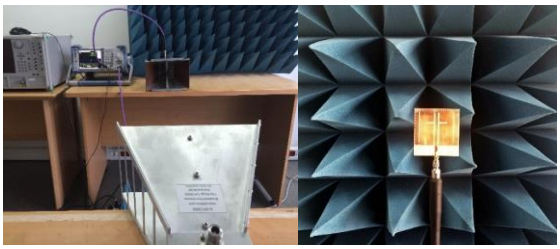

Fig. 9. Measurement setup for maximum far field gain.

The measured far field gain and radiation pattern of the fabricated antennas are given in Fig. 10 and Fig.11. As is seen from Fig. 10, the maximum far field gain of the proposed modified SIW antenna design is almost 1.5 dB and 1 dB higher than the other design at 2.4 and 5.6 GHz bands with a simple design modification to the primary antenna model.

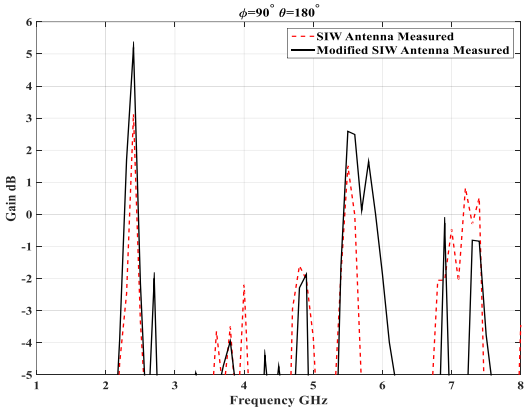

Fig. 10. Measurement results for maximum far field gain.

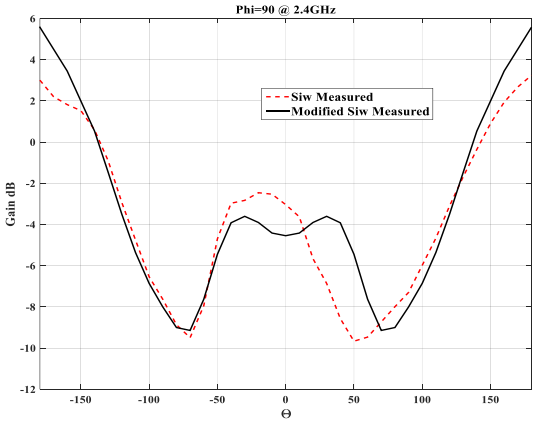

(a)

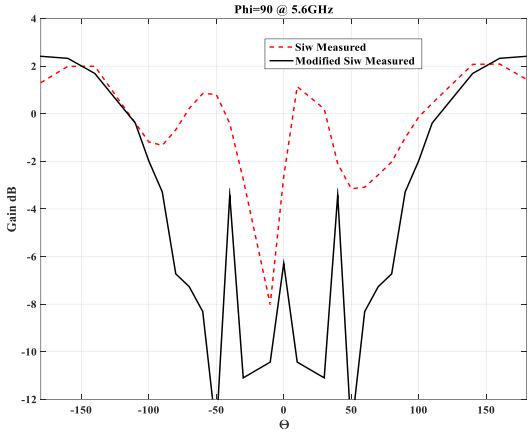

(b)

Fig. 11. Measurement results for radiation pattern: (a) 2.4 GHz and (b) 5.6 GHz.

In Fig. 11, the measured far field gains of prototyped antenna models are given. As is evident, the propagation directions of both antenna designs are from the back. The modified antenna design has almost 3 dB @ 2.4 GHz and 1.5 dB @ 5.6 GHz gain improvement as compared to the counterpart model.

IV. CONCLUSION

As is seen from measurement and simulation results, the proposed dual band antennas designed with SIW technology deliver high performances; further, by adding modifications such as defecting top layers or adding DGS to the design, it is possible to enhance its total performance. The design techniques presented here suggest that the proposed antenna model is a feasible, low cost, high performance dual band antenna design that can easily be integrated in wireless communication systems for ISM band applications.

REFERENCES

[1] M. Petersen, "High performance microwave antennas using SIW technology," Aug. 2017, Available at: http://www.antennasonline.com/main/blogs/high-performance-microwave-antennas-using-siw-technology

[2] M. Esquius-Morote, B. Fuchs, J. Zurcher, and J. R. Mosig, "Novel thin and compact H-plane SIW horn antenna," *In Antennas and Propagation, IEEE Transactions on Antennas and Propagation*, vol. 61, pp. 2911-2920, 2013.

[3] M. Bozzi, A. Georgiadis, and K. Wu, "Review of substrate-integrated waveguide circuits and antennas," *IET Microwaves, Antennas & Propagation*, vol. 5, pp. 909-920, 2011.

[4] Z.-C Hao, W. Hong, J.-X Chen, X.-P Chen, and K. Wu, "Compact super-wide bandpass substrate integrated waveguide (SIW) filters," *IEEE Trans.*

on Microwave Theory and Techniques, vol. 53, pp. 2968-2977, 2005.

[5] Y.-J. Cheng, W. Hong and K. Wu, "Millimeter-wave substrate integrated waveguide multibeam antenna based on the modified r-kr lens," *Microwave Symposium Digest, IEEE MTT-S International*, Atlanta, GA: IEEE, pp. 703-706, 15-20 June 2008.

[6] F. Giuppi, A. Georgiadis, A. Collado, M. Bozzi, and L. Perregrini, "Tunable SIW cavity backed active antenna oscillator," *Electron. Lett*., vol. 46, pp. 1053-1055, 2010.

[7] J. Liu, D. Jackson, and Y. Long, "Substrate integrated waveguide (SIW) leaky-wave antenna with transverse slots," *IEEE Trans. on Antennas and Propagation*, vol. 60, pp. 20-29, Jan. 2012.

[8] E. Arnieri, G. Amendola, L. Boccia, and G. D. Massa, "Substrate integrated radiating waveguides with a coaxial feed," *Antennas and Propagation, The Second European Conference, IEEE*, Edinburgh, pp. 1-4, 11-16 Nov. 2007.

[9] P. Mahouti, M. A. Belen, H. P. Partal, S. Demirel, and F. Günes, "Miniaturization with dumbbell shaped defected ground structure for power divider designs using sonnet," *Applied Computational Electromagnetics*, Williamsburg, VA, USA: IEEE, pp. 1-2, 22-26 Mar. 2015.

[10] R. D. Portilla, "X-band substrate integrated waveguide cavity-backed patch antenna self-oscillating mixer," *Universitat Politècnica de Catalunya Pontificia Universidad Católica del perúcentretecnològic de telecomunicacions de catalunya*, Spain, 2010.

[11] Pasternack's Microstrip Patch Antenna Calculator, August 14, 2017. https://www.pasternack.com/t-calculator-microstrip-ant.aspx

[12] LB8180, 0.8-18 GHz broadband horn antenna, August 14, 2017. Available at: http://www.ainfoinc.com/en/p_ant_h_brd.asp

Mehmet Ali Belen received his M.Sc. degree in Electronics and Communication Engineering from the Süleyman Demirel University in 2011. He has been currently in the Ph.D. program of Yıldız Technical University. His current research interests are in the areas of multivariable network theory, device modeling, computer aided microwave circuit design, monolithic microwave integrated circuits, and antenna arrays.

Peyman Mahouti received his Ph.D. degree in Electronics and Communication Engineering from the Yıldız Technical University in 2016. He has been currently working as a Teaching Assistant in the Yıldız Technical University. The main research areas are optimization of microwave circuits, device modeling, and computer-aided circuit design and antenna designs.

Alper Çalışkan received his M.Sc. degree in Electronics and Communication Engineering from the Yıldız Technical University in 2013. He has been currently in the Ph.D. program of Yıldız Technical University. The main research areas are optimization of microwave circuits, broadband antenna designs, and device modeling.

Aysu Belen received her M.Sc. degree in Electronics and Communication Engineering from the Yıldız Technical University in 2016. She has been currently in the Ph.D. program of Yıldız Technical University. Her main research areas are optimization of microwave circuits, circuits, device modeling, and computer aided circuit design and microwave amplifiers.

Superformula-Based Compact UWB CPW-Fed-Patch Antenna With and Without Dual Frequency Notches

Amjad A. Omar [1], Shaimaa Naser [2], Mousa I. Hussein [3], Nihad I. Dib [2], and Maram W. Rashad [1]

[1] Department of Electrical, Electronic, and Communication Engineering
American University of Ras Al Khaimah, Ras Al Khaimah, UAE
amjad.omar@aurak.ac.ae, maram.rashad@aurak.ac.ae

[2] Department of Electrical Engineering
Jordan University of Science and Technology, Irbid, Jordan
naser.shaimaa@yahoo.com, nihad@just.edu.jo

[3] Department of Electrical Engineering
UAE University, Al-Ain, UAE
mihussein@uaeu.ac.ae

Abstract — This paper presents two new designs of UWB coplanar waveguide (CPW)-fed-patch antennas operating in the FCC frequency band (3.1-10.6 GHz). The first design uses the superformula to produce a circular patch with sawtooth-like circumference. As compared to a regular circular patch antenna whose diameter is 25 mm, the proposed circular patch has a smaller diameter of 18.2 mm. Moreover, the proposed antenna covers the entire FCC band unlike a regular circular patch of the same radius. The second design introduces two frequency notches at 3.3-3.8 GHz (WiMAX) and 5-5.9 GHz (WLAN) using two arc shaped circular slots etched on the circular patch and a split-ring resonator (SRR) that is placed on the opposite side of the substrate. Measurements and simulations using HFSS show that the return loss is better than 10 dB across the band except at the two notch locations in Design II. Results are also presented for the radiation pattern and peak gain of both designs. Each of the proposed antennas has a compact size of 24 mm x 19 mm on a 1.5 mm Rogers Substrate (ε_r=3.85).

Index Terms — Coplanar waveguide, frequency notch, SRR, superformula, UWB.

I. INTRODUCTION

Ultra-wideband antennas (UWB) have attracted much attention in the past few years because they cover a wide frequency spectrum which can be utilized for multi-applications. This makes them very appealing especially for broadband wireless applications such as mobile communications, short range radar, medical imaging, etc. The Federal Communications Commission (FCC) has reserved the frequency band between 3.1 and 10.6 GHz to be an unlicensed band in which UWB antennas are the most appropriate types of antennas [1].

To be compatible with monolithic microwave integrated circuits, UWB antennas have mainly employed microstrip or coplanar waveguide (CPW) feeds. However, CPW has several advantages over microstrip in terms of easier integration with active and passive elements, lower frequency dispersion, the extra design freedom through the ability to vary the characteristic impedance and phase constant by changing the slot and strip widths, and avoiding the excessively thin, and therefore fragile, substrates as in microstrip line [2, 3].

Gielis, in the year 2003, proposed what is known as the superformula which is basically a generalization of the super-ellipse formula [4]. It has six different parameters which when properly selected can produce many complex shapes and curves that are found in nature. The superformula has been used by Simone *et al*. [5] to produce dielectric resonator antennas of different shapes. It has also been used by Bia *et al*. to produce supershaped lens antennas for high frequency applications [6]. Paraforou [7] applied the superformula to get different patch antenna shapes. The same formula has also been used by Naser and Dib [8] to design a compact UWB microstrip-fed patch antenna.

More recently, the superformula was used by Omar *et al* [9] to design UWB CPW fed patch antenna that operates in the FCC band (3.1-10.6 GHz). The patch shape proposed in [9] was circular with sawtooth-like circumference, as shown in Fig. 1, which is used to replace the conventional circular patch antenna [10, 11]. The use of sawtooth patch allows for a reduction of the patch diameter from 25 mm to 18.2 mm without affecting

Submitted On: June 4, 2017
Accepted On: October 11, 2017

the UWB performance. It also allows for an increase in bandwidth. However, no measurements were provided in [9] to verify the design and only simulation results for the return loss and radiation pattern were provided. Moreover, [9] proposed one antenna design only that does not have any frequency notches.

In this paper, we provide measured results for the return loss and group delay of the antenna proposed in [9]. These results are used to verify the design through comparing measurements with HFSS [12] simulations. Simulated results are also provided for the radiation pattern and peak gain across the FCC band. The choice of the circular patch with sawtooth-like circumference was motivated by the fact that repeated patterns on the radiating element are expected to increase the bandwidth as is the case of fractal geometries [13-15].

Moreover, in this paper, the design in Fig. 1 is modified to include two frequency notches that will exclude the WiMAX (3.3-3.8 GHz) and WLAN (5-5.9 GHz) bands from the UWB antenna band [11, 16, 17]. These two notches are generated by etching two arc-shaped radiating slots in the circular patch, and adding a split ring resonator (SRR), as shown in Fig. 2. Measured and simulated results are presented for the return loss and group delay of both designs. Simulation results are also presented for the radiation pattern and peak gain.

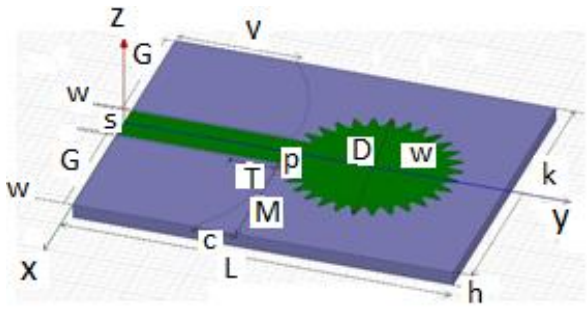

Fig. 1. 3-D view of the UWB antenna (Design I). (ε_r=3.85, tanδ=0.0088, h=1.5 mm, S=4.532 mm, W=0.34 mm, L=40 mm, K=32.4 mm, G=13.6 mm, V=12.7 mm, M=13.5 mm, C=4.25 mm, T=4.76 mm, P=1.94 mm, D=18.2 mm).

Section II presents the superformula and its parameters that were used to produce the designs of Figs. 1 and 2. Section III shows our results for the UWB antenna of Fig. 1 (Design I). Section IV shows our results for the antenna of Fig. 2 (Design II) which has two frequency notches. Section V produces reduced size versions of our two antenna designs by simply shortening the length of the feeding CPW and reducing the lateral and longitudinal extents of the substrates. A comparison is then carried out in this section in terms of size between our designs and several other UWB antennas available in the literature.

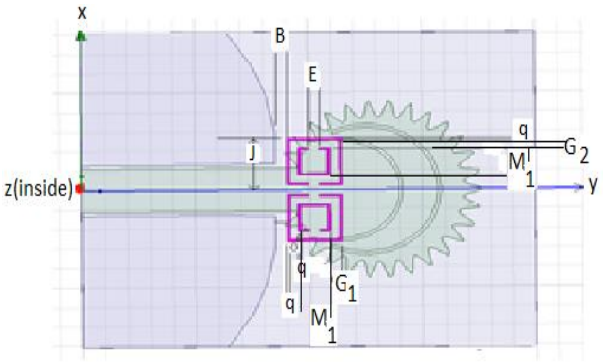

Fig. 2. Top view of the notched UWB antenna with two arc-shaped slots and one SRR (Design II). The SRR is at z=-1.5 mm (i.e., at the bottom side of the substrate), while the feed and patch are at z=0. (J=5.35 mm, q=0.25 mm, O=0.8 mm, M_1=2.55 mm, G_1=1.05 mm, B=1 mm, E=1 mm, the other dimensions are the same as in Fig. 1).

II. ANTENNA DESIGN

The superformula has six parameters: n_1, n_2, n_3, m, a, b. It is given by [4]:

$$r = \left[\left| \frac{\cos(\frac{m\theta}{4})}{a} \right|^{n_2} + \left| \frac{\sin(\frac{m\theta}{4})}{b} \right|^{n_3} \right]^{\frac{-1}{n_1}}. \quad (1)$$

Each of the parameters a and b are chosen to be 1 to ensure symmetry of the antenna patch. The parameters n_1, n_2 and n_3 are positive real numbers. The parameter m determines the number of points, corners, sectors, or hollows fixed on the shape and their spacing, while n_2 and n_3 determine if the shape is inscribed or circumscribed in the unit circle. In our design, the chosen parameters are a = b = 1, m = 30, n_1 = n_2 = n_3 = 5 [9]. These will generate the circular patch shapes with sawtooth- like circumference shown in Fig. 1 and Fig. 2.

The two antenna designs of Fig. 1 and Fig. 2 were fabricated on Rogers substrate (ε_r=3.85, loss tangent= 0.0088) of 1.5 mm thickness. The overall dimension for the antenna in each design is 40 mm x 32.4 mm. This will be optimized in Section IV. The feeding CPW has a center conductor width of 4.53 mm and a slot width of 0.34 mm to yield a 50 Ω impedance. Each slot is slowly tapered out to increase the characteristic impedance of the CPW as it approaches the patch for better matching. In addition, in both designs, the ground plane has been curved for better matching. In Fig. 1, G and M are not equal due to the slot taper.

The diameter of the patch in both designs is D= 18.2 mm, while the optimal diameter of a conventional circular patch operating in the FCC band (3.1-10.6 GHz) is 25 mm [11]. This represents about 30% reduction in the diameter of the patch while maintaining UWB operation, as explained in Section III.

III. MEASURED AND SIMULATED RESULTS OF DESIGN I

Simulations have been performed using the commercial simulator HFSS which employs the finite element method [12]. Figure 3 shows the advantage of using a circular patch of sawtooth-like circumference of 18.2 mm diameter that was obtained using the superformula, as compared to a conventional circular patch antenna of optimal diameter of 25 mm [11], and a conventional circular patch antenna of 18.2 mm diameter. This figure shows that the proposed antenna yields better than 10 dB return loss across the entire FCC band. This was also achieved by the 25 mm diameter conventional circular patch antenna. The small size (18.2 mm) conventional circular patch antenna yielded smaller bandwidth whose lowest frequency is 3.6 GHz instead of 3.1 GHz. So, the use of sawtooth circular patch does increase the bandwidth if compared with conventional circular patch of the same diameter. The sawtooth-like circumference with its repetitive pattern behaves like a fractal geometry to increase the frequency bandwidth.

To verify that our proposed design of Fig. 1 operates as an UWB antenna over the FCC band (3.1-10.6 GHz), measured results for the return loss are obtained and compared with HFSS simulations, as shown in Fig. 4. Both measurements and simulations show a return loss that is better than 10 dB over the FCC band which proves the operation of our antenna as UWB antenna in this band. The difference between measurements and simulations may be due to the inaccuracies in measurements due to calibration errors and the reflections by the walls surrounding the measured antenna.

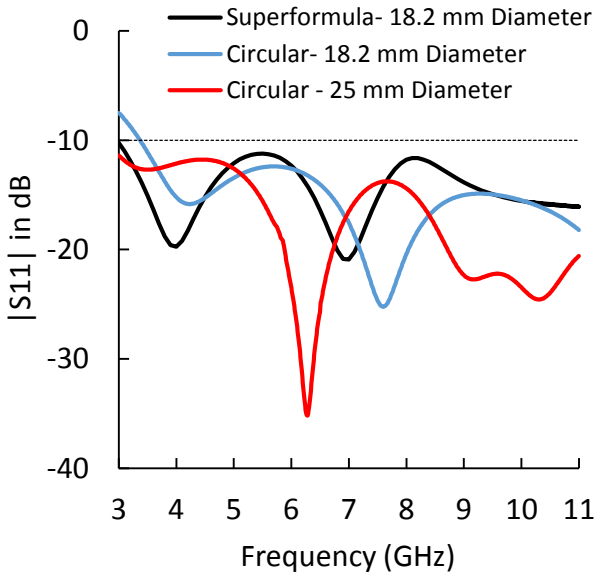

Fig. 3. Simulated $|S_{11}|$ versus frequency of Design I as compared to two UWB antennas with conventional circular patches having 25 mm and 18.2 mm diameters.

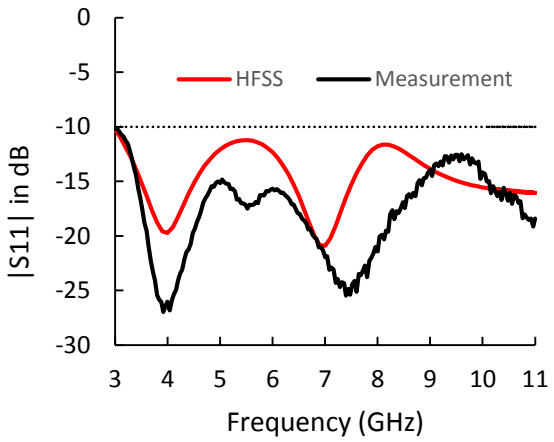

Fig. 4. Measured and simulated $|S_{11}|$ versus frequency for the proposed Design I.

Figure 5 shows measured and simulated results for the group delay of Design I over the FCC band. Both results show small variation of group delay response over the band which is less than 1.5 ns in the measurements and less than 0.5 ns in the simulations. The difference between the simulated and measured group delays is mainly because our antenna was not measured in an anechoic chamber so it suffered from the effect of reflections from the surroundings. This is contrary to the simulations where an absorbing boundary condition was assumed on the faces of the box surrounding the antenna. This is in addition to impedance mismatch at the connectors which can be reduced but not completely eliminated by calibration.

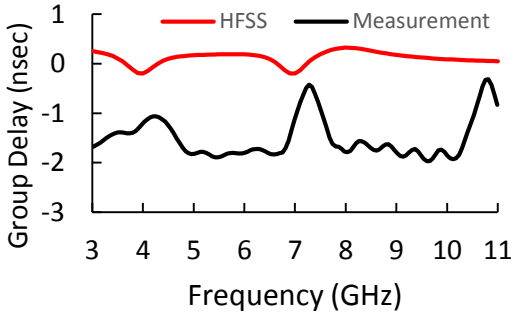

Fig. 5. Measured and simulated group delay for Design I.

The simulated radiation patterns of the proposed antenna (Design I) are shown in Figs. 6, 7, 8 in the E- and H- planes at 4 GHz, 7 GHz and 10 GHz, respectively, where the E-plane corresponds to the yz-plane and the H-plane corresponds to the xz-plane. These figures show that the proposed antenna is linearly polarized and exhibits nearly omnidirectional radiation pattern across the FCC frequency band. The pattern becomes less omni-

directional near the upper frequency range.

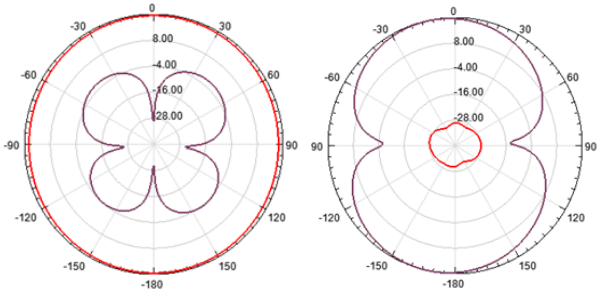

(a) (b)

Fig. 6. Simulated radiation patterns for Design I at 4 GHz: (a) xz-plane (H-plane), and (b) yz-plane (E-plane). E_ϕ is shown in red color, and E_θ in black color.

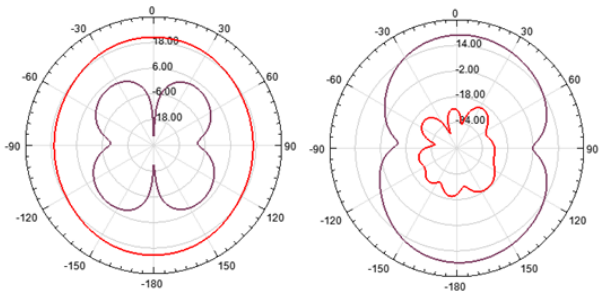

(a) (b)

Fig. 7. Simulated radiation patterns for Design I at 7 GHz: (a) xz-plane (H-plane), and (b) yz-plane (E-plane). E_ϕ is shown in red color, and E_θ in black color.

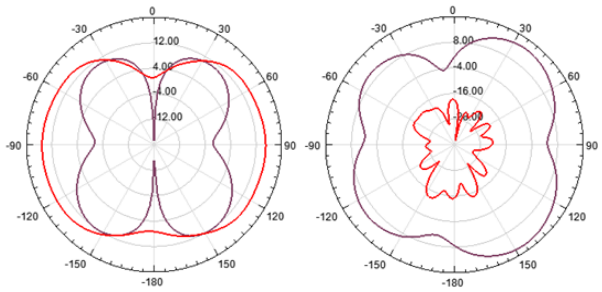

(a) (b)

Fig. 8. Simulated radiation patterns for Design I at 10 GHz: (a) xz-plane (H-plane), and (b) yz-plane (E-plane). E_ϕ is shown in red color, and E_θ in black color.

Figure 9 shows the simulated peak gain of Design I as a function of frequency. The peak gain reaches a maximum of approximately 5 dBi and is almost stable above 4 GHz. The conventional circular patch of 18.2 diameter shows almost the same peak gain performance.

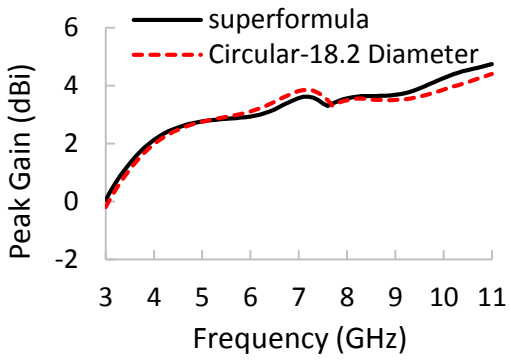

Fig. 9. Simulated peak gain versus frequency for Design I.

IV. MEASURED AND SIMULATED RESULTS OF DESIGN II

As explained in the introduction, Design I was modified to include two frequency notches that correspond to WiMAx (3.3-3.8 GHz) and WLAN (5-5.9 GHz). These notches were created using two arc-shaped slots etched on the sawtooth-like circular patch, as shown in Fig. 2. The arc with larger radius generates the WiMAX notch, while the arc with smaller radius generates the WLAN notch (see Fig. 2). Each arc length is about $\lambda/2$ at the corresponding notch band center frequency. An SRR was built on the bottom side of the substrate opposite to the patch. It is used to control the width of the WLAN frequency notch band and to increase the return loss at the WLAN notch.

To verify that our proposed design of Fig. 2 (Design II) operates as an UWB antenna over the FCC band (3.1-10.6 GHz) with two frequency notches corresponding to the WiMAX and WLAN bands, measured results were obtained for the return loss and compared with HFSS simulations, as shown in Fig. 10. Both measurements and simulations show a return loss that is better than 10 dB over the FCC band except at the notch locations where the return loss reaches 4 dB in measurements and 2 dB in the simulations.

Figure 11 shows measured and simulated results for the group delay of Design II over the FCC band. Both results show a small variation of group delay response over the band which is less than 3.5 ns in the measurements and less than 2 ns in the HFSS simulations. The differences between simulations and measurements may be due to calibration error and reflections from the setup surroundings.

The radiation patterns of the proposed antenna (Design II) are shown in Figs. 12, 13 and 14 in the E- and H- planes at 4 GHz, 7 GHz and 10 GHz, respectively. These figures show patterns that are very similar to those in Figs. 6, 7 and 8 for the case of no frequency notches.

So, the notching technique used in this paper does not cause any significant adverse effects on the radiation pattern. Figure 15 shows the simulated peak gain of Design II as a function of frequency. The peak gain reaches -2.5 dBi at the notch frequencies and has a maximum of about 1.5 dBi.

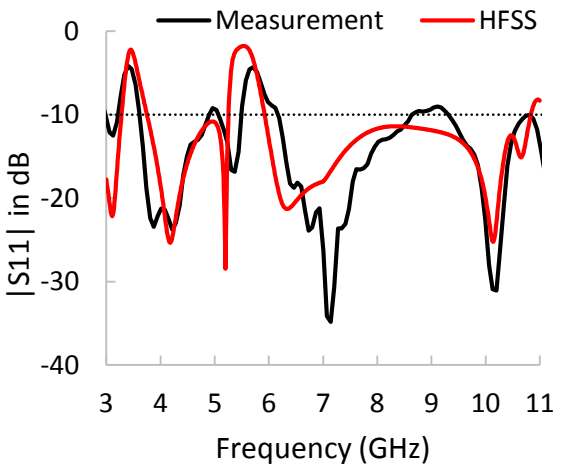

Fig. 10. Measured and simulated $|S_{11}|$ versus frequency for Design II.

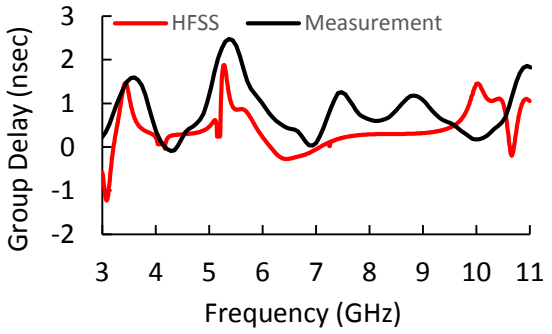

Fig. 11. Measured and simulated group delay for Design II.

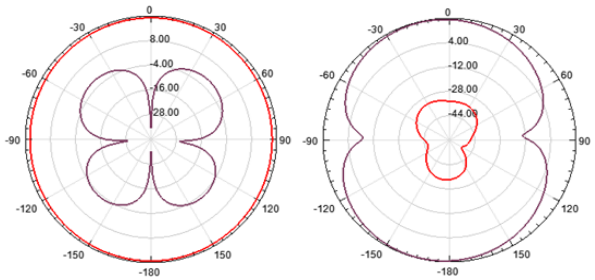

Fig. 12. Simulated radiation patterns for Design II at 4 GHz: (a) xz-plane (H-plane), and (b) yz-plane (E-plane). E_ϕ is shown in red color, and E_θ in black color.

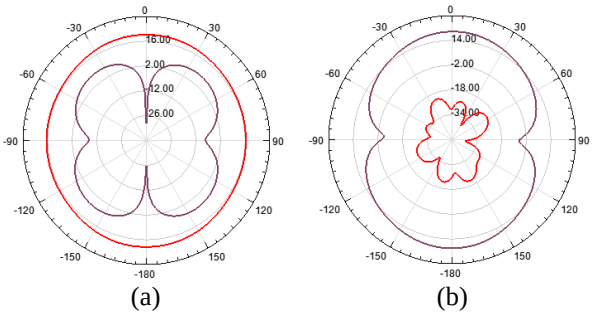

Fig. 13. Simulated radiation patterns for Design II at 7 GHz: (a) xz-plane (H-plane), and (b) yz-plane (E-plane). E_ϕ is shown in red color, and E_θ in black color.

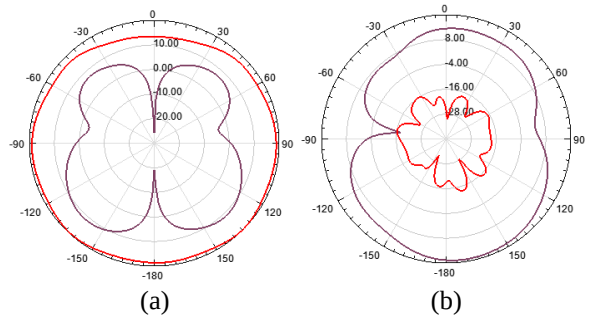

Fig. 14. Simulated radiation patterns for Design II at 10 GHz: (a) xz-plane (H-plane), and (b) yz-plane (E-plane). E_ϕ is shown in red color, and E_θ in black color.

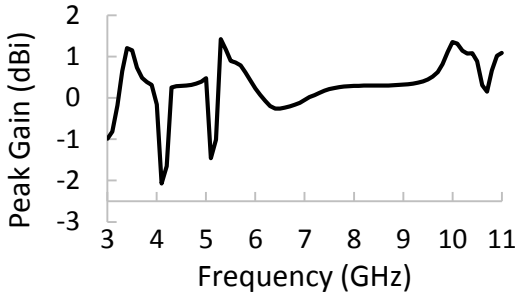

Fig. 15. Simulated peak gain versus frequency for Design II.

V. ANTENNA SIZE COMPARISON

In the designs presented in Figs. 1 and 2, we did not really optimize the size of the antenna which resulted in an antenna whose size is L=40 mm and K=32 mm. However, by simply reducing the feeding line and curved ground lengths (V=3.32 mm, C=0.3 mm) as well as reducing the lateral and longitudinal dimensions of the substrate (L=24 mm and K=19 mm), the final size of our antennas of Figs. 1 and 2 has been reduced to 24 mm × 19 mm. Figure 16 illustrates the simulated and measured return loss of the two antennas of Figs. 1 and 2 for the reduced size. It is clear that the antennas still work well

in the UWB range (return loss better than 10 dB) and the second antenna has notch characteristics around 3.5 GHz and 5.5 GHz.

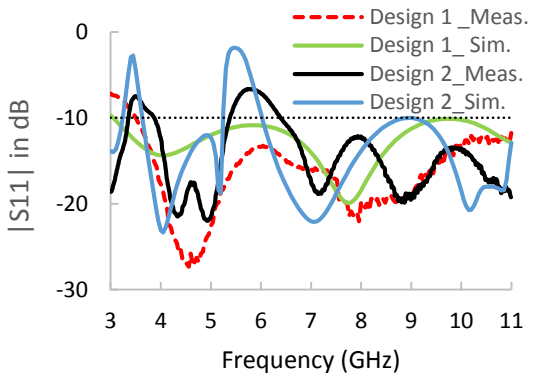

Fig. 16. The simulated and measured S_{11} (dB) for the reduced size antennas of Design I and Design II.

Table 1 shows a comparison between our reduced size designs and several other broadband antennas in terms of size. Our antenna is clearly comparable in size as compared to the other investigated antennas included in the table. In the table, the change in ε_r causes a change in the effective dielectric constant and characteristic impedance of the feed line. It also affects the input impedance of the antenna. This leads to a shift in the operating frequencies towards lower frequencies as ε_r is increased. The change in the impedance also affects the bandwidth of the antenna as the return loss at some frequencies may exceed 3 dB due to increased impedance mismatch leading to these frequencies becoming out of band.

Table 1: Size comparisons for different UWB antennas

Antenna	Our Reduced-Size Antenna	[10]	[11]	[13]	[15]	[18]
Band (GHz)	3-11	2.64-12	2.6-9.5	1.45-4.52	3.1-10.6	3.1-12.3
ε_r	3.85	3	2.33	4.4	9.5	4.4
Size (mm^2)	24 x 19	47 x 47	50 x 50	80 x 40	41.3 x 81.5	24 x 35
Antenna	[19]	[20]	[21]	[22]	[23]	[24]
Band (GHz)	2.7-9.3	2.6-10.8	2.2-17.5	2.615-14	2.69-12.53	2.9-15
ε_r	4.4	2.33	4.4	3.48	4.4	4.4
Size (mm^2)	40 x 50	50 x 50	20 x 24	25 x 37	12 x 18	25 x 38

VI. CONCLUSIONS

This paper proposes two new designs of compact UWB CPW-fed circular patch antennas with sawtooth-like circumference. The first antenna is a UWB antenna operating in the frequency range from 3.1-10.6 GHz. The second antenna has two frequency notches at the WiMAX and WLAN bands. The notches were generated using two arc shaped slots and one SRR. The proposed antenna has smaller size as compared with several other antennas and can be easily designed and fabricated. As far as we know, the proposed design does not have any major shortcoming. However, the designer has to be careful so that the notch generated by the SRR and the notch generated by the smaller circular slot arc are aligned or slightly misaligned to control the frequency bandwidth at the WLAN notch. The differences between measurement and simulations in this paper may be due to calibration errors as well as reflections from the measurement setup walls.

REFERENCES

[1] A. Omar and R. Shubair, "UWB coplanar waveguide-fed-coplanar strips spiral antenna," *10th European Conference on Antennas and Propagation*, Davos, Switzerland, Apr. 2016.

[2] C. P. Wen, "Coplanar waveguide: A surface strip transmission line suitable for nonreciprocal gyromagnetic device applications," *IEEE Trans. Microwave Theory and Techniques*, vol. 17, pp. 1087-1090, 1969.

[3] A. A. Omar and Y. L. Chow, "A solution of coplanar waveguide with airbridges using complex images," *IEEE Trans. Microwave Theory and Techniques*, vol. 40, pp. 2070-2077, 1992.

[4] J. Gielis, "A generic geometric transformation that unifies a wide range of natural and abstract shapes," *American Journal of Botany*, vol. 90, pp. 333-338, 2003.

[5] M. Simeoni, R. Cicchetti, A. Yarovoy, and D. Caratelli, "Circularly polarized supershaped dielectric resonator antennas for indoor ultrawide band applications," *IEEE Int. Symp. Antennas Propag.*, Toronto, July 2010.

[6] P. Bia, D. Caratelli, L. Mescia, and J. Gielis, "Electromagnetic characterization of supershaped lens antennas for high-frequency applications," *43rd European Microw. Conf. Proc.*, Nuremberg, Oct. 2013.

[7] V. Paraforou, "Design and full-wave analysis of supershaped patch antennas," *Master thesis, Delft University of Technology*, Delft, Netherlands, 2013.

[8] S. Naser and N. Dib, "Design and analysis of super-formula-based UWB monopole antenna and its MIMO configuration," *Wireless Personal Communications*, vol. 94, pp. 1-13, 2016.

[9] A. Omar, M. Rashad, M. Al-Mulla, H. Attia, S. Naser, N. Dib, and R. M. Shubair, "Compact design of UWB CPW-fed-patch antenna using the superformula," *5th Int. Conf. on Electronic Devices, Systems, and Applications (ICEDSA-2016)*, UAE, Dec. 2016.

[10] J. Liang, L. Guo, C. C. Chiau, X. Chen, and C. G. Parini, "Study of CPW-fed circular disc monopole

antenna for ultrawideband applications," *IEE Proc. Microwave, Antennas and Propagat*., vol. 152, pp. 520-526, 2005.
[11] J. Y. Siddiqi, C. Saha, and Y. M. M. Antar, "Compact SRR loaded UWB circular monopole antenna with frequency notch characteristics," *IEEE Trans. on Antennas and Propagat*., vol. AP-62, pp. 4015-4020, 2014.
[12] ANSYS-High Frequency Structure Simulator (HFSS). Ansys, Inc., Canonsburg, PA, 2011.
[13] Y. K. Choukiker and S. K. Behera, "Wideband frequency reconfigurable Koch snowlflake fractal antenna," *IET Microwaves, Antennas and Propagation*, vol. 11, pp. 203-208, 2017.
[14] S. Singhal and A. K. Singh, "CPW-fed hexagonal Sierpinski superwideband fractal antenna," *IET Microwaves, Antennas and Propagation*, vol. 10, pp. 1701-1707, 2016.
[15] A. A. Omar, "Design of ultra-wideband coplanar waveguide-fed Koch-fractal triangular monopole antenna," *RF and Microwave Computer-Aided Engineering*, vol. 33, pp. 200-207, 2013.
[16] Z. L. Zhou, L. Li, and J. S. Hong, "Compact UWB printed monopole antenna with dual narrow band notches for WiMAX/WLAN bands," *Electronic Letters*, vol. 47, pp. 1111-1112, 2011.
[17] Y. S. Seo, J. W. Jung, H. J. Lee, and Y. S. Lim, "Design of trapezoid monopole antenna with band-notched performance for UWB," *Electronic Letters*, vol. 48, pp. 673-674, 2012.
[18] M. Hossain, M. Faruque, Md. Islam, M. Islam, and Md. Atiqur Rahman, "Bird face microstrip printed monopole antenna design for ultra wide band applications," *Frequenz*, vol. 70, pp. 473-478, 2016.
[19] S. Hu, Y. Wu, Y. Zhang, and H. Zhou, "Design of a CPW-Fed ultra wide band antenna," *Open Journal of Antennas and Propagation*, vol. 1, pp. 18-22.
[20] J. Y. Siddiqui, C. Saha, and Y. Antar, "Compact SRR loaded UWB circular monopole antenna with frequency notch characteristics," *IEEE Transactions on Antennas and Propagation*, vol. AP-62, pp. 4015-4020, 2016.
[21] A. Abdollahvand, A. Pirhadi, M. Hosseinnezhad, and H. Ebrahimian, "A compact UWB printed monopole antenna with triple-band notched characteristics," *ACES Journal*, vol. 30, no. 4, pp. 374-380, Apr. 2015.
[22] M.-C. Tang, T. Shi, and R. W. Ziolkowski, "Planar ultra-wideband antennas with improved realized gain performance," *IEEE Trans. Antennas Propag*., vol. AP-64, pp. 61-69, 2016.
[23] S. Ojaroudi, Y. Ojaroudi, and N. Ojaroudi, "Compact planar microstrip-fed printed antenna with double band-filtering for UWB application," *ACES Journal*, vol. 30, no. 4, pp. 457-462, Apr. 2015.
[24] Sh. Naser and N. Dib, "Printed UWB pacman-shaped antenna with two frequency rejection bands," *ACES Journal*, vol. 32, no. 3, pp. 186-192, Mar. 2017.

Amjad Omar is a Professor at the Department of Electrical, Electronics, and Communications Engineering at the American University of Ras Al Khaimah (AURAK). He received his Ph.D. in 1993 in Electrical Engineering/Electromagnetics from the University of Waterloo in Canada. He started his career as a Researcher at the Communications Research Center in Ottawa where he worked for 2 years (1993-1994) on the simulation and testing of monolithic microwave integrated circuits. He then worked at several universities in Jordan, UAE, and KSA. He was promoted to Full Professor in Electrical Engineering in January 2014. His research interests are in antennas, numerical electromagnetics, RF circuit design and analysis, NDT for oil and gas, and biological effects of EM radiation on humans.

Shaimaa' A. Naser obtained her B.Sc. in Communications and Electronics Engineering from Jordan University of Science and Technology (JUST), Jordan in 2013. In the same year, she joined the Master program in the Electrical Engineering Department at JUST majoring in Wireless Communications. She obtained her M.Sc. degree in 2015. Her main research interests are in the analysis and design of antennas.

Mousa Hussein received his Ph.D. degree from 1995 to 1997, he was with Research and Development Group at Integrated Engineering Software Inc., Winnipeg, Canada. In 1997 he joined Faculty of Engineering at Amman University, Amman, Jordan, as an Assistant Prof. He is currently with the Electrical Engineering Dept. at the United Arab Emirates University. Hussein's current research interests include, computational electromagnetics, electromagnetic scattering, antenna analysis and design, EMI and signal integrity, Metamaterial, and the implementation of nano particles and plasmonic in electromagnetic applications. Hussein has over 100 publications in international journals and conferences.

Hussein supervised several Ph.D. and M.Sc. students. Hussein is Senior Member of IEEE and the Vice Chair of IEEE-UAE MTT-S Chapter.

Nihad I. Dib obtained his B.Sc. and M.Sc. in Electrical Engineering from Kuwait University in 1985 and 1987, respectively. He obtained his Ph.D. in EE (major in Electromagnetics) in 1992 from University of Michigan, Ann Arbor. Then, he worked as an Assistant Research Scientist in the Radiation Laboratory at the same school. In Sep. 1995, he joined the EE Department at Jordan University of Science and Technology (JUST) as an Assistant Professor, and became a Full Professor in Aug. 2006. His research interests are in computational electromagnetics, antennas and modeling of planar microwave circuits.

Maram W. Rashad obtained her B.Sc. in Electronics and Communication Engineering from American University of Ras Al Khaimah (AURAK), UAE 2016. Her main research interests are in the analysis and design of antennas.

Single-, Dual- and Wide-Band Frequency-Reconfigurable Antenna with Annular Ring Slots

M. C. Lim [1], S. K. A. Rahim [1], M. R. Hamid [2], P. J. Soh [3], M. I. Sabran [1], A. A. Eteng [4], and M. R. Ramli [1]

[1] Wireless Communication Centre (WCC)
Universiti Teknologi Malaysia, 81310, Johor Bharu, Johor, Malaysia
archuan@gmail.com, sharulkamal@fke.utm.my, mursyid@fkegraduate.utm.my, mridduan2@live.utm.my

[2] Radio Communications Engineering
Universiti Teknologi Malaysia, 81310, Johor Bharu, Johor, Malaysia
rijal@fke.utm.my

[3] Advanced Communication Engineering (ACE) CoE, School of Computer and Communication Eng.
Universiti Malaysia Perlis (UniMAP), Kampus Pauh Putra, 02600 Arau, Perlis, Malaysia
pjsoh@unimap.edu.my

[4] Department of Electronic and Computer Engineering, Faculty of Engineering
University of Port Harcourt, Port Harcourt, Nigeria
akaa.eteng@uniport.edu.ng

Abstract ― This paper presents a frequency reconfigurable antenna enabled using a pair of annular ring slots on a coplanar waveguide (CPW) ground plane. Its initial wideband operation mode from 3 GHz to 6 GHz can be reconfigured into six additional modes: a dual–band mode and five single-band modes, with minimum reflection coefficients (S_{11}) of -10 dB. For demonstration and proof-of-concept purposes, metal switches have been used to represent the switches in simulations and measurements. The ON state is emulated using shorted metal switches, whereas the OFF state is emulated using an open. Good agreements are indicated for simulated and measured S_{11} and radiation patterns.

Index Terms ― Frequency reconfigurable antenna, CPW, narrowband, wideband.

I. INTRODUCTION

In the past few decades, wireless communication systems are becoming an essential component of daily human life. An important component of such wireless systems is the antenna, which is required to be multi- or wideband. This feature enables hardware efficiency as access to multiple operating frequency band will be enabled using a single antenna. Besides that, the problems of limited spectrum, regulatory and licensing issues are currently being addressed by the use of cognitive radios (CR). In a CR network, the intelligent radio allows unlicensed users (secondary users) to access spectrum bands licensed to primary users, while avoiding interference with them [1].

To facilitate this, the frequency reconfigurable antenna as it is arguably the most practical option of switching its operation to the desired frequency, instead of utilizing a number of antennas operating in different frequencies for signal transmission or reception. Besides improved performance, multi-frequency operation in a single antenna reduces space and cost. Typically, frequency-reconfigurable antennas can be generally enabled using three methods: mechanical actuation, tuning of material properties and integrating electronic components such as switches or diodes [2]. The third method of using PIN diodes is considered the most practical technique for switching antenna operation between different frequencies [3], [4].

Various previous literature have employed metal switches in proving their concept of reconfiguration. These switches emulate practical microwave switches with realistic amounts of losses. For instance, a frequency reconfigurable tapered slot Vivaldi antenna capable of switching between wideband and narrowband modes using metal switches to control current flow was presented in [5, 6, and 7]. The presence of a metal switch emulates the ON state of a practical microwave switch, whereas its absence emulates the OFF state. Meanwhile, the antenna in [5] uses five ring slots for switching between its wideband mode (from 1.5 GHz to 5 GHz) and another four different sub-bands. Besides

Submitted On: January 21, 2017
Accepted On: October 4, 2017

that, four pair of ring slots were implemented in the ground plane to generate a wideband mode (from 2 GHz to 8 GHz), and reconfiguration to other three lower, middle and upper sub-bands [6]. Next, a Vivaldi antenna with defected ground plane formed using a pair of rectangular ring slot was proposed in [7]. This antenna can be operated in three modes: a wideband mode (from 2.2 GHz to 7.2 GHz), a dual-band WLAN mode (from 2.4 GHz to 2.485 GHz and 5.725 GHz to 5.875 GHz) and a single band WLAN mode (from 2.4 GHz to 2.485 GHz). The rectangular slot functions as a stopband filter for resonance induced by the ring slots.

In this letter, a frequency reconfigurable antenna with capability to reconfigure between wideband and dual-band modes is proposed. The dual-band reconfigurability for this antenna is enabled using a similar concept used for the single-band reconfigurability in [4] and [8]. Besides featuring a compact size of $0.502\lambda_0 \times 0.513\lambda_0 \times 0.023\lambda_0$ at 4.3 GHz, it is capable of switching to six sub-bands with the incorporation of a pair of simple ring slot. This proposed antenna features a wideband mode from 3 GHz to 6 GHz, a dual-band operation centered at 3.7 GHz and 5.8 GHz; and five single-band modes resonant at 4.2 GHz, 4.58 GHz, 4.86 GHz, 5.7 GHz and 6 GHz.

II. ANTENNA DESIGN

An elliptical monopole has been selected as the main radiator based on [9], with annular rings implemented on the ground plane for wideband and narrowband re-configurability. The proposed antenna is designed, simulated and optimized using the commercial electromagnetic solver CST Microwave Studio (MWS), which is based on the Finite Integration Technique (FIT). The structure is meshed using 157,500 hexahedral-shaped mesh cells before being solved numerically using the time domain solver in CST. The boundaries of the structure are set to be open, with additional λ/4 space in all directions based on the lowest simulated frequency. The structure was excited using a 50 Ω port waveguide port. A FR4 substrate, with a relative permittivity (ε_r) of 4.7 and loss tangent (tan δ) of 0.019 is used to ensure a cost-effective implementation. Figure 1 shows the geometry of the proposed antenna operating in its wideband mode (from 3 GHz to 6 GHz in State 1) and dual band mode (centered at 3.7 GHz and 5.8 GHz in State 2) with a S_{11} of -10 dB. Switches are implemented to connect the end points of the rectangular slot, namely S_1 (in State 1) and S_2 (in State 2) in Fig. 1. Table 1 shows the optimized dimensions of the proposed antenna.

To reconfigure resonance, regions with dense surface current distributions are altered by the incorporation of a pair of annular ring slot resonators onto the ground plane. Figure 2 demonstrates its operation in terms of electrical field distribution with and without slot resonator at 3.5 GHz. It is observed that highly dense electrical fields are distributed along the left resonator slot, whereas this intensity is lower on the right ground plane without the resonator slot. A pair of shorting stub placed on the slot circumference as a RF switch effectively alters the current distribution, resulting in resonance at different frequencies [4], [8]. These switch locations also activate the bandpass function of the antenna, determining the suppressed frequencies, and consequently producing operation in the seven bands.

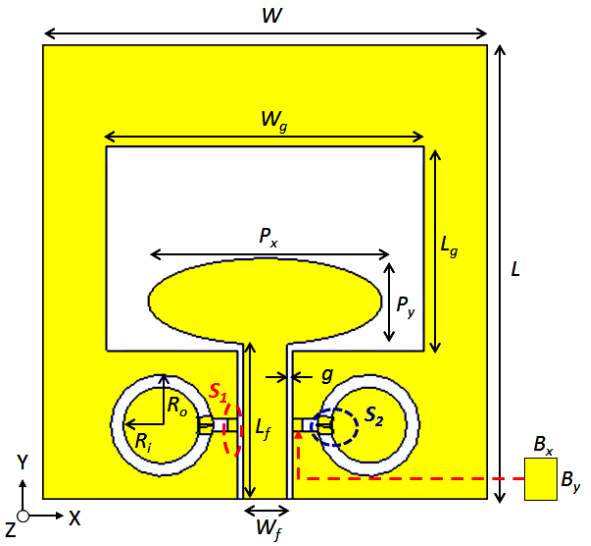

Fig. 1. Geometry of proposed antenna.

Table 1: Parameters of the proposed antenna

Parameter	Dimension [mm]
Width of substrate, W	35
Length of substrate, L	35.8
Gap, g	0.4
Width of CPW ground, W_g	25
Length of CPW ground, L_g	16.11
Width of patch, P_x	18.4
Length of Patch, P_y	6.8
Fed line width, W_f	3.5
Fed line length, L_f	12.2
Ring slot outer radius, R_o	4
Ring slot inner radius, R_i	3
Length of bridge on x, B_x	0.8
Length of bridge on y, B_y	1

The use of either one or two metal switches on each annular ring slot enables reconfigurability between a wide band, a dual band and the five single band modes. They are placed on the two symmetrical ring slots each etched onto the left and the right side of the CPW ground-plane. These switches are placed onto the ring slots with specific clockwise and anti-clockwise rotations, see Fig. 3. The resonator functionality will be

disabled when these switches (S_1) are connected to the ground plane.

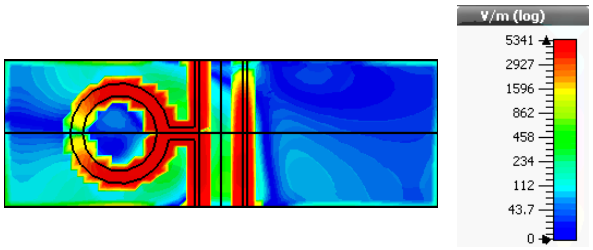

Fig. 2. Simulated E-field distribution.

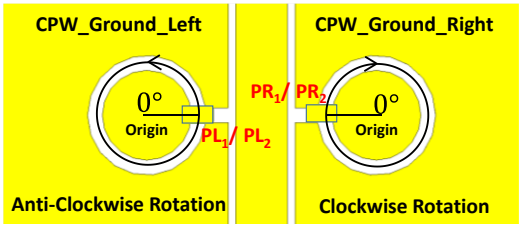

Fig. 3. Geometry of the annular ring slots.

Figure 4 depicts the simulated reflection coefficients for State 1 and State 2. The S_{11} of -13 dB at 4.4 GHz for the State 1 degraded to -4 dB for State 2 upon the shorting of the S_2 annular ring circumference, as illustrated in Fig. 1. This indicates that the ring configuration for the State 2 now functions as a filter. Figures 5 (a) and 5 (b) illustrate the electrical field distributions for the wideband (State 1) and dual-band modes (State 2) at 4.4 GHz. A moderate current density is observed on the ground plane in the wideband mode (State 1). There is a strong current distribution along the perimeter of the resonator in the dual-band mode (State 2), as shown Fig. 5 (b). This length is approximately a quarter-wavelength (λ/4) at 3.7 GHz.

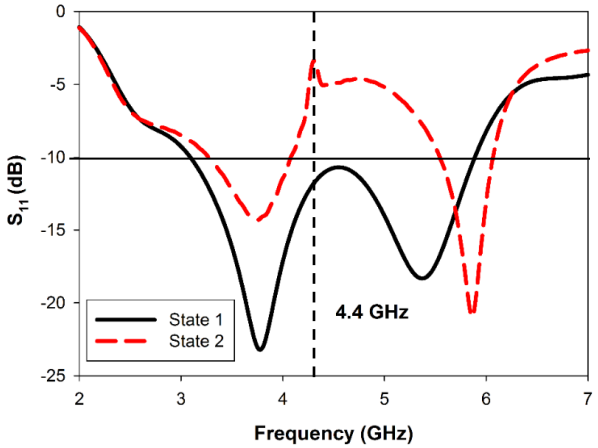

Fig. 4. Simulated reflection coefficients for States 1 and 2.

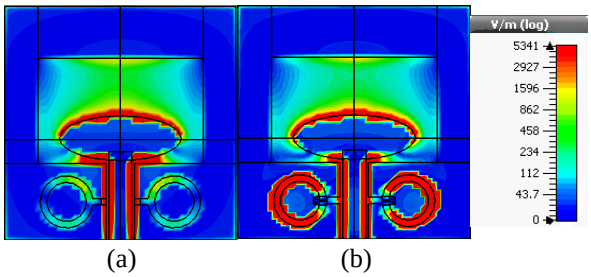

Fig. 5. Simulated E-field distribution at 4.4 GHz for: (a) State 1, and (b) State 2.

To activate the narrowband behavior, the metal switches located at point S_1 need to be disconnected to eliminate wideband mode. The operation of the narrowband states are similar, and is explained by taking State 6 as an example. The simulated S_{11} and S_{21} for this state presented in Fig. 6 indicates a tuned filter behavior, with a pass band at 5.48 GHz located between two stop bands at 2.9 GHz and 6.9 GHz. Placing a shorting stub on each ring slot reduces the electrical field density and isolate both stop bands. The second shorting stub in each slot is used to control the electrical length.

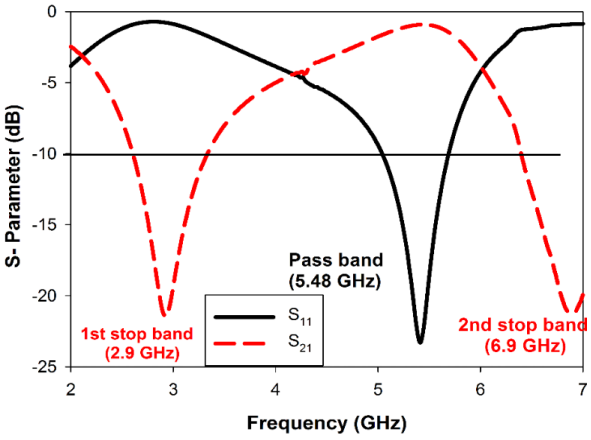

Fig. 6. Simulated S-parameters for State 6.

Figure 7 (a) exhibits the electrical field distribution for the first stop band, with strong electrical fields at 2.9 GHz concentrated in the section S_L (with a length of 14.1 mm). On the other hand, the fields for the second stop band at 6.9 GHz mostly exist within section S_S (with a length of 5.1 mm), as shown in Fig. 7 (b). Both of them are separated by a distance of approximately one sixth of a wavelength in a waveguide ($\lambda_g/6$) at 5.48 GHz in section S_I (with a length of 3.56 mm). The E-Field of the pass band at 5.48 GHz is shown in Fig. 7 (c), indicating high densities in the slot section S_P (with a length of 20.2 mm). The length of this section is approximately equivalent to λ_g at 5.48 GHz. From Fig.

6, the pass band centered at 5.48 GHz is slightly shifted compared to the pass band of State 6 which resonated at 5.7 GHz. This shift is due to the effect of mutual coupling between the patch elements [10]. To further tune the operation of the narrowband modes, locations of these metal switches can be tuned to adjust its electrical length.

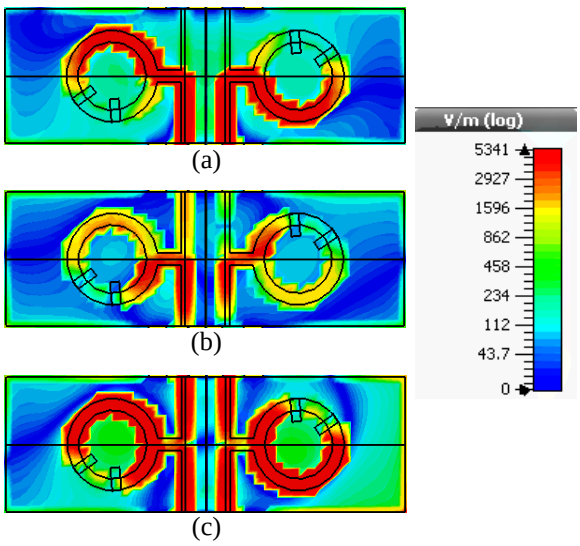

Fig. 7. Simulated E-field distribution of state 6 at: (a) 2.9 GHz, (b) 6.9 GHz, and (c) 5.48 GHz.

III. RESULTS AND DISCUSSION

The proposed antenna has been fabricated to validate its actual antenna performance as seen in Fig. 8. Simulated and measured S_{11} of States 1 (wideband mode) and 2 (dual-band mode) are shown in Fig. 9. The wideband mode is produced by combining and overlapping two resonances at 3.7 GHz and 5.3 GHz [11], resulting in a wider impedance bandwidth. Meanwhile, the dual-band mode is generated by positioning the metal switches in State 2 as listed in Table 2.

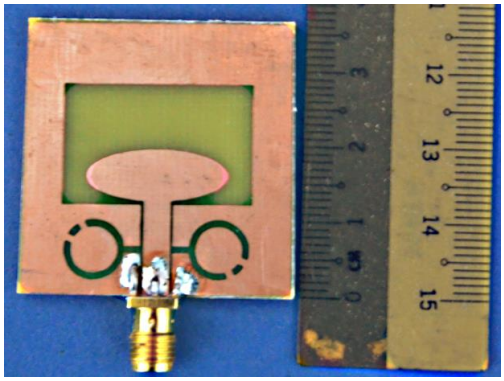

Fig. 8. Photograph of the fabricated antenna (with switch configuration in State 5).

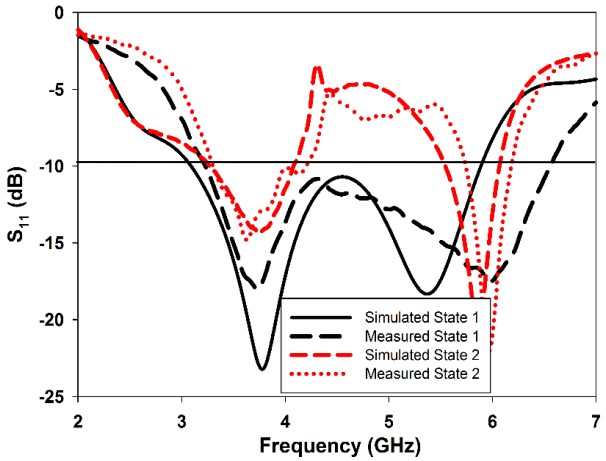

Fig. 9. Simulated vs. measured reflection coefficient for the wideband mode (State 1) and dual-band mode (State 2).

Table 2: Optimal positions of the switches on the annular ring for different states

State #	CPW Ground Left		CPW Ground Right	
	PL_1	PL_2	PR_1	PR_2
S_2	5°	355°	5°	355°
S_3	215°	Nil	215°	Nil
S_4	115°	135°	215°	145°
S_5	115°	155°	205°	245°
S_6	215°	275°	85°	145°
S_7	195°	275°	85°	165°

Figure 10 shows the simulated and measured S_{11} for the five single band modes centered at 4.2 GHz (State 3), 4.58 GHz (State 4), 4.86 GHz (State 5), 5.7 GHz (State 6) and 6 GHz (State 7). The metal switch configuration for States 2 to 7 are summarized in Table 2. Simulated and measured S_{11} for States 3, 4, 5 and 7 as shown in Fig. 10. There exist small discrepancies between the simulated and measured bandwidths. Besides fabrication inaccuracies caused by the small switch dimensions, there is small disagreements between the material properties (ε_r and tan δ) defined in the simulations compared to its actual value. These properties are defined as constants based on the datasheet provided by the manufacturer in simulations, whereas in practice, their variation may be considerable, especially when the antenna is operated throughout a wide frequency band.

Table 3 summarizes the simulated and measured gain and efficiency obtained at resonance when the proposed antenna is operating in the wideband mode. It indicates that the simulated gain of the wideband mode is between 3.6 dBi and 4.17 dBi, whereas its measured gain is between 3.7 dBi and 4.52 dBi within the 3.7 GHz to 6 GHz operating range. Gains for the narrowband mode presented in Table 4 indicate similarity with gain obtained in the wideband mode. For instance, the gain

at 3.7 GHz for State 1 is 3.76 dBi and State 2 is 3.71 dBi, indicating a discrepancy of only 0.06 dBi. One of the key reasons for this is that there exist no parasitic effects originating from components typically used in the DC biasing circuit. The simulated total efficiency of proposed antenna is between 0.81 and 0.98 for the wideband mode, and between 0.93 and 0.98 for the six narrowband modes. All simulated and measured bandwidths are summarized in Table 5.

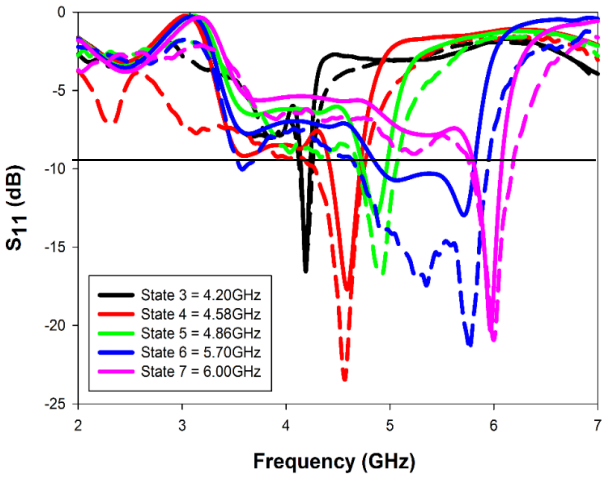

Fig. 10. Simulated (solid line) and measured (dotted line) reflection coefficients (S_{11}) for the single band mode: at 4.2 GHz (State 3), at 4.58 GHz (State 4), at 4.86 GHz (State 5), at 5.7 GHz (State 6), and at 6 GHz (State 7).

Table 3: Gain and total efficiency for the wideband mode

Wideband Mode (State1)							
Frequency band (GHz)	3.7	4.2	4.58	4.86	5.7	5.8	6
Simulated gain (dBi)	3.76	4.16	4.12	3.39	3.6	3.8	4.17
Measured gain (dBi)	3.74	4.43	4.52	4.01	3.7	4.08	4.09
Total efficiency (Simulate)	0.98	0.94	0.93	0.97	0.93	0.9	0.81

Table 4: Gain and total efficiency for the narrowband modes

State	2	3	4	5	6	2	7
Frequency band (GHz)	3.7	4.2	4.58	4.86	5.7	5.8	6
Simulated gain (dBi)	3.7	3.54	3.8	3.63	4.07	4.15	4.07
Measured gain (dBi)	3.06	3.82	2.2	3.29	2.27	3.52	3.87
Total efficiency (Simulated)	0.98	0.96	0.96	0.93	0.94	0.98	0.98

Table 5: Summary of the simulated and measured bandwidths for different modes of the proposed reconfigurable antenna

State	Mode	Bandwidth (Simulated)	Bandwidth (Measured)
1	Wideband	3.07-5.92 GHz (63%)	3.22-6.6 GHz (68%)
2	Dual band	3.2-4.06 GHz (24%) 5.51-6.05 GHz (5%)	3.32-4.2 GHz (23%) 5.53-6.04 GHz (9%)
3	Single band	4.13-4.23 GHz (2%)	4.12-4.24 GHz (3%)
4	Single band	4.42-4.72 GHz (7%)	4.29-4.74 GHz (10%)
5	Single band	4.77-4.98 GHz (4%)	4.7-5.04 GHz (7%)
6	Single band	4.89-5.8 GHz (17%)	4.7-5.93 GHz (23%)
7	Single band	5.81-6.06 GHz (4%)	5.77-6.18 GHz (7%)

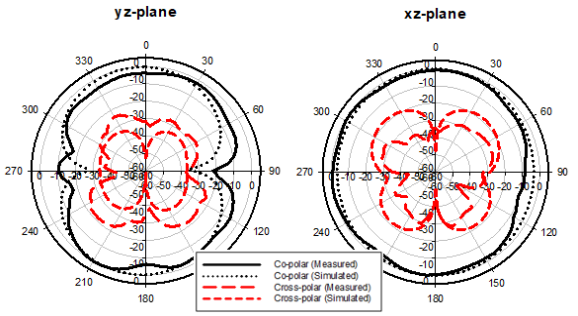

(a)

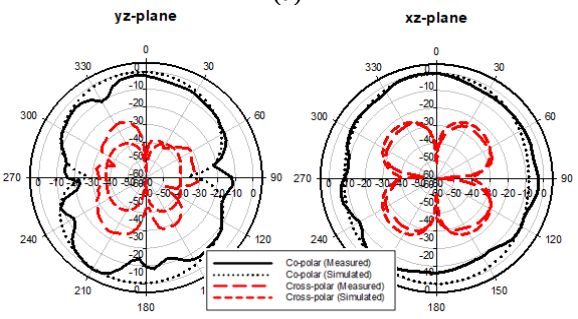

(b)

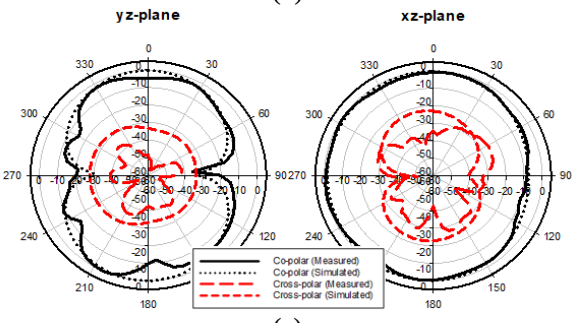

(c)

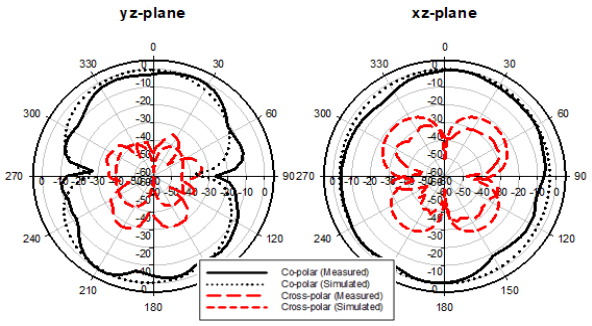

(d)

Fig. 11. Simulated and measured radiation patterns in the: (a) wideband mode: State 1 (at 4.5 GHz), (b) dual-band mode: State 2 (at 3.7 GHz), (c) dual-band mode: State 2 (at 5.8 GHz), and (d) single-band mode: State 4 (at 4.58 GHz).

Figures 11 (a) to 11 (d) illustrate the simulated and measured radiation pattern of proposed antenna measured in an anechoic chamber. The radiation pattern for the wideband mode at 4.5 GHz is plotted in Fig. 11 (a), and for the dual-band mode at 3.7 GHz and 5.8 GHz in Figs. 11 (b) and 11 (c). Finally, the single band radiation patterns at 4.58 GHz for State 4 is illustrated in Fig. 11 (d). As can be seen, all co-polarized patterns in the yz-plane exhibit the conventional monopole characteristic which is bi-directional. Meanwhile, the co-polarized xz-plane fields are quasi-omnidirectional. Good agreements between simulated and measured patterns are observed for the proposed antenna.

IV. CONCLUSION

A compact, 35 mm × 35.8 mm CPW-fed frequency reconfigurable antenna capable of switching between wideband, dual-band and narrowband modes is presented. This is enabled via the proper positioning of switches on a pair of slots etched on the ground plane. These resonators act as bandpass filters to suppress unwanted frequencies. The wideband mode is enabled when the metal stubs are located at the edge of ground plane. Meanwhile, one or two metal stubs are located on the annular ring slot to produce narrowband modes. Finally, the dual-band mode is generated by positioning the two switches (S_2) at the center of the rectangular slot connected to the annular ring resonator. Such features are beneficial for frequency switching in cognitive radios and suited for various wireless applications.

REFERENCES

[1] M. Al-Husseini, L. Safatly, A. Ramadan, A. El-Hajj, K. Y. Kabalan, and C. G. Christodoulou, "Reconfigurable filter antennas for pulse adaption in UWB cognitive radio systems," *Progress In Electromagnetics Research B*, vol. 37, pp. 327-342, 2012.

[2] N. L. Sudhakar Rao, "An overview of tuning techniques for frequency-agile antennas," *IEEE Antennas and Propagation Magazine*, vol. 54, no. 5, pp. 272-226, 2012.

[3] M. I. Lai, T. Y. Wu, J. C. Hsieh, C. H. Wang, and S. K. Jeng, "Design of reconfigurable antennas based on an L-shaped slot and PIN diodes for compact wireless devices," *IET Microwaves, Antennas & Propagation*, vol. 3, p. 47, 2009.

[4] A. Tariq, M. R. Hamid, and H. Ghafouri-Shiraz, "Reconfigurable monopole antennas," *Proceedings of the 5th European Conference on Antennas and Propagation (EUCAP)*, pp. 2160-2164, 2011

[5] T. L. Yim, S. K. A. Rahim, and R. Dewan, "Reconfigurable wideband and narrowband tapered slot Vivaldi antenna with ring slot pairs," *Journal of Electromagnetic Waves and Applications*, vol. 27, pp. 276-287, 2013.

[6] M. R. Hamid, P. Gardner, P. S. Hall, and F. Ghanem, "Reconfigurable Vivaldi antenna," *Microwave and Optical Technology Letters*, vol. 52, pp. 785-787, 2010.

[7] M. R. Hamid, P. S. Hall, P. Gardner, and F. Ghanem, "Switched WLAN-wideband tapered slot antenna," *Electronics Letters*, vol. 46, p. 23, 2010.

[8] R. Hamid, P. Gardner, P. S. Hall, and F. Ghanem, "Vivaldi antenna with integrated switchable band pass resonator," *IEEE Transactions on Antennas and Propagation*, vol. 59, pp. 4008-4015, 2011.

[9] M. C. Lim, S. K. A. Rahim, M. I. Sabran, and A. A. Eteng, "Monopole Ellipse Antenna for Ultra-Wideband Applications," Lecture Notes in Electrical Engineering-Springer, vol. 344, pp. 137-144, 2015.

[10] H. F. Abutarboush, R. Nilavalan, S. W. Cheung, K. M. Nasr, T. Peter, D. Budimir, *et al*., "A reconfigurable wideband and multiband antenna using dual-patch elements for compact wireless devices," *IEEE Transactions on Antennas and Propagation*, vol. 60, pp. 36-43, 2012.

[11] A. K. Gautam, S. Yadav, and B. K. Kanaujia, "A CPW-fed compact UWB microstrip antenna," *IEEE Antennas and Wireless Propagation Letters*, vol. 12, pp. 151-154, 2013.

Lim Meng Chuan was born in Kedah, Malaysia in 1983. He is currently pursuing M.Sc. degree in Universiti Teknologi Malaysia (UTM). He received his dip. in Electronic Engineering (Communication) and B.Sc. degree in Electrical Engineering from Politeknik Sultan Abdul Halim Mu'adzam Shah (POLIMAS) and

Universiti Teknologi Malaysia (UTM) in year 2004 and 2012, respectively. Currently, he is Test Engineer in Multinational Company. His research interests include, Ultra-wideband antenna and reconfigurable antenna.

Sharul Kamal Abdul Rahim received his first degree from University of Tennessee, USA majoring in Electrical Engineering, graduating in 1996, M.Sc. in Engineering (Communication Engineering) from Universiti Teknologi Malaysia (UTM) in 2001, and Ph.D. in Wireless Communication System from University of Birmingham, UK in 2007. Currently, he is an Associate Professor at Wireless Communication Centre, Faculty of Electrical Engineering, UTM. His research interest is Smart Antenna on Communication System.

Mohamad Rijal Hamid received the Ph.D. degree in Electrical Engineering from the University of Birmingham, UK, in 2011. He has been with the Faculty of Electrical Engineering (FKE), UTM, since 2001. His major research interest is reconfigurable antenna design for multimode wireless applications. Currently he is a Senior Lecturer at Communication Engineering Dept., FKE, UTM.

Ping Jack Soh was born in Sabah, Malaysia. He received the Bachelor and Master degrees in Electrical Engineering (Telecommunication) from Universiti Teknologi Malaysia (UTM) in 2002 and 2005, respectively, and the Ph.D. degree in Electrical Engineering from KU Leuven, Belgium in 2013. He is currently a Senior Lecturer at the Advanced Communication Engineering (ACE) CoE, School of Computer and Communication Engineering, Universiti Malaysia Perlis (UniMAP). Soh was the recipient of the IEEE Antennas and Propagation Society (AP-S) Doctoral Research Award in 2012, the IEEE Microwave Theory and Techniques Society (MTT-S) Graduate Fellowship for Medical Applications in 2013 and the International Union of Radio Science (URSI) Young Scientist Award in 2015. He was also the second place winner of the IEEE Presidents' Change the World Competition and IEEE MTT-S Video Competition, both in 2013, besides being awarded the Computer Simulation Technology (CST) University Publication Award in 2011 and 2012.

Mursyidul Idzam Sabran was born in Selangor, Malaysia He obtained his degree in Electrical Engineering (Telecommunication) in 2009 and M.Sc. in Master of Engineering (Electrical) in 2012 from UTM Skudai, Johor Malaysia. He is currently a full-time Ph.D. research student at the Wireless Communication Centre (WCC), Faculty of Electrical Engineering, Universiti Teknologi Malaysia (UTM), Johor, Malaysia.

Akaa A. Eteng obtained the B.Eng. degree in Electrical/Electronic Engineering from the Federal University of Technology Owerri, Nigeria, in 2002, an M.Eng. degree in Electronics and Telecommunications from the University of Port Harcourt, Nigeria in 2008. In 2016, he obtained a PhD in Electrical Engineering from Universiti Teknologi Malaysia. He is currently a lecturer at the University of Port Harcourt, Nigeria.

Muhammad Ridduan Ramli was born in Kuala Terengganu, Malaysia. He obtained his degree in Electrical (Electronic) Engineering in 2015. He is currently a full-time Master by Research Student at the Wireless Communication Centre (WCC), Faculty of Electrical Engineering, Universiti Teknologi Malaysia, Johor, Malaysia.

Dual-Band Antenna for High Gain M2M Communication Using PRS

Sajeela Bibi [1], Rashid Saleem [1], Asim Quddus [2], Sabih ur Rehman [3], and M. Farhan Shafique [4]

[1] Department of Telecommunication Engineering
[2] Department of Electrical Engineering
University of Engineering and Technology, Taxila, 47050, Pakistan
Rashid.Saleem@uettaxila.edu.pk

[3] School of Computing and Mathematics, Charles Sturt University, Australia
sarehman@csu.edu.au

[4] Center for Advanced Studies in Telecommunication
COMSATS Institute of Information Technology, Islamabad, Pakistan
Farhan.shafique@comsats.edu.pk

Abstract ─ A bi-layered, dual-band microstrip antenna for high gain Machine-to-Machine (M2M) communication environment is presented in this paper. This antenna covers WiMAX (3.3-3.7 GHz) and WLAN (4.9-5.1 GHz) bands. The radiating patch is printed on Rogers RT/ Duroid 5880 substrate. A partial ground plane is used to enhance the bandwidth of antenna. A Partial Reflecting Surface (PRS) layer is employed below the antenna layer in order to enhance the gain and bandwidth of the antenna. More importantly, the proposed PRS employed antenna provides gain enhancement of 4.3 dB and 4.4 dB at WiMAX and WLAN bands respectively. Simulated and measured results make this arrangement a potential candidate for high gain Machine-to-Machine (M2M) communication.

Index Terms ─ Antenna, M2M, metasurface, Partial Reflecting Surface (PRS), WiMAX, WLAN

I. INTRODUCTION

A rapid growth in the wireless industry has raised the demand of new technologies such as Internet-of-Things (IoT) and Machine-to-Machine (M2M) communication. However, these communication technologies require a platform that allows range of devices to communicate with each other efficiently [1]. In order to achieve a reliable communication link, these machines or devices require antenna systems that can easily provide multiband access using different wireless services such as Wi-Fi, ZigBee, WiMAX and Wireless LAN (WLAN) [2]. Lately IoT/M2M communication has attracted a lot of interest from researchers and is now playing a pivotal role in providing various applications in the areas of e-health, smart homes and intelligent transport systems [3-4]. Typically, a wireless device, to communicate in IoT communication environment, requires compact high gain and multi-band antennas. Microstrip patch antennas are classified as suitable candidates for multiband operation, primarily due to their small size and easy integration characteristics with other electronic circuitry. Traditionally microstrip antennas are fabricated using single layer structures and these patch antennas have certain inherent drawbacks like low gain and narrow bandwidth [5-6]. In order to overcome these limitations, a commonly adopted technique is to employ a multi-layered structure [7-8]. In [7], authors have presented a design of a dual-layered antenna for multiband communication environment. The proposed design however only results in a 2 dB increase in the antenna gain.

For wideband or ultra wideband antennas which adopt the technique of partial ground radiate in the backward direction resulting in the energy loss in the undesired direction. To overcome this loss, a reflector can be added at the backside of antenna, physically placed with a certain separation beneath the partial ground plane. Metamaterials that are typically designed by arranging a set of small apertures in a regular array are employed to improve the performance of antennas in a similar fashion [9-10]. Specialized meta-surfaces known as Partial Reflecting Surfaces (PRS) are reported widely in the existing literature to enhance the gain of antennas [9-12]. A PRS is commonly placed at a distance of $\lambda_0/2$ from the radiating layer. In [9], the reported antenna aims to create a Fabry-Perot (FP) cavity which comprises of a parallel-plates configuration. In [10-11], the distance between PRS and ground plane is reduced up to $\lambda_0/4$ by replacing ground planes by Artificial Magnetic Conductors (AMCs). However, the AMCs do not help significantly in achieving a compact design. A

Submitted On: April 20, 2017
Accepted On: October 11, 2017

PRS is placed below the antenna in [9] but a gain enhancement of only 3 dB is achieved. The antennas reported in [9-11] operate only on single band. Overall, simultaneously achieving enhanced gain, compactness and a multiband functionality is not trivial in multi-layered structures.

This paper presents an antenna design to cater for IoT/M2M applications that require enhanced gain and multiband capabilities. The proposed design arrangement utilizes a PRS layer below the antenna layer to achieve the desired functionalities. The simulated and measured results show good impedance match and enhanced gain on both WiMAX and WLAN bands.

The rest of this paper is structured as follows: in Section II design configuration is presented, whereas simulated results are presented in Section III. An analysis of PRS is presented in Section IV. Finally, Section V concludes the paper.

II. GEOMETRIC CONFIGURATION

The design of the proposed antenna consists of two layers. First layer comprises of the antenna along with ground plane placed on the rear side. This layer is fabricated on Rogers RT/Duroid 5880 substrate ($\varepsilon_r = 2.2, \tan\delta = 0.0009$) of thickness 1.6 mm. The second layer consists of PRS. This layer is also fabricated on Rogers RT/Duroid 5880 substrate. The distance between two layers is kept at $\lambda_0/8$. Layout of the antenna is shown in Fig. 1. A 50-Ω microstrip feed line is employed to excite the antenna. The dimensions of radiating element are $W_P \times L_P$. A triangular taper with a circular slot is employed as an impedance transformer connected to the feedline, to enhance the overall impedance match. As the proposed design is multi-resonant so three slots having dimensions $L_1 \times 2$ mm (slot 1), $L_2 \times 1.5$ mm (slot 2) and $L_3 \times 1.2$ mm (slot 3), respectively, are introduced in the main radiating element as shown in Fig. 2 (a). Distance between slot 1 and slot 2 is W_2, while the distance between slot 2 and slot 3 is W_3. A partial ground plane having dimensions $O_G \times P_G$ is placed on the flip side of antenna.

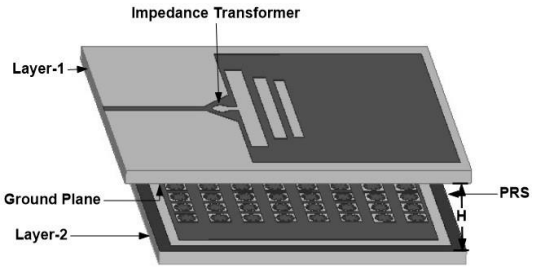

Fig. 1. Layout of the proposed antenna.

In order to enhance the impedance match over the two desired bands, a rectangular parasitic strip with dimensions $M_G \times N_G$ is employed on the flip side of antenna along the partial ground plane. Back view of the antenna layer is shown in the Fig. 2. The optimized antenna design parameters are listed in Table 1.

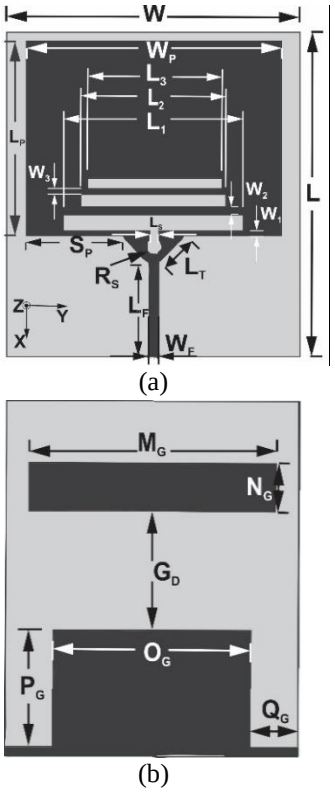

Fig. 2. Geometric configuration of antenna layer: (a) front view and (b) back view.

III. SIMULATED RESULTS

Partially reflecting surfaces (PRSs) are etched on layer 2 of the proposed antenna. The analysis and optimization of these computationally intensive structures is performed using a full-wave Finite Element Method (FEM) based electromagnetic solver (Ansys HFSS™). The whole structure is enclosed in an air box with radiation boundary condition and the antenna is fed through a wave port excitation. In order to get realistic results of simulation, whole structure is simulated at once and no symmetric boundary has been adopted for PRS. This section presents the design architecture and the simulated results.

A. Patch antenna

The technique of etching slots in the patch is employed for size reduction and attaining multi-resonant functionality in the antenna. For this, appropriate selection of position and dimensions of slots is important. The current flow reverses around sides of horizontal slots, which in turn, provides the desired resonances [10]. Effects of three slots on the return loss are shown in Fig. 3.

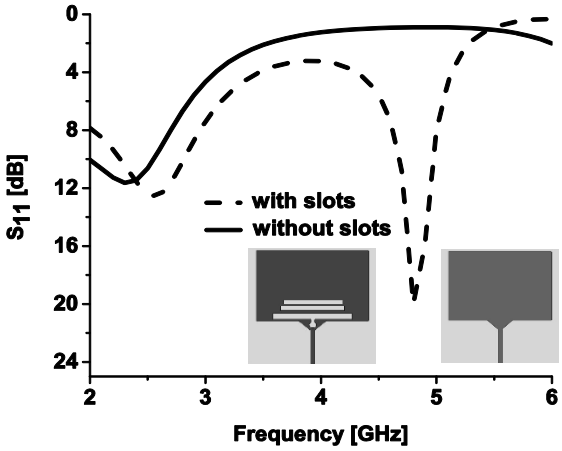

Fig. 3. Simulated return loss of antenna, with and without resonant slots.

Table 1: Parametric values of proposed antenna

Parameter	(mm)	Parameter	(mm)
H	9.66	S_P	11.7
W	35.5	L	1
L	40	L_F	11.8
L_P	24	M_G	30
W_P	30.9	N_G	5.5
L_3	16.3	O_G	24
L_1	21.8	X	0.5
Q_G	5.75	L_2	17.5
W_{PRS}	35.5	T	30
U	29	W_U	2.4
L_{PRS}	35.5	L_U	2.4
P_G	13.2	Y	2
W_F	1.1	R_S	1
W_1	0.6	W_2	1
W_3	0.8	G_D	13.3
L_T	3.1	-	-

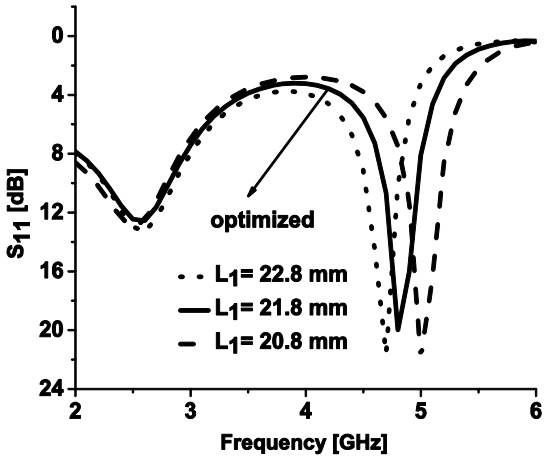

Fig. 4. Effect of slot 1 length variation on WLAN band.

Resonance is created mainly by slot 1 having length L_1 while the following two slots enhance its effect. Lengths of all the three horizontal slots effect the position of resonance at WLAN band. However, this effect can be observed more prominently by varying the length of slot 1 (L_1).

Effects of length variation of slot L_1 on resonance at WLAN is shown in Fig. 4. A triangular region with a circular slot employed as impedance transformer is introduced in the transition region between feed line and main radiating element. This structure is used to enhance the overall impedance match [13].

B. Ground plane

Dimensions of the ground plane effect the excitation mode and the resonance of the antenna. Partial ground plane is used in the proposed antenna as partial ground plane helps to increase the bandwidth of a patch antenna [14]. Figure 5 shows the effects of ground plane dimensions on resonance at WLAN band. It may be observed that the resonance becomes weaker as the width O_G and P_G of the ground plane increases.

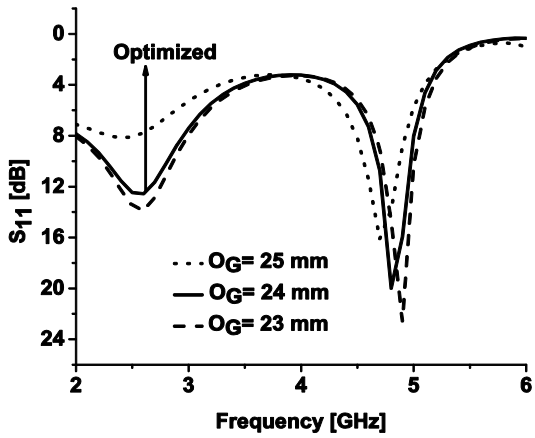

(a)

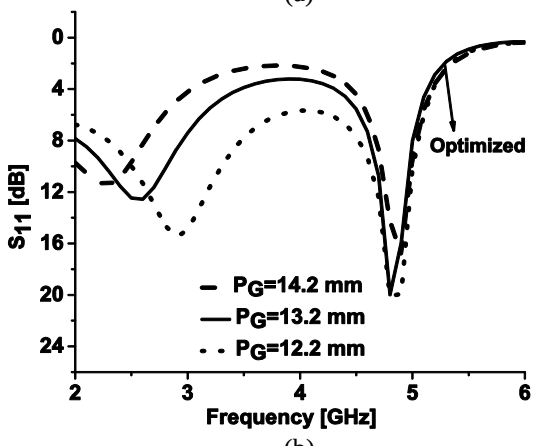

(b)

Fig. 5. Effects of ground plane dimensions on resonance at WLAN: (a) effect of width and (b) effect of length.

IV. PARTIAL REFLECTING SURFACE

The proposed PRS consists of an array of eight-point star-shaped patches arranged in a rectangular grid as shown in Fig. 6. The size of rectangular grid is T × U. The overall array size of the PRS is 7 × 8 cells. The overall dimensions of PRS are L_{PRS} × S_{PRS}. Figure 6 illustrates the dimensions of the proposed PRS. To enhance gain at higher frequency, i.e., WLAN, the size of these patches should be small. However, in order to achieve high gain at low frequency, i.e., WiMAX, the size of these patches should be kept larger. Therefore, dimension of the unit cell is optimized to achieve high gain at both resonant frequencies. Optimized dimensions of the PRS unit cell are listed in Table 1.

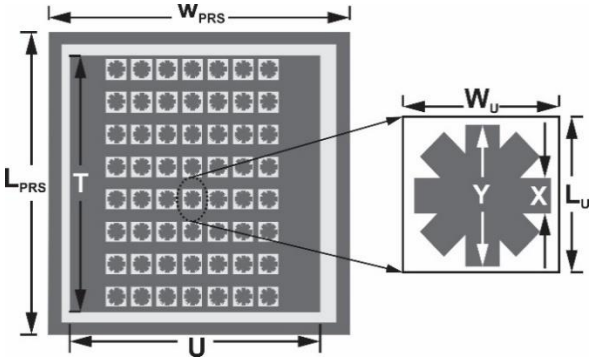

Fig. 6. PRS configuration (PRS and unit cell).

A. Effects of PRS on S-parameter

The PRS-based structure improves the impedance matching at both frequencies, more importantly, at the lower band as shown in the Fig. 7.

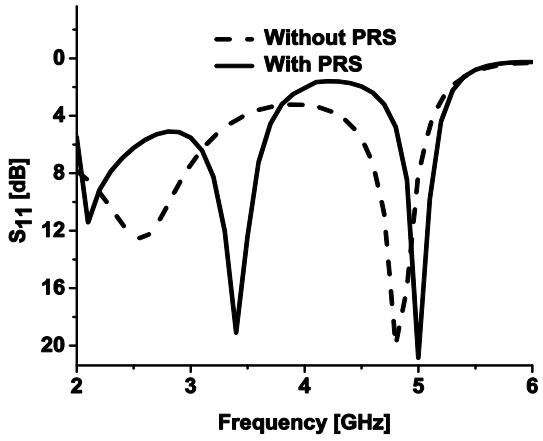

Fig. 7. Simulated effect of PRS on resonances.

B. Effects of PRS on gain

The gain enhancement, results from the electromagnetic coupling or cavity effect initiated between the PRS structure and radiating patch. The PRS significantly enhances the gain at both the desired bands owing to the Fabry-Perot effect as shown in Fig. 8. The gain at 3.5 GHz improves from 2.7 dB to 7 dB and the gain at 5 GHz increase from 3.6 dB to 8 dB.

C. Surface current density

Simulated surface current distributions at resonant frequencies 3.5 and 5 GHz of the proposed antenna, with and without PRS are shown in Fig. 8. It is clear from the figure that at 3.5 GHz current distribution is strong at feedline and ground plane. Current distribution on rectangular patch shows that slot 1 having length L_1 supports the resonating mode at 5 GHz and other two slots help in enhancing its effect.

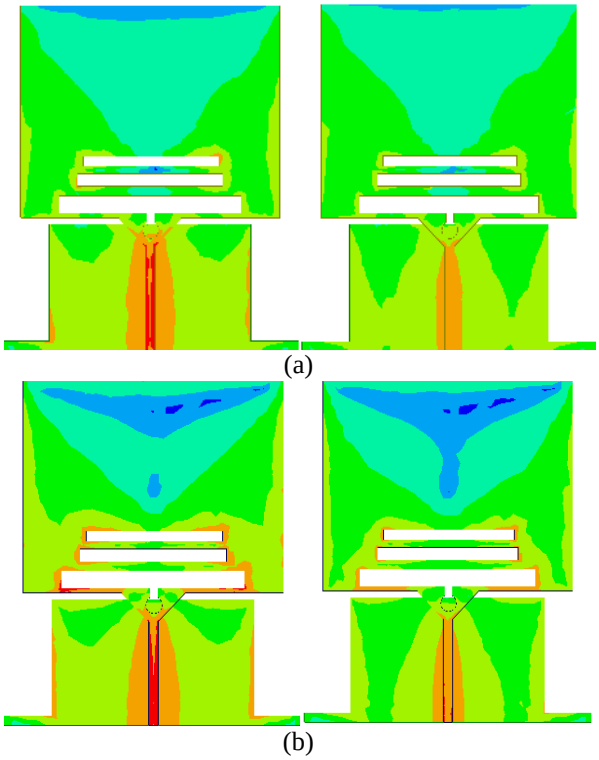

Fig. 8. Simulated surface current distribution at 3.5 GHz (left) and 5 GHz (right): (a) without PRS and (b) with PRS.

V. MEASURED RESULT ANALYSIS

This section presents an analysis of the measured results of the fabricated antenna. A prototype with optimized dimensions as given in Table 1 is fabricated and tested on Rogers RT/Duroid 5880 substrate, as shown in Fig. 9. The measurements were taken on Agilent N5242A PNA-X network analyzer and radiation patterns were measured using Diamond Engineering pattern measurement setup.

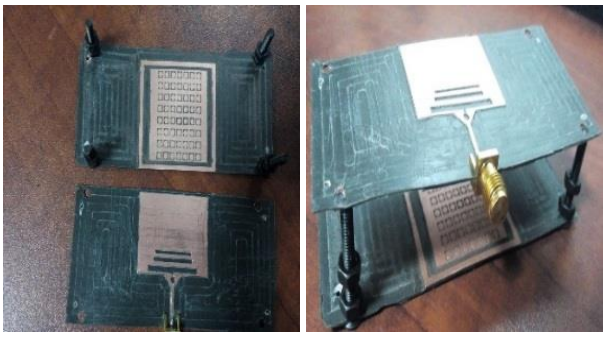

(a) (b)

Fig. 9. Fabricated prototype: (a) Microstrip Patch Antenna (MPA) with PRS and (b) PRS-backed MPA.

A. S-parameter

Measured and simulated return loss of antenna system is shown in Fig. 10. It may be observed that antenna is matched over WiMAX and WLAN bands. There is good agreement between measured and simulated results.

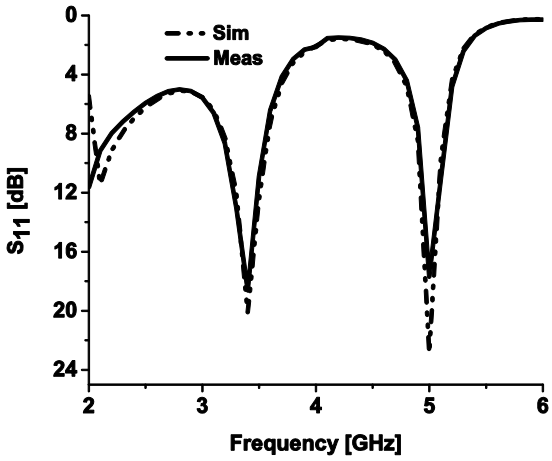

Fig. 10. Simulated and measured return loss of the proposed design.

B. Gain

Measured and simulated gains of the proposed design are shown Fig. 11. It may be observed that the gains at 3.5 and 5 GHz are 5 and 6 dB respectively. A 2-dB difference from the simulated results is due to fabrication and measurement imperfections.

C. Radiation patterns

Measured radiation patterns of the proposed design at 3.5 and 5 GHz with and without PRS are shown in Fig. 12. The antenna has partial ground plane as standard technique to achieve ultra wideband response and consequently the radiation pattern has radiation in both upper and lower direction. The PRS is not backed by a solid ground plane, unlike Artificial Magnetic Conductor (AMC). Thus, it also allows certain radiation to pass through it. It is clear from the figure that proposed PRS-employed antenna exhibits good broadside radiation with a considerable gain.

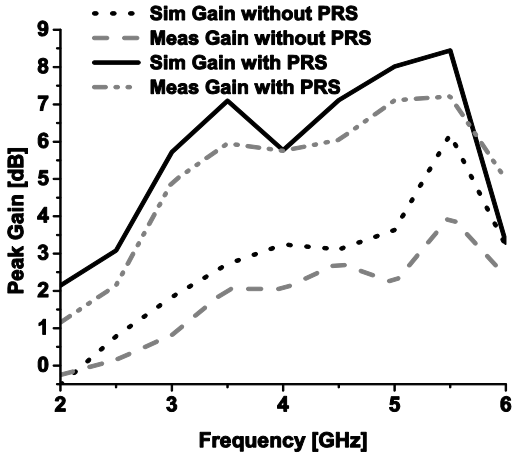

Fig. 11. Simulated and measured gains of antenna with and without PRS.

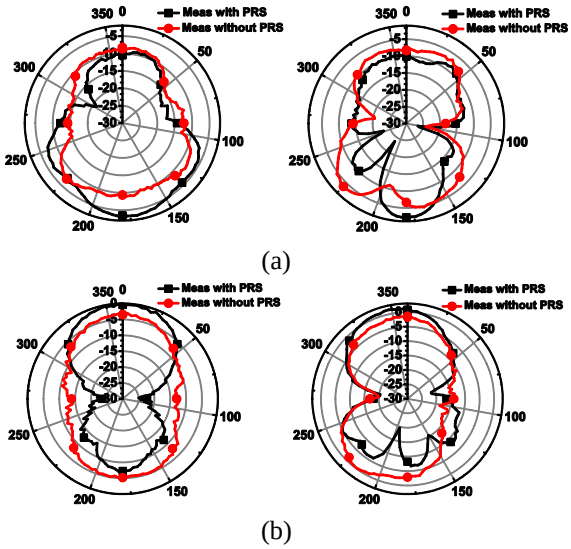

(a)

(b)

Fig. 12. Measured radiation pattern in E-plane (left) and H-Plane (right) at: (a) 3.5 GHz and (b) 5 GHz.

VI. CONCLUSION

A compact PRS-employed bi-layered, dual-band antenna is presented in this paper which provides high gain at WiMAX and WLAN bands. Slots are introduced in the patch to achieve multiband operation. The PRS layer is placed below the antenna layer to achieve an enhanced gain. The antenna has gains of 7 dB and 8 dB at WiMAX and WLAN bands respectively. Simulated and measured results are in good agreement, suggesting

that the antenna is suitable for dual-band high gain applications, for M2M communication and for a wide range of services in e-health, smart cities and intelligent transport systems.

REFERENCES

[1] L. D. Xu, W. He, and S. Li, "Internet of things in industries: A survey," *IEEE Transactions on Indust-rial Informatics*, vol. 10, no. 4, pp. 2233-2243, Nov. 2014.

[2] K. Y. Yazdandoost and R. Miura, "Compact printed multiband antenna for M2M applications," *8th European Conference on Antennas and Propag-ation (EuCAP)*, pp. 2521-2524, 2014.

[3] S. M. R. Islam, D. Kwak, M. H. Kabir, M. Hossain, and K. S. Kwak, "The internet of things for health care: A comprehensive survey," *IEEE Access*, vol. 3, pp. 678-708, 2015.

[4] J. Cheng, M. Zhou, F. Liu, S. Gao, and C. Liu, "Routing in internet of vehicles: A review," *IEEE Transactions on Intelligent Transportation Systems*, vol. 16, no. 5, pp. 2339-2352, 2015.

[5] M. T. Wu and M. L. Chuang, "Multibroadband slotted bow-tie monopole antenna," *IEEE Antennas and Wireless Propagation Letters*, vol. 14, pp. 887-890, 2015.

[6] M. Moosazadeh and S. Kharkovsky, "Compact and small planar monopole antenna with symmetrical L- and U-shaped slots for WLAN/WiMAX applica-tions," *IEEE Antennas and Wireless Propagation Letters*, vol. 13, pp. 388-391, 2014.

[7] P. S. Bakariya, S. Dwari, M. Sarkar, and M. K. Mandal, "Proximity-coupled microstrip antenna for bluetooth, WiMAX, and WLAN applications," *IEEE Antennas and Wireless Propagation Letters*, vol. 14, pp. 755-758, 2015.

[8] B. Feng, W. An, S. Yin, L. Deng, and S. Li, "Dual-wideband complementary antenna with a dual-layer cross-ME-dipole structure for 2G/3G/LTE/WLAN applications," *IEEE Antennas and Wireless Propag-ation Letters*, vol. 14, pp. 626-629, 2015.

[9] D. Germain, D. Seetharamdoo, S. N. Burokur, and A. de Lustrac, "Phase-compensated metasurface for a conformal microwave antenna," *Applied Physics Letters*, vol. 103, no. 12, pp. 124102, Sep. 2013.

[10] A. P. Feresidis, G. Goussetis, S Wang, and J. C. Vardaxoglou, "Artificial magnetic conductor surfaces and their application to low-profile high-gain planar antennas," *IEEE Transactions on Antennas and Propagation*, vol. 53, no. 1, pp. 209-215, Jan. 2005.

[11] A. Hosseini, F. Capolino, and F. De Flaviis, "Gain enhancement of a V-band antenna using a Fabry-Pérot cavity with a self-sustained all-metal cap with FSS," *IEEE Transactions on Antennas and Propagation*, vol. 63, no. 3, pp. 909-921, Mar. 2015.

[12] R. V. S. R. Krishna and R. Kumar, "Slotted ground microstrip antenna with FSS reflector for high-gain horizontal polarization," *Electronics Letters*, vol. 51, no. 8, pp. 599-600, Apr. 2015.

[13] M. Bilal, R. Saleem, M. F. Shafique, and H. A. Khan, "MIMO application UWB antenna doublet incorporating a sinusoidal decoupling structure," *Microw. Opt. Technol. Letters*, vol. 56, no. 7, pp. 1547-1553, Apr. 2014.

[14] R. Saleem, M. Bilal, K. B. Bajwa, and M. F. Shafique, "Eight-element UWB-MIMO array with three distinct isolation mechanisms," *IET Electronics Letters*, vol. 51, no. 4, pp. 311-313, 2015.

Sajeela Bibi received her B.Sc. degree in Telecom Engineering in 2014 from University of Engineering and Technology Peshawar, KPK Pakistan in 2014. She is working as a Research Assistant at University of Engineering and Technology Taxila since then. Recently she is awarded a funded M.S. studentship by UET Taxila. Her main research interests are in UWB systems, meta-materials and high gain antennas.

Rashid Saleem received B.S. Electronic Engineering from Ghulam Ishaq Khan Institute of Engineering Sciences and Technology, Pakistan, in 1999. He pursued a career in the telecommunication industry for several years while continuing education. He received M.S. from UET Taxila through Center for Advanced Studies in Engineering, Pakistan, in 2006 and Ph.D. from The University of Manchester, United Kingdom in 2011. He worked on antennas, channel modeling and interference aspects of Ultra Wideband systems during his Ph.D. and was also member of a team designing and testing arrays for the Square Kilometer Array project. Currently, he is working as Assistant Professor at University of Engineering and Technology (UET), Taxila, Pakistan where he is supervising several postgraduate students and heading the MAP (Microwaves, Antennas and Propagation) research group. His research interests include antennas, mm-wave communication, microwave periodic structures and metamaterials.

Asim Quddus received his B.S. degree in Electronics Engineering in 2012 from International Islamic University, Islamabad, Pakistan. In 2012 he was awarded graduate scholarship by University of Engineering and Technology (UET), Taxila, Pakistan. He received M.S. degree in Electrical Engineering from UET Taxila in 2014. Currently he is a Ph.D. Scholar and working as Research Associate with MAP (Microwaves, Antennas & Propagation) research Engineering, UET Taxila. His research interests include UWB-MIMO antennas, 3-D antennas and RF/microwave periodic structures including EBG and Frequency Selective Surfaces.

Sabih ur Rehman is a Lecturer in Computing with the School of Computing and Mathematics at Charles Sturt University, Australia. Rehman has completed his Ph.D. in the area of Vehicular Ad-hoc Networks for which he was the recipient of competitive scholarship from Charles Sturt University. Rehman obtained his Bachelor degree from University of South Australia, Adelaide in Electronics & Telecommunication Engineering with Honours. Rehman's research expertise lie in the areas of Quality of Service (QoS), Cross-layer Protocol Architecture Designing, Wireless Propagation and Antenna Modeling using mathematical/stochastic models and conducting performance analysis. Rehman's current research is focused on the emerging area of Internet of Things (IoT), especially in the context of Intelligent Transport Systems and Precision Agriculture.

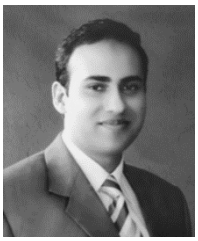

Muhammad Farhan Shafique received the B.Eng. degree from Hamdard University, Karachi, Pakistan, in 2003, M.S. degree from the University of Paris East Marne-La-Vallée, Paris, France, in 2005 and Ph.D. in Electronic and Communications Engineering from The University of Leeds, Leeds, UK in 2010. His research interests involve multilayer microwave device fabrication on LTCC technology, electromagnetic modeling of microwave structures, RF antenna, filters and MEMS packaging. He is also involved in dielectric characterization of materials using microwave techniques and fabrication of ceramic microfluidic devices. He is working as an Associate Director at Center for Advanced Studies in Telecommunications (CAST), where he has established the MCAD (Microwave Components and Devices) research group. He has also setup a wide range of research facilities in the area of RF engineering which involves 4 state-of-the art laboratories. He is a Reviewer of various journals and also a Senior Member IEEE.

A Compact Quad-band CPW-fed Planar Resonator for Multiple Wireless Communication Applications

Aamir Khan [1], Syeda I. Naqvi [1], Farzana Arshad [1], Yasar Amin [1,2], and Hannu Tenhunen [2,3]

[1] ACTSENA Research Group
University of Engineering and Technology (UET), Taxila, 47050, Pakistan
aamirkhan_ciit@yahoo.com, iffat.naqvi@uettaxila.edu.pk, farzana.arshad@uettaxila.edu.pk

[2] iPack VINN Excellence Center
Royal Institute of Technology (KTH), Isafjordsgatn 39, Stockholm, SE-16440, Sweden
yasar.amin@uettaxila.edu.pk

[3] TUCS, Department of Information Technology
University of Turku, Turku-20520, Finland
hannu@kth.se

Abstract ─ This article presents a low-cost, compact antenna with coplanar waveguide (CPW) feed line for multiband wireless applications. The presented multiband radiator is envisioned for integration into microwave circuits and portable RF devices. The prototype is realized on 1.6 mm thick readily available FR4 substrate with a compact geometrical size of 24×32 mm^2. The acquired quad-bands are centered at: 2.45, 3.5, 5.2 and 5.8 GHz justifying the appropriateness of the proposed radiator for the WLAN and WiMAX applications, as well as Bluetooth and ISM wireless standards. From the aspect of integration into transportable handheld devices and system designing, the presented compact antenna illustrates more expandability and flexibility. The radiation characteristics measured in the E and H-planes for desired operating frequencies are monopole-like and omni-directional, respectively. A sufficient gain is also achieved. Simulated as well as experimental results exhibit agreeable behavior.

Index Terms ─ Coplanar Waveguide (CPW), multi-band antennas, WLAN, WiMAX.

I. INTRODUCTION

As the wireless communication standards have expanded affluently, it is desired for the antennas of current and future communication devices to be proficient for operative at multiple frequency bands to sanction various communication services for cellular as well as non-cellular applications. Wireless local area network (WLAN) has become the foremost standard for wireless communication these days. The frequency bands centered at: 2.45, 5.2 and 5.8 GHz are accredited for WLAN standards by the IEEE 802.11 [1]. Although WLAN is the primary internet access solution and provides a lot of amenities, the coverage becomes sparse and restricts its access to indoor use exclusively due to very few outdoor hot spots. As a matter of fact, Worldwide Interoperability for Microwave Access (WiMAX) operates similar to WLAN but at higher speed and covers more distance. The significance of WiMAX would be realized in the near future as a principal supplement to WLAN. The commonly used frequency bands defined by IEEE 802.16 for WiMAX are 2.5, 3.5 and 5.5 GHz [1, 2].

Moreover, the principal features of compactness, robustness, low profile, simplified fabrication, and adaptability in structures are desired for the antennas incorporated in transportable handheld terminals for wireless communication [3]. However, to achieve multiple bands with the employment of a single antenna offers substantial demands. Historically, exclusive strategies have been adapted to design multi resonators. Several earlier reported works had proposed slotted antennas with microstrip feed line to obtain multiband operations [4, 5-12]. An anchor-shaped slotted antenna has been proposed sustaining 2.45, 5.2 and 5.8 GHz WLAN along with 2.5, 3.5 and 5.5 GHz bands for WiMAX applications [4]. However, the size of the antenna is large. A quad-band slotted antenna for WLAN, WiMAX and GPS standards is obtained [5]. As the 1.5 GHz GPS band is obtained, the dimensions of about 56×44 mm^2 do not provide the required compactness. Sharma et al. [6] has presented a slotted dual-band antenna with single microstrip feed for the 2.4 GHz band supporting WLAN as well as 2.5 and 3.5 GHz bands covering WiMAX. The overall prototype size is 60×60 mm^2. A planar balance-shaped slot antenna with L-shaped micro-strip feed line

Submitted On: July 9, 2017
Accepted On: August 26, 2017

appropriate for WLAN/WiMAX triple-bands is proposed [7]. However, the geometry is somehow complicated, and gain is low as well. A multiband antenna covering only 2.45 and 5.2 GHz WLAN frequency bands along with 3.5 GHz WiMAX band has been reported [8]. The prototype is low gain with dimensions of 34×30 mm^2. Multiband antenna obtained in [9] covers the bands for WCDMA, WLAN, UWB, and C-band applications with geometrical dimensioning of 62×64 mm^2. An earlier proposed multi-frequency antenna supports the WiMAX as well as WLAN bands. The dimensions of the structure are 38×25 mm^2 [10]. In [11], a tri-band monopole antenna with microstrip feed line and overall size of 18×12 mm^2 is obtained. A circular shaped dual band patch antenna loaded with vertical slots and fed by meandered stripline is reported in [12]. The overall dimensions of the antenna are 51×41×2 mm^3.

In particular, considerable attention has been drawn towards the coplanar waveguide (CPW) due to their enviable benefits, predominately less dispersal, reduced radiation leakage, the negligible reliance of the characteristic impedance on the thickness of the substrate, and ease of fabrication due to the planar configuration. Integration with other microwave integrated circuits and RF devices as well as mounting is carried out efficiently with CPW feed [1, 13]. Multiband resonances are achieved by planar slotted antennas with CPW-feed on FR4 substrate [14, 15]. A CPW-fed bow-tie-shaped slotted antenna obtaining 2.45, 5.2 and 5.8 GHz WLAN band has been reported with overall dimensions of 60×45 mm^2 [14]. A quad-band prototype with CPW feed and four meander lines is projected and analyzed for L-band (1.15–1.25 and 1.5–1.9 GHz), 2.45 GHz and 3.5 GHz WLAN/WiMAX band [15].The four covered bands are narrow with comparatively large antenna geometry 57.37×67.5 mm^2. In [16], a compact 23×30 mm^2 CPW-fed antenna is reported that operates at three different bands of WLAN/WiMAX. Hence, it has been observed that there is always a tradeoff between the acquired frequency bands and the antenna size or complexity.

This article presents a coplanar waveguide quad-band antenna on FR4 substrate applicable for 2.45, 5.2 and 5.8 GHz WLAN along with 2.5 and 3.5 GHz WiMAX applications. The antenna also supports Bluetooth and ISM wireless applications. It is not merely capable of attaining the WLAN/WiMAX requisite bandwidths, but also affirms miniaturized and simple geometry. The progression of design and the experimental findings of the presented multi-resonant radiator are narrated and analyzed in detail.

II. ANTENNA DESIGN

The proposed planar and monopole prototype is depicted in Fig. 1. The proposed antenna structure is achieved by adding and etching out different slots from a standard rectangular patch through already established mathematical equations [17]. Consider:

$$W = \frac{\lambda}{2}\sqrt{\frac{2}{\varepsilon_r + 1}}, \tag{1}$$

$$L = 0.5\frac{\lambda}{\sqrt{\varepsilon_{reff}}} - 2\Delta L, \tag{2}$$

where W is the width and L is the length of the radiating patch in (1) and (2), respectively, whereas λ is the wavelength, ε_r is the relative dielectric constant and ΔL is the change in length due to fringing field effect and can be obtained using:

$$\Delta L = 0.412h\frac{(\varepsilon_{reff} + 0.3)\left(\frac{W}{h} + 0.264\right)}{(\varepsilon_{reff} - 0.258)\left(\frac{W}{h} + 0.8\right)}, \tag{3}$$

where ε_{reff} is given as:

$$\varepsilon_{reff} = \frac{\varepsilon_r + 1}{2} + \frac{\varepsilon_r - 1}{2}\left(1 + \frac{12h}{W}\right)^{-0.5}. \tag{4}$$

These equations are for a standard rectangular patch; however, ultimate dimensions of the proposed antenna are achieved by using the technique of modify, test, and run. Furthermore, it has already been verified by various simulation analyses that the resonant frequencies can be obtained by making meandered path for the surface currents.

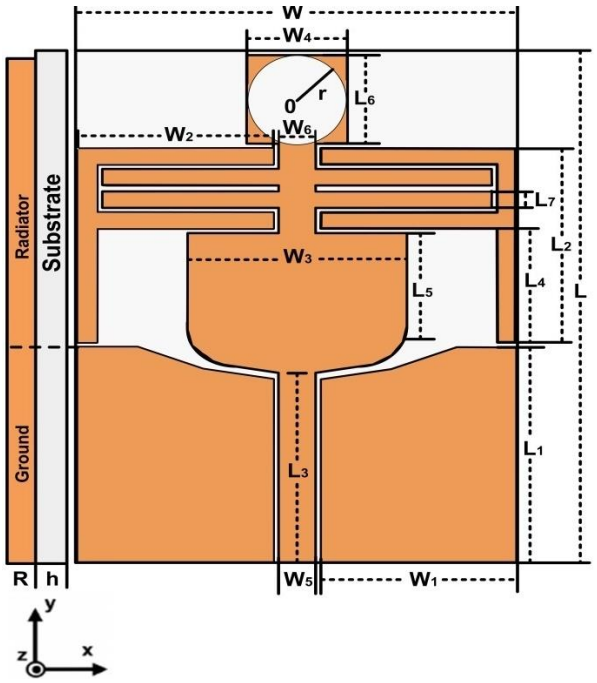

Fig. 1. Layout of the proposed antenna.

The designed radiator is capable of operating at four distinct bands. Great caution has been taken while developing and optimizing the radiator and CPW ground to acquire the preferred operating frequencies. The antenna with dimensions of 24×32 mm^{2}is realized on 1.6 mm thick FR4 substrate with ε_r = 4.4 and δ = 0.02. Table 1 further elaborates the dimensions of the presented design.

Table 1: Optimized parameters of the antenna

Parameter	Size (mm)	Parameter	Size (mm)
L	32	W	24
L_1	13.5	W_1	10.7
L_2	12.1	W_2	10.65
L_3	11.5	W_3	12
L_4	7.1	W_4	5.5
L_5	5.8	W_5	2
L_6	5.5	W_6	2
L_7	1	h	1.6
R	2.65	R	0.035

Figure 2 (a) clearly depicts the emergence of the prototype proposed in this work. To better understand the strategy followed to develop the prototype, the return loss (S_{11}) for the four design stages is plotted in Fig. 2 (b).

To begin with, Antenna1 is designed as shown in Fig. 2 (a). A basic rectangular patch with rounded corners near feed line and a small square patch on the top side linked with the bottom patch by a vertical rectangular strip at the center are the elements contributing the major radiations of the Antenna1. This antenna radiates at 3.6 GHz with $S_{11} < -10$ dB, as shown in Fig. 2 (b). Carrying the initial proposed design as the basis, Antenna2 is modeled by the addition of a circular slot inside the top square patch and a pair of F-shaped strips placed symmetrically at both sides of the Antenna1 as illustrated in Fig. 2 (a). It shifts and improves the first resonance at 3.6 GHz to 3.7 GHz, since the addition of circular slot significantly increases the equivalent electric length. At the same time another resonance at 2.8 GHz is generated as depicted clearly in Fig. 2 (b), because the F-shaped strips are introduced. In the third model, a horizontal strip is introduced in between the two symmetrical F-shaped strips with the aim of escalating the path for the current as shown in Fig. 2 (a). Antenna3 shifts the two resonances obtained by Antenna2 at 2.8 to 2.4 GHz and 3.7 to 4 GHz, as illustrated in Fig 2 (b). Third resonance centered at 5.7 GHz is also obtained. However, this resonance is inadequate in the sense that it does not produce $S_{11} < -10$ dB.

Finally, another horizontal strip of same dimension is introduced in between the F-shaped strips and below the horizontal strip that was added in the previous stage of design evolution as depicted in Fig. 2 (a). The proposed antenna obtained in the fourth step of evolution shifts the radiations of Antenna3 at 2.4 GHz to 2.45 GHz and 4 GHz to 3.4 GHz, whereas improving the impedance matching across the band. Furthermore, resonance at 5.7 GHz for Antenna3 is shifted to 5.8 GHz with $S_{11} < -10$ dB. Fourth radiation at the frequency of 5.2 GHz is also obtained. Thus, the proposed design provides four resonances at 2.45, 3.4, 5.2 and 5.8 GHz supporting WLAN and WiMAX bands, all with $S_{11} < -10$ dB, as shown in Fig. 2 (b). By applying the before mentioned strategy as well as going through some simulations and optimization techniques, the final radiating structure has been obtained with optimum results.

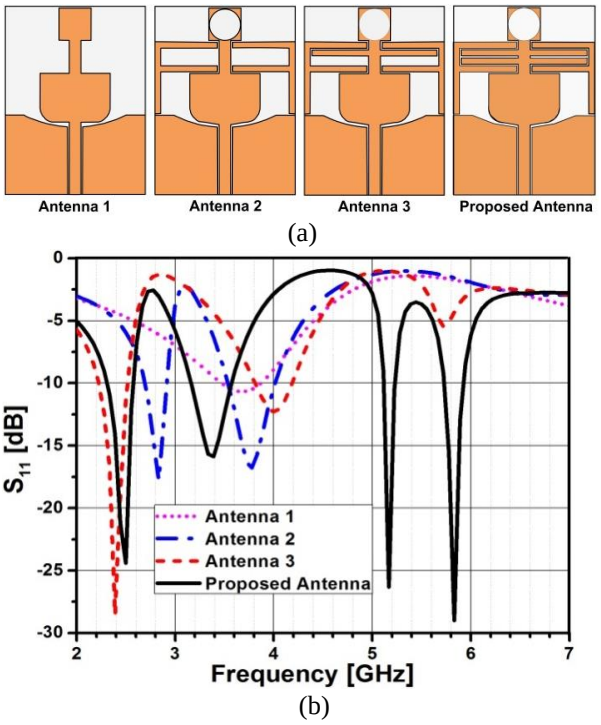

Fig. 2. (a) Design evolution of the proposed antenna, and (b) with subsequent S11.

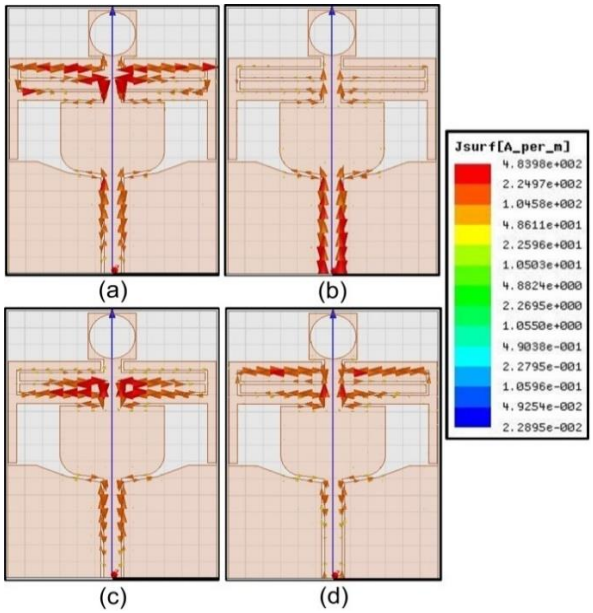

Fig. 3. Current distributions of the antenna for: (a) 2.45, (b) 3.5, (c) 5.2, and (d) 5.8 GHz.

For better investigation of the working principle of the multiband resonator, the analysis of current distribution is carried out at the four resonances 2.45, 3.5, 5.2 and 5.8 GHz, respectively as depicted in Figs. 3 (a)–(d). The current density is mainly observed at the F-shaped strips, the bottom of the rectangular patch and the first horizontal strip at 2.45 GHz, as illustrated in Fig. 3 (a). Whereas for 3.5 GHz, the concentration of the current is widely seen at the bottom of the rectangular patch, as evident in Fig. 3 (b). In the same manner, Fig. 3 (c) illustrates that at 5.2 GHz, major distribution of the current is on the horizontal strips. While for 5.8 GHz, the current density is mainly concentrated at F-shaped and the horizontal strips, as can be seen in Fig. 3 (d).

III. EXPERIMENTAL RESULTS AND DISCUSSION

According to the parameters of the prototype provided in Table 1, the multiband antenna for WLAN and WiMAX standards is fabricated and measured to validate the performance. The simulations were orchestrated using full wave electromagnetic design tool HFSS™, whereas measured results are obtained by the R&S®ZVL13 Vector Network Analyzer.

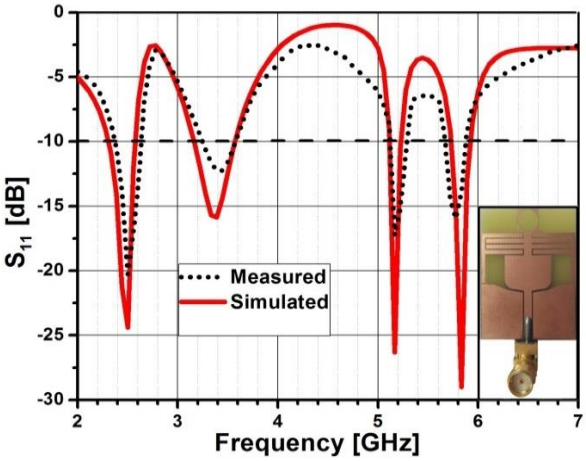

Fig. 4. Measured and simulated return loss of the antenna.

Figure 4 illustrates simulated and measured return loss. It is evident that the bands for wireless communication covered by the radiator are four. The bandwidths and commercial bands covered by the proposed antenna have been narrated in Table 2. The frequency bands measured and considered for S11 <-10 dB are 2.31-2.58 GHz covering the IEEE 802.11b&g WLAN systems (270 MHz bandwidth), 3.16-3.57 GHz suitable for the WiMAX applications (410 MHz bandwidth). Also 5.11-5.23 GHz band supporting the IEEE 802.11a WLAN (120 MHz bandwidth) and 5.72-5.92 GHz for the WLAN/WiMAX applications (200 MHz bandwidth) are obtained. Measured and simulated results are coherent; however, slight variations are due to the inevitable use of coaxial cable and SMA connector for measurement [18, 19].

Table 2: Frequency bands covered by antenna

Band No.	Bandwidth (GHz)	Covered Commercial Bands
1.	2.31-2.58	WLAN (2400-2480 MHz), LTE 2300 (2305-2400 MHz), ISM & Bluetooth (2400-2480 MHz), WiMAX (2500-2690 MHz), LTE 2500 (2500-2690 MHz)
2.	3.16-3.57	WiMAX (3400-3600 MHz)
3.	5.11-5.23	WLAN (5150-5350 MHz)
4.	5.72-5.92	WLAN (5725-5850 MHz), WiMAX (5250-5850 MHz)

The computed peak gain for the proposed antenna has been illustrated in Fig. 5. The peak gain value is 2.27 dB for the 2.45 GHz, 0.99 dB for 3.5 GHz, 1.08 dB for 5.2 GHz and 2.15 dB for the upper 5.8 GHz band. Thus, adequate amount of gain for the antenna has been obtained. However, the maximum achieved efficiency is 73% for the proposed antenna.

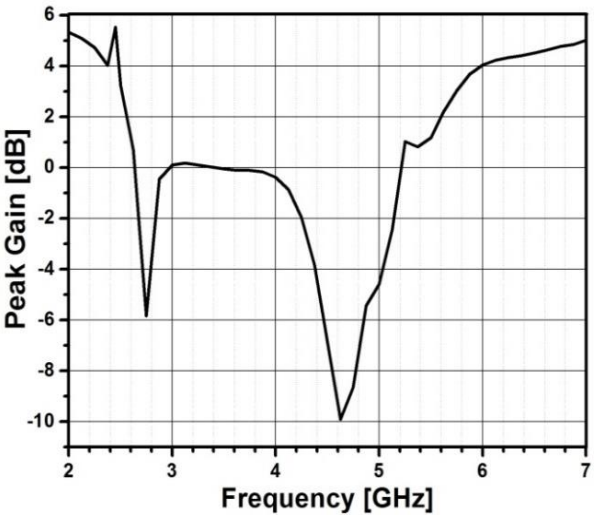

Fig. 5. Peak gain of proposed antenna.

The radiation plots measured in the E(y-z) plane as well as H(x-z) plane, for 2.45, 3.5, 5.2 and 5.8 GHz, have been provided in Figs. 6 (a)–(d). In E-plane the measured radiation plots are bi-directional while for the H-plane, an omni-directional response has been observed. Thus, monopole-like behavior has been obtained. Moreover, along with co-polarization the cross-polarization behavior is also observed in Figs. 6 (a)-(d). It can be seen that the cross-polarization level is less than -20 dB across the two lower frequency bands, i.e., at 2.45 GHz and 3.5 GHz, while the upper frequency bands at 5.2 GHz and 5.8 GHz

acquire the cross-polarization level in between -20 dB and -10 dB. Hence, it is evident from the radiation characteristics that the antenna shows a steady response for the attained operating bandwidth.

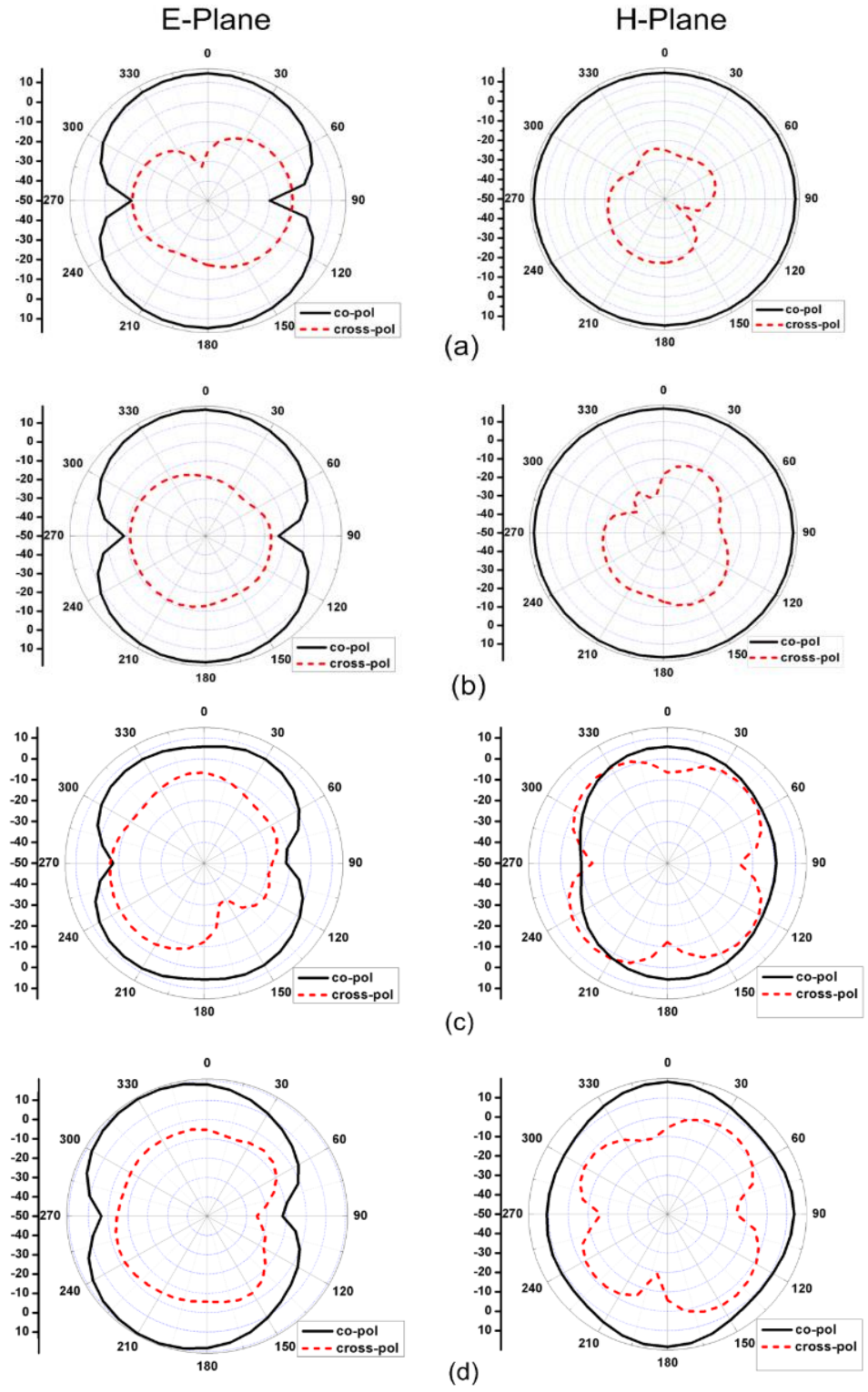

Fig. 6. Measured radiation patterns of antenna at: (a) 2.45 GHz, (b) 3.5 GHz, (c) 5.2 GHz, and (d) 5.8 GHz.

IV. CONCLUSION

The design of CPW-fed multi-band antenna with detailed simulated and measured results is proposed. By the inclusion of F-shaped and horizontal strips to the basic rectangular radiator, four resonances at 2.45, 3.5, 5.2 and 5.8 GHz are achieved supporting WLAN, WiMAX, LTE2300/2500, ISM and Bluetooth frequency bands. With the compact size of 24×32×1.6 mm^3, the prototype mitigates the incorporation into portable terminals. Moreover, steady monopole-like radiation patterns and adequate gains have been achieved for the desired bands. Therefore, the satisfactory outcome proves the significance of the antenna for diverse wireless applications.

ACKNOWLEDGMENT

This work was financially supported by Vinnova (The Swedish Governmental Agency for Innovation Systems) and UET Taxila, Pakistan through the Vinn Excellence Centers Program and ACTSENA Research Group Funding, respectively.

REFERENCES

[1] S. Chaimool and P. Akkaraekthalin, "CPW-Fed Antennas for WiFi and WiMAX," *Advanced Transmission Techniques in WiMAX*, ISBN: 978-953-307-965-3, InTech, 2012. Available from: http://www.intechopen.com/books/advanced-transmission-techniques-in-wimax/cpw-fed-antennas-for-wifi-and-wimax

[2] Y. Liu, Y. Wang, and Z. Du, "A broadband dual-antenna system operating at the WLAN/WiMax bands for laptop computers," *IEEE Antennas and Wireless Propagation Letters*, vol. 14, pp. 1060-1063, May 2015.

[3] R. S. Aziz, A. K. Arya, and S. Park, "Multiband full-metal-rimmed antenna design for smart phones," *IEEE Antennas and Wireless Propagation Letters*, vol. 15, pp. 1987-1990, Mar. 2016.

[4] W. Ren and C. Jiang, "A novel design of multiband printed anchor-shaped slot antenna," *Microwave and Optical Technology Letters*, vol. 58, no. 3, pp. 521-526, Mar. 2016.

[5] Y. F. Cao, S. W. Cheung, and T. I. Yuk, "A multiband slot antenna for GPS/WiMAX/WLAN systems," *IEEE Transactions on Antennas and Propagation*, vol. 63, no. 3, pp. 952-958, Mar. 2015.

[6] A. K. Sharma, A. Mittal, and B. V. R. Reddy, "Slot embedded dual-band patch antenna for WLAN and WiMAX applications," *Electronics Letters*, vol. 51, no. 8, pp. 608-609, Apr. 2015.

[7] W. Ren and C. Jiang, "Planar triple-band balance shaped slot antenna," *Microwave and Optical Technology Letters*, vol. 58, no. 5, pp. 1078-1082, May 2016.

[8] S. C. Basaran, U. Olgun, and K. Sertel, "Multiband monopole antenna with complementary split-ring resonators for WLAN and WiMAX applications," *Electronics Letters*, vol. 49, no. 10, pp. 636-638, May 2013.

[9] B. S. Yıldırım, E. Başaranand, and B. Türetken, "Compact and planar WCDMA/WLAN/UWB antenna with shorted loop and monopole elements," *ACES Journal*, vol. 31, no. 3, pp. 288-293, Mar. 2016.

[10] J. Pei, A. Wang, S. Gao, and W. Leng, "Miniaturized triple-band antenna with a defected ground plane for WLAN/WiMAX applications," *IEEE Antennas and Wireless Propagation Letters*, vol. 10, pp. 298-301, Apr. 2011.

[11] N. Ojaroudi, M. Mehranpour, S. Ojaroudi, and Y. Ojaroudi, "Microstrip-fed monopole antenna with triple band performance for WLAN/WiMAX applications," *ACES Journal*, vol. 29, no. 3, Mar. 2014.

[12] M. R. Ahsan, M. T. Islam, and M. HabibUllah, "A new meandered-stripline fed dual band patch antenna," *ACES Journal*, vol. 30, no. 2, Feb. 2015.

[13] R. N. Simons, *Coplanar Waveguide Circuits, Components, and Systems*. ISBNs: 0-471-16121-7 (Hardback); 0-471-22475-8 (Electronic), John Wiley & Sons, Inc., 2001.

[14] L. C. Tsai, "A dual-band bow-tie-shaped CPW-fed slot antenna for WLAN applications," *Progress In Electromagnetics Research C*, vol. 47, pp. 167-171, Feb. 2014.

[15] K. Yu, Y. Li, and X. Luo, "A CPW-fed quad-band monopole antenna for L-band, WLAN and WiMAX communication applications," *Progress In Electromagnetics Research Symposium (PIERS)*, pp. 3996-4000, Aug. 2016.

[16] L. Li, Z. Z. Li, L. Ming-Fu, J. C. Jiang, and B. Tang, "A novel compact printed slot antenna with triple bands for WiMAX/WLAN applications using remodeling technology," *ACES Journal*, vol. 29, no. 6, June 2014.

[17] C. A. Balanis, *Antenna Theory Analysis and Design*. 3rd edition, John Wiley & Sons, Hoboken, NJ, USA, 2005.

[18] L. Liu, S. W. Cheung, Y. F. Weng, and T. I. Yuk, "Cable effects on measuring small planar UWB monopole antennas," *Ultra Wideband – Current Status and Future Trends*, 2012. Available from: http://dx.doi.org/10.5772/46080

[19] L. Liu, Y. F Weng, S. W Cheung, T. I. Yuk, and L. J. Foged, "Modeling of cable for measurements of small monopole antennas," *The 7th Loughborough Antennas and Propagation Conference (LAPC)*, Loughborough, United Kingdom, article no. 6114153, Nov. 14-15, 2011.

Aamir Khan received his B.Sc. degree in Electrical (Telecommunication) Engineering from COMSATS University, Islamabad, in the year 2015. Currently he is pursuing his degree of M.Sc. in Telecommunication Engineering from UET Taxila. He is also working on Microwave Propagation and Antennas with College of Electrical and Mechanical Engineering (CEME) Pakistan as an Internee. His research interests are Ultra-wide band, Multiband Antennas for current and future wireless standards.

Syeda Iffat Naqvi received her B.Sc. and M.Sc. degree in Computer Engineering and Telecommunication Engineering from UET Taxila, Pakistan in the year 2006 and 2011, respectively. Currently, she is pursuing her degree of Ph.D. in Telecommunication Engineering from (UET) Taxila. She is also a Member of ACTSENA Research Group. Her current research interests include RF and microwave antenna designing for cutting edge wireless technologies. Naqvi is a Member of IEEE and ACES.

Farzana Arshad received her B.Sc. and M.Sc. degree in Software Engineering and Telecommunication Engineering from UET Taxila, Pakistan in the year 2006 and 2010, respectively. Currently, she is working towards her Ph.D. degree in Telecommunication Engineering from UET Taxila. She is also a Member of ACTSENA Research Group. Her current research interests include Low profile Multiband and reconfigurable antenna design.

Yasar Amin is Chairman and Associate Professor of Telecommunication Engineering Department, University of Engineering and Technology Taxila, Pakistan. He is Founder of ACTSENA Research Group at UET Taxila, Pakistan. He has done his B.Sc. in Electrical Engineering in 2001 with specialization in Telecommunication and M.Sc. in Electrical Engineering in 2003 with specialization in System-on Chip Design from Royal Institute of Technology (KTH), Sweden. His Ph.D. is in Electronic and Computer Systems from Royal Institute of Technology (KTH), Sweden, with research focus on printable green RFID antennas for embedded sensors, while he has MBA in Innovation and Growth from Turku School of Economics, University of Turku, Finland.

Hannu Tenhunen is Chair Professor of Electronic Systems at Royal Institute of Technology (KTH), Stock-holm, Sweden. Tenhunen has held Professor positions as Full Professor, Invited Professor or Visiting Honorary Professor in Finland (TUT, UTU), Sweden (KTH), USA (Cornel U), France (INPG), China (Fudan and Beijing Jiatong Universities), and Hong Kong (Chinese University of Hong Kong), and has an Honorary Doctorate from Tallinn Technical University. He has been Director of multiple national large scale research programs or being an Initiator and Director of national or European graduate schools. He as actively contributed on VLSI and SoC design in Finland and Sweden via creating new educational programs and research directions, most lately at European level as being the EU-level Education Director of the new European flagship initiative European Institute of Technology and Innovations (EIT), and its Knowledge and Innovation Community EIT ICT Labs.

A Ring Resonator Based Wide-Band Band Pass Filter with Single Loaded Stub and Compact Structure

Zafar Bedar Khan and Huiling Zhao

Department of Electronics and Information, Northwestern Polytechnical University, Xian, 710072, P. R. China
zafarbedarkhan@mail.nwpu.edu.cn, zhhl@nwpu.edu.cn

Abstract ─ A compact and simple structure of a wide-band band pass filter (BPF) based on ring resonator (RR) topology with only one open circuited stub is proposed. The pass band characteristic of the RR is achieved by placing the output port co-axial to the input port, at a position along the resonator length with maximum electric field. Subsequently wide operating bandwidth is realized by controlling the length of loaded stub due to its degenerate modes. An analytical equation is proposed based on even-odd mode analysis of a simplified transmission line model centrally loaded with stub to theoretically predict the positions of transmission zeros. A cascaded structure of two stub-loaded RRs filter with improved out of band rejection is designed and fabricated at 3 GHz. The insertion loss (IL) and return loss (RL) are better than 1.7 dB and 12.3 dB with a 3-dB fractional bandwidth of 47%. The two transmission zeros at 2.26 GHz and 3.8 GHz show rejections better than 37 dB. Furthermore, the area of the filter is reduced by special placement of the open circuited stubs inside the rings. It is shown that the compact filter is 33% area efficient with comparable performance parameters.

Index Terms ─ Open circuited stub, ring resonator, transmission zeros, wide-band band pass filter.

I. INTRODUCTION

Band pass filter (BPF) is one of the most important passive devices used in modern communication systems for sharp out of band rejection, low insertion loss, desired wide pass-bands and low cost [1-3]. Microstrip dual-mode Ring Resonators (RR) with simple structure, having two transmission zeros near the pass band have been shown to be promising candidates for high performance wide-band BPF [3] incorporating the above mentioned characteristics. In general, two degenerated modes can be excited by introducing a perturbation element along an orthogonal plane of RR. To properly split these two modes, different perturbation elements with various configurations have been introduced in a ring resonator with respect to its two ports [4-17]. In [4], the two degenerate-mode frequencies of the stepped-impedance ring resonator are controlled through the length ratio of two line sections with different characteristic impedances. As simple perturbation elements, lumped capacitors are placed at the diagonal corners of a symmetrical ring in series and/or shunt formats [5-6]. Small patches and/or notches placed at the corners of square-loop [7], hexagonal-loop resonators [8] and narrow slots etched on ground plane underneath a symmetrical ring strip conductor [9] are other perturbation elements proposed in the literature. Many researchers have reported RR based design of wide-band BPFs [10-17]. In [10-12], RR based BPF design with relatively narrower fractional bandwidth (FBW) (10% ~ 11%) were presented. Owing to the coupled lines in the proposed designs in [10-11], the insertion loss (IL) was slightly higher at 2.3 dB and 2.4 dB respectively. Six and four-transmission zeros respectively were implemented in [13-14] at the cost of complex structures with discontinuities and coupling gaps. Moreover, the achieved fractional bandwidth (FBW) was around 20% and 21% respectively, which was less as compared to other reported works. The structure of RR based wide-band BPF reported in [15] allowed the tuning of the center frequency as well as the BW by tuning the voltage of varactors. The design required external voltage to be provided to three varactors through wires which may not prove viable at higher frequencies due to parasitic effects. Subsequently in [16], complementary split ring resonators with cascaded high pass and low pass filters were used to demonstrate wide-band BPF with improved FBW. The complex structure (with coupling gaps) on two layers of the substrate may be relatively difficult to manufacture as compared to a single sided micro-strip structure, for example reported in [17]. A wide-band BPF was introduced in [17] using RR and two stubs. The reported technique avoided mismatches due to no coupling gaps and thus a low insertion loss (IL) of better than 1.6 dB and a good FBW of 49.3% was achieved. Firstly, band-stop characteristics were realized by orthogonal placement of input/output ports on the ring resonator. Subsequently, two stubs were used to attain wide band pass characteristics of the structure owing to the degenerate modes of the stubs.

In this paper, it is established that comparable FBW

Submitted On: April 13, 2017
Accepted On: October 4, 2017

can be achieved from a single RR and a single loaded tuning stub making the BPF structure simpler and area efficient as compared to [17]. In Section IIA, the analytical investigation of the surface currents/voltages nulls and subsequent simulation is performed assuming transmission line model of the RR. Based on the analysis and simulation, instead of orthogonal placement (as established in [17]), co-axial placement of the input/ output ports is proposed with output port at the position of minimum current and maximum voltage implying maximum electric field. The proposed co-axial placement of the ports thus results in the band pass characteristic of the RR (circumventing the band-stop design step as suggested in [17]).

Subsequently, in Section IIB, a single open-circuited stub is demonstrated to be sufficient to achieve a wide-band response of the BPF owing to the degenerate modes induced by different stub lengths. The presented circuit is analytically solved and an equation is derived theoretically predicting the transmission zeros (TZs). In Section IIC, a cascaded arrangement of two RR with one stub each is designed and fabricated which further improves the out of band rejection. Furthermore, in Section IID, it is shown that, the compact placement of the stub itself inside the RR of the cascaded structure proves to be area efficient maintaining comparable performance. Compact wide-band BPF with two cascaded RR and specially placed stubs is also designed and fabricated. The measurements show good conformance with the simulated response at the center frequency (CF) of 3 GHz.

II. PROPOSED METHODOLOGY FOR FILTER DESIGN

The following analysis is performed for a fundamental design frequency of 3 GHz. A substrate with a dielectric constant of 2.2 and thickness 0.8 mm, and system impedance of 50Ω is considered for all calculations. Advance design system (ADS) software is used for the simulation work. All the measurements were performed on Agilent's PNA model no. E8363B.

A. Band pass characteristic of RR using co-axial feed lines

A ring resonator can be analyzed by an equivalent straight transmission line as shown in Fig. 1 (a). Knowing the distribution of voltage and current along this straight resonator makes it possible to decide the positions of the input/output feed lines which ensure the odd or even mode excitation. For the resonator shown in Fig. 1 (a), the input admittance can be given as:

$$Y_{in} = jY_0 \tan\theta . \quad (1)$$

For resonance condition it can be deduced that,

$$\theta = n\pi$$
$$l_r = \frac{n\lambda_g}{2}, \quad (2)$$

where θ is the electrical length, lr is the physical resonator length and λg is the guided wavelength at the resonance frequency. From (1) it can further be inferred that the voltage and current along the resonator length are functions of cosθ and sinθ respectively.

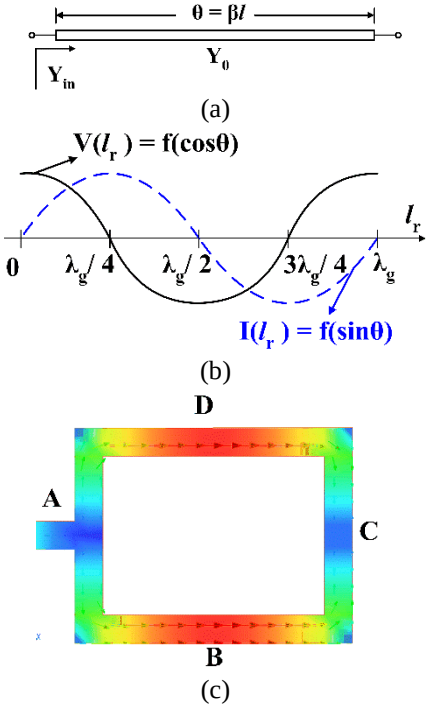

Fig. 1. (a) Straight transmission line resonator, (b) voltage and current waveform along the resonator length lr = λg, and (c) simulated surface current distribution on the RR at fundamental frequency.

Now for a resonator with a length of one full guided wavelength (lr = λg) [3] (n=2 from (2)), the voltage and current nulls along the resonator length at fundamental frequency are plotted in Fig. 1 (b). Simulated surface current on RR (formed by folding the straight resonator in Fig. 1 (a)) is shown in Fig. 1 (c). Voltage nulls are observed at position 'B & D' (corresponding to (λg /4) and (3λg /4) in Fig. 1 (b)) due to maximum current (arrows shown in red color in Fig. 1 (c)). Current nulls are at 'A & C' (corresponding to 0 and (λg /2) in Fig. 1 (b)) due to maximum voltage. This gives a very clear idea that fundamental frequency or any odd mode resonance cannot be tapped at point 'B' (or 'D'), thus band stop characteristic is expected as established in [17]. Conversely, band pass characteristic of the RR

is expected at point 'C' due to presence of maximum electric field at the fundamental resonance frequency.

The proposed co-axial feed lines (at α = 0°) are placed at 'A & C' without any coupling gap as shown in Fig. 2 (a). The simulated and measured S-parameter response is depicted in Fig. 2 (b). As evident, the co-axially placed feed lines give a band pass response centered at the fundamental design frequency of 3 GHz.

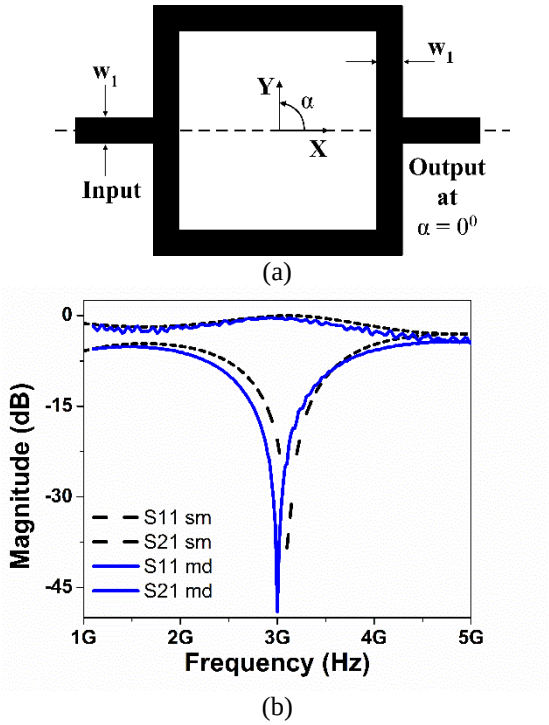

Fig. 2. (a) RR with co-axial feed lines, and (b) S-parameters response (sm = simulated, md = measured).

B. Wide-band characteristic by using one stub

It is an established fact that the frequency response of an RR can be varied by controlling the length of the loaded stub [3, 11]. Furthermore, the impedance of the stub is kept higher than the RR for better return loss (RL) [17]. The concept is employed here to get the wide-band response of the co-axially fed RR at 3 GHz. For the purpose, the stub may be loaded at position 'B or D' (refer to Fig. 1 (c)). Figure 3 (a) shows a stub with length ls = λg /4 loaded at position 'D' of the co-axially fed RR. Please note that the stub length (ls) is designed at the fundamental design frequency for an optimized impedance of 64Ω.

Simulated frequency response with varying stub length is depicted in Fig. 3 (b). Degenerate modes can be observed with the introduction of the stub. It is clearly seen that with increasing length of the stub (ls), the frequency BW is widened with the best response at ls = λg /4. The final dimensions (in mm) of the RR filter in Fig. 3 (a) at 3 GHz for 50Ω system were taken as: lr = λg = 73, w_1 = 2.44, ls = 18.43, w_2 = 1.65. Widths of both the feed lines were kept same as w_1.

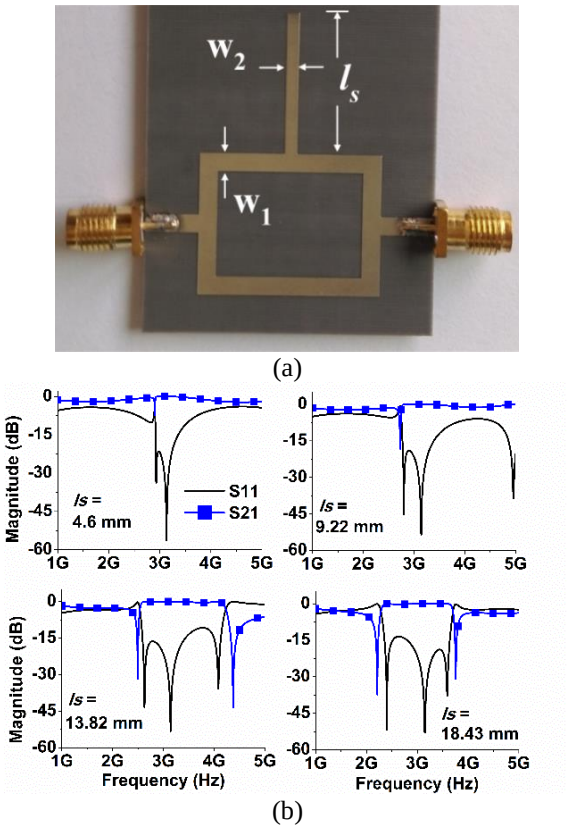

Fig. 3. (a) Fabricated RR with single loaded stub, and (b) simulated S-parameters with varying stub length ls.

1) Theoretical Analysis for Determination of Transmission Zeros

As stated earlier and shown in Fig. 3 (b), the RR based BPF has a sharp skirt due to presence of (at least) two transmission zeros. Lower and higher transmission zero (TZ) frequencies (f_{TZ1} & f_{TZ2} respectively) are theoretically predicted using even and odd mode analysis of the RR BPF structure with one open sub shown in Fig 3 (a). For the purpose, again a simple transmission line centrally loaded with an open stub is adopted as shown in Fig. 4 (a). The central plane (AA') in Fig. 4 (a) is equivalent to an electric and a magnetic wall when the odd- and even-modes are excited respectively. Therefore, following the odd mode and even mode half circuits shown in Figs. 4 (b) & (c) respectively, the admittance equations can be derived as:

$$Y_{ino} = \frac{Y_0}{j \tan(\theta/2)} \quad \text{(for odd mode)}, \tag{3}$$

$$Y_{in\,e} = jY_0 \frac{2\tan(\theta/2)+R\tan(k\theta)}{2-R\tan(\theta/2)\tan(k\theta)} \quad \text{(for even mode)}, \tag{4}$$

where $Y_{in\ o}$ and $Y_{in\ e}$ are the odd and even mode

admittance respectively. R is the impedance ratio defined as Zs/Z_0 (or admittance ratio Z_0/Zs), whereas $k = \theta s / \theta$ is defined as electrical length ratio. Since for this work, $Z_0 = 50\Omega$, $Zs = 64\Omega$, $\theta s = \pi/4$ and $\theta = 2\pi$ has been chosen based on the presented analysis, therefore R = 0.78 and k = 1/8.

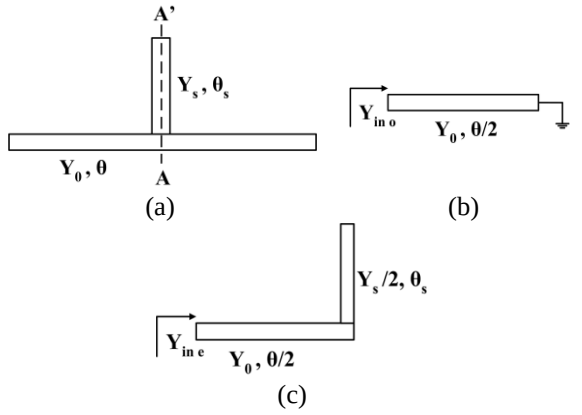

Fig. 4. (a) A simple transmission line model with centrally laoded open stub, (b) even mode circuit, and (c) odd mode circuit.

Please note from (3) that at resonant condition, odd mode frequency can be found out which corresponds to the center frequeny (CF). That is at Yin o = 0, $\theta = n\pi$, (and since n was selected as 2 in Subsection IIA), the center (odd mode) frequency is clculated to be 2.99 GHz which is almost the design frequency considered in this work. Moreover transmission zeros can be predicted by setting S21 equation equal to zero, as,

$$S21 = |Y_{in\,o}| - |Y_{in\,e}| = 0 . \quad (5)$$

Using (3) and (4) in (5), and after some manipulations, following equation can be derived:

$$S21 = |Y_{in\,o}| - |Y_{in\,e}| = \frac{1}{\tan(\theta/2)} - R\tan(k\theta) - 2\tan(\theta/2) = 0 . \quad (6)$$

Equation (6) is solved and the result is plotted against normalized frequency (f/f_0, where f_0 = CF = 3 GHz) on the x-axis as shown in Fig. 5. The lower and higher TZ frequencies f_{TZ1} and f_{TZ2} are respectively predicted to be at $0.77f_0$ (f_{TZ1} = 2.3 GHz) and $1.2f_0$ (f_{TZ2} = 3.6 GHz). Although two more TZs are theoratically expected at about 0.57 GHz and 5.1 GHz, but for our work, we are only interested in the TZs nearest to the CF.

2) Practical Demonstration

Simulated and measured responses of this asymmetric structure with one RR and a loaded stub are shown in Fig. 6. Good agreement is observed. The 3-dB FBW is 47% (from 2.32-3.73 GHz). The measured IL and RL are better than 1.6 dB and 13 dB respectively. Two transmission zeros at 2.26 GHz and 3.8 GHz give a rejection of -24.17 dB and -23.53 dB respectively. The difference of the theoretical and experimental values of f_{TZ1} and f_{TZ2} are noted to be 1.7% and 5.5%, being reasonably acceptable. It may be noted here that the area of the designed BPF is 14.8 cm^2 (3.7 cm × 3.79 cm), which as compared to an area of 22 cm^2 (4.4 cm × 5.0 cm) (if implemented at the same design frequency by method given in [17]), gives an area reduction of 48%.

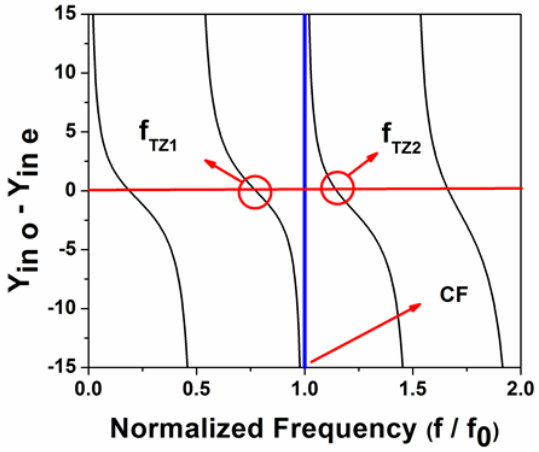

Fig. 5. Theoretically predicted transmission zeros plotted against frequency normalized at CF = 3 GHz.

C. Cascaded wide-band BPF (CWBF)

Out of band rejection of the transmission zeros of the RR with single stub can be improved by cascading two or more such structures. In this work only two BPFs of Fig. 3 (a) were cascaded to prove the point. Figure 7 (a) shows the manufactured cascaded wide-band RR BPF with an area of 34.02 cm^2 (8.1 cm × 4.2 cm). Note that the distance (d) between the two RR was optimized at about $\lambda g/4$, i.e., d = 18.43 mm. It can be seen in Fig. 7 (b) from the measured response that the transmission zeros at 2.26 GHz and 3.8 GHz are now at -55.5 dB and -37 dB giving a considerable improvement as compared to measured response in Fig. 6.

Here the 3-dB FBW is 46.5% which is close to 47% as in previous section. The slight variation may be due to manufacturing tolerance. The IL and RL are better than 1.7 dB and 12.3 dB respectively. The reported area of the CWBF (34.02 cm^2) is about 36% less than if it was implemented with the methodology in [17] at 3 GHz (in the latter case the area comes out to be 53.68 cm^2 (8.8 cm × 6.1 cm)). Please note that the area reduction given by the implemented simple structures shown in this sub-section and the previous one is quite significant compared to [17].

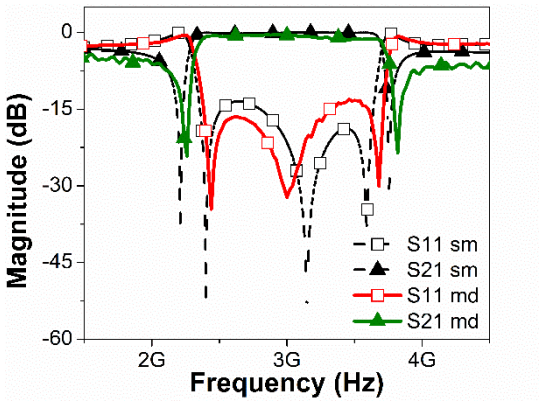

Fig. 6. S-parameters response of fabricated RR with single loaded stub with $l_s = \lambda_g/4$ (sm = simulated, md = measured).

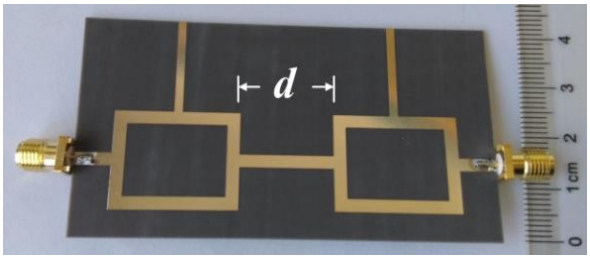

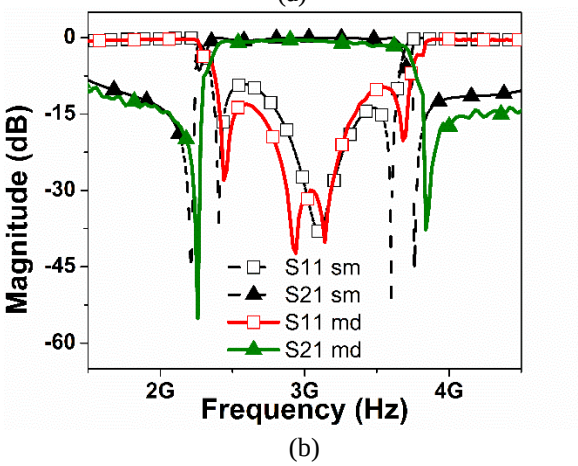

Fig. 7. (a) Fabricated cascaded RR with loaded stubs, and (b) S-parameters response (sm = simulated, md = measured).

D. Compact cascaded wide-band BPF (CCWBF)

As shown in Fig. 8 (a), the open stubs are placed inside the RR in order to save area without much compromise on the performance. The internal couplings of the stub with the RR were ignored for this analysis and the distance (d) between the two RRs was taken to be 18.43 mm. The area of the CCWBF came out to be 8.1 cm × 2.8 cm giving an improvement of about 33% as compared to the one shown in Fig. 7 (a).

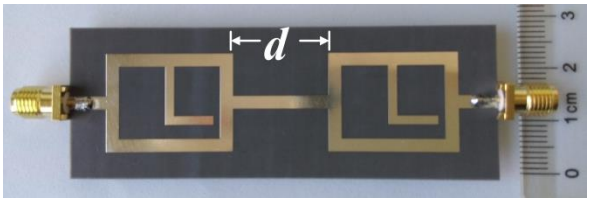

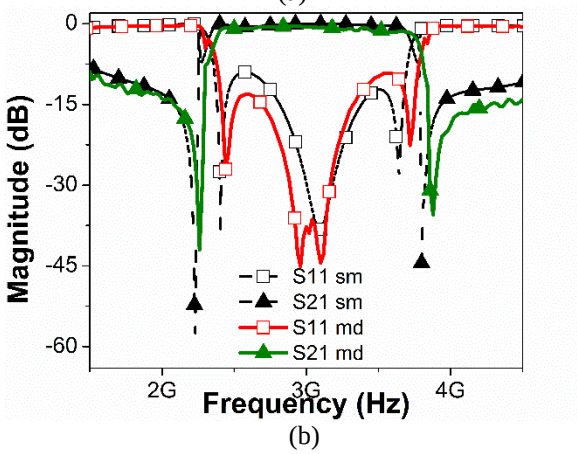

Fig. 8. (a) Fabricated compact cascaded RR with loaded stubs, and (b) S-parameters response (sm = simulated, md = measured).

The S-parameter response of the CCWBF is shown in Fig. 8 (b). It is evident that the performance of the compact cascaded BPF is comparable to the cascaded BPF shown in Fig. 7 (b). The measured transmission zeroes at 2.28 GHz and 3.88 GHz are at -42 dB and -37 dB respectively. Overall the IL and RL are better than 1.8 dB and 11.2 dB with a difference of about 6% and 8% respectively as compared to cascaded filter. The 3-dB FBW came out to be 47.3%. Slight shift in the pass-band edge frequencies may be contributed to the internal couplings of the stub with RR and/or manufacturing tolerance which are reported to be 2.35 - 3.77 GHz.

E. Comparison with previous works

A comparison of the proposed technique with previously presented work is summarized in Table 1. It may be noted that as compared to previous work, the proposed methodology presents a simplified structure with only single stub operational over a comparable or better FBW with low IL. It is also evident that the proposed wide band filter has a very compact area which is an added advantage of the proposed technique. Of course if sharp roll-off is a critical design parameter, designs proposed in [12-14] may be adopted with limited BW. But if it is not the case, then the proposed designed offers reasonably good performance parameters over a wide bandwidth in less area.

Table 1: Comparison of proposed technique with previous work

Works	Parameters					
	Structure	FBW (%)	$\|S_{11}\|$ (dB)	$\|S_{21}\|$ (dB)	Tx[a] Zeros	Area
[10]	Triangular RR+2 coupled transmission lines	11.2	> -10	2.3	2	>1.15λg × 0.5λg
[11]*	RR + coupled transmission lines	10	-40 (at CF)	2.4	3	~0.5λg × 0.5λg
[12]**	2RR + 2 open Stubs	10.7	-40 (at CF)	-1.63	6	Not given exactly, but large than 0.5λg × 0.5λg
[13]	RR+ 2 transmission lines + 2stubs	20.6	> -12.5	< -2.2	6	1.06λg × 0.61λg
[14]	RR+ 2 transmission lines + 2stubs	21.9	> -12.5	< -2	5	~0.76λg × 0.33λg
[17]	RR + 2 stubs	49.3	> -13.3	< -1.6	2	0.42λg × 0.29λg
This work	RR + single stub	47	> -12.3	< -1.7	2	0.1λg × 0.04λg

[a] Transmission;
* Only BPF with two cascaded basic cells is considered;
** Only passive filter is considered.

III. CONCLUSION

Based on the voltage and current analysis along the ring resonator length, a co-axial scheme of feed lines is proposed which ensures the band-pass characteristic of the RR. The wide-band response was achieved by loading the RR with a single λg /4 open stub. The structure of the RR wide-band BPF was simplified and made area efficient as compared to [17] owing to the co-axial placement of feed lines and only one stub. The theoretical prediction of the TZs through presented analysis agrees well with the measured values with error less than 5.5%. Subsequently, cascaded (CWBF) and compact cascaded (CCWBF) wide-band BPF were designed and fabricated with latter showing an area reduction of 33% due to the special placement of the stub inside the RRs. The cascaded structure improved the out of band rejection with two transmission zeros at 2.26 GHz and 3.8 GHz with rejection better than 37 dB. The achieved 3-dB FBWs of the designed cascaded/ compact cascaded filters were 46% / 47.3% with an IL and RL better than 1.7 dB / 1.8 dB and 12.3dB / 11.2 dB respectively.

REFERENCES

[1] L. Zhou, Y. Z. Yin, W. Hu, and X. Yang, "Compact bandpass filter with sharp out-of-band rejection and its application," *Applied Computational Electromagnetics Society (ACES) Journal*, vol. 32, no. 3, pp. 249-255, Mar. 2017.

[2] A. K. Tiwary and N. Gupta, "Compact wide band printed filter with improved out-of-band performance," *Applied Computational Electromagnetics Society (ACES) Journal*, vol. 29, no. 3, pp. 224-230, Mar. 2014.

[3] K. Chang, *Microwave Ring Circuits and Antennas*. Wiley, New York, 1996.

[4] M. Matsuo, H. Yabuki, and M. Makimoto, "Dual-mode stepped impedance ring resonator for band-pass filter applications," *IEEE Trans. Microw. Theory Techn.*, vol. 49, no. 7, pp. 1235-1240, 2001.

[5] B. T. Tan, S. T. Chew, M. S. Leong, and B. L. Ooi, "A dual-mode bandpass filter with enhanced capacitive perturbation," *IEEE Trans. Microw. Theory Techn.*, vol. 51, no. 8, pp. 1906-1910, 2002.

[6] M. F. Lei and H. Wang, "An analysis of miniaturized dual-mode bandpass filter structure using shunt-capacitance perturbation," *IEEE Trans. Microw. Theory Techn.*, vol. 53, no. 3, pp. 861-867, 2005.

[7] A. Gorur, "Description of coupling between degenerate modes of a dual-mode microstrip loop resonator using a novel perturbation arrangement and its dual-mode bandpass filter applications," *IEEE Trans. Microw. Theory Techn.*, vol. 52, no. 2, pp. 671-677, 2004.

[8] R. J. Mao and X. H. Tang, "Novel dual-mode bandpass filters using hexagonal loop resonators," *IEEE Trans. Microw. Theory Techn.*, vol. 54, no. 9, pp. 3526-3533, Sep. 2006.

[9] B. T. Tan, J. J. Yu, S. T. Chew, M. S. Leong, and B. L. Ooi, "A miniaturized dual-mode ring band-pass filter with a new perturbation," *IEEE Trans. Microw. Theory Techn.*, vol. 53, no. 1, pp. 343-348, 2005.

[10] J. S. Hong and S. Li, "Theory and experiment of dual-mode microstrip triangular patch resonators and filters," *IEEE Trans. Microw. Theory Techn*.,

vol. 52, no. 4, pp. 1237-1243, Apr. 2004

[11] M. Salleh, G. Prigent, O. Pigaglio, and R. Crampagne, "Quarter-wavelength side-coupled ring resonator for bandpass filters," *IEEE Trans. Microw. Theory Techn.*, vol. 56, no. 1, pp. 156-162, Jan. 2008.

[12] R. Gomez-Garcıa, J. I. Alonso, and D. Amor-Martin, "Using the branch line directional coupler in the design of microwave bandpass filters," *IEEE Trans. Microw. Theory Techn*., vol. 53, pp. 3221-3229, 2005.

[13] W. Feng, X. Gao, W. Che, and Q. Xue, "Bandpass filter loaded with open stubs using dual-mode ring resonator," *IEEE Microw. Wireless Compon. Lett*., vol. 25, no. 5, pp. 295-297, 2015.

[14] K. Deng, Z. Chen, and W. Feng, "Bandpass filter with four transmission zeros using dual-mode ring resonator," *Progress in Electromagnetics Research PIER Letters*, vol. 56, pp. 129-132, 2015.

[15] H. Zhu and A. Abbosh, "Compact tunable bandpass filter with wide tuning range using ring resonator and short-ended coupled lines," *Electron. Lett*., vol. 51, no. 7, pp. 568-570, 2015.

[16] M. Oliaei, M. Tayarani, and M. Karami, "Compact microstrip bandpass filter improved by DMS and ring resonator," *Progress In Electromagnetics Research PIER Letters*, vol. 45, pp. 7-12, 2014.

[17] L.-H. Hsieh and K. Chang, "Compact, low insertion-loss, sharp-rejection, and wide-band microstrip bandpass filters," *IEEE Trans Microw. Theory Tech*., vol. 51, no. 4, pp. 1241-1246, 2003.

Zafar Bedar Khan received his B.E. (Avionics) degree from National University of Sciences and Technology, Pakistan and M.S. (Electronics & Comm.) degree from Hanyang University, South Korea in 2002 and 2010 respectively. Khan has been working as a Research Engineer in an R&D organization in Pakistan in the field of RF Front-end Design. He is currently pursuing his Ph.D. degree in Northwestern Polytechnical University, Xian, China. His research interests include RF passive component design for RF front-end application in Radar and communication systems.

Huiling Zhao received her Ph.D. degree in Circuit and System from Northwestern Polytechnical University, Xian, China in 2002. Zhao is currently a Professor in the Department of Electronics and Information, Northwestern Polytechnical University, China. She has been a Visiting Associate Professor in the Duke University, USA from 2006 to 2007. Zhao's main research interests include optimization algorithm development for beam forming, computational electromagnetics, microwave and millimeter wave circuit and antenna design.

LTCC Distributed-Element Bandpass Filter with Multiple Transmission Zeros Using Non-Resonating Node

Yang Zhan [1], Wei Qin [1], Qian-Yuan Lu [2], and Jian-Xin Chen [1*]

[1] School of Electronics and Information
Nantong University, Nantong, 226019, China
[*]jjxchen@hotmail.com

[2] Xinglin College
Nantong University, Nantong, 226019, China

Abstract ─ A distributed-element low temperature co-fired ceramic (LTCC) bandpass filter (BPF) with multiple transmission zeros using non-resonating node (NRN) is proposed. By fully taking advantage of the LTCC technology in 3-dimentional (3-D) environment, the employed dual-mode stub-loaded stepped-impedance resonator (SIR) and the NRN are reasonably folded, and miniature circuit size can be obtained. Meanwhile, four transmission zeros are produced in both sides of the passband to realize sharp rejection skirts. For demonstration, a four-pole LTCC BPF using the NRN centered at 3.65 GHz is designed, fabricated and measured. Simulated and measured results are presented, showing good agreement.

Index Terms ─ Bandpass filter (BPF), low temperature co-fired ceramic (LTCC), non-resonating node (NRN), transmission zeros (TZ).

I. INTRODUCTION

Recently, the rapid development of modern wireless communications systems demands ever-greater functionality, higher integration, and more compact formats. It is well known that high-performance miniaturized bandpass filter (BPF) plays an important role in various communication systems [1-2]. Corresponding to this trend, lots of BPFs with size-reduction methods have been extensively studied and explored using various technologies, such as multilayer printed circuit board (PCB) [3], low-temperature co-fired ceramic (LTCC) [4-7] and high-temperature ceramic (HTC) with high dielectric constant [8]. Among them, the LTCC design technology, as one of the most promising methods, has emerged as an attractive solution for high-integration applications owing to its high level of compactness, mature multilayer fabrication and integration capability in 3-dimentional (3-D) environment.

Over the past decades, the limited frequency spectrums become more and more crowded and the high isolation between RF bands becomes a challenging issue. However, due to the relative low Q factor of the LTCC technology, the stopband roll-off of the LTCC BPF could not be satisfied in many applications. Generally, it is necessary to generate the transmission zeros (TZs) near to the passband for improving stopband rejection which can be realized by introducing bypass or cross-coupling between nonadjacent resonators in the filters [9].

In this letter, we present a compact LTCC BPF with sharp cutoff skirts by embedding the non-resonating node (NRN) without increasing the overall circuit size. Benefiting from the NRN and the extra source-load (S-L) coupling in 3-D environment, multiple TZs are realized to improve the roll-off and rejection level of the stopband.

II. FILTER DESIGN AND ANALYSIS

The planar configuration layout of the proposed four-pole BPF is shown in Fig. 1, which is composed of two dual-mode stub-loaded stepped-impedance resonators (SIRs) [4] (i.e., resonators 1/2 and 3/4), a NRN and a pair of coupled feed lines. The employed transmission lines of the BPF are reasonably folded in 3-D environment, operating as asymmetric striplines, for constructing a compact LTCC BPF, as shown in Fig. 2. The NRN is embedded between the two dual-mode resonators so that the overall circuit size of the BPF is not enlarged. Generally, The NRN structure can introduce more TZs to improve the passband selectivity [9]. The NRN is implemented with a half-wavelength resonator whose resonant frequency is far away from the central frequency of the proposed LTCC BPF.

Figure 3 shows the coupling scheme of the proposed filter. S and L indicate the source and load of the filter, respectively. Due to the NRN effect in this design, two TZs (i.e., TZ_1 and TZ_2 shown in Fig. 4) close to the passband can be generated. At the same time, in the small 3-D space in Fig.2 (a), various

Submitted On: April 13, 2016
Accepted On: October 12, 2017

parasitic couplings are inevitably existed, which are slight and can be neglected except for the S-L coupling. Although the S-L coupling is weak, it is highly desired for generating two extra TZs (i.e., TZ_3 and TZ_4 in Fig. 4). Meanwhile, it is helpful for shifting both TZ_1 and TZ_2 towards the central frequency so that the passband selectivity can be further enhanced. As a consequence, the proposed four-pole BPF designed by combing the effects of the NRN and the S-L coupling owns four TZs in the stopbands. The desired filter response centered at 3.65 GHz with 1.08 GHz bandwidth (i.e., fractional bandwidth (FBW) = 29.6%) has four TZs at normalized frequencies $S_1 = -j7.9$, $S_2 = -j2.1$, $S_3 = j1.3$, and $S_4 = j2.4$ with a maximum in-band return loss of 16 dB. Synthesis of such coupling scheme with the NRN follows the approach in [10, 11], the corresponding coupling matrix of can be obtained:

$$M = \begin{bmatrix} & S & 1 & 2 & NRN & 3 & 4 & L \\ S & 0 & 0.7865 & 0.43 & -0.25 & 0 & 0 & 0.00127 \\ 1 & 0.7865 & 0.5 & 0 & 1.97 & 0 & 0 & 0 \\ 2 & 0.43 & 0 & -1.1 & -2.3 & 0 & 0 & 0 \\ NRN & -0.25 & 1.97 & -2.3 & -15 & -1.97 & 2.3 & 0.25 \\ 3 & 0 & 0 & 0 & -1.97 & 0.52 & 0 & 0.7865 \\ 4 & 0 & 0 & 0 & 2.3 & 0 & -1.12 & 0.43 \\ L & 0.00127 & 0 & 0 & 0.25 & 0.7865 & 0.43 & 0 \end{bmatrix}.$$

The diagonal elements are determined by:

$$M_{i,i} = \frac{f_0^2 - f_i^2}{\Delta f \cdot f_i}. \quad (1)$$

Here, the parameters f_0 and Δf are the central frequency and the bandwidth of the filter, respectively. And f_i is the resonant frequency of the i th resonator (i = 1, 2, 3 or 4). The whole structure is finely tuned and optimized so as to meet our specifications, which is performed using the commercial software high frequency structure simulator (HFSS). The simulated responses of the proposed filter together with the ideal circuit responses are plotted in Fig. 4. The parameters in Fig. 2 (b) for simulation are listed in Table 1, and the diameters of via holes are all set as 0.15 mm.

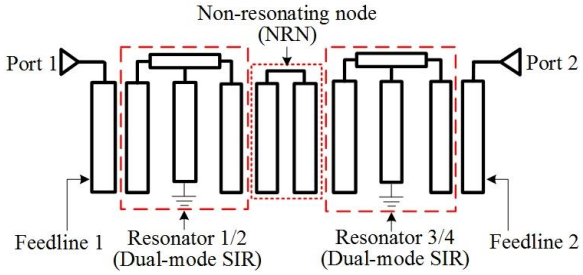

Fig. 1. Planar configuration sketch of the proposed BPF.

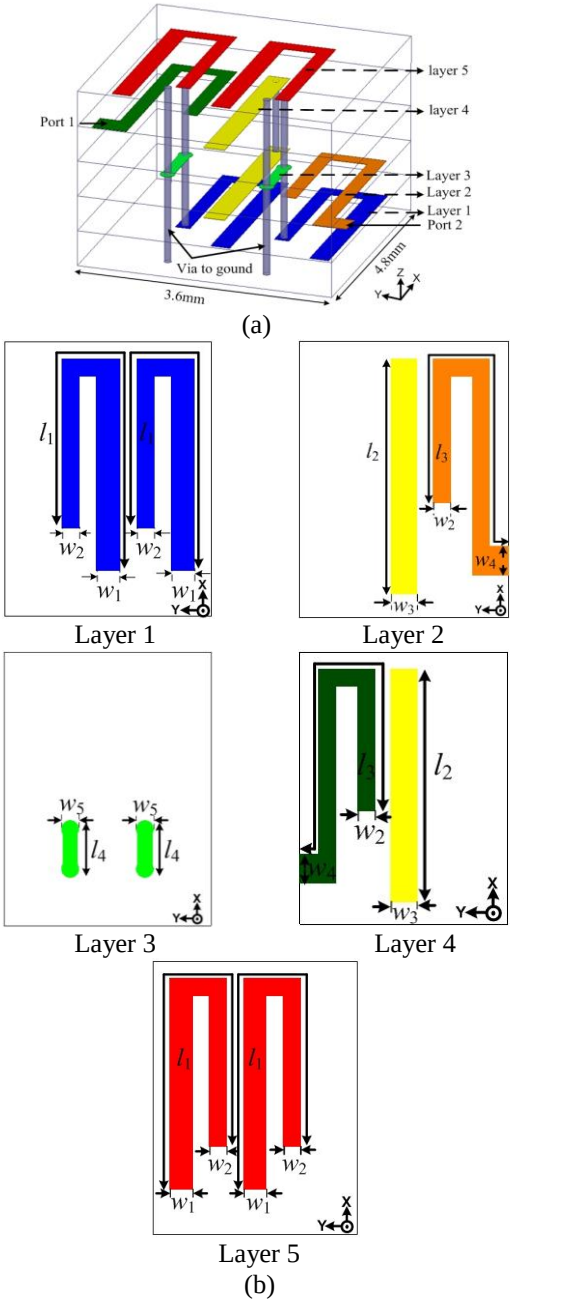

Fig. 2. Structure of the proposed LTCC BPF using the NRN (top and bottom ground are not shown). (a) 3-D view and (b) layout.

Table 1: Dimensions of the proposed LTCC BPF in Fig. 2

Parameters	l_1	l_2	l_3	l_4	w_1
Value (mm)	7.7	4.1	6.745	1	0.4
Parameters	w_2	w_3	w_4	w_5	
Value (mm)	0.3	0.45	0.5	0.25	

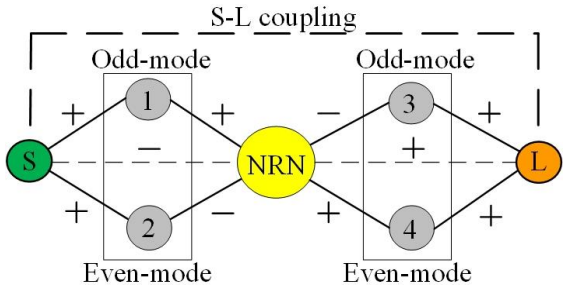

Fig.3. Coupling scheme of the proposed LTCC BPF.

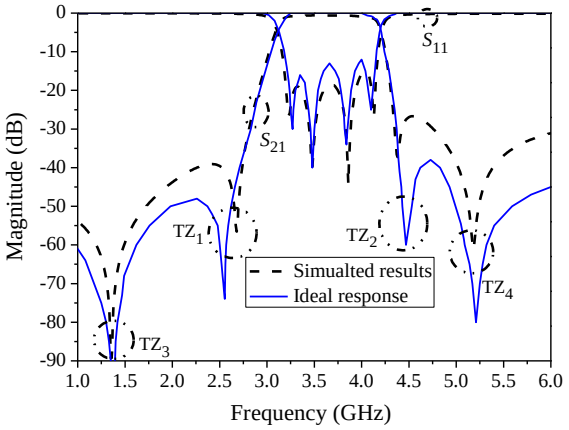

Fig. 4. Ideal responses and simulated S-parameters of the proposed LTCC BPF.

III. RESULTS AND DISCUSSION

To verify the proposed idea, the proposed BPF is designed and fabricated. Figure 5 shows the photograph of the proposed four-pole LTCC BPF mounted on the test board (Rogers 4003c with dielectric constant $\varepsilon_r = 3.38$ and thickness h = 32 mil), and the configuration of the LTTC wafer is shown in Fig. 2. It consists of seven metal layers (the top and bottom ground are not shown) and 14 ceramic sheets (LTCC Ferro A6-M substrate with a constant of 5.9 and a loss tangent of 0.001). Each sheet has a thickness of 0.1 mm. The BPF size is 4.8×3.6×1.4 mm^3 (i.e., electrical size is $0.14\lambda_g \times 0.11\lambda_g \times 0.04\lambda_g$, where λ_g is the guided wavelength of the stripline at 3.65 GHz). The measured S-parameter results of the proposed filter plotted in Fig. 6 are accomplished by using E5071C network analyser. It exhibits a center frequency of about 3.65 GHz, an insertion loss (IL) of approximately 1.4 dB and the return loss is better than 15 dB. Four transmission zeros are realized to obtain a sharper stopband roll-off and improve the selectivity of the proposed BPF significantly. Slight discrepancies between the simulated and measured results can be attributed to fabrication tolerance and test implementation. Comparisons of this design with some reported BPFs using the NRN are summarized in Table 2 in terms of electrical performance and circuit size. Compared with the BPFs based on the substrate integrated waveguide (SIW) [9], LTCC [11, 12], and PCB [13] technologies, it can be found that the proposed LTCC BPF shows evident size reduction and has a wider FBW. The more TZs can improve the passband selectivity effectively.

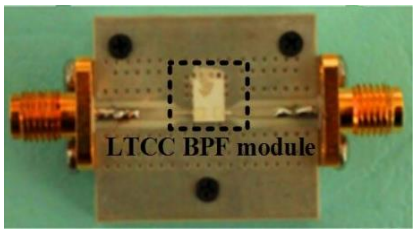

Fig. 5. Photograph of the LTCC BPF.

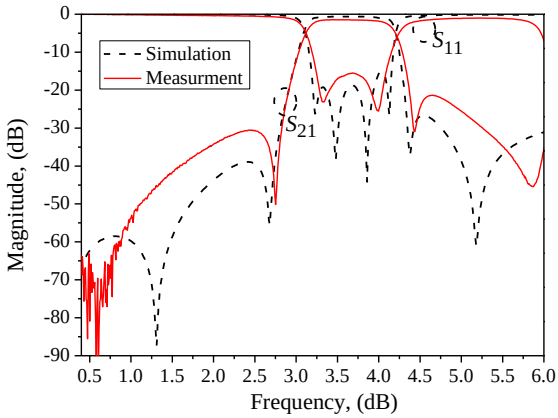

Fig. 6. Simulated and measured results of the proposed LTCC BPF.

Table 2: Performance comparison with previous works with NRN

Ref.	Techn-ology	f_0 (GHz)/ IL (dB)	TZ	Filter Order/FBW	Electrical Size ($\lambda_g \times \lambda_g \times \lambda_g$ at f_0)
[9]	SIW	5/1.6	2	2/3%	1.09×1.09×0.03
[11]	LTCC	3.45/1.2	2	4/8.7%	0.49×0.4×0.02
[12]	LTCC	58.6/2.8	2	4/3.92%	1.49×1.16×0.24
[13]	PCB	1.4/1.86	3	4/10%	1.54×0.09×0.017
This work	LTCC	3.65/1.4	4	4/29.6%	0.14×0.11×0.04

VI. CONCLUSION

In this letter, a compact distributed-element LTCC BPF with four TZs using the NRN has been presented. The proposed filter has the advantage of sharp cutoff skirts and good in-band performance. The design procedures of the BPF based on the coupling matrix have been given. The proposed filter has multiple TZs, compact size and good passband performance, which

makes it competitive for application in microwave communication systems.

ACKNOWLEDGMENT

The work was supported by the National Natural Science Foundation of China under Grants 61271136 and 61501263, and by Six Types of Talents Project of Jiangsu Province (2011-DZXX-014), and the Nantong Application Research Technology Program (GY12015021, GY12016013)

REFERENCES

[1] M. Salehi and L. Noori, "Miniaturized microstrip bandpass filters using novel stub loaded resonator," *Applied Computational Electromagnetics Society (ACES) Journal*, vol. 30, no. 6, pp. 692-697, June 2015.

[2] A. Boutejdar, N. M. Eltabit, A. A. Ibrahim, E. P. Burte, and M. A. Abdalla, "New compact dual bandpass filter using coupled double-ring resonators and DGS-technique," *Applied Computational Electro-magnetics Society (ACES) Journal*, vol. 31, no. 2, pp. 132-137, Feb. 2016.

[3] K. Ma, L. Fan, and S. Zhang, "Compact mult-ilayer self-packaged filter with surface-mounted packaging," *Electron. Lett*., vol. 51, no. 7, pp. 564-566, Apr. 2015.

[4] J.-X. Chen, Y. Zhan, and Q. Xue, "Novel LTCC distributed-element wideband bandpass filter based on the dual-mode stepped-impedance resonator," *IEEE Trans. Compon. Packag. Manuf. Technol*., vol. 5, no. 3, pp. 372-380, Mar. 2015.

[5] J.-X. Chen, C. Shao, and Q.-Y. Lu, "Compact LTCC balanced bandpass filter using distributed-element resonator," *Electron. Lett*., vol. 49, no. 5, pp. 354-356, Feb. 2013.

[6] H. Tang, J.-X. Chen, Y. Ge, Q.-Y. Lu, J. Shi, and Z.-H. Bao, "Novel LTCC switchable bandpass filter using vertically short-ended sir," *Microwave Opt. Technol. Lett*., vol. 56, no. 4, pp. 999-1002, Apr. 2014.

[7] J.-X. Chen, Y. Ge, H. Tang, L.-H. Zhou, J. Shi, and Z.-H. Bao, "Compact LTCC dual-band bandpass filter with high selectivity using the vertical s-shaped short-ended SIR," *Microwave Opt. Technol. Lett*., vol. 55, no. 6, pp. 1345-1348, June 2013.

[8] M. Makimoto and S. Yamashita, Microwave Resonators and Filter for Wireless Communication: Theory, design and application, Berlin, Germany: Springer-Verlag, 2001.

[9] W. Shen, X.-W. Sun, W.-Y. Yin, J.-F. Mao, and Q.-F. Wei, "A novel single-cavity dual mode substrate integrated waveguide filter with non-resonating node," *IEEE Microw. Wirel. Compon. Lett*., vol. 19, no. 6, pp. 368-370, June 2009.

[10] G. Macchiarella, "Generalized coupling coefficient for filters with nonresonant nodes," *IEEE Microw. Wirel. Compon. Lett*., vol. 18, no. 12, pp. 773-775, Dec. 2008.

[11] L.-S. Wu, X.-L. Zhou, W.-Y. Yin, L. Zhou, and J.-F. Mao, "A substrate-integrated evanescent-mode waveguide filter with nonresonating node in low-temperature co-fired ceramic," *IEEE Trans. Microwave Theory & Tech*., vol. 58, no. 10, pp. 2654-2662, Oct. 2010.

[12] H. Chu, Y. X. Guo, and X. Q. Shi, "60 GHz LTCC 3D cavity bandpass filter with two finite transmission zeros," *Electron. Lett*., vol. 47, no. 5, pp. 324-326, Mar. 2011.

[13] S.-R. Manuel and G.-G. Roberto, "A class of high-selectivity microstrip transversal bandpass filter using non-resonating nodes," *Proceedings of the 40th European Microwave Conference*, pp. 292-295, 2010.

Yang Zhan was born in Nanjing, Jiangsu Province, China, in 1991. He received the B.Sc. degree from Nantong University, Nantong, China, in 2013, where he is currently pursuing the M.Sc. degree in Electro-magnetic Field and Microwave Technology. His current research interests include antennas, microwave filters, and baluns.

Zhan was the winner of iWEM 2014 Student Innovation Competition in Sapporo, Japan.

Wei Qin was born in Jiangsu, China. He received the B.Sc. degree in Electronic Engineering from Southeast University (Nanjing, China) in 2007, the M.Sc. degree in Electromagnetic Fields and Microwave Technology also from Southeast University in 2010, and the PhD degree in Electronic Engineering from City University of Hong Kong (Hong Kong, China) in 2013.

From July 2013 to November 2013, he was a Senior Research Associate with the State Key Laboratory of Millimeter Waves (HK), City University of Hong Kong. Since 2014, he has been with the School of Electronics and Information, Nantong University, Nantong, Jiangsu Province, China, where he is currently an Associate Professor. His research interest focuses on deign and application of microwave devices and antennas.

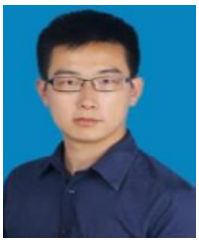

Qing-Yuan Lu received the B.Sc. degree from NJU, Nanjing, China, in 2010, and the M.Sc. degree in Electromagnetic Fields and Microwave Technology in NTU, China in 2014. Since 2014, he has been with Xinglin College, Nantong University, Nantong, Jiangsu Province, China, where he is currently an Assistant. His research interests include microwave balanced circuits and antenna, etc.

Jian-Xin Chen was born in Nantong, Jiangsu Province, China, in 1979. He received the B.S. degree from Huai Yin Teachers College, Jiangsu Province, China, in 2001, the M.S. degree from the University of Electronic Science and Technology of China (UESTC), Chengdu, China, in 2004, and the Ph.D. degree from the City University of Hong Kong, Kowloon, Hong Kong, in 2008. Since 2009, he has been with Nantong University, Jiangsu Province, China, where he is currently a Professor. He has authored or coauthored more than 80 internationally referred journal and conference papers. He holds 11 Chinese patents and 3 U.S. patents. His research interests include microwave active/passive circuits and antennas, LTCC-based millimeter-wave circuits and antennas.

Chen was the recipient of the Best Paper Award presented at the Chinese National Microwave and Millimeter-Wave Symposium, Ningbo, China, in 2007. He was Supervisor of 2014 iWEM Student Innovation Competition winner in Sapporo, Japan.

Forward Scattering from a Three Dimensional Layered Media with Rough Interfaces and Buried Object(s) by FDTD

S. H. Mirjahanmardi, P. Dehkhoda, and A. Tavakoli

Department of Electrical Engineering, Amirkabir University of Technology, Tehran, Iran
s.h.mirjahanmardi@gmail.com, pdehkhoda@aut.ac.ir, tavakoli@aut.ac.ir

Abstract **–** In this paper, the finite difference time domain (FDTD) method is implemented to analyze the scattered field from a three dimensional structure including two-layer rough interfaces with or without buried object(s). The effects of different parameters such as rough interface correlation length as well as its root mean square (rms) height, the moisture content of the soil, also the buried object position and size on the scattered field are studied. Simulations show that by increasing the soil moisture, the level of scattering from the structure (without the buried object) is increased. In addition, it is shown that the same amount of moisture change, but in different percentage level, shows completely different effect on the scattering level. Furthermore, it is observed that changing the correlation length in the small perturbation range does not have a significant effect on the scattering coefficients. Moreover, images from the buried objects are obtained to show the visualization of object observation with different materials in a background. The solution has been validated by the finite integration based commercial software, CST.

Index Terms **–** Buried object, electromagnetic scattering, finite difference time domain (FDTD), imaging, layered media, and rough surfaces.

I. INTRODUCTION

Electromagnetic scattering from rough surfaces has always been a subject of interest for scientists and researchers due to its vast range of applications. One of the most common problems related to rough surface scattering is the detection of buried objects. Cancer tissues, underground water and petroleum, and buried endangers waste are examples of buried targets to be detected. The importance and usefulness of the research on detection of buried objects is even more pronounced when it comes to have precise images in medical applications such as cancer detection. Forward scattering is the first step toward final detection.

The proposed methods in forward scattering can be categorized to analytical, semi-analytical and numerical techniques. Analytical techniques, when applicable, are the most optimal choices to solve scattering from rough surfaces without buried objects. However, for problems which include objects an extension of these techniques is possible only for canonical objects [1], [2]. Furthermore, analytical methods are limited to the region of validity [2], [3]. As an example of semi analytic approach, the extended boundary condition method has been utilized to find the scattering waves from a multilayer rough surface structure [4].

Numerical methods are neither limited to have canonical objects nor to the need of having a confined regime of validity. Hence, they are capable of solving difficult problems of scattering from stratified rough surfaces backgrounds with arbitrary shapes of embedded objects, although they are not as fast as analytical techniques. For instance, the steepest descent fast multi-pole method (SDFMM), which was introduced by Jandhyala [5], [6], is used by El-Shenawee to analyze rough layered structures with buried object(s) [7]. Several hybrid methods, such as the combination of Method of Moments (MoM) with Physical Optics (PO) approach [8] or Kirchhoff method [9] are also applied to the these types of problems.

Among the research that have been done in the area of scattering from rough surfaces media [4], [5], [10] studied the case that there is no object buried. Only a few works concentrated on the multilayer cases with object(s) [7], [8], [11], [12]. This problem will is fully studied in this paper.

One of the efficient methods to solve the scattering from rough surfaces is the finite difference time domain (FDTD) [13] solution. This method is so flexible that makes it a suitable choice to solve problems with complex geometries. In fact; when FDTD is applied to a scattering problem from buried object(s), the changes in the object(s) shape(s) and surfaces do not add significant complexity to the method. FDTD formulation also does not result in complex matrix equations (such as inverse operations) and therefore enhances the speed of calculation(s) dramatically. As an example, Kuang et al. [14] used FDTD to solve the problem of scattering from an object above a single rough layer. Also, Guo et al. has applied a parallel FDTD to the same problem [15] to make the

Submitted On: June 30, 2016
Accepted On: August 12, 2017

codes faster. These papers study the scattering from one single object located above a structure with only one rough layer.

In this paper, in order to complete our previous studies in [16], [17], a FDTD code is implemented to solve the forward scattering from a two-layer rough surfaces structure with or without a buried object(s) as shown in Fig. 1. Thereafter, the effects of different parameters such as moisture content of the background medium as well as rough surfaces parameters are studied. Up to our best of knowledge, no report which used this numerical method for composite layer includes buried objects with rough interfaces has published. In addition, the effect of moisture for different layers has not been studied using this method till now. The problem structure is shown in Fig. 1 which T1, T2 and T3 are the thickness of the upper layer, lower layer and the object location along z-direction, respectively. Notice that the bottom of the structure is truncated and an absorbing boundary is placed in order to reduce the computation space, knowing that negligible waves are reflected thereafter. T1, T2, and T3 are calculated by considering the distance between average line of the rough surfaces. The paper is organized as the following. In Section II, the model formulations as well as absorbing layer type are discussed. In Section III the convergence of the FDTD code is verified and validated by CST Microwave studio commercial software. Section IV is devoted to study the effect of different parameters of the structure and buried object(s) on scattering coefficients. The object parameters, frequency range, and surface dimensions are chosen according to [7], [14] in order to find buried metals.

II. THEORY

FDTD method has attracted many researchers attention because of its nature which can be applied to the complex structures without the need to have the problem's Green function and matrix inverse operation. In this method, Maxwell equations are discretized both in time and space domains. The explicit nature of FDTD has made it an attractive technique in terms of simplicity; however, it has its own limitation when it comes to stability conditions [18]–[20]. One of the conditions that should be satisfied in FDTD to make it stable is Courant factor constraint [21]. To avoid long text, the readers are referred to [18]–[20]. In order to apply FDTD to the models such as the one shown in Fig. 1, the whole structure should be discretized (space discretization). Because of the limitation of the computer storages, the considered space should be truncated and limited to determined edges. Due to this truncation, some portions of the waves that hit the truncated borders are reflected. These reflections produce spurious solutions and make the solution invalid; therefore, to prevent this event a specific type of layer is utilized to absorb these unwanted reflections, perfect matched layer. This absorbing layer surrounds the truncated space, and is matched to the structure in any direction. Thus, only negligible portion of the waves will reflect back to the main space of interest. Here, we use the convolutional perfect matched layer (CPML) for our problem. This well-known type of perfect matched layer is highly effective in absorbing the evanescent waves as explained in [22].

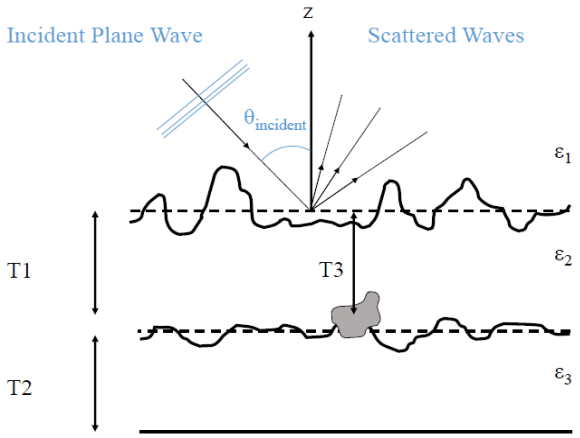

Fig. 1. A three dimensional structure with two-layered rough surfaces and a buried object, illuminated by a plane wave.

To calculate far field scattering coefficients, magnetic (A) and electric (F) potential vectors are employed and the wellknown far-field relations of [23] are used. Then, the bistatic scattering coefficient is calculated using the following equation (as stated in [24]):

$$\sigma_{pq} = \lim_{r\to\infty}\left(\frac{4\pi r^2}{S}\frac{\left|E_p^s\right|^2}{\left|E_q^i\right|^2 .cos(\theta_i)}\right), \qquad (1)$$

where, subscripts p and q represent the vertical (V) and horizontal (H) polarization type of the incident and scattered fields, respectively. Also S is the total surface of the illuminated area (m^2). In addition, E^i and E^s are the incident field and the scattered field, respectively. As mentioned, the structure under the study has two rough interfaces that are created by the Gaussian function that is introduced in [25] and formulated as the following:

$$W(K_x, K_y) = \frac{h^2 l_x l_y}{4\pi} exp[-(K_x^2 l_x^2 + K_y^2 l_y^2)/4], \qquad (2)$$

where, $K_x = 2x/L_x$ and $K_y = 2y/L_y$ in which L_x and L_y are the lengths of the surface along x and y directions, respectively. Also h is the root mean square (rms) height of the surface, and l_x and l_y are the correlation lengths of the rough surfaces directed in the x and y directions, respectively. Please note that in all cases presented in this paper, the ground surface along x and y directions are truncated to $L_x = L_y = 7\lambda_0$ surface. The dimension of the structure in z-direction varies case to case; therefore, the amount of that will be mentioned in each case. Please

note that as this surface is created randomly, an averaging process is necessary. In order to do that, 10 surfaces are created then averaged. In order to minimize the reflection effects of the truncations efficiently, eight CPML cells are considered at the edges of the model. The size of each cell will be stated later. An incident Gaussian plane wave with the center frequency of f_{center} and the maximum frequency of f_{max} excites the structure normally. The incident field relation is introduced in below:

$$E^i(t) = (E_V \hat{v} + E_H \hat{h}) e^{-(t-\frac{1}{c}\hat{k}.\bar{K})^2/\tau^2}, \quad (3)$$

where E_V and E_H are the vertical and horizontal components of the electric field with their unity direction vectors ($\hat{v}$ and $\hat{h}$), respectively. c is light velocity, $\hat{k}$ is the propagation direction unity vector; R is the observing point position vector, and τ is the width of the Gaussian pulse in time domain, which can be obtained by the following relation [18]:

$$\tau = \frac{\sqrt{2.3}}{\pi f_{max}}. \quad (4)$$

III. METHOD CONVERGENCE AND VERIFICATION

It is essential for any numerical method to be checked in order to study whether the results converge to a specific value [26] or not. In this section, the method convergence is examined. As a verification example consider the structure shown in Fig. 1 with $\epsilon_1 = 1$, $\epsilon_2 = 4.5\text{-}j0.6$, and $\epsilon_3 = 6.5\text{-}j0.798$. The rough surface parameters are $l_x = l_y = 0.1\lambda_0$ and h = $0.1\lambda_0$ for both interfaces. Thicknesses are $T1 = 0.4\lambda_0$ and $T2 = 1.3\lambda_0$. A perfect electric conductor (PEC) sphere with $0.2\lambda_0$ radius is placed at the center of the structure at $T3 = 0.3\lambda_0$. Where, λ_0 is the wavelength at f_{center}.

Considered incident wave is $V = \theta$ polarized with $E_\theta = 1V/m$, f_{center} = 300 MHz, and f_{max} = 600 MHz. The structure is discretized and the FDTD code is applied to calculate the total electric field (Ey) at $0.3\lambda_0$ below the object location. To obtain converged results, the cells dimension is decreased from $0.1\lambda_0$ to $0.025\lambda_0$. Then, the relative rms error is calculated in each case, which shows the amount of (Ey) convergence versus decreasing the cell size. The relative rms error at each discretization level for the Ey component is declared in Table 1. It can be realized that as the cell size is decreased, the results are converged. From here and by considering the computation time, it is decided to choose cell size of 25 mm in each direction for the simulations that are done in this study.

To evaluate the developed FDTD code, CST Microwave Studio is used as a reference [27]. Since CST does not create a Gaussian random surface, we have to consider a deterministic rough surface both in CST and our code for the validation purposes. To do this, sinusoidal interfaces with peak-to-peak value of $0.1\lambda_0$ and a number of 8 oscillations in the $7\lambda_0 \times 7\lambda_0$ truncated area are are selected. The structures parameter shown in Fig. 2 are $\epsilon_1 = 1$, $\epsilon_2 = 4.5\text{-}j0.6$, $\epsilon_3 = 6.5\text{-}j0.798$, $T_1 = 0.4\lambda_0$ and $T_2 = 1.3\lambda_0$. A lossy sphere with $\epsilon_2 = 2.9\text{-}j0.0029$ and a radius of $R = 0.2\lambda_0$ is placed at $T_3 = 0.3\lambda_0$. A 1 ns delayed θ-polarized incident Gaussian plane wave illuminates the model obliquely with $\theta_i = 30^o$ and $\phi_i = 0^o$, where ϕ is the polar angle. Here, to avoid long text, only x-component of the magnetic field (Hx) at $0.6\lambda_0$ is shown and compared with CST in Fig. 3. As it is observed, two methods are in excellent agreement. For other observing points, the same agreement were achieved (not presented here).

Table 1: Relative error different discretization level

Cell Size ($\lambda_0 = 1m$)	Relative RMS Error (%)
0.1	--
0.06	20.65
0.05	13.81
0.04	8.36
0.03	8.01
0.025	3.65

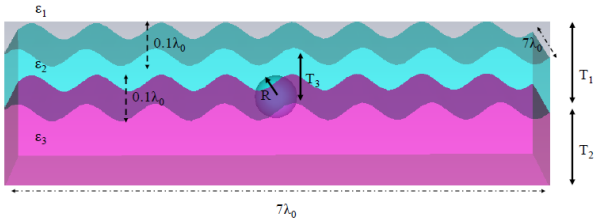

Fig. 2. Validation structure in CST. The peak to peak value for each interface is $0.1\lambda_0$. The dimesnions of the structure are $7\lambda_0 \times 7\lambda_0$ with $T_1 = 0.4\ \lambda_0$ and $T_2 = 1.3\lambda_0$. A sphere with $R = 0.2\lambda_0$ is located at $T_3 = 0.3\lambda_0$. The layers materials are $\epsilon_1 = 1$, $\epsilon_2 = 4.5\text{-}j0.6$, $\epsilon_3 = 6.5\text{-}j0.798$.

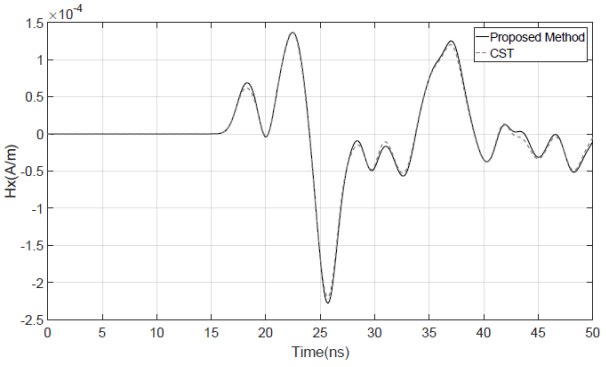

Fig. 3. The comparison between the proposed method and CST for the magnetic field in the x-direction (Hx) at $0.6\lambda_0$ below the upper rough layer. A lossy sphere with $\epsilon_r = 2.9\text{-}j0.0029$ and the radius of $0.2\lambda_0$ is centrally placed at $T_3 = 0.3\lambda_0$.

IV. NUMERICAL RESULTS

In this section the effects of important parameters on scattering coefficients are studied. These parameters include buried object characterizes such as its depth, size, and shape as well as the background structure parameters such as correlation length, rms height of the rough interfaces, and the moisture level of the layers. For all cases, the radar cross section is normalized to the area of the truncated surface $7\lambda_0 \times 7\lambda_0$ is calculated, scattering coefficient (σ). Following subsections are devoted to the results of different case studies. In each study, the σ obtained from the model in the case that an object exists and is buried in layers are compared with the situation in which there is no object. Case study I shows the results of the structure with a buried PEC brick at different depths. In case II, the effect of correlation length of the upper rough surface is studied, while case III focuses on the rough surface rms height impact on σ. Then, the effect of moisture content of the upper layer is examined. Finally, an image of multiple objects is created.

A. Case study I

In the first attempt, consider a rectangular PEC brick with x,y, and z dimensions of $1\lambda_0 \times 1\lambda_0 \times 0.6\lambda_0$, respectively, which is buried in the model and located at the center of averaged line of a two layer structure with the following parameters: $l_x = l_y = 0.1\lambda_0$, $h = 0.1\lambda_0$, $T_1 = 0.4\lambda_0$ with $\epsilon_2 = 4.5\text{-}j0.6$ and $T_2 = 1.3\lambda_0$ with $\epsilon_3 = 6.5\text{-}j0.798$. Two vertical locations (depths) $T_3 = 0.1\lambda_0$ and $T_3 = 0.7\lambda_0$ are considered. It should be noted that the incident field normally excites the structure, and has similar properties to the incident wave introduced in Section III. The VV radar cross sections normalized to the area of the truncated surface ($7\lambda_0 \times 7\lambda_0$) for these two cases in the presence and absence of the buried object are shown in Fig. 4. In this figure, the scattered coefficient for VV case shows that when the object is placed in deeper position, the discrimination between the results of the structure with and without buried object becomes smaller. Moreover, the results from HH polarization are almost similar to the results of VV polarization with small difference in the level of scattering coefficient. Besides, if the cross polarized scattered field (VH or HV) is investigated, it can be seen that there is no rational change in them so that they are not presented here to avoid long text. More to the point, the maximum level of σ is near - 30 dB in cross polarized cases. Also, as it can be seen in Fig. 4 that the results of the three states are the same at observation around 0º. From here it is concluded that to have a better observation of the buried object a bistatic observation is supposed to be performed rather than only backscattered or specular angle.

To further examine this case; the plane wave is angled from -85º to 0º, then σ is calculated at backscattered and specular angles. Figure 5 shows these results in the presence and absence the object. In this figure, the incident angle is changed from -85º to 0º with 5º step. For the backscattered results the probe is placed in the same angle of the incident wave, while for the specular results the probe is placed at the opposite angle. Please note that increasing the object dimension increases the difference between the results with the object and without it. In addition, it is worth mentioning that it was observed that whether the object became smoother, its impact on co-polarized coefficients became less.

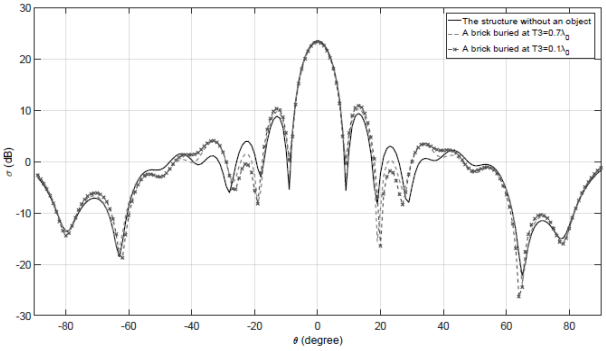

Fig. 4. VV scattering coefficient versus observation angles for three cases of the structure without buried object, buried PEC brick at $T_3 = 0.7\lambda_0$ and buried PEC brick at $T_3 = 0.1\lambda_0$. The incident wave angle is 0º, and background parameters are $l_x = l_y = 0.1\lambda_0$, $h = 0.1\lambda_0$, $T_1 = 0.4\lambda_0$, $T_2 = 1.30$, with $\epsilon_2 = 4.5\text{-}j0.6$ and $\epsilon_3 = 6.5\text{-}j0.798$.

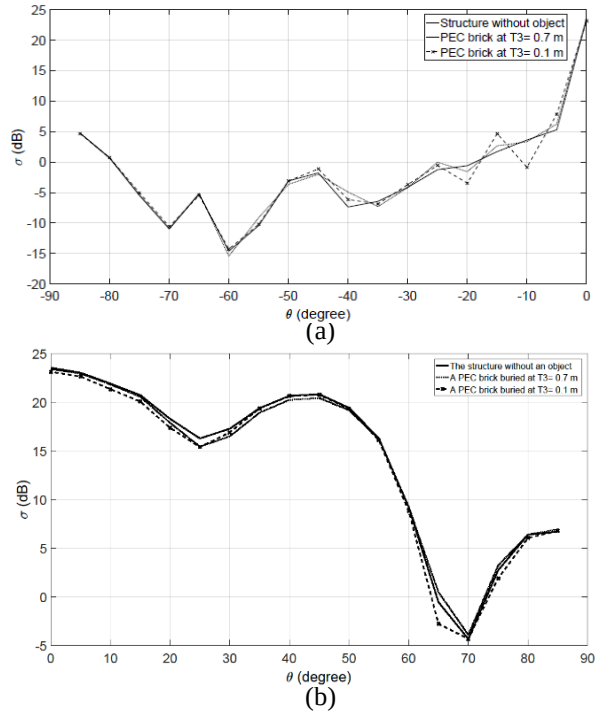

Fig. 5. (a) σ for backscattered angles and (b) specular angles in the presence and absence the PEC brick (same structure introduced in case I) for VV polarization. The step angle is 5 º.

B. Case study II

In this step, the effects of correlation lengths of the upper rough surface in the directions of x and y (l_x and l_y) on the scattering coefficient are discussed. Problem parameters are $h = 0.1\lambda_0$, $T_1 = 0.4\lambda_0$ with $\epsilon_2 = 4.5\text{-}j0.6$ and $T_2 = 1.3\lambda_0$ with $\epsilon_3 = 6.5\text{-}j0.798$. A rectangular PEC brick with $1\lambda_0 \times 1\lambda_0$ cross section and $0.6\lambda_0$ height is placed at $T_3 = 0.5\lambda_0$. In the following two studies, $l_x = l_y$ and two different values of $0.2\lambda_0$ and $0.4\lambda_0$ are considered for them. The introduced values are in the range of small perturbation [25]. In both cases, the scattering results of the structure with buried object and without it are compared. The incident wave is $V = \theta$ polarized with $E_\theta = 1V\text{=}m$, $f_{center} = 300$ MHz, and $f_{max} = 600$ MHz that illuminates the structure normally. As it can be observed in Fig. 6, the change in correlation length does not lead to significant variations in σ. The same result was obtained by Sarabandi et al. in [28].

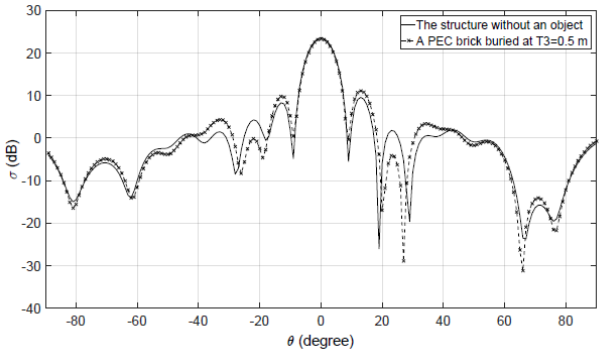

(a)

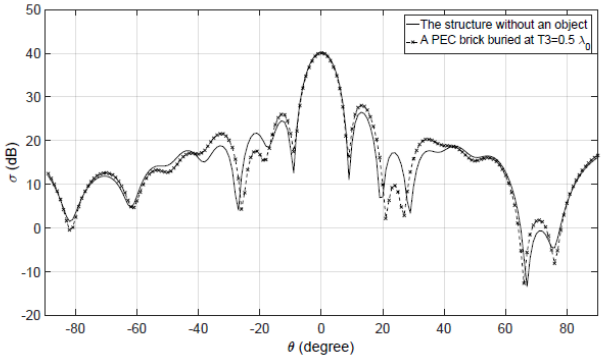

(b)

Fig. 6. Co-polorized scattering coefficient (VV) variation versus observation angle: (a) $l_x = l_y = 0.2\lambda_0$, (b) $l_x = l_y = 0.4\lambda_0$. Ground parameters are $h = 0.1\lambda_0$, $T_1 = 0.4\lambda_0$ with $\epsilon_2 = 4.5\text{-}j0.6$ and $T_2 = 1.3\lambda_0$ with $\epsilon_3 = 6.5\text{-}j0.798$. The incident wave is Gaussian with $1V\text{=}m$ amplitude and a $1\lambda_0 \times 1\lambda_0 \times 0.6\lambda_0$ PEC brick is located at $T_3 = 0.5\lambda_0$.

C. Case study III

Here we study the impact of rms height (h) of the upper rough surface on the scattering coefficient (σ). In order to investigate the effect of this parameter, rms height of the first layer is set to two values: $0.3\lambda_0$ and $3\lambda_0$. The rms height of the lower rough layer is kept constant and equal to $0.1\lambda_0$.

Layers thicknesses are $T_1 = 3.30\lambda_0$ and $T_2 = 3.0\lambda_0$, also $l_x = l_y = 0.1\lambda_0$. A $1\lambda_0 \times 1\lambda_0 \times 0.6\lambda_0$ PEC brick is buried at $T_3 = 3.50\lambda_0$. The incident wave is a Gaussian one with 1 *V/m* amplitude which excites the structure normally. Figure 7 shows the variation of scattering coefficient as the roughness is increasing. It can be seen that when the rms height of the upper layer is increased, the maximum level of σ is decreased. This observation means that the increase in rms height can make detecting the object more difficult. It should be noted that based on both Fig. 7 (a) and Fig. 7 (b), at some angles the difference between two curves are more than other observation angles.

D. Case study IV

In this step, the effect of content moisture of a specific soil on σ is investigated. Electromagnetically, a soil layer has four components; air, bulk soil, bound water and free water. Apparently, the complex constant of soil dielectric constant depends on the frequency. In addition, the physical temperature, the salinity, the total volumetric water content, the relative fractions of bound and free water, the bulk soil density, the shape of the soil particles, and the shape of water inclusions affects the complex dielectric constant of any soil [29].

From [29], the moisture of soil (Wv) is defined as the product of the gravimetric moisture content (Wm) and bulk density of the dry soil sample. Please note that, the gravimetric moisture content (Wm) is defined as: [(wet soil weight)-(dry soil weight)] / (dry soil weight).

We chose the upper layers soil in Fig. 1 to be similar to the soil studied in [28]. Table 2 shows its dielectric constant versus different moisture percentages.

Consider the structure with these parameters: $h = 0.1\lambda_0$, $T_1 = 0.4\lambda_0$ with the permittivity defined in Table 2, and $T_2 = 1.30$ with $\epsilon_3 = 6.5\text{-}j0.798$. Incident wave is again a Gaussian wave with 1 *V/m* which illuminates the model normally. A $1\lambda_0 \times 1\lambda_0 \times 0.6\lambda_0$ PEC brick is also located at $T_3 = 0.5\lambda_0$. Figure 8 shows the scattering coefficients of the structure with and without the object having the upper layer moisture level of 2.4%.

Table 2: Moisture percentage of a typical soil given in [28] and its dielectric constant

Wv (%)	Dielectric Constant
0	$3.3 - j0.35$
2.4	$3.8 - j0.50$
7.3	$4.4 - j0.63$
12	$5.1 - j0.80$
18	$8.2 - j0.40$
24	$9.8 - j1.65$
34	$15.4 - j1.65$
39	$27.1 - j2.90$

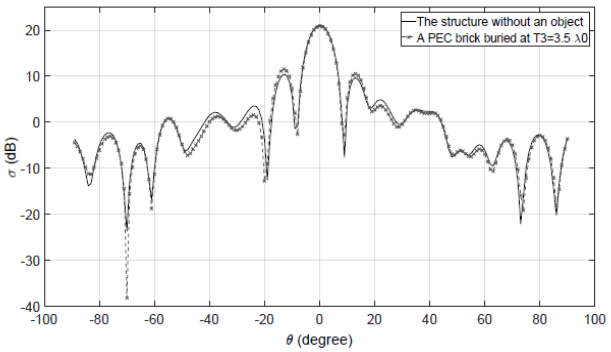

(a)

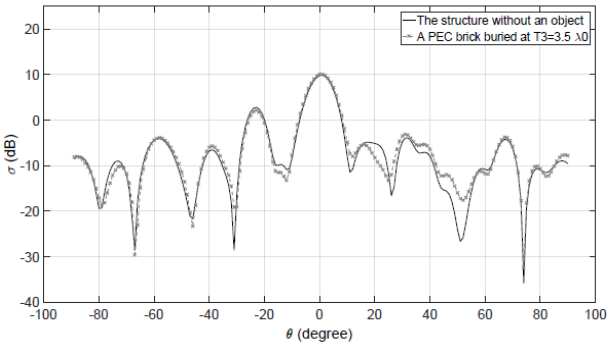

(b)

Fig. 7. Scattering coefficients for: (a) $h = 0.3\lambda_0$, and (b) $h = 3.0\lambda_0$. The structure parameters are $l_x = l_y = 0.1\lambda_0$, $h = 0.1\lambda_0$, $T_1 = 3.3\lambda_0$ with $\epsilon_2 = 4.5\text{-}j0.6$ and $T_2 = 3.0\lambda_0$ with $\epsilon_3 = 6.5\text{-}j0.798$. The incident wave is a perpendicular Gaussian with amplitude $1V/m$ and $1\lambda_0 \times 1\lambda_0 \times 0.6\lambda_0$ PEC brick is located at $T_3 = 3.5\lambda_0$.

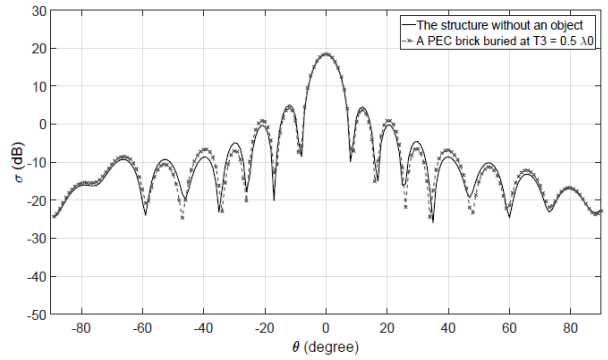

Fig. 8. VV scattering coefficient of the structure with 2.4% moisture versus observation angle for the structure without buried object, and with buried PEC brick at $T_3 = 0.5\lambda_0$ when the incident angle is normal, and background parameters are $l_x = l_y = 0.1\lambda_0$, $h = 0.1\lambda_0$, $T_1 = 0.4\lambda_0$, $T_2 = 1.3\lambda_0$, with $\epsilon_2 = 3.8\text{-}j0.50$ and $\epsilon_3 = 6.5\text{-}j0.798$.

The same process of calculating σ is done for the same structure, but with different moisture defined in Table 2. In this study, no buried object is considered and σ of the structure for different moisture percentages are compared. It is observed that by increasing the amount of moisture, the level of scattering coefficient is increased (Fig. 9). This result is due to the effect of the moisture; it means that the higher percentage of water in soil reflects the waves more, and consequently increases the level of scattering coefficients.

The interesting point is that when the moisture percentage is changed up to 12%, the increase in σ is not as much as when the moisture increased after 18%. Also, the difference between the results in the presence of an object and it absence becomes less than 0.1 dB for 18% moisture (not shown here). In other words, as the moisture increases, two curves in Fig. 8 become more indistinguishable, and buried object detection becomes more difficult.

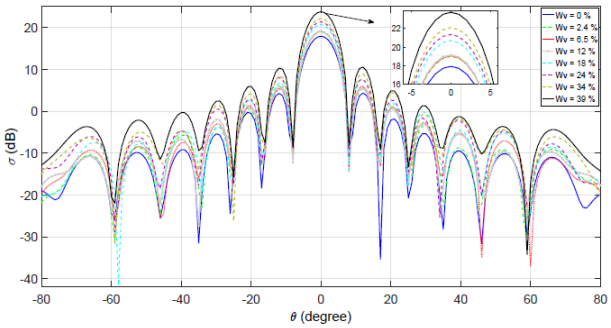

Fig. 9. VV Co-polarized scattering coefficient from a structure without object versus the level of first layer moisture level. The structure parameters are $l_x = l_y = 0.1\lambda_0$, $h = 0.1\lambda_0$, $T_1 = 0.4\lambda_0$ and $T_2 = 1.3\lambda_0$ with $\epsilon_3 = 6.5\text{-}j0.798$; the incident wave is $1V/m$ normal Gaussian pulse.

E. Case study V

To give the reader a visualized perspective in regards to what is done, three cubes with the same sizes ($0.5\lambda_0 \times 0.5\lambda_0 \times 0.5\lambda_0$) but different materials are buried beneath the structure in a surface which is parallel to the surface of rough interfaces in an equilateral triangular form with $2\lambda_0$ side. The depth of these three cubes is $0.5\lambda_0$. The structure is shown in Fig. 10 (a). Cube 1 is a perfect conductor with $\sigma_1 = \text{inf}$, cube 2 is a lossy object with $\epsilon_2 = 2.9$ and $\sigma_2 = 4.3 \times 10^{-1}$, and cube 3 has $\epsilon_3 = 2.9$ and $\sigma_3 = 4.3 \times 10^{-5}$.

Figure 10 (b) is captured from the top of the first surface while looking into the medium. If the reflected waves are observed versus time; first, reflected waves from the first rough surface are received; thereafter, the reflected waves from these three cubes are observed after a while. As it is shown in Fig. 10 (b) (the image is captured when the reflections from the cubes are received) the pec cube (cube 1) has reflected the waves more than other cubes. Cube 2 which its material is different from the background's material ($\sigma = 4.3 \times 10^{-5}$)

is detectable (more wave reflections) but cube 3 which shares the same material with the background cannot be observed easily. In sum, it can be concluded that up to a specific level of similarity between the buried objects and the background, they can be detected; thereafter, it would be difficult to distinguish them from the medium. In addition, as it can be seen from the reflected waves coming from the cubes, if the objects are close to each other the coupling between them will produce ambiguities in term of the exact shape of the buried object.

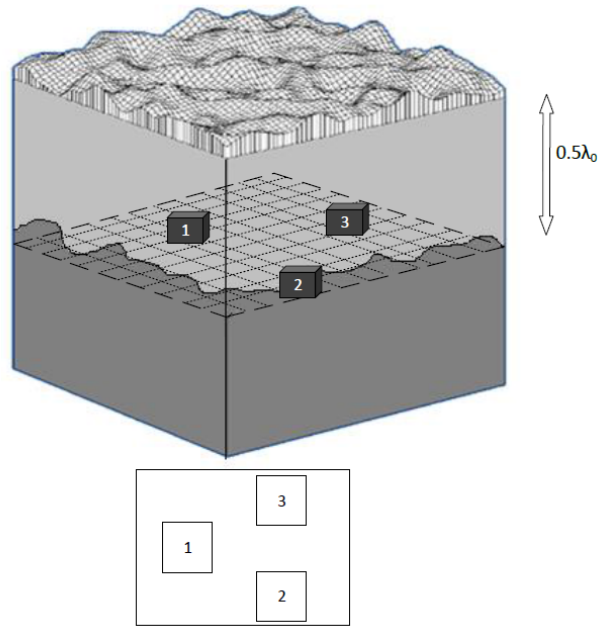

(a)

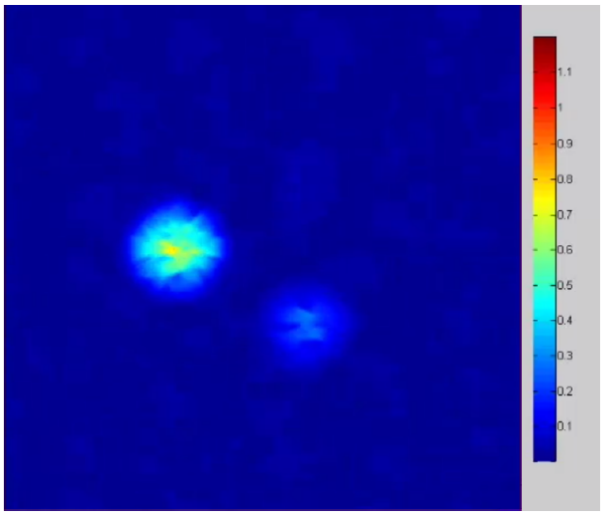

(b)

Fig. 10. (a) The structure which includes three cubes with the same size ($0.5\lambda_0$), but different materials. (b) Reflected waves captured from the top of the model when the reflection from the cubes are obtained, while looking into the depth of the system.

V. CONCLUSION

This paper was devoted to investigate the effect of some important parameters of a two layered rough surfaces medium with buried object(s) on the scattering coefficients. In the first attempt; after convergence check, the implemented code was verified by CST Microwave Studio. Studying different cases showed that when the object is placed at a deeper location, its effect on scattering coefficient becomes insignificant. Also, as the buried object size gets bigger, the scattering coefficient can be distinguished from scattering of the structure without any object. However, the effect of sharp objects such as a cube or a rectangular is more than those of smoother objects like a sphere. In another attempt, it was discussed that changing the size of correlation length in small perturbation regime had no significant effects on the results. Other observation was about the increase in rms height that could make detecting the object more difficult. Finally, it was observed that different moisture levels of soil had different effects on the scattering results. Lower moisture had lower scattering coefficient and when the moisture increased, the σ level increased. In addition, it was observed that increasing the scattering coefficient was more significant at moistures more than approximately 12%. In other words, a same amount of change but in different levels of soil moisture has completely different effects on σ.

ACKNOWLEDGMENT

The authors would like to acknowledge Dr. Hasan Zamani and Dr. Mehdi Rabbani (both are with Amirkabir University of Technology) because of their valuable supports and ideas while doing this work

REFERENCES

[1] D. E. Lawrence and K. Sarabandi, "Electromagnetic scattering from a dielectric cylinder buried beneath a slightly rough surface," *IEEE Transactions on Antennas and Propagation*, vol. 50, no. 10, pp. 1368-1376, 2002.

[2] M. A. Fiaz, F. Frezza, L. Pajewski, C. Ponti, and G. Schettini, "Scattering by a circular cylinder buried under a slightly rough surface: The cylindrical-wave approach," *IEEE Transactions on Antennas and Propagation*, vol. 60, no. 6, pp. 2834-2842, 2012.

[3] J. T. Johnson and R. J. Burkholder, "Coupled canonical grid/discrete dipole approach for computing scattering from objects above or below a rough interface," *IEEE Transactions on Geoscience and Remote Sensing*, vol. 39, no. 6, pp. 1214-1220, 2001.

[4] C. H. Kuo and M. Moghaddam, "Scattering from multilayer rough surfaces based on the extended boundary condition method and truncated singular

value decomposition," *IEEE Transactions on Antennas and Propagation*, vol. 54, no. 10, pp. 2917-2929, 2006

[5] V. Jandhyala, "Fast multilevel algorithms for the efficient electromagnetic analysis of quasi-planar structures," *Department of Electrical and Computer Engineering, University of Illinois at Urbana-Champaign*, 1998.

[6] V. Jandhyala, B. Shanker, E. Michielssen, and W. C. Chew, "Fast algorithm for the analysis of scattering by dielectric rough surfaces," *JOSA A*, vol. 15, no. 7, pp. 1877-1885, 1998.

[7] M. El-Shenawee, C. Rappaport, E. L. Miller, and M. B. Silevitch, "Three-dimensional subsurface analysis of electromagnetic scattering from penetrable/PEC objects buried under rough surfaces: Use of the steepest descent fast multipole method," *IEEE Transactions on Geoscience and Remote Sensing*, vol. 39, no. 6, pp. 1174-1182, 2001.

[8] H. T. Chen and G.-Q. Zhu, "Model the electromagnetic scattering from three-dimensional PEC object buried under rough ground by mom and modified PO hybrid method," *Progress In Electromagnetics Research*, vol. 77, pp. 15-27, 2007.

[9] H. Ye and Y.-Q. Jin, "A hybrid analytic-numerical algorithm of scattering from an object above a rough surface," *IEEE Transactions on Geoscience and Remote Sensing*, vol. 45, no. 5, pp. 1174-1180, 2007.

[10] A. K. Fung, M. R. Shah, and S. Tjuatja, "Numerical simulation of scattering from three-dimensional randomly rough surfaces," *IEEE Transactions on Geoscience and remote sensing*, vol. 32, no. 5, pp. 986-994, 1994.

[11] J. He, T. Yu, N. Geng, and L. Carin, "Method of moments analysis of electromagnetic scattering from a general three-dimensional dielectric target embedded in a multilayered medium," *Radio Science*, vol. 35, no. 2, pp. 305-313, 2000.

[12] M. El-Shenawee, "Polarimetric scattering from two-layered two dimensional random rough surfaces with and without buried objects," *IEEE Transactions on Geoscience and Remote Sensing*, vol. 42, no. 1, pp. 67-76, 2004.

[13] K. Yee, "Numerical solution of initial boundary value problems involving Maxwell's equations in isotropic media," *IEEE Transactions on Antennas and Propagation*, vol. 14, no. 3, pp. 302-307, 1966.

[14] L. Kuang and Y.-Q. Jin, "Bistatic scattering from a three-dimensional object over a randomly rough surface using the FDTD algorithm," *IEEE Transactions on Antennas and Propagation*, vol. 55, no. 8, pp. 2302-2312, 2007.

[15] L.-X. Guo, J. Li, and H. Zeng, "Bistatic scattering from a three dimensional object above a two-dimensional randomly rough surface modeled with the parallel FDTD approach," *JOSA A*, vol. 26, no. 11, pp. 2383-2392, 2009.

[16] S. Mirjahanmardi, A. Tavakoli, H. Zamani, and P. Dehkhoda, "Electromagnetic scattering from a buried sphere in a two-layered rough ground," in *Antennas and Propagation & USNC/URSI National Radio Science Meeting, 2015 IEEE International Symposium on. IEEE*, pp. 506-507, 2015.

[17] S. Mirjahanmardi, A. Tavakoli, and P. Dehkhoda, "Bistatic scattering from a buried object in a two-layered media with two rough interfaces using FDTD," *ISSEEM*, 2014.

[18] A. Z. Elsherbeni and V. Demir, "The finite-difference time-domain method for electromagnetics with MATLAB simulations," *The Institution of Engineering and Technology*, 2016.

[19] U. S. Inan and R. A. Marshall, *Numerical Electromagnetics: The FDTD Method*. Cambridge University Press, 2011.

[20] A. Taflove and S. C. Hagness, *Computational Electrodynamics*. Artech House, 2005.

[21] R. Courant, K. Friedrichs, and H. Lewy, "On the partial difference equations of mathematical physics," *California Univ. Los Angeles*, Tech. Rep., 1959.

[22] J. A. Roden and S. D. Gedney, "Convolutional PML (CPML): An efficient FDTD implementation of the CFS-PML for arbitrary media," *Microwave and Optical Technology Letters*, vol. 27, no. 5, pp. 334-338, 2000.

[23] C. A. Balanis, *Antenna Theory: Analysis and Design*. John Wiley & Sons, 2016.

[24] L. Tsang, J. A. Kong, K.-H. Ding, and C. O. Ao, *Scattering of Electromagnetic Waves, Numerical Simulations*. John Wiley & Sons, vol. 25, 2004.

[25] J.-J. Wu, "Simulation of rough surfaces with FFT," *Tribology International*, vol. 33, no. 1, pp. 47-58, 2000.

[26] J. C. Rautio, "The microwave point of view on software validation," *IEEE Antennas and Propagation Magazine*, vol. 38, no. 2, pp. 68-71, 1996.

[27] CST Microwave Studio, ver. 2010, Computer Simulation Technology, Framingham, MA, 2010.

[28] K. Sarabandi and T. Chiu, "Electromagnetic scattering from slightly rough surfaces with inhomogeneous dielectric profiles," *IEEE Transactions on Antennas and Propagation*, vol. 45, no. 9, pp. 1419-1430, 1997.

[29] M. T. Hallikainen, F. T. Ulaby, M. C. Dobson, M. A. El-Rayes, and L.-K. Wu, "Microwave dielectric behavior of wet soil-part 1: Empirical models and experimental observations," *IEEE Transactions on Geoscience and Remote Sensing*, no. 1, pp. 25-34, 1985.

Seyed Hossein Mirjahanmardi received his bachelor and master degrees (with honors) from Shiraz University and Amirkabir University of Technology, respectively. He has worked on numerical electromagnetic methods such as finite difference time domain to evaluate the scattering of rough surfaces structures. He is currently perusing his Ph.D. in Microwave Imaging at the University of Waterloo.

Parisa Dehkhoda received the B.S. degree from Tehran University, Tehran, Iran, and the M.S. and Ph.D. degrees from the Amirkabir University of Technology, Tehran, Iran, all in Electrical Engineering. She is currently an Assistant Professor in the Electrical Engineering Department, Amirkabir University of Technology. Her research interests include electromagnetic compatibility, scattering and inverse scattering, and microstrip antennas.

Ahad Tavakoli was born in Tehran, Iran, on March 8, 1959. He received the B.S. and M.S. degrees from the University of Kansas, Lawrence, KS, USA, in 1982 and 1984, respectively, and the Ph.D. degree from the University of Michigan, Ann Arbor, MI, USA, in 1991, all in Electrical Engineering. Currently, he is a Professor with the Department of Electrical Engineering, Amirkabir University of Technology, Tehran, Iran. His research interests include electromagnetic compatibility, scattering of electromagnetic waves, and microstrip antennas.

Left-Handed Metamaterial Lens Applicator with Built-in Cooling Feature for Superficial Tumor Hyperthermia

Yonghui Tao [1], Erfu Yang [2], and Gang Wang [3]

[1] Department of Electronic and Information Engineering
Jinling Institute of Technology, Nanjing, 211169, China
yhtao87@jit.edu.cn

[2] Space Mechatronic Systems Technology Laboratory (SMeSTech), Strathclyde Space Institute
Department of Design, Manufacture and Engineering Management, University of Strathclyde
704 James Weir Building, 75 Montrose Street, Glasgow G1 1XJ, United Kingdom
erfu.yang@strath.ac.uk

[3] Key Laboratory of Electromagnetic Space Information
Department of Electronic Engineering and Information Science
University of Science and Technology of China, Hefei, 230026, China
gwang01@ustc.edu.cn

Abstract ─ In all hyperthermia schemes with left-handed metamaterial (LHM) lens applicator, water bolus are used to prevent skin from being overheated during the hyperthermia treatment. Owing to water's high refraction index, high reflection usually occurs at the interface between low-index LHM lens and water bolus, and between water and skin, which will lead to the low efficiency of hyperthermia. In this paper, we propose a new LHM lens applicator with built-in cooling feature for superficial tumor hyperthermia. Both simulation and experiment demonstrated that microwave hyperthermia with the proposed applicator may concentrate more microwave energy into deeper tissue if compared to hyperthermia with normal LHM lens.

Index Terms ─ Hyperthermia, metamaterial lens, microwave, tumor, water bolus.

I. INTRODUCTION

Left-handed metamaterials (LHM) lens provide new prospects for hyperthermia treatment of superficial tumors. Superficial tumors generally occur at depth no more than several centimeters beneath the skin [1], which is within the near-field focusing depth of LHM lens.

Although losses of LHM will destroy Pendry's perfect lens [2], applicators with LHM lens are still very attractive to superficial tumor hyperthermia for two reasons. First, super-resolved focus of LHM lens characterized by half-power beam-width has been demonstrated in several experiments [3-6] with low-loss LHM slabs. It is the microwave power within half-power beam-width, not within the beam-width charactering the LHM lens resolution defined in [2], which makes dominant contribution to hyperthermia of tumor. Second, a focusing spot of moderate size in tissue is preferred for heating a large or diffusive superficial tumor. Tiny focal spots of LHM applicator, if acquired, will find application in tumor ablation or hyperthermia of early small size tumors.

Potentials of LHM lens applicator for tumor hyperthermia have been demonstrated both numerically and experimentally [7-9]. Furthermore, potential of conformal hyperthermia with LHM applicator was also demonstrated [10]. Due to flexibility of focal point adjustment in both lateral and depth directions of a flat LHM lens, it is reasonable that a relatively large heating zone in tissue can be readily generated if we deploy several microwave sources (antennas) behind a flat LHM lens applicator, and a tilted heating zone in tissue, viz.; a heating zone in tissue with different depth of penetration across the array, can be obtained by properly adjusting the distance between the lens and sources. In [11], it is further demonstrated that conformal hyperthermia with low-loss LHM lens applicator can be realized by generating a tilted heating zone in tissue. In addition to adjusting the source-to-lens distance, we find that adjusting the phase of microwave sources may also control the inclination of heating zone.

All these hyperthermia with low-loss LHM lens applicators use water bolus to prevent skin from being overheated during the hyperthermia treatment. As is well-known, water has a refraction index higher than

Submitted On: May 1, 2017
Accepted On: October 4, 2017

skin, and it is generally hard to build LHM lens with high effective refraction index. Therefore, high reflection usually occurs at the interface between low-index LHM lens and water bolus, and between water and skin, which will lead to the low efficiency of hyperthermia (i.e., to heat a certain tumor, the more time and higher source power are needed).

In this paper, we propose a new LHM lens applicator with built-in cooling feature, i.e., cooling water is filled into partial structures of LHM lens, for superficial tumor hyperthermia. In Section II, hyperthermia with proposed applicator is demonstrated. In Dection III, the design of LHM lens applicator with built-in cooling feature is illustrated. In Section IV, the performance of proposed lens is confirmed by experimental researches.

II. HYPERTHERMIA WITH LHM LENS APPLICATOR WITH BUILT-IN COOLING FEATURE

Figure 1 shows the scheme of conformal hyperthermia with LHM lens applicator proposed in [11]. In this scheme, several microwave sources ($S_1, S_2, \cdots S_n$, *representing antenna phase centers in practice*) may be set behind a flat LHM lens applicator. The LHM lens will focus microwave emitted from source S_i $(i=1,2,...,n)$ at a corresponding focal point F_i $(i=1,2,...,n)$ in tissue. Therefore, different heating zones enclosing focal point F_i $(i=1,2,...,n)$ can be generated. According to LHM lens' focusing theory, the focusing depth dF_i, lens thickness D=4 cm, source-lens distance dS_i and water bolus thickness h=0.5 cm satisfy the equation:

$$\mathrm{d}F_i = (D - \mathrm{d}S_i)/K - h, \tag{1}$$

where K is usually greater than 1, which indicates the influence of the random inhomogeneity of biological tissue and microwave attenuation on focusing position. Obviously, as the water bolus between tissue and lens is applied, not only the high reflection is generated, but also the focus depth is directly decreased.

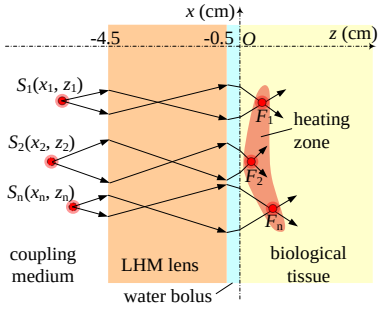

Fig. 1. Conformal hyperthermia scheme with LHM lens applicator proposed in [11].

So we consider a new conformal hyperthermia scheme with LHM lens applicator with built-in cooling feature as shown in Fig. 2. It is observed that in this scheme cooling water with height of h is filled into partial structures of LHM lens. The Equation (1) should be modified to:

$$\mathrm{d}F_i = (D - \mathrm{d}S_i - k_w h)/K, \tag{2}$$

where k_w is generally less than 1, which indicates the influence of cooling water filled in lens structures on focus depth. Obviously, by applying this new applicator the focus depth can be increased, as the high reflections are prevented. By integral optimization of the water bolus and lens structures, the hyperthermia efficiency should be improved.

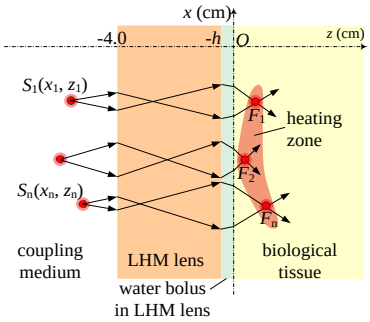

Fig. 2. Conformal hyperthermia scheme with LHM lens applicator with build-in cooling feature.

III. DESIGN OF LHM LENS APPLICATOR WITH BUILT-IN COOLING FEATURE

To facilitate filling water in LHM lens structures, we consider designing the lens based on a volumetric negative refractive-index transmission-line (NRI-TL) metamaterial structure, which is capable of building three-dimensional LHM lens by stacking planar NRI-TL metamaterials in a multilayer manner [12]. Figure 3 depicts the three-dimensional sketch of conformal hyperthermia scheme as NRI-TL metamaterial lens with built-in cooling feature applied. And the electromagnetic simulation software HFSS is used to design the proposed lens.

In simulation, in order to reduce computational costs, the model of partial device including antennas and lens is simplified as shown in Fig. 4. Figure 5 illustrates the model of practical hyperthermia scheme as the proposed LHM lens is applied. It is observed that, to emulate infinite periodicity in the *y* direction, a single NRI-TL metamaterial lens composed of a pair of PCB layers is deployed between two metal plates (simulated by perfect E walls in HFSS model), spaced 1.3 cm apart. And the side walls except the one meets the tissue are set as absorbing boundary (simulated by perfect H walls) to avoid to avoid leak of radiation. A coaxial connector with inner/outer diameter of 1.27 mm/4.1 mm located at

2 cm away from lens is used as the antenna.

The LHM lens is four 4 thick (*z* direction) and 15 cells width (*x* direction). And the initial cell is designed based on the structure presented in [12] and has refractive index of $n_{\text{eff}} = -3.68 + 0.61i$ at 2.45 GHz without built-in cooling water, which means the lens has a size of 4×15 cm. The water with a thick of 0.5 cm, which is the same as the water bolus applied in hyperthermia scheme proposed in [11], is filled in the cell close to tissue.

And then the parameters of lens cell can be optimized by using the automatic optimization function of HFSS. And the electric field distribution can be calculated by using the field calculator of HFSS. Figure 6 (a) shows the electric field distribution in tissue obtained by the hyperthermia scheme with optimized LHM lens. Owing to cavity effects, a hot zone is obtained adjacent to skin. And the maximum electric field amplitude in this zone is measured to be 71.2 V/m. Meanwhile, it is observed that another hot spot is located at the position of 1 cm below skin. And the maximum electric field amplitude in this spot is 41.2 V/m measured at (z=0.96 cm, x=0).

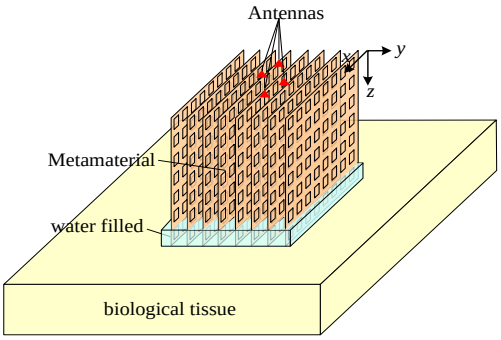

Fig. 3. Three-dimensional sketch of conformal hyperthermia scheme as NRI-TL metamaterial lens with built-in cooling feature applied.

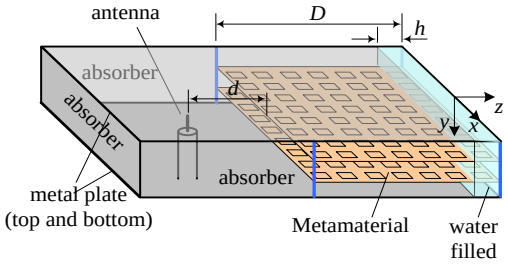

Fig. 4. Simplified model of partial device including antenna and lens.

In order to evaluate the performance of the proposed lens applicator, the electric field distribution obtained in the scheme with conventional LHM lens is also presented in Fig. 6 (b). A light spot is observed at the location of 0.5 cm below skin. The maximum electric field amplitude of 39.7 V/m is measured at (z=0.56 cm, x=0.05 cm). And the field amplitude measured at (z=0.96 cm, x=0) is 11.6 V/m, which is just 28.2% of that measured at the same position as the proposed LHM lens is applied.

In summary, for the same hyperthermia scheme, while the proposed LHM lens applicator is applied, the focusing depth is increased and more microwave energy is concentrated in tissue.

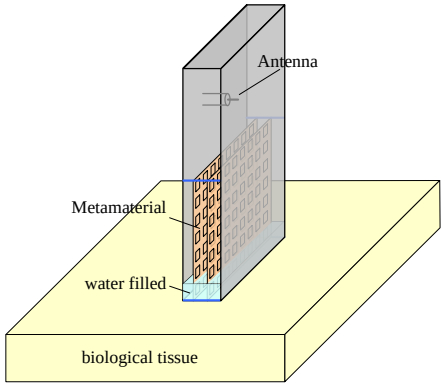

Fig. 5. The simulation model of practical hyperthermia scheme as the LHM lens applicator with built-in cooling feature applied.

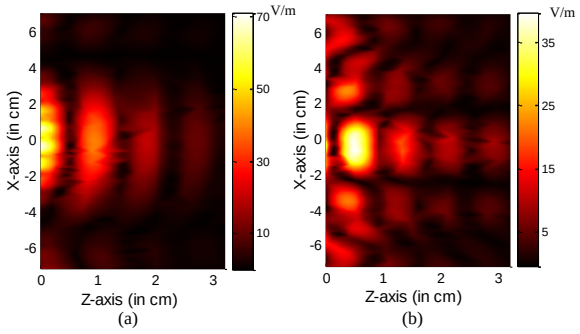

Fig. 6. Electric field distribution in tissue acquired with hyperthermia scheme with: (a) LHM lens applicator with built-in cooling feature, and (b) traditional LHM lens.

To explore whether the proposed lens is suitable for conformal hyperthermia, the performance of this lens is compared with ideal LHM lens applied in [11], as depicted in Table1 1.

In previous works, it is found that the temperature distribution depends on specific absorption rate (SAR) distribution (or power distribution), and SAR over 10% (power over -10 dB) have contribution to heat tumor. In [11], it is indicated that 50% SAR zone (-3 dB power zone) of single source should not be too small to realize

conformal hyperthermia. It is found that the -3 dB width obtained with the proposed lens is more than twice of that acquired by ideal lens. Meanwhile, it is also observed the -3 dB depth decreases greatly owing to cavity effects. But considering the heat generated in skin will be dissipated quickly by circulated cooling water, and the -5 dB depth is close to that acquired by ideal lens, it is concluded the -3 dB depth decreasing could not cause too much deterioration to heat depth. In conclusion, the proposed lens is suitable for conformal hyperthermia.

Table 1: Comparison on the performance of the proposed LHM lens applicator with the ideal LHM lens used in [11]

	Maximum -3 dB Width	-3 dB Depth	-5 dB Depth	-10 dB Depth
Proposed LHM lens	1.81 cm	0.32 cm	1.1 cm	1.32 cm
Ideal LHM lens	0.72 cm	1.05 cm	1.23 cm	2.01 cm

IV. EXPERIMENT WITH LHM LENS APPLICATOR OF BUILT-IN COOLING FEATURE

Experimental setup for testing the performance of LHM lens applicator with built-in cooling feature is depicted in Fig. 7. Coaxial connectors are used as probe and antenna to provide the fixed-point excitations inside the metal plate. And in all experiments, the distance between antenna and lens is fixed to 2 cm. As pictured in Fig. 8, coaxial connectors are connected with two ports of vector network analyzer (VNA) respectively. It is observed that the metal plate with antenna is fixed on a vertical graduated holder, as the other plate with probe is fixed on electric displacement platform (EDP). So just by operating the holder and electric displacement platform, the probe can be moved in the whole focusing zone to measure the transmission coefficient S_{21} between antenna (port 1) and probe (port 2). And then the normalized focusing field can be calculated.

Figure 9 shows the focusing field distribution obtained by LHM lens applicator with 0.3 cm and 0.5 cm built-in cooling feature. Obviously, the thinner the water filled in lens, the more and the deeper the microwave energy can be concentrated in focusing region. Analogously, as depicted in Fig. 10, the thicker the water deployed behind the common LHM lens, the less and the shallower the microwave energy can be focused. And it is found that, at the same thickness of water, the new LHM lens with built-in water acquire higher focusing depth and concentrate more energy in focus region, which mean the focusing performance is improved.

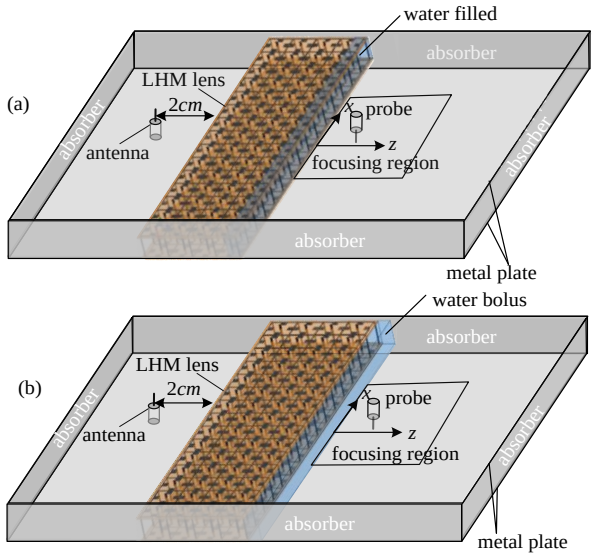

Fig. 7. Diagram of experimental setup including antenna and lens: (a) LHM lens with built-in cooling feature, and (b) common LHM lens.

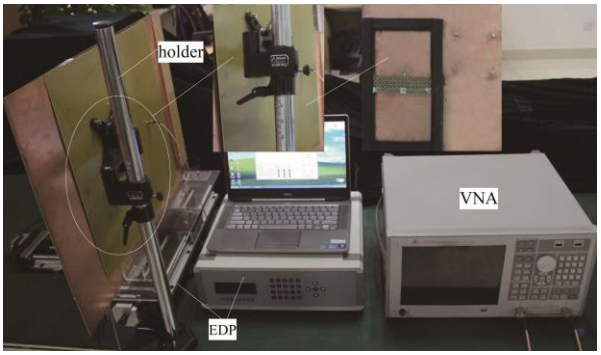

Fig. 8. Picture of the experimental setup.

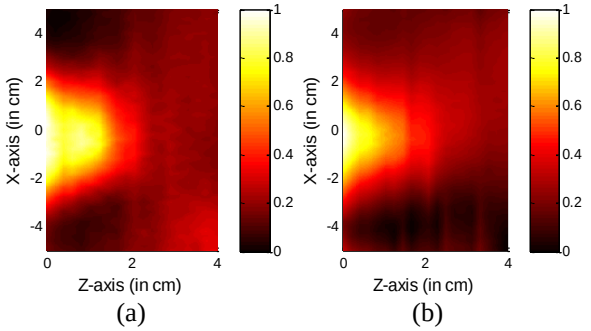

Fig. 9. Electric field distribution in focusing region acquired by applying proposed lens with: (a) 0.3 cm water filled, and (b) 0.5 cm water filled.

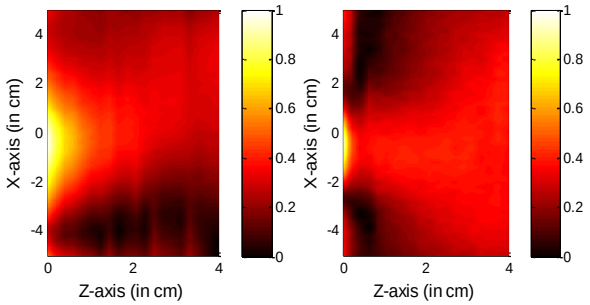

Fig. 10. Electric field distribution in focusing region acquired by applying traditional lens with: (a) 0.3 cm water bolus, and (b) 0.5 cm water bolus behind.

V. CONCLUSION

To avoid the high reflection introduced by cooling water bolus used for preventing skin being overheated during the hyperthermia treatment, we present a new LHM lens applicator with built-in cooling feature. The simulation results indicate that as the normal LHM lens and water bolus are replaced by this new applicator, more microwave energy can be concentrated in tissue and the focus depth is increased, which is supported by further experimental studies.

ACKNOWLEDGMENT

This work is supported by Scientific Research Foundation for Doctors of Jinling Institute of Technology (Grant No. jit-b-201718).

REFERENCES

[1] E. Jones, J. Oleson, L. Prosnitz, T. Samulski, Z. Vujaskovic, D. Yu, L. Sanders, and M. Dewhirst, "Randomized trial of hyperthermia and radiation for superficial tumors," *J. Clinical Oncol*., vol. 23, pp. 3079-3085, 2005.

[2] J. B. Pendry, "Negative refraction makes a perfect lens," *Phys. Rev. Lett*., vol. 85, pp. 3966-3969, 2000.

[3] K. Aydin, I. Bulu, and E. Ozbay, "Subwavelength resolution with a negative-index metamaterial superlens," *Appl. Phys. Lett.*, vol. 90, pp. 254102, 2007.

[4] J. Zhu and G. Eleftheriades, "Experimental verification of overcoming the diffraction limit with a volumetric Veselago-Pendry transmission-line lens," *Phy. Rev. Lett.*, vol. 101, pp. 013902, 2008.

[5] A. K. Iyer and G. V. Eleftheriades, "Mechanisms of subdiffraction free-space imaging using a transmission-line metamaterial superlens: An experimental verification," *Appl. Phys. Lett.*, vol. 92, pp. 131105, 2008.

[6] S. Rudolph, C. Pfeiffer, and A. Grbic, "Design and free-space measurements of broadband, low-loss negative-permeability and negative-index media," *IEEE Trans. Antennas Propagat.*, vol. 59, pp. 2989-2997, Aug. 2011.

[7] G. Wang and Y. Gong, "Metamaterial lens applicator for microwave hyperthermia of breast cancer," *Int. J. Hyperthermia*, vol. 25, pp. 434-455, 2009.

[8] Y. Gong and G. Wang, "Superficial tumor hyperthermia with flat left-handed metamaterial lens," *Prog. Electromagn. Res.*, vol. 98, pp. 389-405, 2009.

[9] M. Velazquez-Ahumada, M. Freire, and R. Marque, "Metamaterial focusing device for microwave hyperthermia," *Microw. Opt. Tech. Lett.*, vol. 53, pp. 2868-2872, 2011.

[10] Y. Tao and G. Wang, "Hyperthermia of large superficial tumor with a flat LHM lens," *IEEE MTT-S International Microwave Symposium*, pp. 1-3, 2012.

[11] Y. Tao and G. Wang, "Conformal hyperthermia of superficial tumor with left-handed metamaterial lens applicator," *IEEE Trans. Biomed. Eng*., vol. 59, no. 12, pp. 3525-3530, 2012.

[12] S. Rudolph, C. Pfeiffer, and A. Grbic, "Design and free-space measurements of broadband, low-loss negative-permeability and negative-index media," *IEEE Trans. Antennas Propagat.*, vol. 59, pp. 2989-2997, Aug. 2011.

Yonghui Tao received her Ph.D. degree from University of Science and Technology of China, Hefei, China, in Engineering Electronic Science and Technology in 2014, the B.S. and M.S. degrees from Jiangsu University, China, in 2008 and 2011, respectively.

From 2015 to 2017, she was with University of Science and Technology of China as a Postdoctoral Research Fellow supported by the Chinese government. She is currently a Lecturer with Jinling Institute of Technology.

Her research interests involve microwave hyperthermia, metamaterials, and passive RFID/Sensor.

Erfu Yang is a Lecturer at the Space Mechatronic Systems Technology Laboratory (SMeSTech) in the Department of Design, Manufacture and Engineering Management (DMEM) at the University of Strathclyde, Glasgow, UK. He received his Ph.D. degree in Robotics

in the interdisciplinary area of Robotics and Autonomous Systems from the University of Essex, Colchester, UK, within the School of Computer Science and Electronic Engineering.

His main research interests include robotics, autonomous systems, mechatronics, manufacturing automation, computer vision, image/signal processing, nonlinear control, process modelling and simulation, condition monitoring, fault diagnosis, multi-objective optimizations, and applications of machine learning and artificial intelligence including multi-agent reinforcement learning, fuzzy logic, neural networks, bio-inspired algorithms, and cognitive computation, etc. He has over 70 publications in these areas, including more than 30 journal papers and 5 book chapters.

Gang Wang received the B.S. degree from University of Science and Technology of China, Hefei, China, in 1988, the M.S. and Ph.D. degrees from Xidian University, Xi'an, China, in Electrical Engineering in 1991 and 1996, respectively.

From 1996 to 1998, he was with Xi'an Jiaotong University as a Postdoctoral Research Fellow supported by the Chinese government. From 1998 to 2000, he was an Associate Professor with Xi'an Jiaotong University. In 2001, he was a Visiting Researcher with the ITM Department of Mid-Sweden University. From 2002 to 2003, he was a Postdoctoral Research Associate with the Department of Electrical and Computer Engineering, University of Florida. From 2003 to 2010, he was with Jiangsu University, China, as a Chair Professor. He is currently a Full Professor with University of Science and Technology of China.

His research interests include ultrawideband electromagnetics, passive RFID/Sensor, metamaterials, and modern optimization techniques for microwave circuit and antenna design.

A Hybrid FEM-GO Approach to Simulate the NSA in an Anechoic Chamber

Qian Xu [1], Yi Huang [2], Xu Zhu [2], Lei Xing [1], Paul Duxbury [3], and John Noonan [3]

[1] College of Electronic and Information Engineering
Nanjing University of Aeronautics and Astronautics, Nanjing, 211106, China
emxu@foxmail.com

[2] Department of Electrical Engineering and Electronics
University of Liverpool, Liverpool, L69 3GJ, United Kingdom
yi.huang@liv.ac.uk

[3] Microwave Vision Group
Haydock, WA 119UY, United Kingdom

Abstract ─ A hybrid FEM-GO method is proposed and a new CAD tool based on it is developed for anechoic chamber simulation. The proposed method can deal with a chamber with arbitrary shape and arbitrary layout of radio absorbing material. The normalized site attenuation values are simulated and match the measurement results well. It is shown that the proposed method is an efficient and effective way for chamber design and simulation.

Index Terms ─ Anechoic chamber, finite element method, geometric optics, normalized site attenuation.

I. INTRODUCTION

Anechoic chambers have been widely used for antenna, radar and electromagnetic compatibility (EMC) measurements and tests. There are three key figures of merit to characterize the performance of anechoic chambers: normalized site attenuation (NSA), field uniformity (FU) and site voltage standing wave ratio (SVSWR) [1-2]. Normally, before a chamber is handed over to the customer, an evaluation test from an independent third-part is necessary. If the test fails to pass the required standards/specs, modifications have to be made which is both time consuming and cost ineffective. Thus, a prediction of the chamber performance during the design process is needed to ensure a good safety margin to pass the requirements.

However, the design of chambers is difficult and heavily dependent on the designer's experience [3]. The radio absorbing material (RAM) is normally expensive and its size is closely linked to its performance and cost. There is a trade-off between the performance and cost, a better RAM (better absorption rate) normally means more expensive and a larger RAM size. The objective of this paper is to develop an efficient and systematic approach for the anechoic chamber designers to estimate the chamber performance accurately during the design process. The ultimate goal is to minimize the cost (optimize the layout of the RAM) and to maximize the chamber performance.

A number of computational electromagnetics (CEM) methods have been used for chamber simulation which can be mainly categorized into two classes: full-wave method and high frequency approximation method. The mesh type, complexity and the electrical size for different methods are summarized in Fig. 1, where *N* means the number of freedoms/unknowns.

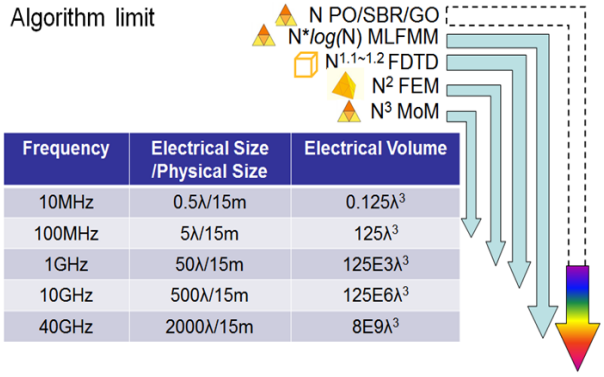

Frequency	Electrical Size /Physical Size	Electrical Volume
10MHz	0.5λ/15m	$0.125\lambda^3$
100MHz	5λ/15m	$125\lambda^3$
1GHz	50λ/15m	$125E3\lambda^3$
10GHz	500λ/15m	$125E6\lambda^3$
40GHz	2000λ/15m	$8E9\lambda^3$

Fig. 1. Comparison of different CEM methods: PO: physical optics; SBR: shooting bouncing ray; GO: geometric optics; MLFMM: multilevel fast multipole algorithm; FDTD: finite-difference time-domain; FEM: finite element method; MoM: method of moment.

For the full-wave method, transmission line matrix (TLM) [4], MoM/FEM (method of moment/finite element method) [5] and FDTD (finite-difference time-domain) [6] have been used to simulate this study. Because the size of chambers is normally electrically large, even

Submitted On: February 2, 2015
Accepted On: June 19, 2017

with a high performance computer, large electrical size problems with complex material scenarios are not easy to solve due to the required large memory and time consumption. Another issue is, in the full-wave method, the detailed material property distribution (as a function of the frequency and depth) should be known, and the antenna 3D structures need to be defined. In the design process, these details may not be completely available.

For the high frequency approximation method, such as the geometric optics (GO) has been proven to be a fast and efficient way to simulate this problem [7-12]. However, the RAM model directly determines the accuracy of the simulated result. The RAM reflectivity has been characterized by using analytical models which include: a cosine approximation [8], an effective medium [13], a homogenization model [14] and a multi-layer model [9]. Thus, the RAM is not fully described and a simplified analytical model over a wide frequency range and a wide incident angle is normally not available. The complexity of the analytical model also reduces the speed of GO, because the reflected field needs to be calculated using complex equations or an iterative method.

In this paper, we hybridize a full-wave method (FEM) and a high frequency method (GO) to realize a systematic approach for the chamber design. In the micro level, the RAM is analyzed using the FEM. By using the periodical boundary condition (PBC) only one RAM element needs to be analyzed. After the FEM analysis is completed, the reflection coefficients of the RAMs are saved in a database. The GO is used to simulate the whole chamber which is electrically large; the local reflection coefficient will be extracted from the database obtained from the FEM. Thus, the FEM and the GO are combined seamlessly. Finally, the simulated results are verified by measurements completed by an independent third party.

II. THEORY

In this section, the proposed hybrid method is introduced with essential details.

A. GO

It is well known that in the GO, the electric field is assumed to propagate like light as shown in Fig. 2. At the boundary of different materials, the wave is reflected and transmitted.

The E-field at the field point can be expressed as [15-16]:

$$\vec{\boldsymbol{E}} = \vec{\boldsymbol{E}}_{\boldsymbol{0}} \cdot \left\{\prod \bar{\bar{\boldsymbol{R}}}_{\boldsymbol{i}}\right\} \cdot \left\{\prod \bar{\bar{\boldsymbol{T}}}_{\boldsymbol{i}}\right\} \cdot \left\{\prod \boldsymbol{e}^{-\gamma_i l_i}\right\} \cdot \boldsymbol{SF}, \qquad (1)$$

where $\boldsymbol{A_0}$ and $\boldsymbol{A}$ in Fig. 2 are the cross-sectional area of the ray tubes at the source point and field point of interest, they will be used to calculate the spreading factor ($\boldsymbol{SF} = \sqrt{\boldsymbol{A_0}}/\sqrt{\boldsymbol{A}}$). $\vec{\boldsymbol{E}}_{\boldsymbol{0}}$ is the E-field at the source point (reference point), $\vec{\boldsymbol{E}}$ is the E-field at the field point. $\prod \bar{\bar{\boldsymbol{R}}}_{\boldsymbol{i}}$ and $\prod \bar{\bar{\boldsymbol{T}}}_{\boldsymbol{i}}$ are the reflection and transmission coefficient dyads along the whole ray path, $\prod \boldsymbol{e}^{-\gamma_i l_i}$ is the total phase variations and losses along the whole path.

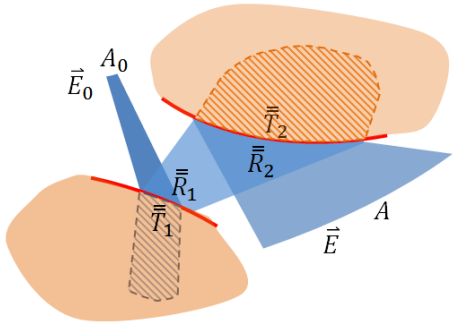

Fig. 2. Wave propagation in GO.

In the anechoic chamber simulation, only reflections are considered. Thus, Equation (1) can be simplified as:

$$\vec{\boldsymbol{E}} = \vec{\boldsymbol{E}}_{\boldsymbol{0}} \cdot \left\{\prod \bar{\bar{\boldsymbol{R}}}_{\boldsymbol{i}}\right\} \cdot \left\{\prod \boldsymbol{e}^{-\gamma_i l_i}\right\} \cdot \boldsymbol{SF}, \qquad (2)$$

where $\bar{\bar{\boldsymbol{R}}}$ relates the incident field $\vec{\boldsymbol{E}}^{\boldsymbol{i}}$ and reflected field $\vec{\boldsymbol{E}}^{\boldsymbol{r}}$ as:

$$\vec{\boldsymbol{E}}^{\boldsymbol{r}} = \begin{bmatrix} \boldsymbol{E}^{\boldsymbol{r}}_{\parallel} \\ \boldsymbol{E}^{\boldsymbol{r}}_{\perp} \end{bmatrix} = \bar{\bar{\boldsymbol{R}}} \cdot \vec{\boldsymbol{E}}^{\boldsymbol{i}} = \begin{bmatrix} \boldsymbol{R}_{\parallel\parallel} & \boldsymbol{R}_{\parallel\perp} \\ \boldsymbol{R}_{\perp\parallel} & \boldsymbol{R}_{\perp\perp} \end{bmatrix} \begin{bmatrix} \boldsymbol{E}^{\boldsymbol{i}}_{\parallel} \\ \boldsymbol{E}^{\boldsymbol{i}}_{\perp} \end{bmatrix}, \qquad (3)$$

where $\boldsymbol{E}_{\parallel}$ and $\boldsymbol{E}_{\perp}$ are the decomposed parallel component and perpendicular component of the E-field (Fig. 3).

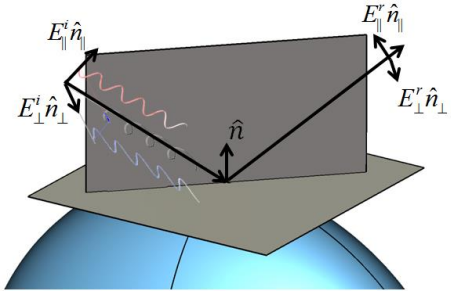

Fig. 3. Decomposed incident and reflected waves.

When the GO is applied to the anechoic chamber scenario, as shown in Fig. 4, the rays between the transmitting (Tx) antenna and the receiving (Rx) antenna need to be found out [17]. Once the routes of the rays are known, the incident angles are known, Equation (3) will be used to calculate the reflected field. Finally, the vector superposition is performed at the Rx antenna to calculate the total E-field.

There are issues to be carefully treated. When the ray is launched from the Tx antenna, an initial E-field $\vec{\boldsymbol{E}}_{\boldsymbol{0}}$ needs to be determined. This requires the radiation pattern of the antenna to be known, we consider the radiation pattern as a function of $(\boldsymbol{\theta}, \boldsymbol{\varphi})$, then an interpolation is implemented for an arbitrary launching angle.

Another issue is that $\overline{\overline{\boldsymbol{R}}}$ needs to be determined; we may have different RAM types in a chamber. Since the reflection coefficient is a complex number, and it is related to the incident angle, frequency and polarization. It is noted in Equation (3), $\overline{\overline{\boldsymbol{R}}}$ includes four elements: $\boldsymbol{R}_{\parallel\parallel}$, $\boldsymbol{R}_{\parallel\perp}$, $\boldsymbol{R}_{\perp\parallel}$ and $\boldsymbol{R}_{\perp\perp}$, they can be considered as a function of incident angle and frequency $\boldsymbol{R}_{ij} = \boldsymbol{R}_{ij}(\boldsymbol{\theta}, \boldsymbol{\varphi}, \boldsymbol{f})$ (i, j can be $\parallel$ or $\perp$). We use a 3D matrix to save each element in the database. In the next section, the FEM is used to obtain the $\overline{\overline{\boldsymbol{R}}}(\boldsymbol{\theta}, \boldsymbol{\varphi}, \boldsymbol{f})$ for different types of RAM. The workflow is shown in Fig. 5, we use the triangular surface mesh in the model described by .stl file [18].

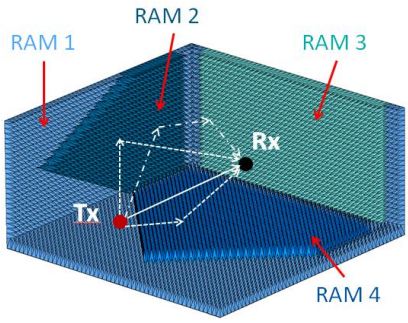

Fig. 4. GO rays in an anechoic chamber with four different types of RAM.

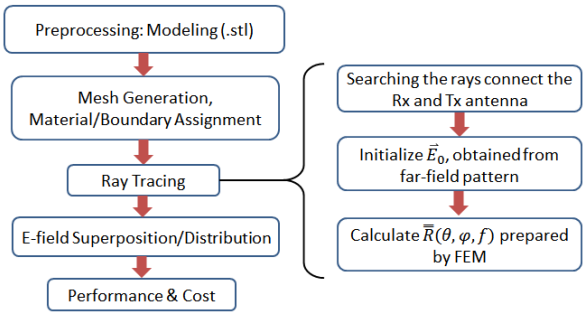

Fig. 5. The workflow of the FEM-GO.

B. FEM analysis

The FEM analysis is performed before the rays are launched, and only need to be analyzed once for each material. All the data obtained from the FEM simulation will be saved in a database/matrix which will be used by the GO.

It should be noted that the reflection coefficient $\overline{\overline{\boldsymbol{R}}}$ can be obtained from measurement using the arch method [19]. It can also be obtained from simulation; the simulation model in the FEM is shown in Fig. 6. By applying the PBC, only one unit cell needs to be analyzed [20]. For each incident angle, two orthogonal incident waves/modes need to be analyzed, shown in Fig. 7. Frequency sweep is adopted for each incident angle. When all the simulation/measurements are finished, $\overline{\overline{\boldsymbol{R}}}$ is ready. Since we can only simulate some discrete incident angles, for an arbitrary incident angle, the reflection coefficient can be obtained using interpolation.

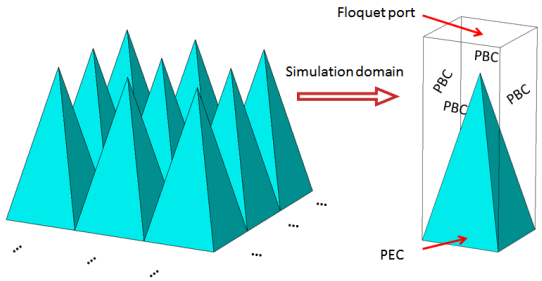

Fig. 6. The simulation model of the pyramid absorber.

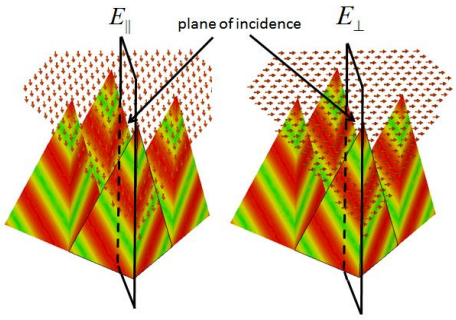

Fig. 7. Two orthogonal incident waves/modes.

A typical value of $\overline{\overline{\boldsymbol{R}}}$ at 3 GHz is shown in Fig. 8 (magnitude) and Fig. 9 (phase) with different incident angles. A 5° step is used for both $\boldsymbol{\theta}$ and $\boldsymbol{\varphi}$ directions, for other values 2D interpolation is used; note that at the edge of the figure (large incident angle) the transition is not very smooth, this is because we have used the nearest available value to interpolate it.

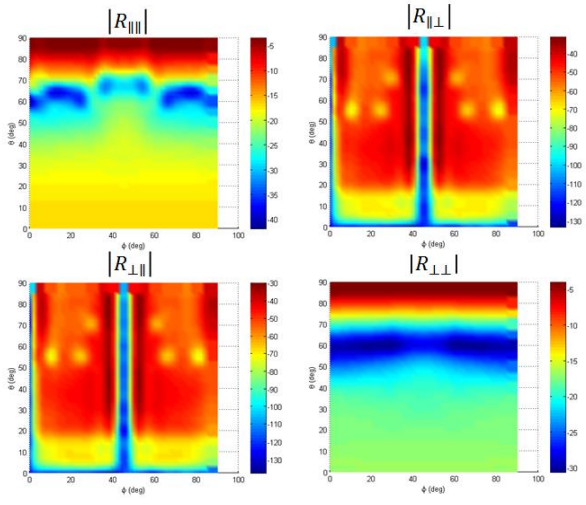

Fig. 8. Typical magnitude values of each element of $\overline{\overline{\boldsymbol{R}}}$; unit: dB.

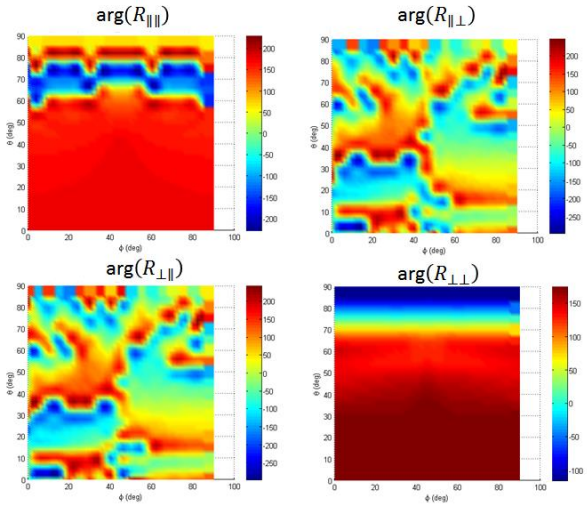

Fig. 9. Typical phase values of each element of $\overline{\overline{\boldsymbol{R}}}$; unit: degree.

C. NSA definition

After the FEM-GO analysis is finished, the NSA values can be extracted from the E-field distribution. The test scenario is shown in Fig. 10. The measurement distance can be 3 m, 10 m or 30 m, depending on the relevant standards. The radiation power is assumed to be 1 W and the NSA value can be obtained from [21]:

$$\boldsymbol{NSA_{dB} = 46.76 + Gain(dBi) - 20\log(f) - 20\log(E_{max})}, \quad (4)$$

where f is the frequency of interest in MHz, $\boldsymbol{E_{max}}$ is the maximum magnitude of the electric field strength in V/m at the location of receiving antenna by scanning the height from 1 m to 4 m.

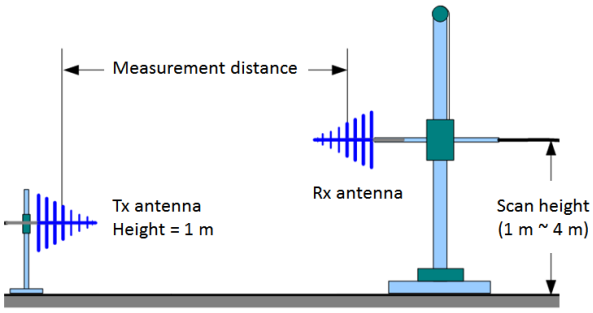

Fig. 10. NSA measurement setup.

III. SIMULATION AND MEASUREMENTS

The simulation and verification for an ideal chamber has been done and a very good agreement has been obtained in [22]. In this paper, we compare the simulated results and the measured results for a real chamber.

The size of the selected chamber is 9 m × 6 m × 6 m ($L \times W \times$ H). It is shown in Fig. 11 (a), which is a semi-anechoic chamber for EMC tests and the simulation model is given in Fig. 11 (b). Three different types of RAMs are used which are shown in different colors. Triangular meshes are used to represent the chamber, the mesh number is 70.

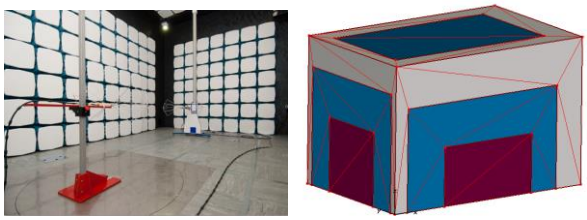

(a) (b)

Fig. 11. (a) Test chamber and (b) the simulation model.

The test scenarios are shown in Fig. 12 and listed in Table 1. Four different locations of the Rx antenna in the turntable region are tested: left (L), right (R), front (F), and center (C). At each location, there are two height values and two polarizations for the Tx antenna. These make 2 × 2 × 4 = 16 cases in total.

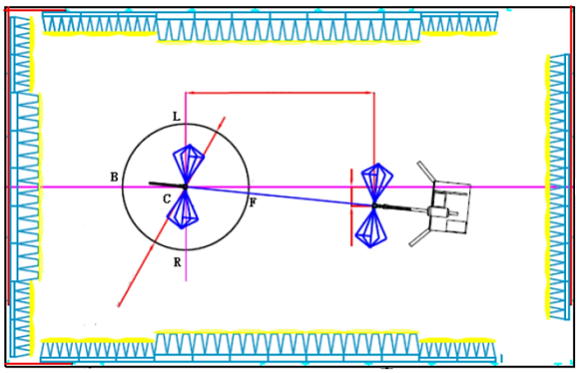

Fig. 12. Test scenarios with Tx and Rx antenna.

Table 1: NSA test scenarios

Polarization	Height	Tx Position
Horizontal (H)	Lower (L)	Center (C)
		Front (F)
Vertical (V)	Upper (U)	Right (R)
		Left (L)

The simulation time for each scenario is around 2 minutes on a standard personal computer; the memory consumption is around 600 MB. The rays between the Tx and Rx (two height values) antennas are shown in Fig. 13.

A typical result is shown in Fig. 14, the limit in the CISPR standard [1] is also given in the same figure. As can be seen, they are in a very good agreement. We have also compared the NSA values of all 16 cases, all the errors are in the range of ±2 dB.

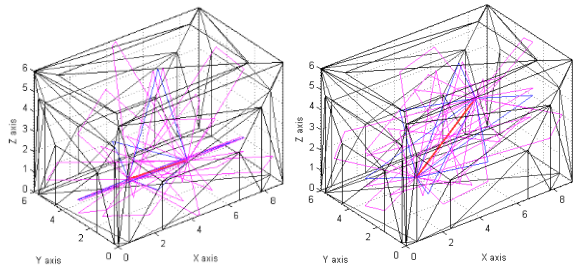

Fig. 13. (a) Rx antenna height is 1 m; (b) Rx antenna height is 4 m.

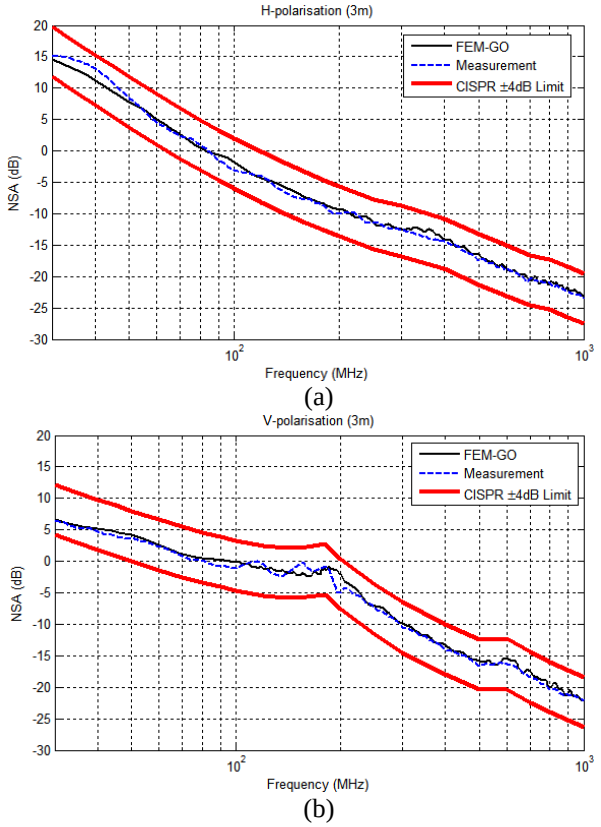

Fig. 14. Simulated and measured NSA values for the lower height, left Tx antenna position in Table 1. (a) Horizontal polarization and (b) vertical polarization.

IV. CONCLUSION

A systematic approach has been proposed in this paper for anechoic chamber performance prediction and analysis, which combines both the full-wave method (FEM) and the high frequency approximation method (GO). It has been shown that the proposed method is efficient and accurate for the anechoic chamber simulation and suitable for real work chamber design. The results from simulation and measurement show that the error was smaller than ± 2 dB over the whole frequency range.

It should be noted that although GO is very fast, prepared data from the FEM is needed. To obtain $\bar{\bar{R}}$ at different incident angle, polarization, frequency is time consuming. However, this kind of simulation/arch measurement needs to be done only once. After it is finished the data can be reused, which saves much computing time compared with other methods.

Future work may include more detailed research on different kinds of chambers (e.g., tapered, compact chambers) and the limitation of the hybrid method.

ACKNOWLEDGMENT

This project was supported in part by the Center for Global Eco-Innovation with project No. 139 and MVG (Microwave Vision Group), National Natural Science Foundation of China (61701224 and 61601219) and Nature Science Foundation of Jiangsu Province (BK20160804).

REFERENCES

[1] CISPR 16-1-4: *Specification for Radio Disturbance and Immunity Measuring Apparatus and Methods - Part 1-4: Radio Disturbance and Immunity Measuring Apparatus - Antennas and Test Sites for Radiated Disturbance Measurements*, IEC Standard, Ed. 3.1, July 2012.

[2] IEC 61000-4-3: *Electromagnetic Compatibility (EMC) - Part 4-3: Testing and Measurement Techniques - Radiated, Radio-Frequency, Electromagnetic Field Immunity Test*, IEC Standard, Ed. 3.1, Apr. 2008.

[3] L. H. Hemming, *Electromagnetic Anechoic Chambers: A Fundamental Design and Specification Guide*. New York: Wiley-IEEE Press, 2002.

[4] Available: *https://www.cst.com/Applications/Article/Intelligent-Representation-Of-Anechoic-Chamber-Wall-Cuts-Electromagnetic-Simulation-Time-95*

[5] D. Campbell, G. Gampala, C. J. Reddy, M. Winebrand, and J. Aubin, "Modeling and analysis of anechoic chamber using CEM tools," in *Proceedings of AMTA Conference*, Bellevue, 2012.

[6] N. V. Kantartzis and T. D. Tsiboukis, "Wideband numerical modelling and performance optimisation of arbitrarily-shaped anechoic chambers via an unconditionally stable time-domain technique," *Electrical Engineering*, vol. 88, iss. 1, pp. 55-81, Nov. 2005.

[7] B. K. Chung, C. H. The, and H. T. Chuah, "Modeling of anechoic chamber using a beam-tracing technique," *Progress In Electromagnetics Research (PIER)*, vol. 49, pp. 23-38, 2004.

[8] S. R. Mishra and T. J. F. Pavlasek, "Design of absorber-lined chamber for EMC measurements using a geometrical optics approach," *IEEE Trans. Electromagnetic Compatibility*, vol. EMC-26, no. 3, pp. 111-119, Aug. 1984.

[9] M. K. Mansour and J. Jarem, "Anechoic chamber

design using ray tracing and theory of images," in *IEEE Southeastcon '90 Proceedings*, New Orleans, pp. 689-695, 1990.

[10] C. L. Holloway and E. F. Kuester, "Modeling semi-anechoic electromagnetic measurement chambers," *IEEE Trans. Electromagnetic Compatibility*, vol. 38, no. 1, pp. 79-94, Feb. 1996.

[11] M. Lin, J. Ji, C. G. Hsu, and H. Hsieh, "Simulation and analysis of EMC chambers by ray tracing method," in *IEEE International Symposium on Electromagnetic Compatibility*, Honolulu, pp. 1-4, 2007.

[12] S. M. J. Razavi, M. Khalaj-Amirhosseini, and A. Cheldavi, "Minimum usage of ferrite tiles in anechoic chambers," *Progress In Electromagnetics Research B (PIER B)*, vol. 19, pp. 367-383, 2010.

[13] B. K. Chung and H. T. Chuah, "Modeling of RF absorber for application in the design of anechoic chamber," *Progress In Electromagnetics Research, (PIER)*, vol. 43, pp. 273-285, 2003.

[14] E. F. Kuester and C. L. Holloway, "A low-frequency model for wedge or pyramid absorber arrays-I: Theory," *IEEE Trans. Electromagnetic Compatibility*, vol. 36, no. 4, pp. 300-306, Nov. 1994.

[15] C. A. Balanis, *Advanced Engineering Electromagnetics*. John Wiley & Sons, 1989.

[16] C. Yang, B. Wu, and C. Ko, "A ray-tracing method for modeling indoor wave propagation and penetration," *IEEE Trans. Antennas Propagat.*, vol. 46, no. 6, pp. 907-919, June 1998.

[17] C. Saeidi, A. Fard, and F. Hodjatkashani, "Full three-dimensional radio wave propagation prediction model," *IEEE Trans. Antennas Propagat*., vol. 60, no. 5, pp. 2462-2471, May 2012.

[18] M. Bruns, *Automated Fabrication: Improving Productivity in Manufacturing*. Prentice Hall, 1993.

[19] IEEE Std. 1128-1998: *IEEE Recommended Practice for Radio-Frequency (RF) Absorber Evaluation in the Range of 30 MHz to 5 GHz*, IEEE Standard, Apr. 1998.

[20] J. Jin, *The Finite Element Method in Electromagnetics*. 3rd Ed., Wiley, 2014.

[21] V. P. Kodali, *Engineering Electromagnetic Compatibility: Principles, Measurements, Technologies, and Computer Models*, 2nd Ed., New York: Wiley-IEEE Press, 2001.

[22] Q. Xu, Y. Huang, X. Zhu, L. Xing, P. Duxbury, and J. Noonan, "NSA simulation in semi-anechoic chamber using ray tube tracing method," *9th IET International Conference on Computation in Electromagnetics (CEM 2014)*, London, UK, Mar. 2014.

Qian Xu received the B.Eng. and M.Eng. degrees from the Department of Electronics and Information, Northwestern Polytechnical University, Xi'an, China, in 2007 and 2010, respectively, and the Ph.D. degree in Electrical Engineering from the University of Liverpool, Liverpool, U.K., in 2016.

He was an RF Engineer in Nanjing, China, in 2011, an Application Engineer with CST Company, Shanghai, China, in 2012, and a Research Assistant with the University of Liverpool, in 2016. He is currently an Associate Professor in College of Electronic and Information Engineering, Nanjing University of Aeronautics and Astronautics, Nanjing, China. His current research interests include anechoic chamber, reverberation chamber, computational electromagnetics and statistical electromagnetics.

Yi Huang received the B.Sc. degree in Physics from Wuhan University, Wuhan, China, in 1984, the M.Sc. (Eng.) degree in Microwave Engineering from the Nanjing Research Institute of Electronics Technology (NRIET), Nanjing, China, in 1987, and the D.Phil. degree in Communications from the University of Oxford, Oxford, U.K., in 1994.

He was a Radar Engineer with the NRIET, and a Member of Research Staff with the University of Birmingham, Birmingham, U.K., the University of Oxford, Oxford, U.K., and the University of Essex, Colchester, U.K. He was a Research Fellow with the British Telecom Laboratories in 1994, and then with the Department of Electrical Engineering & Electronics, University of Liverpool, Liverpool, U.K., as a Faculty Member, in 1995, where he is currently a Full Professor of Wireless Engineering, the Head of High Frequency Engineering Research Group, M.Sc. Program Director, and the Deputy Head of Department. He has authored over 200 refereed papers in leading international journals and conference proceedings, and is the Principal Author of the popular book Antennas: from Theory to Practice (Wiley, 2008). He has received many research grants from research councils, government agencies, charity, EU, and industry, acted as a Consultant to various companies, and served on a number of national and international technical committees. His current research interests include wireless communications, applied electromagnetics, radar, and antennas.

Huang is a Fellow of the IET. He has been an Editor, and an Associate Editor or a Guest Editor of

four international journals. He has been a Keynote/ Invited Speaker and Organizer of many conferences and workshops (e.g., IEEE iWAT 2010, WiCom 2006, 2010, and LAPC2012). He is currently the Editor-in-Chief of Wireless Engineering and Technology, Associate Editor of the IEEE Antennas and Wireless Propagation Letters, and a U.K. and Ireland Rep. to the European Association of Antennas and Propagation.

Two-Section Impedance Transformer Design and Modeling for Power Amplifier Applications

Sobhan Roshani* and Saeed Roshani

Department of Electrical Engineering, Kermanshah Branch, Islamic Azad University, Kermanshah, Iran

Abstract ─ In this paper, two-section impedance transformer network (TSITN) is modeled and used for power amplifiers applications. The artificial neural network (ANN) is used to propose an appropriate model for TSITN. The proposed model could predict the desired input and output impedances at desired frequencies using TSITN dimensions, which could be suitable for input and output matching network of a power amplifier. Using two-section impedance transformer network instead of conventional impedance transformer network (ITN) could miniaturize the input and output matching network size.

Index Terms ─ Matching network, neural network, power amplifier, two-section impedance transformer network.

I. INTRODUCTION

Conventional transformers, like quarter-wave impedance transformer, suffer from several disadvantages, such as narrow bandwidth and large size [1-2]. The two-section transformer is firstly proposed in [3], which could operate at main frequency and its second harmonic. In [1], a TSITN is analyzed and the closed form equations are obtained for resistive real impedance matching. In [4], the TSITN working at two arbitrary frequencies is studied and analyzed. The main problem of these typical two-section transformers is that they are only analyzed and designed to transfer impedance to only resistive real impedance. However, according to the load pull and source pull analyses in power amplifier applications, complex impedance with real and imaginary parts is needed.

A TSITN, which could be used in dual band systems, is reported in [5]. The presented TSITN could match two complex impedances at two different frequencies. Another ITN is presented in [6]. The presented ITN in this work could match two frequency variant complex impedances at two different frequencies. This ITN could be used for power amplifier circuits with frequency variant load impedances.

A Quad-Band Four-Section ITN is designed and analyzed in [7], however the equations are complicated and PSO optimization algorithm is used to find the required design parameters. The PSO algorithm is also used in [8] to find the design parameters of the ITN.

So far, impedance transformer networks have been used in several microwave devices, such as: power amplifiers [9-11], LNAs [12], phase shifters [13] and other microwave devices.

In power amplifiers applications, transformer networks are commonly used for Doherty power amplifiers; however, they could be used for any types of amplifiers, such as class A and other classes of amplifiers. In most of the cited works, the TSITN is only analyzed for matching at resistive real impedance, which is not suitable for power amplifier applications. Also, a few approaches provide analyses of two-section ITN and other types of ITN for complex impedances matching with time consuming numerical calculations [5], [14-16]. To the best knowledge of the authors, there is not any approach to derive the closed form equations for analysis of TSITN for complex impedances matching applications.

According to the mentioned problems for two-section transformers, a model which could predict the desired input and output impedances at desired frequencies using TSITN dimensions is still matter of challenge and discussion. In this paper, two ANN models are proposed for TSITN for power amplifier applications. The proposed models could predict the specifications of TSITN, which ease the design process of the amplifier input and output matching circuits.

II. TWO-SECTION ITN

A typical TSITN is depicted in Fig. 1. The TSITN includes two transmission lines with different dimensions. The transformer network could match input impedance of Z_{in} to output impedance of Z_{out}. Therefore, this network could be used in the input or the output of the circuits like power amplifiers. This network is suitable to match the obtained impedance from source pull or load pull analyses to the desired circuit. The relation between input and output impedances in Fig. 1 can be defined as:

$$Z_{out\,2} = Z_2 \frac{Z_{out} + jZ_2 \tan(\theta_2)}{Z_2 + jZ_{out} \tan(\theta_2)}, \quad (1)$$

Submitted On: August 27, 2017
Accepted On: October 4, 2017

$$Z_{in} = Z_1 \frac{Z_{out\,2} + jZ_1 \tan(\theta_1)}{Z_1 + jZ_{out\,2} \tan(\theta_1)}, \quad (2)$$

where, Z_{in} and Z_{out} are complex impedances. The other parameters in Equations (1) and (2) are defined in Fig. 1. As seen in these equations, there are four variables (Z_1, θ_1, Z_2 and θ_2) within two equations, so, there is no unique answer to TSITN dimensions. Subsequently, the ANN modelling is presented in this paper, to predict the TSITN dimensions. A typical power amplifier matching network is shown in Fig. 2 (a). As can be seen in this figure, the output matching network should match Z_{loud} to Z_0 at the drain of the active device. Also, the input matching network should match Z_{source} to Z_0 at the gate of the active device. According to Fig. 2 (b), two-section ITN could be applied at the input and output of the circuit to match the desired impedance.

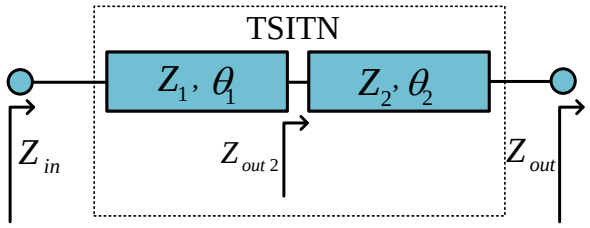

Fig. 1. A typical TSITN.

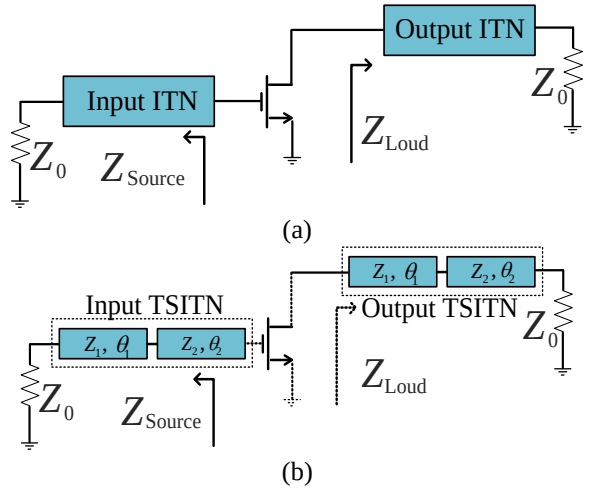

Fig. 2. (a) A typical power amplifier matching network. (b) Applied TSITN for matching network of the power amplifier.

III. PRESENTED ANN MODEL FOR TSITN

As shown in Fig. 2, the TSITN could be used as input or output matching network. For the case in which TSITN is considered as the output matching circuit of the amplifier, the value of Z_{out} in Fig. 1 is considered as Z_0, while Z_{in} in Fig. 1 is considered as complex impedance. Design of TSITN for input matching of the power amplifier is similar to design of TSITN for output matching, so, only design and modeling of TSITN for output matching is considered, in this paper. For prediction of the desired Z_{in}, an ANN model of TSITN is proposed, as shown in Fig. 3. According to this model, the desired complex impedance in any frequency could be predicted, using dimensions of the TSITN. The frequency is arbitrary parameter in the presented model; therefore, this model could be used in any power amplifier circuits. A TSITN is simulated and designed in computer aided design software, advanced design system (ADS) 2008, to acquire the database for the proposed ANN model. The TSITN is simulated in ADS schematic design section using S-parameters analysis. The S-parameter analysis in ADS could calculate the scattering parameters (S-parameters) of a circuit and convert scattering parameters to Z-parameters. After simulating several TSITNs with different dimensions and obtaining the impedances in different frequencies, 150 data of input and output parameters are extracted to form the database. The TSITN is modeled with multi-layer perceptron (MLP) and radial basis function (RBF) networks in this paper, which will be described in subsections A and B, respectively. The proposed ANN networks are trained and tested using MATLAB R2012b software. The MATLAB built-in functions of "newff" and "newrb" are utilized in the proposed MATLAB codes for MLP and RBF networks, respectively.

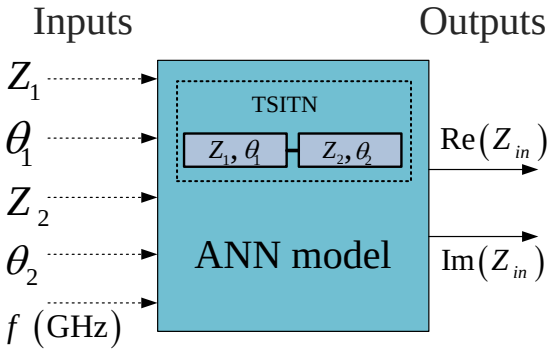

Fig. 3. The proposed ANN model for TSITN.

A. MLP network

MLP neural network is a feedforward network, which uses backpropagation algorithm for finding the weights between neurons. The MLP network has three main layers (input, hidden and the output layers). The hidden layer may include one layer or several layers. The number of hidden layers is chosen, according to the problem and data set. In most of applications, high precision could be achieved with only one layer or two layers [17]. The neuron numbers in the ANN layers can be selected proportional to the data and the number of output/input parameters. Higher number of neurons or hidden layers may increase the accuracy of the network,

but it could raise the complexity and simulation time of the network. MLP networks are presented, according to conditions of the defined network shown in Fig. 3. Several MLP structures have been tested and the best network is chosen to model the presented circuit. The total number of data set is 150, which is constant during the simulation in all of the ANNs, in this paper. The data are normalized and about 80% of data are considered for testing and the rest are considered for training process. Several MLP structures with different number of neurons and hidden layers are tested, to find the best network. Error results of different MLP structures are shown in Table 1. Each network is applied 100 times with number of epoch 3000 and the best error results are listed in the table. Mean absolute and root mean squared errors (MAE and RMSE) of different presented networks are reported in this paper to compare the precision of the networks. The errors for each considered output is reported in Table 1. Effects of different number of neurons on the MLP networks MAE are shown in Fig. 4. According to Fig. 4, approximately, the errors decrease, as the number of neurons increases. However, high number of layers and neurons increase the simulation time and complexity of the network and may result in over-fitting of the network. Therefore, the network with 7 neurons in each layer is assumed as the best structure with the best error results. The best configuration for the presented MLP is shown in Fig. 5.

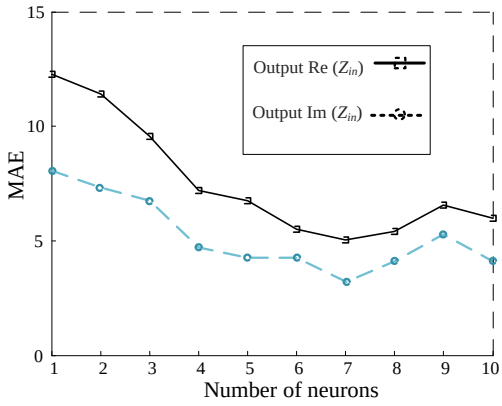

Fig. 4. The MAE of MLP networks versus different number of neurons.

In this paper, MAE and RMSE errors are calculated for all of the presented neural networks, using the following equations:

$$\mathrm{MAE} = \frac{\sum_{i=1}^{N} |Y_{\mathrm{Re}i} - Y_{\mathrm{Pr}i}|}{N}, \tag{3}$$

$$\mathrm{RMSE} = \sqrt{\frac{\sum_{i=1}^{N} (Y_{\mathrm{Re}i} - Y_{\mathrm{Pr}i})^2}{N}}. \tag{4}$$

In Equations (3) and (4), N is total number of data, while $Y_{\mathrm{Re}i}$ and $Y_{\mathrm{Pr}i}$ are respectively, real and predicted outputs of the network. Real and predicted values of Re (Z_{in}) and Im (Z_{in}) for the best obtained MLP networks are shown in Figs. 6 and 7, respectively. According to these figures, the presented MLP model has modeled the TSITN, accurately.

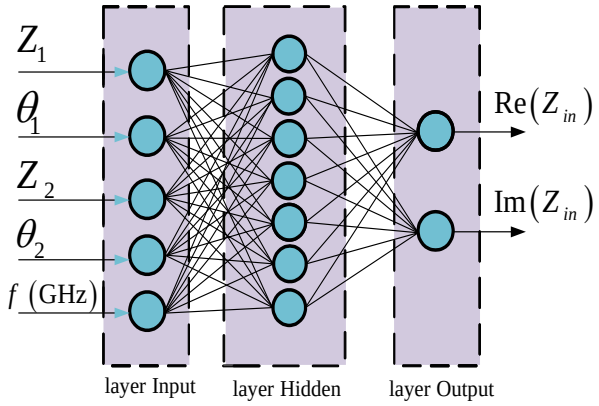

Fig. 5. Structure of the best presented MLP neural network.

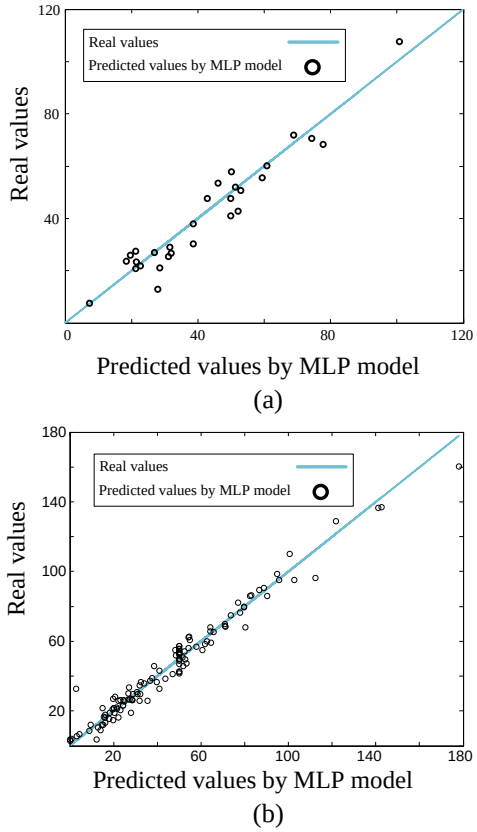

Fig. 6. Real and predicted values comparison, using the best obtained MLP structure for real part of Z_{in}: (a) test and (b) train data.

Table 1: Obtained results for different structures of MLP networks

Number of Neurons	MAE Test-Re (Zin)	RMSE Test-Re (Zin)	MAE Test-Im (Zin)	RMSE Test-Im (Zin)
1	12.27	18.48	8.05	13.74
2	11.41	18.18	7.34	9.39
3	9.56	18.43	6.75	8.18
4	7.20	12.71	4.70	7.08
5	6.75	8.59	4.26	5.42
6	5.50	8.07	4.25	5.91
7	5.15	6.38	3.61	4.73
8	5.40	7.06	4.10	8.20
9	6.55	8.55	5.27	7.77
10	5.99	9.89	4.10	6.13

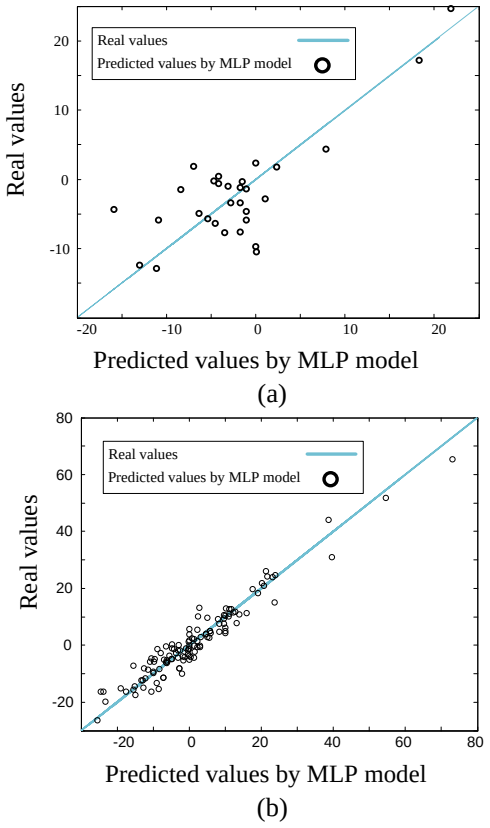

Fig. 7. Real and predicted values comparison, using the best obtained MLP structure for imaginary part of Z_{in}: (a) test and (b) train data.

B. RBF network

RBF ANN is a feedforward ANN and its structure is similar to MLP network. However, the RBF network has one hidden layer and the activation functions are radial basis functions [18]. Conventional structure of a RBF ANN is depicted in Fig. 8. The outputs of neurons in hidden layer will be summed, by the output layer neurons. This procedure is defined in Equations (5) and (6):

$$q_i = \exp\left(-\frac{\|X_i - C_i\|^2}{\sigma_i^2}\right), \quad (5)$$

$$y = \sum_{i=1}^{n} w_i q_i . \quad (6)$$

In Equations (5) and (6), the parameter X shows input vector of the hidden layer, y shows output of the network, C is center of the basis function and σ is the Gaussian function spread. Parameters of presented RBF model is listed in Table 2. The obtained results of the presented RBF model is listed in Table 3.

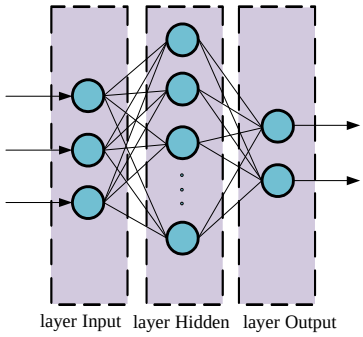

Fig. 8. Typical RBF structure.

Table 2: Parameters of presented RBF model

Hidden layer function	Radial basis
Output layer function	Linear
Input neuron numbers	5
Output neuron numbers	2
Maximum number of neurons	100
Train data numbers	120
Test data numbers	30

IV. RESULTS OF THE PROPOSED MODELS

The obtained RMSE and MAE results of the presented models using MLP and RBF ANNs are listed in Table 3. The errors are reported for both real and imaginary parts of the predicted Z_{in}. According to the results, two proposed MLP and RBF networks have modeled the TSITN in different frequency ranges, precisely.

Table 3: Obtained results for presented MLP and RBF networks

Errors	ANN	
	MLP	RBF
MAE-train for Re (Zin)	3.97	0.11
MAE-train for Im (Zin)	2.90	0.11
MAE-test for Re (Zin)	5.15	7.85
MAE-test for Im (Zin)	3.61	4.86
RMSE-train for Re (Zin)	5.59	0.22
RMSE-train Im (Zin)	3.76	0.20
RMSE-test for Re (Zin)	6.38	14.31
RMSE-test for Im (Zin)	4.73	8.36

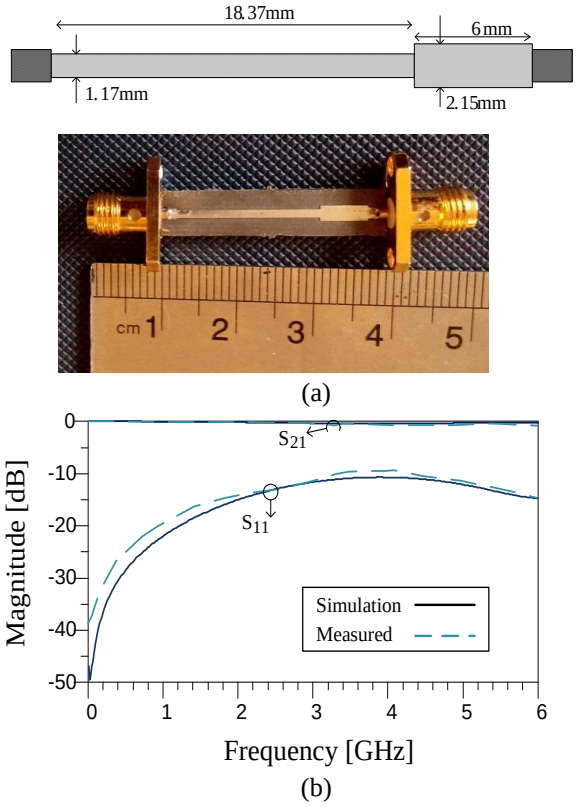

Fig. 9. (a) Layout, photograph, and (b) frequency response of the fabricated impedance transformer.

A. Data validation

For validation of the impedance transformer network proposed model, the data of a sample TSITN is applied to the proposed model. The layout and photograph of the fabricated TSITN are depicted in Fig. 9 (a). The obtained S_{11} and S_{21} of the fabricated TSITN are illustrated in Fig. 9 (b). The specifications of the applied substrate is $\varepsilon_r = 2.2$ and thickness = 0.508 mm. This TSITN transfers 50 Ω output matching port to (52.23 + 7.67j) Ω in the output of the desired power amplifier at 1 GHz. After applying this data to the proposed MLP model, the predicted value was obtained (42.65 + 9.59j) Ω, which shows acceptable accuracy for validation data.

V. CONCLUSION

In this paper, MLP and RBF networks are presented to model two-section impedance transformer network for power amplifier and impedance matching applications. The presented models could describe the impedance transformer network behavior versus the different frequencies. Compared to the other impedance transformer design approaches in which the complicated and time consuming equations should be solved for finding the design parameters, the presented model can easily predict the design parameters of impedance transformer using artificial neural networks. Several structures have been tested to find the best network, which can model the presented impedance transformer, accurately. Finlay, data of a fabricated transformer is applied to the proposed model. The results show that the presented model is accurate and could be considered as reliable model for high frequency amplifiers with desired transforming matching values.

ACKNOWLEDGMENT

The authors would like to thank the Kermanshah Branch, Islamic Azad University for the financial support of this research project.

REFERENCES

[1] C. Monzon, "Analytical derivation of a two-section impedance transformer for a frequency and its first harmonic," *IEEE Microw. Wireless Comp. Lett*., vol. 12, pp. 381-382, 2002.

[2] T. K. Ishii, *Microwave Engineering*. Oxford University Press on Demand, 1989.

[3] Y. L. Chow and K. L. Wan, "A transformer of one-third wavelength in two sections-for a frequency and its first harmonic," *IEEE Microw. Wireless Comp. Lett*., vol. 12, no. 1, pp. 22-23, 2002.

[4] C. Monzon, "A small dual-frequency transformer in two sections," *IEEE Trans. Microwave Theory Tech*., vol. 51, pp. 1157-1161, 2003.

[5] Y. Wu, Y. Liu, and S. Li, "A dual-frequency transformer for complex impedances with two unequal sections," *IEEE Microw. Wireless Comp. Lett*., vol. 19, pp. 77-79, 2009.

[6] X. Liu, Y. A. Liu, S. Li, F. Wu, and Y. A. Wu, "Three-section dual-band transformer for freq-uency-dependent complex load impedance," *IEEE Microw. Wireless Comp. Lett*., vol. 19, pp. 611-613, 2009.

[7] H. Jwaied, F. Muwanes, and N. Dib, "Analysis and design of quad-band four-section transmission line impedance transformer," *Applied Computational Electromagnetics Society (ACES) Journal*, vol. 22, no. 3, pp. 381-387, 2007.

[8] M. Khodier, "Design and optimization of single, dual, and triple band transmission line matching transformers for frequency-dependent loads," *Applied Computational Electromagnetics Society (ACES) Journal*, vol. 24, no. 5, pp. 446-452, 2009.

[9] M. Hayati and S. Roshani, "A broadband Doherty power amplifier with harmonic suppression," *AEU-Int. J. Electron. C*., vol. 68, pp. 406-412, 2014.

[10] P. Saad, P. Colantonio, L. Piazzon, F. Giannini, K. Andersson, and C. Fager, "Design of a concurrent dual-band 1.8-2.4-GHz GaN-HEMT Doherty power amplifier," *IEEE Trans. Microwave Theory Tech*., vol. 60, pp. 1840-1849, 2012.

[11] M. Hayati and S. Roshani, "A novel miniaturized

power amplifier with nth harmonic suppression," *AEU-Int. J. Electron. C.*, vol. 68, pp. 1016-1021, 2014.

[12] P. Mousavi, M. Fakharzadeh, S. H. Jamali, K. Narimani, M. Hossu, H. Bolandhemmat, G. Rafi, and S. Safavi-Naeini, "A low-cost ultra low profile phased array system for mobile satellite reception using zero-knowledge beamforming algorithm," *IEEE Trans. Antennas Propag.*, vol. 56, no. 12, pp. 3667-3679, 2008.

[13] P. Mousavi, I. Ehtezazi, S. Safavi-Naeini, and M. Kahrizi, "A new low cost phase shifter for land mobile satellite transceiver," *IEEE Antennas and Propagation Society International Symposium*, vol. 2, pp. 229-232, July 2005.

[14] Q. He, Y. Liu, M. Su, and Y. Wu, "A compact dual-frequency transformer for frequency-dependent complex impedance load," in *IEEE Asia-Pacific Microwave Conference Proceedings (APMC)*, pp. 1241-1243, 2012.

[15] Y. Wu, Y. Liu, S. Li, C. Yu, and X. Liu, "A generalized dual-frequency transformer for two arbitrary complex frequency-dependent impedances," *IEEE Microw. Wireless Comp. Lett.*, vol. 19, no. 12, pp. 792-794, 2009.

[16] R. K. Barik, P. K. Bishoyi, and S. S. Karthikeyan, "Design of a novel dual-band impedance transformer," in *IEEE Conference on Electronics, Computing and Communication Technologies (CONECCT)*, pp. 1-4, July 2015.

[17] M. Hayati, F. Shama, S. Roshani, and A. Abdipour, "Linearization design method in class-F power amplifier using artificial neural network," *J. Comput. Electron.*, vol. 13, pp. 943-949, 2014.

[18] W. Yao, J. Fang, P. Zhao, S. Liu, J. Wen, and S. Wang, "TCSC nonlinear adaptive damping controller design based on RBF neural network to enhance power system stability," *J. Electr. Eng. Technol.*, vol. 8, pp. 252-261, 2013.

Sobhan Roshani received the B.Sc. degree in Electrical Engineering from Razi University, Kermanshah, Iran in 2010, M.Sc. degree in Electrical Engineering from Iran University of Science & Technology - IUST, Tehran, Iran in 2012 and Ph.D. in Electrical Engineering from Razi University in 2016. His research interest includes switching power amplifiers, microwave circuits, optimization and neural networks.

Saeed Roshani received the B.Sc. degree in Electrical Engineering from Razi University, Kermanshah, Iran in 2008, M.Sc. degree in Electrical Engineering from Shahed University, Tehran, Iran in 2011 and Ph.D. in Electrical Engineering from Razi University in 2015. He has published more than 40 papers in ISI Journals and Conferences and two books. His research interest includes the microwave and millimeter wave devices and circuits.

Radio Frequency Attenuation by Rocket Plume From Ground Study to In-flight Prediction

Éva Dieudonné [1,2], Abelin Kameni [1], Lionel Pichon [1], and David Monchaux [2]

[1] CentraleSupélec, Univ. Paris-Sud, Université Paris-Saclay
Sorbonne Universités, UPMC Univ Paris 06
3 & 11, rue Joliot-Curie, Plateau de Moulon 91192 Gif-sur-Yvette CEDEX, France
evadieudonne@outlook.fr, abelin.kameni@geeps.centralesupelec.fr, lionel.pichon@geeps.centralesupelec.fr

[2] CNES-DLA | Centre National d'Études Spatiales - Direction des lanceurs
52, rue Jacques Hillairet 75612 Paris CEDEX, France
david.monchaux@cnes.fr

***Abstract* –** Radio frequency communication between the space launcher and the mission control are unusually disturbed by the exhaust plume present in rocket engines. This paper presents the computation of radio wave propagation through the exhaust plume. Thus, frequency-domain finite element method and time-domain discontinuous Galerkin method are implemented for computations in case of a ground domain experiments. Numerical results compared to those obtained from ground experiment show good approximation of the propagation through the plasma over a wide frequency band. For the launcher in flight, an asymptotic method is proposed and has the advantage to give a fast evaluation of the scattering solution. In this case, the exhaust plume area is considered as a perfectly conducting trapezium whose parameters are extracted from the distribution of the plasma permittivity. Results related to the asymptotic method appear to be in good agreement with results based on the full wave approaches.

***Index Terms* –** Asymptotic method, electromagnetic, finite element, plasma, rocket plume, scattering.

I. INTRODUCTION

During a space flight, it is crucial to ensure and maintain the radio frequency (RF) communications between the launcher and the mission control. The high quality reception of radio waves is very important to guarantee security during the flight. Unfortunately, the propagation of emitted and received waves is disturbed by the exhaust plume of the launcher. Corrective measures can be established but are expensive. So, the interest of a sufficiently accurate predictive model is obvious.

The exhaust plume from the space launcher is inhomogeneous plasma whose behavior can be studied through computational fluid dynamic (CFD) models described by Navier-Stokes's and Vlasov's equations [1–4]. The plasma characteristics such as the permittivity, the collision frequency and the plasma frequency are deduced from those CFD models. Generally a frequency dependence of the permittivity is assumed and introduced in the Maxwell's equations whose resolution allows determining attenuation of RF transmission.

Today, only few works are dedicated to study RF transmission during a space flight [5–8]. The Kinefuchi team's has proposed to compute attenuation of RF waves with the plume in the cases of the ground experiment and the launcher in flight [5, 9, 10]. These works deal with all problems of jet impact on radio communications by addressing both, the chemical reactions within the engine, the CFD analysis of the plasma, and the electromagnetic interaction. The Fromentin-Denozière team's works also combine these different aspects to describe the electromagnetic signature of rocket engine plumes [8]. In this paper, aerothermochemical properties of the plume are computed and electromagnetic signature is obtained thanks to the study of the wave reflected by the plasma.

In these studies, numerical models of electromagnetic interaction are based on Finite Difference Time Domain method (FDTD). The computational domain is formed by the plasma whose shape has an important impact on the results. In case of simple shapes of the plasma, the FDTD method gives satisfactory results. Unfortunately practical rocket plumes are of arbitrary shape and the use of a staircase mesh in FDTD method may lead to significant errors.

Numerical calculation in 3D need RAM intensively and are time consuming. In [5], it was shown that 2D calculations are sufficient for the description of physical phenomena. In a 2D approach the electric field has only one component (out of plane component, z-component). However, high frequency calculations corresponding to the case where the wavelength is small compared to

Submitted On: March 28, 2017
Accepted On: August 12, 2017

the size of the plasma region still leads to heavy computational costs. It is why, in this case, an asymptotic method can be used for the prediction of the far field. Such diffraction method has been described in [11]. It considers that the far field scattered by the plasma is similar to the far field scattered by a perfectly conducting trapezium.

In this paper the attenuation of the radio frequency communication by a rocket plume of a spatial launcher is studied with 2D different methods. Two numerical discretization techniques are used for the computations: a frequency domain finite element method and a time domain discontinuous Galerkin method. Both of these methods are suited for unstructured meshes able to take into account arbitrary shapes of the rocket plume. They provide adequate tools for lowest frequencies. For high frequencies an asymptotic method has been developed using [12–14] and considers the plasma as a perfect conducting trapezium whose geometrical parameters are deduced from the distribution of permittivity.

The plasma is characterized by a frequency dependent permittivity given by the Drude relation:

$$\varepsilon_r(\omega) = 1 - \frac{\omega_p^2}{\omega(\omega - i\nu_e)}, \tag{1}$$

where ν_e is the electron collision frequency (s^{-1}), ω_p the plasma frequency (s^{-1}) and ω the frequency ($\omega = 2\pi f$, s^{-1}). The electron collision frequency is the probability of collision between an electron and another species. The plasma frequency describes the frequency at which the electron density varies in the plasma:

$$\omega_p = \sqrt{\frac{N_e q_e^2}{\varepsilon_0 m_e}}, \tag{2}$$

where N_e is electron density (m^{-3}), q_e is elementary electric charge (1.602×10^{-19} A·s), m_e is mass of an electron (9.109×10^{-31} kg), and ε_0 is permittivity of vacuum ($(36\pi \times 10^9)^{-1}$ $s^4 \cdot A^2 \cdot kg^{-1} \cdot m^{-3}$).

In this work, both cases regarding a ground experiment and the launcher in flight are studied. For the ground experiment, the plasma shape is a cylinder. For the launcher in flight, ν_e and ω_p are extracted from a map given in [5].

This paper is organized as follows: Section II presents the ground configuration. This configuration validates the numerical methods and gives first information about plasma properties. Section III presents the numerical methods used in ground configuration for the in-flight estimation. This section also presents an asymptotic method for a fast estimation of the in-flight attenuation.

II. GROUND EXPERIMENT

A. Configuration study

The ground experiment carried out by Kinefuchi team consists of two antennas placed on each side of a jet engine as in Fig. 1.

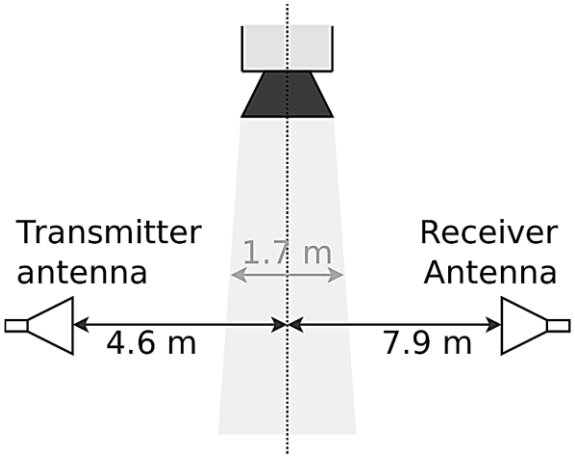

Fig. 1. Kinefuchi antenna setup in ground experiment (Fig. 2 in [10]).

A source antenna is placed at a distance 4.6 m and a receiving antenna is placed at 7.9 m. The thickness of the plasma is 1.7 m. The field is recorded versus time in order to divide the engine firing period into periods with distinct electromagnetic properties. Three periods can be observed: Early period, Middle period and Last period. The normalized diffracted field is obtained by the ratio between z-component of electric field E in the presence of the plasma and z-component of electric field E_0 without plasma: $|E/E_0|$ (Table 3 in [10], Table 2).

The method used in Kinefuchi works to estimate the parameters ν_e and ω_p, from experimental results is not described in [10]. In this work, we propose a method to obtain our own homogeneous parameters ν_e and ω_p.

Let define the attenuation L_{dB} (in dB) from the normalized scattered field E/E_0 as:

$$L_{dB} = -20\log_{10}\left(\left|\frac{E}{E_0}\right|\right). \tag{3}$$

Assuming that the plasma is a layer of thickness y, reflection is negligible compared to attenuation and under normal incident wave, it is possible to express E/E_0 in the following form:

$$\frac{E}{E_0} = \exp\left(-i\frac{\omega}{c}\sqrt{\varepsilon_r}y\right). \tag{4}$$

So L_{dB} can be written in this form (in $m \cdot s^{1}$), even if $\omega_p^2/(\omega^2 + \nu_e^2)$ is smaller than 1:

$$L_{dB} = \frac{20\log(e)}{c}\frac{q_e^2}{\varepsilon_0 m_e}\frac{1}{2}\left(\frac{N_e \nu_e y}{\omega^2 + \nu_e^2}\right), \tag{5}$$

$$L_{dB} = 4.6 \times 10^{-5}\left(\frac{N_e \nu_e y}{\omega^2 + \nu_e^2}\right). \tag{6}$$

This expression can be found in [2] (Equation 14) in $cm^2 \cdot s^{-1}$.

The curve $1/L_{dB}$ as a function of ω^2 is linear [15]:

$$\frac{1}{L_{dB}} = \left(\frac{1}{4.6\times10^{-5}N_e\nu_{ey}}\right)\omega^2 + \left(\frac{\nu_e^2}{4.6\times10^{-5}N_e\nu_{ey}}\right), \quad (7)$$

and it is easy to obtain the parameters ν_e and ω_p from Equation (7) where the slop a and the origin b are defined ($1/L_{dB} = a\omega^2 + b$):

$$\nu_e = \sqrt{\frac{b}{a}}, N_e = \frac{1}{4.6\times10^{-5}N_e a y}. \quad (8)$$

So we obtained (Table 1):

Table 1: Our parameters ν_e and ω_p obtained from the curve $1/L_{dB}$

	Early	Middle	Last
ν_e ($\times10^9$ s^{-1})	38.22	78.35	107.53
ω_p ($\times10^9$ s^{-1})	5.16	6.92	11.74

Our results of $\omega_p$and ν_e are close to those given in Table 2 in [10]. The value of ν_e in Last period is quite different from that given in [10]. The method used in [10] is not defined exactly so it's not possible to know how this value is obtained. However our values of ν_e give a better estimation of the attenuation for the frequency 5.6~GHz and 8.5~GHz (see Section C, Table 2).

B. Numerical modeling

The plasma is modeled as a cylinder as shown in the configuration given by Fig. 1. A time domain and a frequency domain approaches are used to describe attenuation of RF waves. Both methods use a triangular mesh to discretize more accurately the computational domain.

For the frequency domain computations, a Finite Element Method (FEM) is applied. This approach provides a fast response to a discrete set of frequencies. Many softwares are able to solve Maxwell equations with the finite element method. The commercial software COMSOL already used in our laboratory is employed.

For the time domain computations, a nodal Discontinuous Galerkin (DG) method is applied. The numerical code has been developed in our laboratory. This approach allows determining through one simulation, the RF waves attenuation for a frequency band defined by the transient incident signal. The DG method is suitable for high order spatial elements which allow to reduce dispersion error commonly encountered in FDTD methods, and to improve the solutions accuracy.

1) Frequency domain method

The symmetry of the system assumes to use half of the plasma and a Perfect Magnetic Conductor (PMC) boundary condition as shown in Fig. 2. The computational domain is surrounded by a Perfect Matched Layer (PML) of 1 m thickness. The spatial discretization in PML region is 5 elements per wavelength (λ/5), whereas it is 10 elements per wavelength λ/10) elsewhere. The excitation is generated by a dipole located at the point S and the electric field is recorded at the point R.

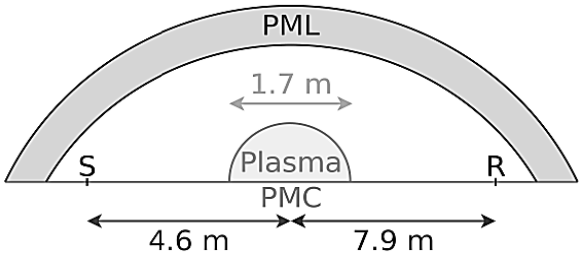

Fig. 2. Box calculation for 2D FEM (not to scale).

2) Time domain method

To easily deal with frequency dependence of the permittivity, the Maxwell-Ampère equation is rewritten in terms of conductivity:

$$\sigma(\omega) = -i\omega(\varepsilon_r - 1)\varepsilon_0. \quad (9)$$

Both Maxwell's equations, formed by the Faraday's law and the inverse Fourier transform of Ampère's law give us the following:

$$\mu_0\frac{\partial\vec{H}}{\partial t} + \vec{\nabla}\times\vec{E} = \vec{0}, \quad (10a)$$

$$\varepsilon_0\frac{\partial\vec{E}}{\partial t} - \vec{\nabla}\times\vec{H} + \sigma(t) * \vec{E} = \vec{0}, \quad (10b)$$

where "$*$" designed the convolution product of functions $\sigma(t)$ and $\vec{E}(t)$. Note that $\sigma(t)$ is the inverse Fourrier transform of $\sigma(\omega)$ obtained from the vector fitting technique [16] widely used in time domain modeling of dispersive media. The convolution term is computed thanks to an iterative process including the solutions at all the previous time steps [17]. This term is introduced in time domain computations as an explicit term.

A time domain DG method based on upwind fluxes is assumed in this work. The simulation domain is delimited by an efficient PML recently proposed for time domain scattering problems [18]. In the initial mesh, the spatial discretization is PML region is 0.33 element per wavelength, whereas it is 1 element per wavelength elsewhere. Elements of order p=8 are used in these computations. In this case, the number of nodes in an element is given by $0.5(p+1)(p+2)$.

The simulations consist in propagating a modulated Gaussian pulse with and without the plasma. This pulse is given by (11) with a frequency band between 0 and 10~GHz:

$$u(t) = \sin(2\pi f_0 t)\exp[-a(t-t_{ho})^2], \quad (11)$$

where $f_0 = 5.5$ GHz, $a = 2.4\times10^{19}$ s^{-1} and $t_{ho} = 7\times10^{-10}$ s.

C. Numerical results

Numerical results from FEM and DG computations

are compared to those provided by Kinefuchi's works (Table 3 in [10]).We also added a comparison to analytical results obtained from 1D approximation [19] (Plasma is assumed to be a layer with a thickness of 1.7 m) and Mie series [20] (Plasma is assumed to be a circular cylinder with a diameter of 1.7 m). The values obtained from these different methods are presented in Table 2.

Table 2. Comparison of experimental and numerical values of normalized scattered field

Frequency	Method	Early	Middle	Last
	Exp	0.199	0.174	0.039
	FDTD	0.188	0.129	0.102
2.3 GHz	1D	0.174	0.187	0.028
(S-Band)	Mie	0.250	0.271	0.147
	FEM	0.250	0.271	0.147
	DG	0.251	0.268	0.141
	Exp	0.319	0.258	0.022
	FDTD	0.310	0.200	0.034
5.6 GHz	1D	0.340	0.236	0.037
(C-Band)	Mie	0.303	0.196	0.021
	FEM	0.302	0.195	0.022
	DG	0.308	0.201	0.015
	Exp	0.519	0.300	0.063
	FDTD	0.424	0.241	0.024
8.5 GHz	1D	0.510	0.306	0.054
(X-Band)	Mie	0.510	0.298	0.072
	FEM	0.509	0.297	0.073
	DG	0.523	0.318	0.078

The 1D results are very close to the experimental values because this model was used to compute the parameters ω_p and ν_e. The difference is due to the fact that the straight line is not passing by all the points.

Both DG and FEM results are validated by comparison to the Mie solution. Mie solution matches the experimental results except for the low frequency. In fact, the good agreement between numerical and experimental data is due to the validity of homogeneous parameters for high frequencies.

DG method allows obtaining the entire frequency band with one calculation thanks to a Fourier transform of the recorded field. On the other hand, the FEM requires a calculation of each frequency. We display all the results on a graph versus frequency for comparison (Fig. 3).

The mean error calculation (relative to Mie) shows errors less than 1% for Early and Middle with FEM and less than 8% with DG. The error is greater for the Last period, less than 5\% for FEM and less than 18\% for DG. The high error obtained by the DG method is due to the increase of the relative error observed at low frequencies.

It is also observed that DG, FEM, Mie converge to the 1D solution when the frequency increases. This convergence shows that homogeneous parameters are even more acceptable if the frequencies are high. Therefore, high frequencies assumptions made in the 1D method, may allow obtaining a better estimation of the parameters for 2D calculations.

The methods studied for the ground configuration will be used by CNES in future work to validate CFD models.

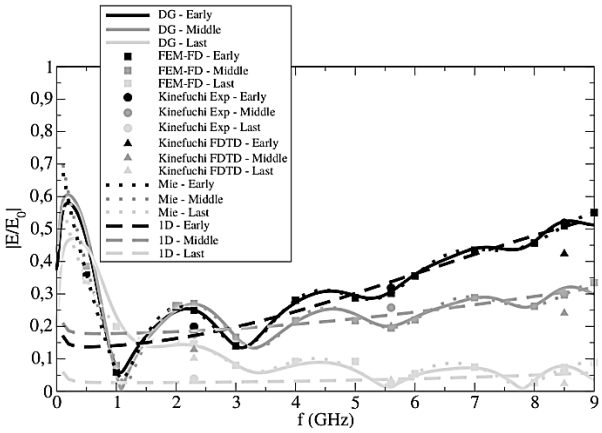

Fig. 3. Comparison of calculation methods for the normalized scattered field versus the frequency.

III. IN-FLIGHT ATTENUATION ESTIMATION

In this section the finite element method in frequency domain (FEM) and an asymptotic method based on the diffraction theory are used to calculate attenuation of RF waves during a flight. In the asymptotic method the plume geometry is considered as a trapezium. The advantage of such approach is to avoid a memory-intensive calculation FEM and to allow a fast estimation of the attenuation. The main difficulty is the choice of the trapezium parameters. In this work we propose a new method TIP^3 (Trapezium Isovalues Permittivity Predict Parameter) to derive these parameters from a map of the permittivity.

A. Configuration study

The rocket studied in this work is the second stage of the MV5 launcher flight at 85 km of altitude [5]. A look angle τ is introduced to describe the configuration at each altitude (Fig. 4).

Kinefuchi team performed CFD calculation deriving a map of ω_p and ν_e. Maps of ω_p and ν_e are extracted from Fig. 17 in [5] with a numerical code developed in MatLab and incorporate in FEM calculation (Fig. 5).

In-flight measurement of the attenuation L_{dB} is carried out at the frequency 300~MHz (Figs. 22 and 23 in [5], grey points in Fig. 7).

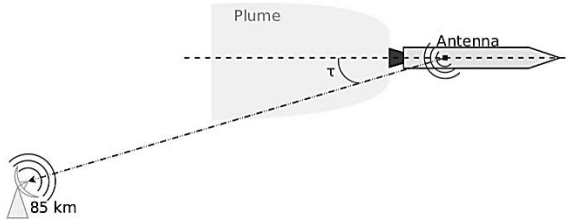

Fig. 4. In-flight configuration. Launcher fly at 85 km of the ground antenna, τ is the look angle (Fig. 1 in [5]).

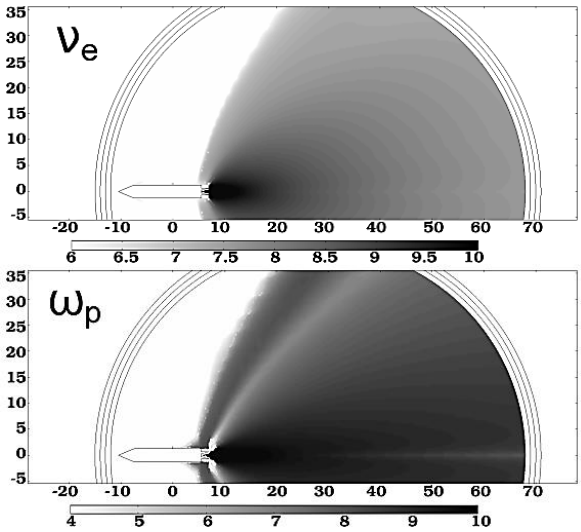

Fig. 5. Map of $\log_{10}(\omega_p)$ and $\log_{10}(\nu_e)$ in calculation domain.

B. 2D finite element method

The calculation domain is represented in Fig. 6.

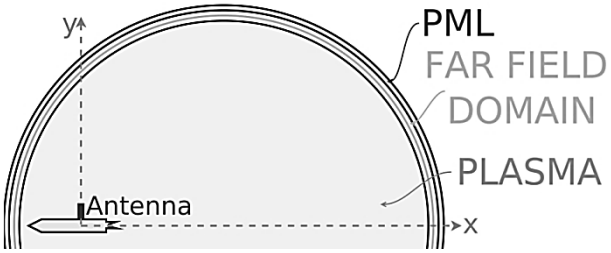

Fig. 6. Geometrical representation. Radiuses of the arc are 40 m, 41 m, 42 m and 43 m.

The far-field calculation is used for reducing the size of the computational domain, because attenuation is measured at 85 km of the launcher.

A cardioids antenna is placed at $x = 7$ m of the nozzle exit and at $y = 1.25$ m (radius of launcher) of the launcher middle.

The spatial discretization is 10 elements per wavelength (λ/10) and the domain is surrounded by a PML. The attenuation (in dB) is calculated and shown in Fig. 7.

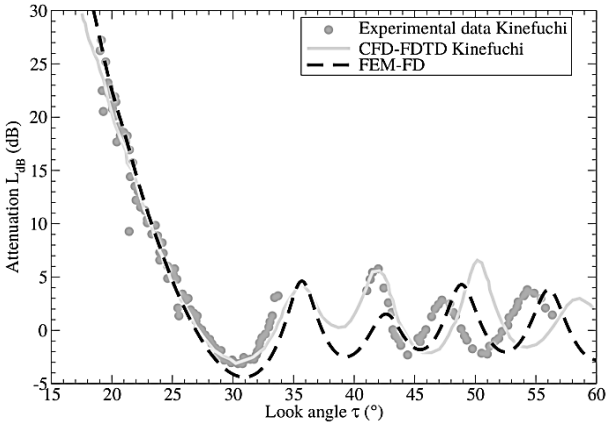

Fig. 7. Attenuation obtained by FEM.

A good agreement is observed between FEM and experimental data. The differences might be due to the poor quality of map of ω_p and ν_e resulting from the literature.

We perform simulations in frequency domain using the FEM method. The attenuation curves versus the look angle τ are shown for different frequency values in the Fig. 8.

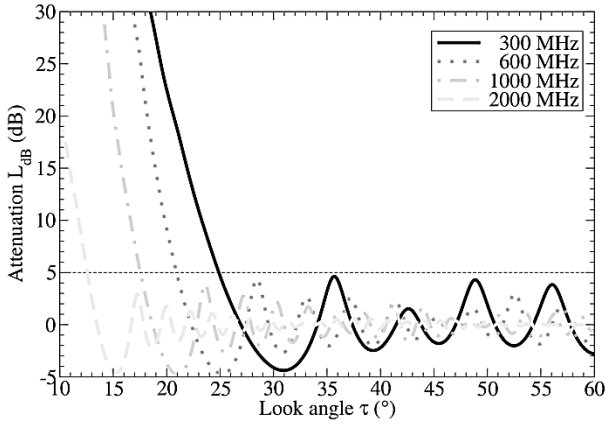

Fig. 8. Attenuation in dB obtained by the FEM method for different frequency values.

These curves present a similar behavior. We remark a shift of the first minimum. After this first minimum, attenuations remain below 5 dB. So even if the global curve is not correctly fitted, a good prediction of this minimum constitutes an interesting result. A statement of the look angle τ_{min} for which the first minimum occurs is shown in Fig. 13 (black points).

A linear regression (black curve in Fig. 13) is achieved and it shows a very good correspondence (all

points are on the function): Equation (12):

$$\tau_{min} = -84.80 + 115.75\lambda^{0.075}. \quad (12)$$

This equation allows an immediate obtaining of τ_{min} for any frequency between 200 MHz and 2 GHz.

C. Diffraction by trapezoidal perfect conductor

We propose in this section an asymptotic method for the prediction of the far field. The numerical code is developed in MatLab software. Trapezium parameters are defined in Fig. 9.

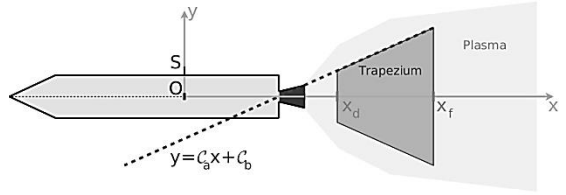

Fig. 9. Trapezium characteristics.

The objective is obtaining the trapezium characteristics directly from the permittivity. For beginning, the trapezium published in Kinefuchi's works [5] which have these properties is considered: $x_d = 20$ m, $x_f = 64$ m, $C_a = 0.43$ and $C_b = -2.61$. This trapezium is deduced to flight measurements. Unfortunately the in-flight measures are quite difficult to get.

That is why the trapezium parameters are extracted from the map of the permittivity. So we compared the trapezium of Kinefuchi [5] and the cartography of permittivity (Fig. 10).

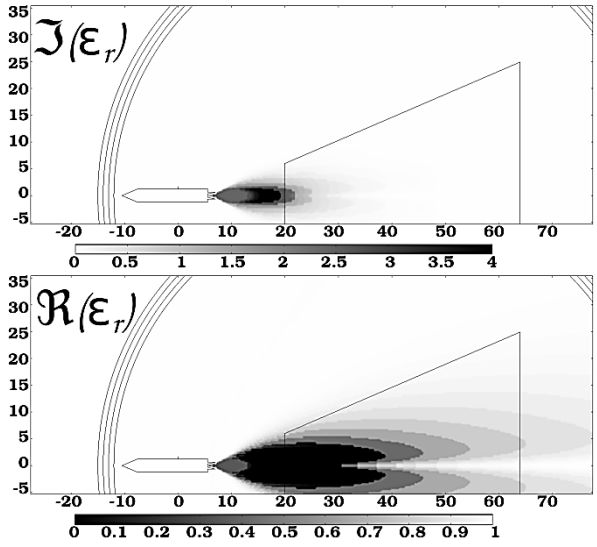

Fig. 10. Comparison between Kinefuchi trapezium and permittivity.

We observed that the basis of the trapezium near to the launcher corresponds to value 2.5 in the representation of $\Im(\varepsilon_r)$. We also observed that the basis of the trapezium far to the launcher corresponds to value 0.85 in the representation of $\Re(\varepsilon_r)$.

Isovalues of $\Im(\varepsilon_r) = 2.5$ and $\Re(\varepsilon_r) = 0.85$ are drawn and the correspondence between the adapted trapezium and the trapezium defined by these isovalues are confirmed (Fig. 11).

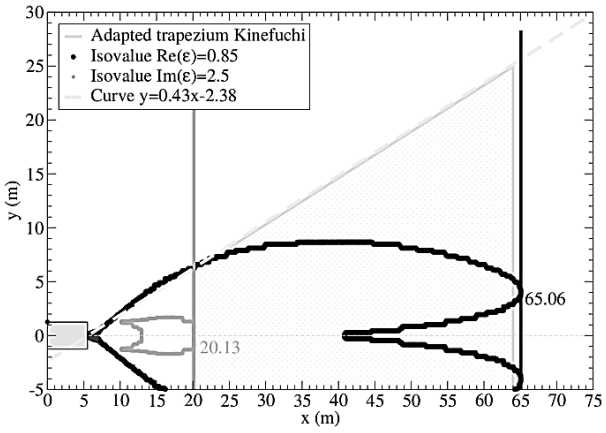

Fig. 11. Comparison between the trapezium of Kinefuchi and the trapezium defined by isovalues of the permittivity.

The maximum values of x for isovalues $\Im(\varepsilon_r) = 2.5$ and $\Re(\varepsilon_r) = 0.85$, give x_d and x_f. The slope of the trapezium is determined by the line passing through the center of the throat and the end of the nozzle, so $C_a = 0.43$ and $C_b = -2.38$.

This method is generalized to all frequencies. x_d and x_f for all frequencies are determined with the use of the isovalues like made for 300 MHz. Figure 12 shows the variations of x_d and x_f versus wavelength and linear regression.

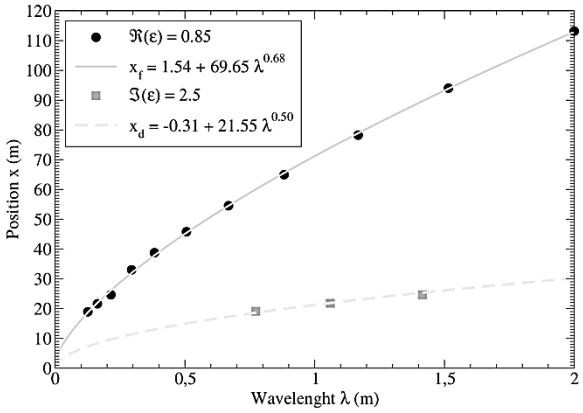

Fig. 12. x_d and x_f versus wavelength and linear regression.

The values x_d and x_f is given by:

$$x_d = -0.31 + 21.55\lambda^{0.50}, \quad (13)$$

$$x_f = 1.54 + 69.65\lambda^{0.68}. \quad (14)$$

The method TIP^{3}c is defined. This method gives the trapezium parameters: x_d by Equation (13), x_f by Equation (14), $C_a = 0.43$ and $C_b = -2.38$.

TIP^{3}c shows a significant difference in τ_{min} (Fig. 13) compared to FEM. The method TIP^{3}p is defined to correct that. This method gives the trapezium parameters: x_d by (13), x_f by Equation (14), C_a by Equation (15) and $C_b = -2.38$:

$$C_a = 0.06 + 0.39\lambda^{0.23}. \quad (15)$$

The values τ_{min} for methods TIP^3 and FEM are shown in Fig. 13.

Light-grey curve (TIP^{3}c) corresponds to black curve (FEM) with an error less than 5% in $\lambda = [0.565 - 1.090]$ m. So the value $C_a = 0.43$ given by the geometry of the nozzle is correct for this frequency range. It's interesting to remark that half of the nozzle opening (0.65 m) is included to this range. Grey curve (TIP^{3}p) has an error less than 5% up to $\lambda = 0.037$ m and also an error less than 1% up to $\lambda = 0.1$ m.

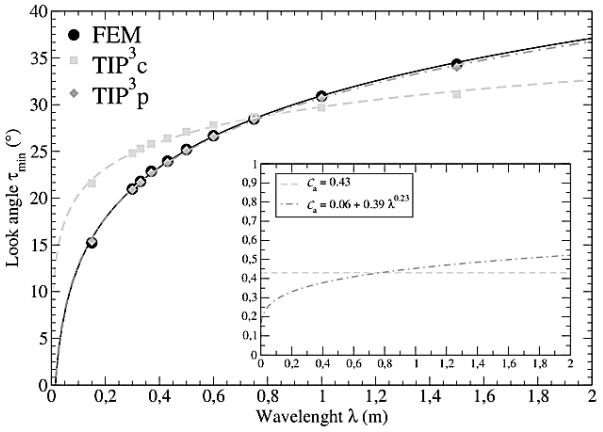

Fig. 13. τ_{min} dots: exact values and line: linear regression). Expression of C_a.

Some attenuation curves obtained from the FEM and the asymptotic methods using TIP^{3}p are shown in Fig. 14.

A good angular behavior is reproduced by the TIP^{3}p method. Nevertheless an overestimation of the attenuation after the first minimum τ_{min} is noted for frequency values beyond 600~MHz. The FEM computations show that this attenuation is smaller than 5 dB for greater angles than τ_{min}. With the TIP^{3}p method, the variations of attenuation more than 5 dB can be ignored for the angles greater than τ_{min}.

Figure 15 shows $\log_{10}(E/E_0)$ in plasma and TIP^{3}p perfectly conducting trapezium cases.

Interference fringe corresponding to the first minimum follow the slope of the trapezium. The trapezium serves as a mask increasing attenuation in the shadow. However the reflection at the corner of the trapezium scatters the field in the shadow of the trapezium, thus modifying the slope of the attenuation for a low angle. The position of the bases causes the first interference fringe to follow the slope of the trapezium.

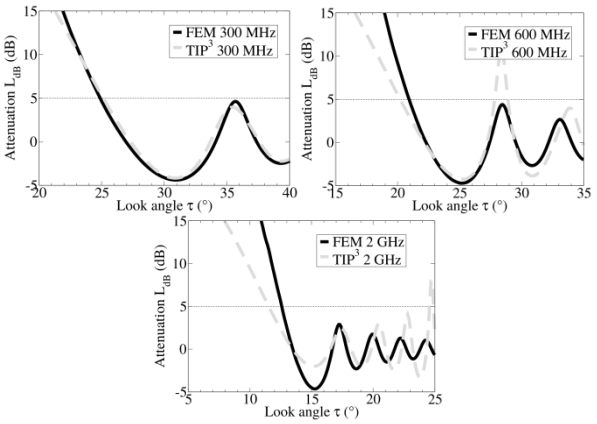

Fig. 14. Attenuation at 300 MHz, 600 MHz and 2 GHz.

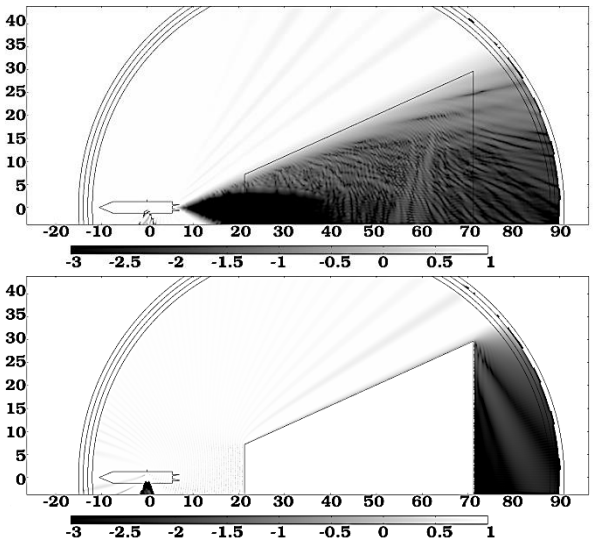

Fig. 15. Comparison between normed electric field in presence of the plasma and the normed electric field in presence of the TIP^{3}p perfectly conducting trapezium at 300 MHz ($\log_{10}$).

IV. CONCLUSION

In this paper the radio-frequency communication attenuation through a plasma rocket plume was studied using different methods.

The analysis of the ground experiment revealed the importance of the attenuation phenomena through the plasma. A frequency-domain finite element method (FEM) and a time domain discontinuous Galerkin method (DGTD) provided a good estimation of the attenuation. DGTD allows unstructured meshes while providing a

frequency response over a wide frequency band using a transient excitation. FEM gives a fast response for a discrete set of frequencies. The ground experiment gives an estimate of the parameters of the plasma and validates the calculation tools (CFD and FEM) in order to deduce the attenuation in-flight.

In the case of the launcher in flight, attenuation of RF communications is computed by the FEM method using maps of ν_e and ω_p from the literature. To face the problem of the heavy computational time that occurs with FEM approach for high frequencies, an asymptotic technique is presented. It is proposed when the shape of the plume is considered as a trapezium whose parameters are deduced from the knowledge of the permittivity distribution (TIP^{3}p). A complete validation was proposed for a wide range of frequency values. The numerical method dedicated to the diffraction by a perfectly conducting trapezium associated with the method TIP^{3}p allows a rapid estimation of the attenuation in-flight.

REFERENCES

[1] R. R. Mikatarian, C. J. Kau, and H. S. Pergament, "Fast computer program for nonequilibrium rocket plume predictions," *AeroChem TP-282*, 1972.

[2] L. D. Smoot and D. L. Underwood, "Prediction of microwave attenuation characteristics of rocket exhausts," *AIAA 6th Solid Propellant Rocket Conference*, 65-181, 1965.

[3] L. D. Smoot and T. J. Seliga, "Rocket exhaust plume radar attenuation and amplitude/phase noise," *J. Spacecraft*, 4, pp. 774-780, 1967.

[4] J. A. Blevins, R. A. Frederick, and H. W. Coleman, "An assessment of microwave measurement techniques in rocket exhaust applications," *32nd Aerospace Sciences Meeting & Exhibit*, 94-0671, 1994.

[5] K. Kinefuchi, K. Okita, I. Funaki, and T. Abe, "Prediction of in-flight radio frequency attenuation by a rocket plume by applying CFD/FDTD coupling," *49th AIAA/ASME/SAE/ ZSEE Joint Propulsion Conference*, 2013-3790, 2013.

[6] L. Glen McMillion, "A simple method for predicting RF attenuation through a rocket exhaust plume," *U.S. Army Research Office*, 1997.

[7] B. Van der Veek, S. Chintalapati, D. R. Kirk, H. Gutierrez, and R. F. Bun, "Modeling and validation of Ku-band signal attenuation through rocket plumes," *Journal of Spacecraft and Rockets*, 50, pp. 992-1001, 2013.

[8] B. Fromentin-Denozière, D. Gueyffier, and J. Simon, "Numerical modelling of the radar signature of rocket exhaust plumes," *International Conference on Electromagnetics in Advanced Applications (ICEAA 2012)*, pp. 400-403, 2012.

[9] K. Kinefuchi, I. Funaki, and T. Abe, "Frequency-dependent FDTD simulation of the interaction of microwaves with rocket-plume," *IEEE Transactions on Antennas and Propagation*, 58, pp. 3282-3288, 2010.

[10] K. Kinefuchi, I. Funaki, H. Ogawa, T. Kato, S. Tachikawa, T. Shimada, and T. Abe, "Investigation of micromawe attenuation by solid rocket exhausts," *47th AIAA Aerospace Science Meeting and Exhibit*, 2009-1386, 2009.

[11] K. Kinefuchi, I. Funaki, and T. Abe, "Prediction of in-flight frequency attenuation by rocket plume applying diffraction theories," *Journal of Spacecraft and Rockets*, 50, pp. 150-158, 2013.

[12] J. H. Whitteker, "Diffraction over flat-topped terrain obstacle," *Proceedings IEE*, 137, 1990.

[13] G. Millington, R. Hewitt, and F. S. Immirzi, "Double knife-edge diffraction in field-strength predictions," *Proceedings IEE*, 507, 1962.

[14] G. Millington, R. Hewitt, and F. S. Immirzi, "The Fresnel surface integral," *Proceedings IEE*, 508, 1962.

[15] K. M. Mphale, P. V. C. Luhanga, and M. L. Heron, "Microwave attenuation in forest fuel flames," *Combustion and Flame*, 154, pp. 728-739, 2008.

[16] B. Gustavsen and A. Semlyen, "Rational approx.-imation of frequency domain responses by vector fitting," *IEEE Trans. Power Delivery*, 14, pp. 1052-1061, 1999.

[17] M. Boubekeur, A. Kameni, L. Bernard, A. Modave, and L Pichon, "3-D modeling of thin sheets in the discontinuous Galerkin method for transient scattering analysis," *IEEE Trans. Magn*., 50, pp. 493-496, 2014.

[18] A. Modave, A. Kameni, J. Lambrechts, E. Delhez, L. Pichon, and C. Geuzaine, "An optimum PML for scattering problems in the time domain," *Eur. Phys. J. Appl. Phys*., 64, pp. 24502, 2013.

[19] É. Dieudonné, N. Malléjac, C. Amra, and S. Enoch, "Surface and bulk scattering by magnetic and dielectric inhomogeneities: A first-order method," *J. Opt. Soc. Am. A*, 30, pp. 1772-1779, 2013.

[20] J. Van Bladel, *Electromagnetic Fields*. John Wiley & Sons, pp. 743, 2007.